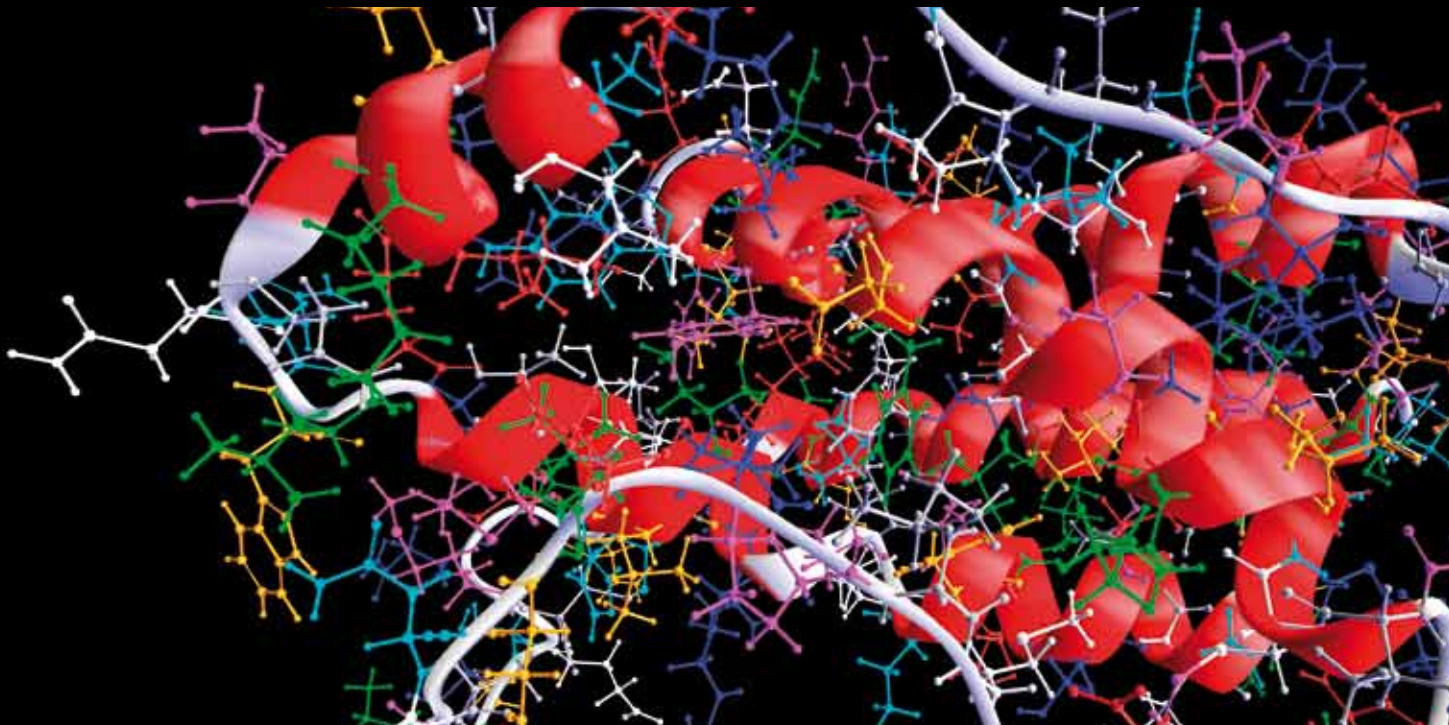


NUMERICAL METHODS AND APPLICATIONS IN BIOMECHANICAL MODELING

GUEST EDITORS: EDDIE Y. K. NG, HARVEY S. BOROVETZ, EDUARDO SOUDAH,
AND ZHONGHUA SUN





Numerical Methods and Applications in Biomechanical Modeling

Computational and Mathematical Methods in Medicine

Numerical Methods and Applications in Biomechanical Modeling

Guest Editors: Eddie Y. K. Ng, Harvey S. Borovetz,
Eduardo Soudah, and Zhonghua Sun



Copyright © 2012 Hindawi Publishing Corporation. All rights reserved.

This is a special issue published in “Computational and Mathematical Methods in Medicine.” All articles are open access articles distributed under the Creative Commons Attribution License, which permits unrestricted use, distribution, and reproduction in any medium, provided the original work is properly cited.

Editorial Board

Emil Alexov, USA
Georgios Archontis, Cyprus
Dimos Baltas, Germany
Chris Bauch, Canada
Maxim Bazhenov, USA
Thierry Busso, France
Carlo Cattani, Italy
Sheng-yong Chen, China
William Crum, UK
Ricardo Femat, Mexico
Alfonso T. García-Sosa, Estonia
Damien Hall, Australia

Volkhard Helms, Germany
Seiya Imoto, Japan
Lev Klebanov, Czech Republic
Quan Long, UK
C-M Charlie Ma, USA
Reinoud Maex, France
Simeone Marino, USA
Michele Migliore, Italy
Karol Miller, Australia
Ernst Niebur, USA
Kazuhisa Nishizawa, Japan
Hugo Palmans, UK

David James Sherman, France
Sivabal Sivaloganathan, Canada
Nestor V. Torres, Spain
Nelson J. Trujillo-Barreto, Cuba
Gabriel Turinici, France
Kutlu O. Ulgen, Turkey
Edelmira Valero, Spain
Jacek Waniewski, Poland
Guang Wu, China
Henggui Zhang, UK

Contents

Numerical Methods and Applications in Biomechanical Modeling, Eddie Y. K. Ng, Harvey S. Borovetz, Eduardo Soudah, and Zhonghua Sun
Volume 2013, Article ID 727830, 2 pages

Modeling the Chemoelectromechanical Behavior of Skeletal Muscle Using the Parallel Open-Source Software Library OpenCMISS, Thomas Heidlauf and Oliver Röhrle
Volume 2013, Article ID 517287, 14 pages

Contribution to the Determination of In Vivo Mechanical Characteristics of Human Skin by Indentation Test, Marie-Angèle Abellan, Hassan Zahouani, and Jean-Michel Bergheau
Volume 2013, Article ID 814025, 11 pages

Theoretical Hill-Type Muscle and Stability: Numerical Model and Application, S. Schmitt, M. Günther, T. Rupp, A. Bayer, and D. Häufle
Volume 2013, Article ID 570878, 7 pages

Influence of Distal Resistance and Proximal Stiffness on Hemodynamics and RV Afterload in Progression and Treatments of Pulmonary Hypertension: A Computational Study with Validation Using Animal Models, Zhenbi Su, Wei Tan, Robin Shandas, and Kendall S. Hunter
Volume 2013, Article ID 618326, 12 pages

Application of Computational Lower Extremity Model to Investigate Different Muscle Activities and Joint Force Patterns in Knee Osteoarthritis Patients during Walking, Kyung Wook Nha, Ariunzaya Dorj, Jun Feng, Jun Ho Shin, Jong In Kim, Jae Ho Kwon, Kyungsoo Kim, and Yoon Hyuk Kim
Volume 2013, Article ID 314280, 9 pages

Numerical Stability of Partitioned Approach in Fluid-Structure Interaction for a Deformable Thin-Walled Vessel, Kelvin K. L. Wong, Pongpat Thavornpattanapong, Sherman C. P. Cheung, and Jiyuan Tu
Volume 2013, Article ID 638519, 10 pages

The Robotic Lumbar Spine: Dynamics and Feedback Linearization Control, Ernur Karadogan and Robert L. Williams II
Volume 2013, Article ID 985248, 12 pages

Analytical Solutions for the Mathematical Model Describing the Formation of Liver Zones via Adomian's Method, Abdelhalim Ebaid
Volume 2013, Article ID 547954, 8 pages

Excitation-Contraction Coupling between Human Atrial Myocytes with Fibroblasts and Stretch Activated Channel Current: A Simulation Study, Heqing Zhan and Ling Xia
Volume 2013, Article ID 238676, 9 pages

Hybrid Mesh for Nasal Airflow Studies, Mohammed Zubair, Mohammed Zulkifly Abdullah, and Kamarul Arifin Ahmad
Volume 2013, Article ID 727362, 7 pages



Multiobjective Optimization Design of Spinal Pedicle Screws Using Neural Networks and Genetic Algorithm: Mathematical Models and Mechanical Validation, Yongyut Amaritsakul, Ching-Kong Chao, and Jinn Lin

Volume 2013, Article ID 462875, 9 pages

Standardization of Malaysian Adult Female Nasal Cavity, Chih Fang Lee, Mohd. Zulkifly Abdullah, Kamarul Arifin Ahmad, and Ibrahim Lutfi Shuaib

Volume 2013, Article ID 519071, 11 pages

Editorial

Numerical Methods and Applications in Biomechanical Modeling

Eddie Y. K. Ng,¹ Harvey S. Borovetz,² Eduardo Soudah,³ and Zhonghua Sun⁴

¹ *Nanyang Technological University, School of Mechanical and Aerospace Engineering, Singapore 639798*

² *Department of Bioengineering, University of Pittsburgh, Pittsburgh, PA 15261, USA*

³ *International Center for Numerical Methods in Engineering (CIMNE), Department of Biomedical Engineering, Universidad Politecnica de Catalunya, C/ Gran Capitan, s/n, 08034 Barcelona, Spain*

⁴ *Department of Imaging and Applied Physics, Curtin University, Perth, WA 6102, Australia*

Correspondence should be addressed to Eddie Y. K. Ng; mykng@ntu.edu.sg

Received 18 November 2013; Accepted 18 November 2013

Copyright © 2013 Eddie Y. K. Ng et al. This is an open access article distributed under the Creative Commons Attribution License, which permits unrestricted use, distribution, and reproduction in any medium, provided the original work is properly cited.

Numerical methods in biomedical research belong to a rapidly developing field which provides a state-of-the-art tool for biomedical research and applications. Reliable predictions will lead to patient-specific simulations in the next decade to improve the diagnosis and treatment of diseases. The main focus of this special issue is on the interface between numerical methods and biomedical applications for the human body. It is also interesting to have quantitative analysis from the molecular up to the whole organ level. The goal of this special issue is to bring together experts in related fields of computational biomedical research, for example, multiscale flow modeling, blood flow propagation, fluid-solid coupling, inverse problems in biomechanics, high performance computing of multiphysics discretization schemes, cardiovascular biomechanics, and porous media, to both foster engagement across areas of numerical methods and to identify novel applications to challenging biomedical modeling problems. The special issue has 12 papers and the details of these papers are as follows.

One paper presents the state-of-the-art parallelization technique taking advantage of the unique anatomical fiber architecture of skeletal muscles. The authors demonstrate the model's capability of simulating different aspects of nonisometric muscle contraction and the chemoelectromechanical behavior in complex skeletal muscles such as the tibialis anterior muscle.

The construction of artificial muscles is one of the most challenging developments in recent biomedical science. Another paper discusses the theoretical Hill-type muscle and stability model in determining the force-velocity relations of different animal species, which are based on the literature data from biological experiments. It showed that an antagonistic muscle actuator can help in stabilising a single inverted pendulum model in favour of a control approach using a linear torque generator.

One of the papers shows how the computational lower extremity model based on the inverse dynamic analysis and an optimization technique can be used to investigate different muscle activities and joint force patterns in knee osteoarthritis (OA) patients during walking. It provides insight into biomechanical changes in OA patients and evaluation of the postoperative functional outcomes of the OA treatments.

Another paper describes the use of an indentation test in determination of in vivo mechanical characteristics of human skin. It proposes a triphasic in vivo model of intact skin based on a general phenomenological thermohydrromechanical and physicochemical (THMPC) approach of heterogeneous media.

One of the papers develops a computational model based on measurements from a hypoxic neonatal calf model of pulmonary hypertension (PH) to investigate the interplay between vascular and ventricular measures in the setting of

progressive PH. Good agreement was observed between the 2D numerical model and the animal measurements. In the authors' simulated disease treatment, the model suggests that targeting proximal vascular remodeling, and in turn stiffness, may aid in recovery by further reducing RV afterload and power requirements.

Another paper proposes the analytical solutions for the mathematical model in describing the formation of liver zones via Adomian decomposition method with a system of nonlinear integropartial differential equations. This paper may shed light on the mathematical aspects of the formation of liver zones and explaining the distribution of two types of the liver cells.

One of the papers suggests creating a standardized nasal cavity model for adult Malaysian females. Computational fluid dynamic (CFD) analysis was performed to better understand the characteristics of the standardized model. The Malaysian female standardized model is larger in cross-sectional area when compared to the standardized Caucasian model, thus leading to lower average velocity magnitudes.

The accuracy of the numerical result is closely related to mesh density as well as its distribution. The aim of another paper is to evaluate the hybrid mesh with unstructured mesh and study its effect on the flow parameters inside the nasal cavity by considering the complexity of its anatomical architecture. The hybrid mesh reported lower grid convergence index (GCI) than the unstructured mesh and thus its usefulness in nasal airflow studies.

The mathematical analysis for optimizing numerical performance based on different time integration schemes that pertain to both the fluid and solid accelerations is presented in one of the papers. The choice of time integration schemes has a significant influence on the stability of fluid-structure interaction coupling. This implies that in addition to material and its geometric properties, the choice of time integration schemes is critical in determining the stability of the numerical computation.

Another paper studies an integrated myocyte-Isac-Fb electromechanical model to investigate the effect of fibroblasts (Fbs) and stretch activated ion channel current (Isac) on cardiac electrical excitation conduction and mechanical contraction. The numerical results indicated that Fbs and Isac coupling caused diverse effects on action potential morphology during repolarization, depolarized the resting membrane potential of the human atrial myocyte, slowed down wave propagation, and decreased strains in fibrotic tissue.

Medical schools can benefit from a tool, system, or method that will help instructors train students and assess their tactile proficiency throughout their education. The robotic lumbar spine has the potential to satisfy these needs in palpatory diagnosis. One of the papers demonstrates the dynamic model and nonlinear control of a 15-degree-of-freedom, cable-actuated robotic lumbar spine (RLS) that enables the solution of positive and continuous cable tensions for cable-actuated robots.

Another paper investigates the multiobjective optimization design of spinal pedicle screws using neural networks

and genetic algorithm to achieve an ideal with high bending and pullout performances simultaneously. The optimal design has significantly higher fatigue life and comparable pullout strength as compared with commercial screws.

In this special issue, we have provided examples of recent progress in computational and mathematical methods in biomedicine, for the benefit of students, researchers, health-care professionals, and teachers.

Acknowledgment

We thank the authors of these 12 papers for their contribution to this special issue.

Eddie Y. K. Ng
Harvey S. Borovetz
Eduardo Soudah
Zhonghua Sun

Research Article

Modeling the Chemoelectromechanical Behavior of Skeletal Muscle Using the Parallel Open-Source Software Library OpenCMISS

Thomas Heidlauf^{1,2} and Oliver Röhrle^{1,2}

¹ Universität Stuttgart, Institut für Mechanik (Bauwesen), Lehrstuhl II, Pfaffenwaldring 7, 70569 Stuttgart, Germany

² Stuttgart Research Centre for Simulation Technology, Pfaffenwaldring 5a, 70569 Stuttgart, Germany

Correspondence should be addressed to Thomas Heidlauf; thomas.heidlauf@mechbau.uni-stuttgart.de

Received 25 July 2013; Revised 28 August 2013; Accepted 13 September 2013

Academic Editor: Eduardo Soudah

Copyright © 2013 T. Heidlauf and O. Röhrle. This is an open access article distributed under the Creative Commons Attribution License, which permits unrestricted use, distribution, and reproduction in any medium, provided the original work is properly cited.

An extensible, flexible, multiscale, and multiphysics model for nonisometric skeletal muscle behavior is presented. The skeletal muscle chemoelectromechanical model is based on a bottom-up approach modeling the entire excitation-contraction pathway by strongly coupling a detailed biophysical model of a half-sarcomere to the propagation of action potentials along skeletal muscle fibers and linking cellular parameters to a transversely isotropic continuum-mechanical constitutive equation describing the overall mechanical behavior of skeletal muscle tissue. Since the multiscale model exhibits separable time scales, a special emphasis is placed on employing computationally efficient staggered solution schemes. Further, the implementation builds on the open-source software library OpenCMISS and uses state-of-the-art parallelization techniques taking advantage of the unique anatomical fiber architecture of skeletal muscles. OpenCMISS utilizes standardized data structures for geometrical aspects (FieldML) and cellular models (CellML). Both standards are designed to allow for a maximum flexibility, reproducibility, and extensibility. The results demonstrate the model's capability of simulating different aspects of nonisometric muscle contraction and efficiently simulating the chemoelectromechanical behavior in complex skeletal muscles such as the tibialis anterior muscle.

1. Introduction

Skeletal muscles' ability to actively generate force in a controlled fashion allows us to consciously move our body. The force generation is achieved through complex processes on multiple scales and multiple parts of the musculoskeletal system, for example, neural stimuli generation, depolarization at neuromuscular junctions, force generation within skeletal muscle sarcomeres, force transmission to the tendons, and sensory feedback to the nervous system. These processes are extremely complex, strongly coupled with each other, and by far not fully understood. Like in many other research areas, detailed simulation frameworks appealing to realistic models can provide an effective tool to investigate functional and structural interrelations of skeletal muscle force generation. An improved understanding of the physiological mechanisms may also lead to a better understanding of mechanisms behind musculoskeletal disorders.

State-of-the-art simulations taking into account the force generating capabilities of skeletal muscles are subject to either phenomenological descriptions using discrete [1–4] or continuum-mechanical models [5–7]. The most commonly used skeletal muscle modeling frameworks investigating the musculoskeletal system as a whole are based on discrete mechanics, that is, rigid-body dynamics simulations, in which the skeletal muscles are described by Hill-type models (cf. the review by Zajac [8]). Although such models are widely used to analyze movement, they exhibit significant drawbacks. All functional and structural properties are lumped together to a few parameters. For example, Hill-type skeletal muscle models are described at a point in space through spring constants, damper properties, and one overall activation level, and the calculated muscle force acts along a predefined line of action. Since such models lack a volumetric representation of the skeletal muscles, they are not capable of properly taking into account structural properties,

for example, complex fiber architectures, motor unit fiber distributions, or the interaction of a skeletal muscle with surrounding tissue, for example, bones, muscles, or fat tissue.

While continuum-mechanical skeletal muscle models can take into account complex muscle fiber distributions [9], regional activation properties, and a dynamically generated line of action [7], they are computationally more challenging and restrict their findings purely to mechanical aspects of muscle force generation; for example, see [6]. Further, researchers appealing to continuum-mechanical models mainly focus on skeletal muscles in isolation. However, considering natural motor unit (MU) recruitment principles to activate specific skeletal muscle fibers by action potentials (APs, electrical signals of short duration), one has to replace such single scale continuum-mechanical models with multi-scale, multiphysics models that take into account the entire pathway from neural stimulation to muscle force generation and feedback to the neural system.

Models describing the excitation-contraction coupling (ECC) do exist [10, 11] but are typically limited to describe the force generation within a sarcomere and, hence, on the cellular level and not on the level of an entire skeletal muscle. Models that are guided by either the natural principles of MU recruitment, MU fiber distributions, or muscle force generation on the cellular level and its effect on the force generation of an entire skeletal muscle are rare and do often have significant limitations. For example, Hernández-Gascón et al. [12] include a phenomenological description of the cellular processes and ignore biophysical principles of AP propagation and crossbridge dynamics. Fernandez et al. [13] use a neuron model to simultaneously generate an AP at all neuromuscular junctions that is propagated through the muscle tissue using the three-dimensional (3D) bidomain equations neglecting functional structures such as MU fiber distributions or the fact that APs propagate along a single muscle fiber and do not effect neighboring ones. Furthermore, the model describing the cellular behavior of a sarcomere was adopted from cardiac mechanics. Böl et al. [14] couple 3D electrical field equations with phenomenological fiber models. The model of Röhrle and coworkers is currently the only one that can take into account a biophysical cell model, which includes multiple subcellular models including fatigue, and allows for spatial descriptions, MU fiber distributions, MU recruitment principles, and skeletal muscle force generation [15–18].

However, the chemoelectromechanical model of Röhrle and coworkers has framework-inherent limitations that do not allow its extension to a fully coupled framework embracing neural inputs, force generation, and feedback mechanisms. The major limitation is the fact that the cellular equations are only unidirectionally coupled to the mechanical model. The behavior of a single skeletal muscle fiber is precomputed and stored in a look-up table. Within the mechanical model, the cellular variables associated with force generation, that is, the crossbridge concentrations in the attached pre- and postpower stroke state (A_1 and A_2 , resp.), are copied into a detailed 3D structural model and homogenized to compute the resulting stress tensor. Any geometrical variations of a skeletal muscle fiber due to a

contraction, for example, a length change, are not considered. The same applies to feedback, that is, an alternation of the recruitment sequence due to the mechanical state. The choice of precomputing the cellular behavior has been chosen to reduce the overall computational cost. This was necessary as the original framework is based on serial legacy code (CMISS) appealing to data structures not necessarily suitable for parallelization. Further, only isometric contractions were considered. The isometric case provided justification for neglecting the force-velocity relationship. In reality, however, series elastic elements against which the muscle shortens during tension development prevent true isometric conditions.

The aim of this contribution is to introduce a completely new, computationally efficient, fully coupled, multiphysics simulation framework for skeletal muscle modeling providing the basis to include biophysical motor unit recruitment and feedback mechanisms at a later stage. The framework is based on the open-source software library OpenCMISS [19], which, together with the entire model described in this contribution, can be downloaded from <https://github.com/OpenCMISS>. OpenCMISS was designed to achieve maximal flexibility and efficiency through the use of new data structures such as FieldML [20], access to well-established model repositories via CellML [21, 22], and a distributed-memory foundation for executing large problems. The new libraries and the data structure provide the basis to combine different mesh regions with different dimensionality, for example, 0D models for the cellular behavior, 1D models for the AP propagation, and 3D models for the mechanical model, within one framework. This allows for a strong and bidirectional coupling of the chemoelectrical cellular behavior and the mechanical model—a major advantage over commercially available software packages. Furthermore, the modular organization of the framework allows for straightforward extensions of the model and substitution of model components, for example, the cellular model.

2. Materials and Methods

Figure 1 provides an overview of the proposed computational framework. The individual parts of the framework (model of the half-sarcomere, propagation of the AP, and continuum-mechanical model) are presented in the subsequent sections. Here, the interactions and couplings between the individual model parts are explained.

The muscle fibers of one MU are stimulated through their corresponding motoneuron at the neuromuscular junction. In the proposed model, the neural discharges are modeled as an ionic current that is applied at the center of a fiber, which represents the neuromuscular junction. In this contribution, the MU discharge times are predefined, for example, by a regular frequency. However, computing the discharge rates of a motoneuron pool, one could, for example, also appeal to the model of Fuglevand et al. [23], as shown in Röhrle [16], or to a biophysical model like the one by Negro and Farina [24]. The coupling of a motoneuron-pool model to the muscle model is unidirectional; that is, the flow of information between the models only occurs from the motoneuron-pool model to the

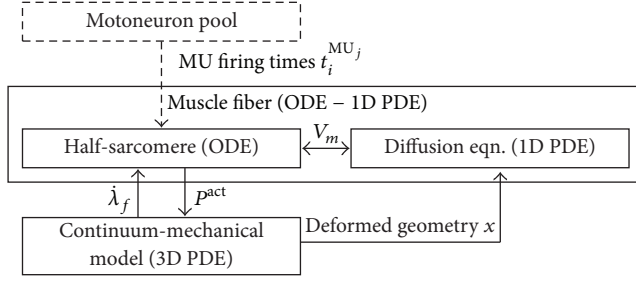


FIGURE 1: Overview of the modeling framework. Each box indicates a model part. The couplings between the parts are indicated through arrows together with the transferred information. The membrane voltage, V_m , couples the half-sarcomere model to the diffusion equation. Together, they represent the electrophysiological behavior of the muscle fiber. Further, $\dot{\lambda}_f$ is the shortening velocity, and P^{act} is the active stress. The model of the motoneuron pool is not part of the proposed model, which is symbolized by a dashed box.

muscle model. Hence, the MU recruitment and firing times can be precomputed independently of the muscle model.

In contrary to [15], the governing equations for describing the bioelectrical field and those of 3D finite elasticity theory are solved in a strongly coupled way, where the solution of the mechanics influences the bioelectrical fields and vice versa.

The bioelectrical field itself is determined by solving the so-called monodomain equation, which is a reaction-diffusion equation. The monodomain equation is solved using an operator splitting technique providing the mathematical justification to separately treat the reaction part, which is given by the half-sarcomere model [11], and the diffusion part, which describes the AP propagation. The half-sarcomere model is biophysically based and is described by a set of ordinary differential equations (ODEs) in time, that is, exhibiting no spatially varying quantities (0D). The diffusive part is described by a transient 1D partial differential equation (PDE). Since the two parts of the monodomain equation are solved separately, the operator splitting technique requires a mapping of the membrane voltage, V_m , between the two parts at each time step. Among many other cellular quantities, the half-sarcomere model (reaction term) computes the active stress contribution at a particular location along a skeletal muscle fiber. The active stress, P^{act} , enters the constitutive equation through a mapping (homogenization) to the continuum-mechanical model. In return, the shortening velocity, $\dot{\lambda}_f \leq 0$, is passed from the continuum-mechanical model to the half-sarcomere model.

To take into account the length changes due to skeletal muscle tissue deformations, the bioelectrical field equations are solved on a deforming/moving domain. Thus, the equations describing the AP propagation along the muscle fibers have to be adjusted to the deformation. This can be achieved either by modifying the conductivity tensor or by solving the monodomain equation on the deformed geometry. In this contribution, the latter is employed.

In the following sections, the different parts of the computational framework, that is, the mechanical model (Section 2.1), the half-sarcomere model (Section 2.2), and the

AP propagation model (Section 2.3), are introduced. Furthermore, implementation and high-performance computing aspects of the resulting multiphysics discretization schemes are presented in Section 2.4.

2.1. The Mechanical Problem. In continuum mechanics, the motion of a body \mathcal{B} is described by the placement function χ that assigns each point \mathbf{X} in the reference configuration at time t_0 a corresponding point \mathbf{x} in the actual (deformed) configuration at time $t > t_0$; that is, $\mathbf{x} = \chi(\mathbf{X}, t)$. The deformation of a body is commonly measured by the deformation gradient tensor

$$\mathbf{F} := \frac{\partial \chi(\mathbf{X}, t)}{\partial \mathbf{X}} = \frac{\partial \mathbf{x}}{\partial \mathbf{X}} \quad (1)$$

and the strain by the Green-Lagrangian strain tensor $\mathbf{E} := (1/2)(\mathbf{C} - \mathbf{I})$, where $\mathbf{C} = \mathbf{F}^T \mathbf{F}$ is the right Cauchy-Green deformation tensor and \mathbf{I} denotes the second-order identity tensor.

Inertia forces and body forces are assumed to be small compared to the forces acting in the muscle. Thus, the balance of linear momentum reduces to

$$\text{div } \mathbf{T} = \mathbf{0}, \quad (2)$$

where \mathbf{T} denotes the Cauchy stress tensor. The Cauchy stress can be derived from the second Piola-Kirchhoff stress tensor, \mathbf{S} , via a scaled covariant push forward operation: $\mathbf{T} = J^{-1} \mathbf{F} \mathbf{S} \mathbf{F}^T$, with $J := \det \mathbf{F}$ being the Jacobian.

The stress tensor (e.g., \mathbf{T} or \mathbf{S}) is derived from a constitutive equation. A constitutive equation characterizes the material behavior under load; that is, it relates the stress in a body to the strain. Skeletal muscle tissue is generally considered to be transversely isotropic and hyperelastic. Furthermore, muscle tissue is considered to be incompressible under physiological conditions. The second Piola-Kirchhoff stress tensor of a hyperelastic material can be derived from a strain energy function W defined per unit reference volume by

$$\mathbf{S} = 2 \frac{\partial W}{\partial \mathbf{C}} - p \mathbf{C}^{-1}, \quad (3)$$

with hydrostatic pressure p entering (3) as Lagrange multiplier associated with the incompressibility constraint $J - 1 = 0$; see, for example, [25].

For transversely isotropic materials, the strain energy function can be expressed in terms of the right Cauchy-Green deformation tensor and a second-order structural tensor $\mathcal{M} = \mathbf{a}_0 \otimes \mathbf{a}_0$, where \mathbf{a}_0 denotes a unit vector in the reference configuration pointing in the fiber direction. Applying the theory of invariants (see Spencer [26]), the strain energy function of a transversely isotropic material can be expressed as

$$W(\mathbf{C}, \mathcal{M}) = W(I_1, I_2, I_3, I_4, I_5), \quad (4)$$

with principal invariants $I_1 = \text{tr } \mathbf{C}$, $I_2 = (1/2)[(\text{tr } \mathbf{C})^2 - \text{tr}(\mathbf{C}^2)]$, and $I_3 = \det \mathbf{C} = J^2$ and mixed invariants $I_4 = \text{tr}(\mathbf{C} \mathcal{M})$ and $I_5 = \text{tr}(\mathbf{C}^2 \mathcal{M})$.

TABLE 1: Parameters of the passive part of the constitutive equation.

c_{10}	c_{01}	b_1	d_1
$6.352e^{-10}$ kPa	3.627 kPa	$2.756e^{-5}$ kPa	43.373 [—]

Following the idea of a fiber-reinforced material (cf. Spencer [27]), the strain energy function is split into an isotropic part W^{iso} that represents the ground matrix and an anisotropic part W^{ani} that represents the embedded fibers. Furthermore, a term W^{act} is introduced to represent the muscle's ability to actively generate force via crossbridge cycling:

$$W(I_1, I_2, I_3, I_4, I_5) = W^{\text{iso}}(I_1, I_2) + W^{\text{ani}}(I_4, I_5) + W^{\text{act}}. \quad (5)$$

On the right-hand side of (5), a dependence on the third principal invariant has directly been omitted due to the incompressibility constraint $I_3 = (\det \mathbf{F})^2 = 1$. Being based on the principle of superposition, the ansatz in (5) neglects any couplings between the individual parts of the strain energy leading to the assumptions that (i) the active behavior is independent of the other terms and (ii) there is no interaction between the fibers and the matrix.

In the following, first the terms representing the passive behavior of skeletal muscle are introduced before describing the active part of the strain energy.

2.1.1. Passive Material Behavior. For the isotropic contribution, the Mooney-Rivlin material description is employed; see, for example, Holzapfel [28]. This material description is known to be well suited for representing J -like stress-stain curves of soft biological tissues:

$$W^{\text{iso}}(I_1, I_2) = c_{10}(I_1 - 3) + c_{01}(I_2 - 3). \quad (6)$$

The material parameters of the Mooney-Rivlin model, c_{10} and c_{01} , are determined in a uniaxial compression test using the experimental data of Zheng et al. [29]. The set of parameters used within this work is summarized in Table 1. For the anisotropic contribution, a polynomial strain-energy function of the fiber stretch, $\lambda_f = \sqrt{I_4} > 0$, has been adopted from Markert et al. [30]:

$$W^{\text{ani}}(\lambda_f) = \sum_{i=1}^N \left(\frac{b_i}{d_i} (\lambda_f^{d_i} - 1) - b_i \ln \lambda_f \right), \quad (7)$$

where N is the number of polynomial terms and b_i and d_i denote material parameters. Note that the anisotropic contribution applies only to the tensile range, that is, for $\lambda_f > 1$. A uniaxial extension test in fiber direction is used to fit material parameters b_i and d_i to the experimental data of Hawkins and Bey [31]. A single polynomial term ($N = 1$) was found to be sufficient to reproduce the experimental data.

2.1.2. Active Contractile Behavior. In many physiological conditions the mechanical behavior of skeletal muscle is dominated by its active, force generating behavior. In accordance

with previously published skeletal muscle models [6, 15, 32], it is assumed that the active stress only acts in fiber direction. Furthermore, the generated force depends on the length of the muscle [33] and the shortening velocity [34]. Following this, the active part of the strain energy W^{act} is assumed to be a function of deformation, represented through the fiber stretch λ_f , the rate of deformation $\dot{\lambda}_f$, and the fiber direction. Proceeding from (3), the active part of the stress tensor yields

$$\begin{aligned} \mathbf{S}^{\text{act}} &= 2 \frac{\partial W^{\text{act}}}{\partial \mathbf{C}} = 2 \frac{\partial W^{\text{act}}}{\partial \lambda_f} \frac{\partial \lambda_f}{\partial I_4} \frac{\partial I_4}{\partial \mathbf{C}} \\ &= \frac{1}{\lambda_f} \frac{\partial W^{\text{act}}}{\partial \lambda_f} \mathbf{a}_0 \otimes \mathbf{a}_0 = \frac{P^{\text{act}}}{\lambda_f} \mathbf{a}_0 \otimes \mathbf{a}_0. \end{aligned} \quad (8)$$

In (8), the scalar-valued active stress function, P^{act} , which takes the form of a nominal (or engineering) stress, is introduced. Further, the active stress function, P^{act} , is assumed to depend on a constant maximum active stress $P^{\text{max}} = 7.3 \text{ N/cm}^2$ (cf. [31]), a function relating the generated stress to the muscle length $f_\ell(\lambda_f)$, and a function that links the macroscopic continuum-mechanical system to the quantities at the microscale $\bar{\gamma}$, which depends on the level of activation α and the velocity $\dot{\lambda}_f$:

$$P^{\text{act}} = P^{\text{max}} f_\ell(\lambda_f) \bar{\gamma}(\alpha, \dot{\lambda}_f). \quad (9)$$

The function $\bar{\gamma}$ is determined in a biophysical model at the microscale (see Section 2.2). The force-length relation is adopted from Röhrle et al. [15] (see also [6]):

$$\begin{aligned} f_\ell(\lambda_f) &= \begin{cases} -\frac{25}{4} \left(\frac{\lambda_f}{\lambda_f^{\text{opt}}} \right)^2 + \frac{25}{2} \frac{\lambda_f}{\lambda_f^{\text{opt}}} - 5.25, & \text{if } 0.6 \leq \frac{\lambda_f}{\lambda_f^{\text{opt}}} \leq 1.4 \\ 0, & \text{otherwise.} \end{cases} \end{aligned} \quad (10)$$

In (10), λ_f^{opt} denotes the optimal fiber stretch, which, based on experimental data [31], is assumed to take a value of 1.2.

In summary, the second Piola-Kirchhoff stress tensor, \mathbf{S} , yields

$$\begin{aligned} \mathbf{S} &= \mathbf{S}^{\text{iso}} + \mathbf{S}^{\text{ani}} + \mathbf{S}^{\text{act}} - p \mathbf{C}^{-1}, \\ \mathbf{S}^{\text{iso}} &= 2c_{10} \mathbf{I} + 2c_{01} (I_1 \mathbf{I} - \mathbf{C}), \\ \mathbf{S}^{\text{ani}} &= b_1 \left(\lambda_f^{d_1-2} - \lambda_f^{-2} \right) \mathbf{a}_0 \otimes \mathbf{a}_0, \end{aligned} \quad (11)$$

$$\mathbf{S}^{\text{act}} = \lambda_f^{-1} P^{\text{max}} f_\ell(\lambda_f) \bar{\gamma}(\alpha, \dot{\lambda}_f) \mathbf{a}_0 \otimes \mathbf{a}_0.$$

2.2. The Micromodel of a Half-Sarcomere. The basis for modeling subcellular processes in the present contribution is the Shorten et al. [11] model. The Shorten model describes the complex, nonlinear, biophysical processes leading from electrical excitation to contraction and force generation of a half-sarcomere by means of ODEs. Two versions of the model

using slightly different parametrizations allow the distinction between slow-twitch (type I) and fast-twitch (type II) muscle fibers. The model has been validated on mouse muscles.

To model the entire ECC, the half-sarcomere model [11] combines several submodels describing (a) membrane electrophysiology, (b) calcium release from the sarcoplasmic reticulum (SR), (c) calcium dynamics, (d) crossbridge dynamics, and (e) fatigue. In more detail, the individual parts are as follows. (a) For a description of the Hodgkin-Huxley electrophysiology of action potentials via ionic currents that pass through various channels and pumps (sodium channels, delayed rectifier and inverse rectifier potassium channels, chloride channels, and Na^+ - K^+ pumps) in the sarcolemma and T-tubules, see Adrian and Peachey [35] and Wallinga et al. [36]. (b) Intracellular calcium release from the sarcoplasmic reticulum to the cytosol in response to membrane depolarization through RyR calcium release channels is described by a ten-state model originally proposed by Ríos et al. [37]. This submodel couples the T-tubule membrane voltage to the opening of the dihydropyridine receptor/RyR complex. (c) The released calcium (Ca^{2+}) ions bind in the cytosol to parvalbumin and ATP along with troponin on the myofilaments. Moreover, intracellular magnesium ions (Mg^{2+}) compete with Ca^{2+} for parvalbumin and ATP binding sites. After being transported back to the SR via Ca^{2+} -ATPase, Ca^{2+} binds to calsequestrin. The description of the calcium dynamics goes back to the model of Baylor and Hollingworth [38]. (d) The binding of two Ca^{2+} ions to troponin C leads to a conformational change in the troponin molecule that removes the blocking tropomyosin from the actin filament and thereby allows the myosin head to attach to the actin binding sites. This model is based on an eight-state model of crossbridge dynamics in skeletal muscle using the generic models of Razumova et al. [39, 40] and Campbell et al. [41, 42]. (e) Muscle fatigue is modeled through subcellular mechanisms on the basis of phosphate dynamics. The accumulation of phosphate (P_i) is believed to be the primary mechanism behind metabolic fatigue. Here, P_i is formed from the energy-providing reaction of ATP to adenosine diphosphate (ADP) during crossbridge cycling when weakly bound crossbridges isomerize into strongly bound crossbridges. The produced phosphate is transported passively to the SR where it precipitates with Ca^{2+} [11].

Although the degree of detail of the model of Shorten et al. [11], for example, modeling the signaling pathway of the ECC or fatigue, is not essential for the presented overall modeling framework, the authors refrain from simplifying the model, as this will be the basis for further developments that will build on different biophysical components. Moreover, the complexity of the model introduces new challenges for efficiency and parallelization.

According to the sliding filament theory [43], the active force production in skeletal muscle is due to crossbridge cycling. The crossbridge dynamics model, which depends on all above-described models, defines the force producing step called power stroke as the transition between the two attached states, that is, the prepower stroke state A_1 and the postpower stroke state A_2 . Therefore, one can assume that

the actively generated stress in a half-sarcomere under isometric conditions is proportional to the concentration of crossbridges in the postpower stroke state A_2 [40]. The value of A_2 is normalized using the value of A_2 at maximum tetanic stimulation α^{\max} ; that is, $A_2(\alpha)/A_2(\alpha^{\max}) \in [0, 1]$.

The half-sarcomere model [11] was developed for isometric contractions. Truly isometric conditions, however, do not exist in skeletal muscle, since (i) contractile tissue is in series with elastic components of the musculoskeletal system stretching under contraction-induced stress increase and (ii) various nonuniformities exist along the muscle fiber; that is, while one part of the fiber shortens, another part is stretched.

The scaling quantity γ , (cf. (9)) is found by multiplying the normalized concentration of crossbridges in the postpower stroke state by Hill's hyperbolic force-velocity relation [34]:

$$\gamma = \frac{A_2(\alpha)}{A_2(\alpha^{\max})} \left[\frac{F^{\text{iso}} + a}{b - \dot{\lambda}_f} b - a \right]. \quad (12)$$

In (12), F^{iso} denotes the maximum isometric active force, and a and b are the Hill parameters, which are chosen such that $a/F^{\text{iso}} = 0.25$ [44, 45] and $b/\dot{\lambda}_f^{\max} = 0.25$ [46] with $\dot{\lambda}_f^{\max}$ being the maximum shortening velocity at zero force production.

To extend the single half-sarcomere model to a model of a muscle fiber, the electrophysiological characteristic of propagating APs along the length of fibers is considered. The equations representing the AP propagation are presented in Section 2.3.

2.3. Action Potential Propagation. The propagation of an AP along a skeletal muscle fiber is initiated at the neuromuscular junction located in the middle of the length of each fiber. Starting at the neuromuscular junction, the short-term depolarization of the muscle-fiber membrane voltage travels along the length of the fiber towards its ends.

The macroscopic electrical conductivity of muscle tissue perpendicular to the fiber direction is up to one magnitude lower than the conductivity along the fiber direction [47, 48], and electrical stimulation from one fiber to adjacent ones is not observed. Therefore, the propagation of an AP along a skeletal muscle fiber is modeled as a 1D system. The propagation of APs in biological tissue is typically modeled using the bidomain equations; see, for example, Pullan et al. [49]. In the 1D case, the bidomain equations reduce to the simpler monodomain equation, a reaction-diffusion equation [50, 51], which is given by

$$\frac{\partial}{\partial s} \left(\sigma \frac{\partial V_m}{\partial s} \right) = A_m \left(C_m \frac{\partial V_m}{\partial t} + I_{\text{ion}} \right). \quad (13)$$

In (13), s denotes the spatial variable describing the position along the path of the fiber, σ is the conductivity, V_m represents the membrane voltage, A_m reflects the ratio of the membrane surface area to the volume, and C_m is the capacitance of the cell membrane per unit area. Depending on the twitch type of the fiber, two different values are used for the membrane capacitance, that is, $C_m = 0.58 \mu\text{F}/\text{cm}^2$ for slow-twitch fibers and $C_m = 1.0 \mu\text{F}/\text{cm}^2$ for fast-twitch fibers [11]. The value of $A_m = 500 \text{ cm}^{-1}$ is identical for both fiber types [52].

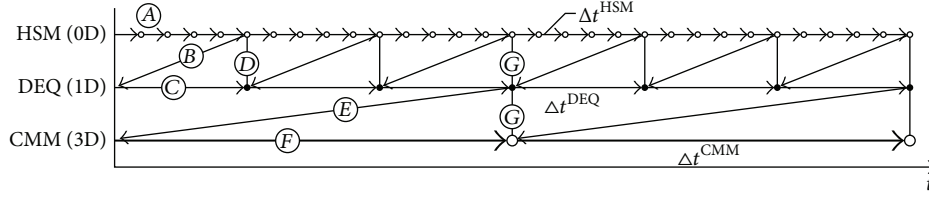


FIGURE 2: Time-stepping scheme, where Δt is the time step, HSM denotes the half-sarcomere model, DEQ is the diffusion equation, and CMM is short for the continuum-mechanical model.

Furthermore, the reaction term I_{ion} depends nonlinearly on V_m and denotes the sum of ionic currents crossing the cell membrane of the sarcolemma and the T-tubule.

2.4. High-Performance Computing. After introducing the individual submodels and their interactions, this section focuses on efficient solution strategies for this complex and computationally very demanding multiphysics model describing phenomena on different length and time scales. To achieve this, various concepts of software engineering, for example, advanced discretization schemes for multiphysics problems, parallelization, or staggered solution schemes, are adopted. These concepts have been implemented within the open-source software library OpenCMISS [19].

2.4.1. Operator Splitting. For the numerical treatment of the monodomain equation (cf. (13)), it is convenient to apply an operator splitting technique (or fractional-step method) to separate the nonlinear reaction term from the diffusion term; see, for example, Sundnes et al. [50, 53]. Applying the first-order accurate Godunov-type splitting, (13) yields

$$\frac{V_m^* - V_m^k}{\Delta t} = -\frac{1}{C_m} I_{\text{ion}}(V_m^k), \quad (14a)$$

$$\frac{V_m^{k+1} - V_m^*}{\Delta t} = \frac{1}{A_m C_m} \frac{\partial}{\partial s} \left(\sigma \frac{\partial V_m^{k+1}}{\partial s} \right), \quad (14b)$$

where Δt refers to the time step, V_m^k and V_m^{k+1} denote the values of the membrane voltage at discrete times $k\Delta t$ and $(k+1)\Delta t$, respectively, and V_m^* is the value at the intermediate time t^* . The advantage of the operator-splitting approach is that different numerical methods can be applied to the different subsystems; that is, the nonlinear reaction (14a) is solved using an implicit multistep ODE integration method as commonly done for highly nonlinear, stiff, biophysical cell models (see Pullan et al. [49]), while one uses the backward-Euler method for the diffusion equation (14b). Furthermore, different time steps can be used for the different subsystems (subcycling). For the discretization of the spatial derivative term in (14b) the finite element method (FEM) [54] is applied.

2.4.2. Discretization in Space and Time. The solution of the bioelectrical field equations, (14a) and (14b), requires an extremely small time step and a very fine mesh due to the rapid changes and steep gradients occurring in physiological cell models; see [49, 52]. On the other hand, using a similarly spatial and temporal discretization for the solution

of the 3D mechanical model is prohibitively expensive and unnecessary, as changes on the scale of an entire muscle occur at considerably larger time scales.

Following the idea of different characteristic length scales, a multiphysics discretization scheme is proposed: a much finer mesh is used for the bioelectrical model than for the continuum-mechanical system. First, a relatively coarse 3D finite element (FE) mesh of the muscle's geometry is generated. Then, relatively fine 1D FE muscle fiber meshes are embedded in the 3D elements (cf. [18]). The governing equations of the continuum-mechanical model, (2), and the incompressibility constraint are discretized using the coarse 3D mesh, while the diffusion part of the bioelectrical field equation, (14b), is solved on the 1D fiber meshes. Some variables exist on both meshes, and thus, transfer operations between the two meshes are required. The transfer from the coarse 3D FE mesh to the fine 1D fiber meshes is called interpolation, while the transfer in the opposite direction is termed homogenization. The homogenization and interpolation processes are discussed for each affected variable in Section 2.4.3.

Due to the different characteristic time scales of the different physical phenomena, a staggered solution scheme with three different time steps is applied in this work. A schematic representation of the time-stepping scheme is shown in Figure 2. First, the half-sarcomere models, (14a), are solved for 50 time steps with time step size Δt^{HSM} . The symbol (A) in Figure 2 denotes the solution process for computing the states of the half-sarcomere model for time $t + \Delta t^{\text{HSM}}$. Note, for simplicity and readability of Figure 2, only a fractional number of time steps are depicted. In case of computing the cellular states, which will be used within the next time step of the diffusion equation, only 5 instead of the actual 50 time steps are depicted in Figure 2. Each discretization point of the monodomain equation is associated with its own half-sarcomere model. The half-sarcomere model is mathematically described by ODEs in time, which do not rely on any spatial quantities. Therefore, each half-sarcomere model can be solved independently of all other half-sarcomere models. The final values of the membrane voltage computed in these steps are used as starting values for the diffusion equation (14b). This process is denoted by (B) in Figure 2. Following the solution of the diffusion equation (14b) with time step Δt^{DEQ} , which is indicated by (C) in Figure 2, the updated values of the membrane voltage are used as initial conditions for the next solution step of the half-sarcomere model (indicated by (D) in Figure 2). This procedure is repeated a number of times (3 times in Figure 2, 1000 times in the actual computations) before the values

of the active stress γ are homogenized ($\gamma \rightarrow \bar{\gamma}$). The homogenization process is denoted in Figure 2 by (E). The homogenized values $\bar{\gamma}$ enter the continuum-mechanical model, (2), through the stress tensor, which is given by (11). The continuum-mechanical model is only solved in time increments of size Δt^{CMM} (cf. step (F) in Figure 2). Further, the values of the sarcomere velocity are interpolated and applied to the half-sarcomere models; see (G). At the same time, the position of the nodes of the 1D fiber meshes is updated based on the calculated deformation. The described steps are repeated until the final time is reached.

2.4.3. Homogenization and Interpolation. As described above, some variables are shared between the different discretizations. For example, the values of the active stress field are determined in the model of the half-sarcomere, that is, at the nodes of the 1D fiber meshes. In order to include the active stress field in the continuum-mechanical constitutive equation, which is evaluated at the integration points, for example, the Gauß points, associated with the weak formulation of the 3D finite elements, the values need to be homogenized. Like in Röhrle et al. [15], the homogenization is achieved by computing the arithmetic mean of all 1D nodal values that are closest to a certain Gauß point of the continuum-mechanical 3D FE mesh. Other elaborate homogenization techniques like those proposed in [55, 56] could be adopted but are not further considered here.

The positions of the nodes of the 1D fiber meshes are defined in terms of the local element coordinate system of the 3D geometric FEs. Using this definition, their actual positions can be determined from the deformation of the muscle's geometry, that is, from the actual configuration. Using the basis functions of the 3D FEs for the interpolation, the nodal positions of the 1D fiber meshes are updated after each solution of the mechanical submodel.

Further, information about sarcomere velocity is required in the half-sarcomere models located at the nodes of the 1D fiber meshes; see (12). The sarcomere velocity cannot be determined in the biophysical model of the half-sarcomere, as the velocity also relies on the boundary conditions of the continuum-mechanical model of the entire muscle. Therefore, the local sarcomere velocity $\dot{\lambda}_f$ is approximated by a backward finite difference scheme: $\dot{\lambda}_f = (\eta_i^{k+1} - \eta_i^k) / \Delta t^{\text{CMM}}$, where η_i represents the distance between two adjacent nodes and k and $k + 1$ denote two consecutive time steps of the continuum-mechanical model. To avoid unrealistic high variations in sarcomere velocity and to mimic the structural links between adjacent skeletal muscle fibers, the average of the velocity is calculated over a patch of seven sequential nodes of one fiber.

2.4.4. Data Structure. The open-source software library OpenCMISS [19] provides a highly flexible framework for the simulation of coupled multiphysics problems. Being arranged in a hierarchical fashion, the concepts of regions, meshes, fields, and so forth (see [19] for details) allow for couplings between different physical problems at different length and time scales. The presented skeletal muscle model is built on a

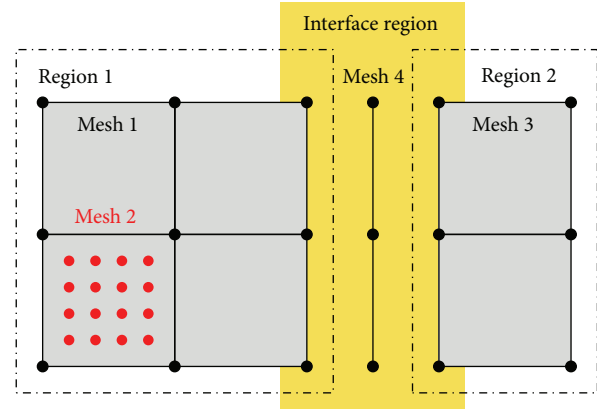


FIGURE 3: Schematic drawing of regions and meshes in OpenCMISS. Different regions can be coupled via interface conditions. Several meshes can be associated with a region.

single region, since the different physical models occupy the same space (volume-coupled problem). When the interaction of a skeletal muscle with neighboring structures such as other muscles, bone, fat, or skin is of interest, these structures can be added to the model as additional regions; see Figure 3. To couple different regions, their interaction can be defined via interface conditions, for example, contact.

The region used for the chemoelectromechanical muscle model contains two meshes: a 3D representation of the geometry that is used for the continuum-mechanical model (mesh 1 in Figure 3) and a second mesh (mesh 2 in Figure 3) consisting of a number of 1D fibers that are used for the solution of the bioelectrical model. The 1D fiber meshes are embedded in the 3D FEs.

Fields are a key data structure in OpenCMISS. Any quantity that can be associated with a mesh is represented in OpenCMISS as a field. A field variable can be constant across the mesh, it can vary from element to element, from node to node, from interpolation point (e.g., Gauß point) to interpolation point, or from data point (arbitrarily located) to data point. The representation of fields in OpenCMISS is based on FieldML [20], which provides field transfer operators (homogenization or interpolation) to handle different spatial scales; see also Section 2.4.3.

Further, OpenCMISS employs nested control loops to handle different temporal scales. In the presented model, two separate control loops for the continuum-mechanical model and the bioelectrical problem, each with its own time step size, are linked to a superior main control loop. The control loop for the mechanical model is only associated with a single solver, while the bioelectrical control loop is connected to a solver for the diffusion equation and a second solver for the half-sarcomere model.

The half-sarcomere model is provided in CellML format [21]. CellML is a markup language for the description of subcellular models based on XML (Extensible Markup Language). In a multiscale model, CellML can be used to conveniently describe the physical processes occurring at a single point within a model at a larger spatial scale. A CellML model

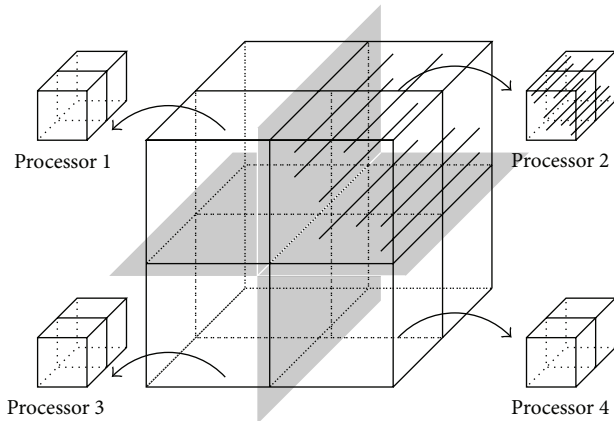


FIGURE 4: Schematic drawing of the domain decomposition as realized for the chemoelectromechanical skeletal muscle model. The decomposition of the 3D mesh of the muscle geometry does not split any of the muscle fiber meshes.

repository containing more than 500 models is available for download at <http://www.cellml.org/>, among them the biophysical model of a half-sarcomere of Shorten et al. [11]. In OpenCMISS, the time step sizes for the CellML models can be chosen independently of the time step sizes used to solve equations representing different physics. For example, the half-sarcomere model, (14a), requires a much smaller time step than the diffusion equation, (14b), and hence, subcycling of the CellML model is employed.

2.4.5. Parallelization. OpenCMISS is developed for parallel computations in a heterogeneous multiprocessing environment [19], where the MPI standard (<http://mpi-forum.org/>) is used for distributed memory parallelization and the OpenMP standard (<http://openmp.org/>) is used for shared memory parallelization.

The implementation of the distributed memory parallelization in OpenCMISS builds on the concept of domain decomposition. For the presented chemoelectromechanical skeletal muscle model, the domain is decomposed in such a way that each 1D embedded fiber mesh is uniquely assigned to a processor; see Figure 4. This approach reduces the amount of communication between the individual processors to a minimum for the bioelectrical model. Parallel efficiency is hereby guaranteed by the fact that the diffusion part of the bioelectrical model is evaluated 1000 times more often than the continuum-mechanical model ($\Delta t^{\text{CMM}} = 1000 \Delta t^{\text{DEQ}}$). Hence, a user-defined domain decomposition, rather than a computed decomposition based on the graph partitioning packages ParMETIS (<http://glaros.dtc.umn.edu/gkhome/metis/parmetis/overview>) or Scotch (<http://www.labri.fr/perso/pelegrin/scotch/>), which is typically used within OpenCMISS, is optimal with respect to the entire chemoelectromechanical model.

Although currently not implemented, the individual muscle fiber meshes within a single computational domain could be further parallelized using an OpenMP shared memory parallelization. Further, the integration of the ODEs

TABLE 2: Execution time in seconds and resulting speedup for 1, 2, and 4 processors.

No. of processors	36 fibers		400 fibers	
	Time [s]	Speedup [—]	Time [s]	Speedup [—]
1	10004.32		177759.11	
2	6940.91	1.441	81360.24	2.185
4	4625.88	1.500	41763.99	1.948

describing the half-sarcomere model is highly suitable for parallel execution on GPGPUs.

3. Results

3.1. Computational Model. To analyze the performance of the computational framework, a simple geometric model is considered. A cubic geometry with 2 cm edge lengths is generated and discretized using eight triquadratic/trilinear Lagrange finite elements (Taylor-Hood elements). A fiber direction is defined that is uniformly aligned and parallel to an edge of the cube. A total of 400 muscle fiber meshes are evenly distributed in the cubic geometry, and each fiber is discretized using 60 linear Lagrange finite elements.

First, the muscle is passively stretched in fiber direction by 20% to reach the optimal fiber stretch of $\lambda_f^{\text{opt}} = 1.2$. Under isometric conditions (the muscle specimen is fixed at the optimal length), a 100 Hz tetanic stimulation frequency is applied to the central half-sarcomere model of all fibers in the model.

To analyze the speedup in a parallel environment, the described model is executed on 1, 2, and 4 processors. A speedup of 2.18 is achieved when going from 1 to 2 processors, while a speedup of 1.95 is achieved when comparing 2 to 4 processors. Further, the simulations were repeated using only 36 1D fiber meshes instead of 400. In this case, a speedup of 1.44 is achieved when going from 1 to 2 processors, while a speedup of 1.50 is achieved when comparing 2 to 4 processors. Table 2 lists the timing results and speedup factors for an Intel Xeon Processor E5520 and 8 GB of RAM.

In the example with 400 fibers, the solution of the bioelectrical model dominates the total computing time. Here, a speedup factor of 2.18, which exceeds the theoretically achievable value of 2, occurs, which can be explained by a significantly higher number of cache misses on 1 processor than on multiple processors, as the size of the bioelectrical model for each processor scales down proportionally to the number of processors. (No ghost elements exist, and no communication between the processors is required in the bioelectrical model.) The other end of the spectrum is marked by the example using only 36 fibers, that is, 3×3 fibers per 3D element, leading to a one by one correspondence between the number of Gauß points in the plane perpendicular to the fibers and the number of embedded fibers. (The 3D elements use $3 \times 3 \times 3$ Gauß points.)

Note that the discretization for the mechanics is independent of the number of embedded fibers and is identical in both cases. In case of 36 fibers, the speedup factors are very poor, since the solution of the continuum-mechanical

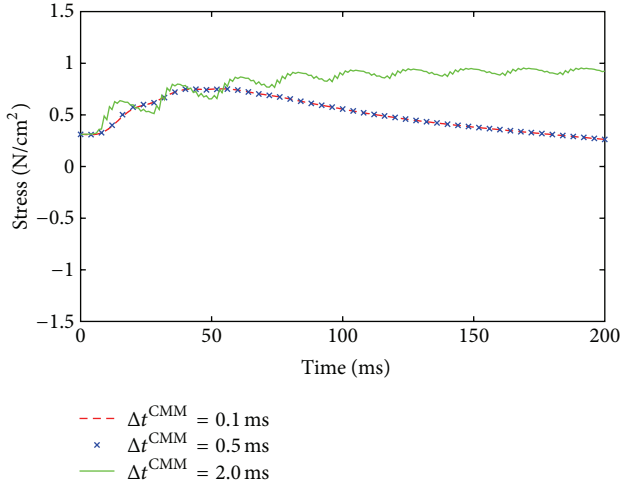


FIGURE 5: Model behavior for different time step sizes of the continuum-mechanical model, Δt^{CMM} . The solutions for the smaller two time steps almost coincide (red dashed line and blue crosses), while the solution for the largest time step size shows a nonphysical, oscillatory behavior.

problem claims a larger fraction of the total computing time. The poor scaling of the continuum-mechanical model is due to the few 3D elements. Together with the required ghost elements each processor has to compute (i) 8 FEs when 1 processor is used, (ii) 8 FEs when 2 processors are used, and (iii) 6 FEs when 4 processors are used. (All elements that share a surface with an actual element of the domain are ghost elements.) For practical applications, however, a finer discretization of the continuum-mechanical model is desirable to achieve a higher accuracy and a better approximation of the muscle's geometry. Furthermore, the application of more fibers is preferable for a realistic muscle simulation.

Within this work, different time step sizes are used for the solution of the different submodels. Critical time step sizes for the bioelectrical model have already been investigated in Davidson [52]. Here, the model behavior for different time step sizes of the continuum-mechanical model, Δt^{CMM} , are investigated. Figure 5 shows the stress evolution of a shortening contraction ($v = 0.1v_{\text{max}}$) of a muscle that is uniformly stimulated at 50 Hz. The results for three different time step sizes ($\Delta t^{\text{CMM}} = 0.1$ ms, 0.5 ms, and 2.0 ms) are shown, whereof the solutions for the smaller two time steps almost coincide (red dashed line and blue crosses) and the solution for the largest time step size ($\Delta t^{\text{CMM}} = 2.0$ ms) depicts significant deviations and oscillatory behavior.

3.2. Force-Velocity Relation. Under nonisometric conditions, the force-velocity relation plays an important role in skeletal muscle simulations. To illustrate the influence of the velocity on the force, a geometrically simple model is examined. Again, a rectangular tissue block with uniform fiber direction and 2 cm length is first stretched in fiber direction by 20% to reach the optimal muscle length. In a second step, all fibers are jointly stimulated with 50 Hz, and the muscle specimen is allowed to shorten at a certain velocity v . The numerical

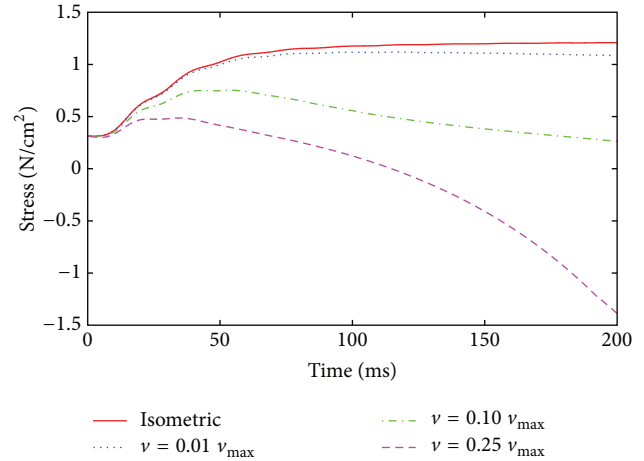


FIGURE 6: Force-velocity behavior I. Shown are shortening contractions at four different velocities using the fully coupled chemoelectromechanical skeletal muscle model.

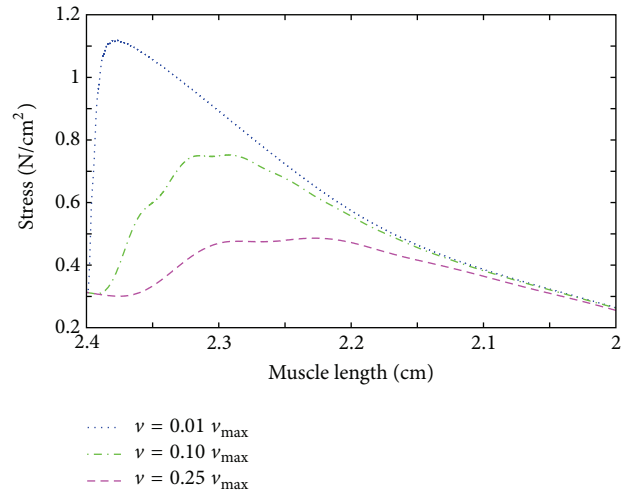


FIGURE 7: Force-velocity behavior II. For three different shortening contractions, the stress is plotted versus the actual muscle length.

experiment is repeated under isometric conditions and at 1, 10, and 25% of the maximum shortening velocity of 200 mm/s. The results are depicted in Figure 6. The model predicts lower forces at higher velocities.

The decline in the force by choosing a shortening velocity of 10 and 25% of the maximum shortening velocity is a direct result of the force-length relationship and due to the fact that the muscle reaches for higher velocities lengths at which it can produce much less force in a shorter amount of time. To segregate the influence of the force-length relation, Figure 7 shows the same results as Figure 6, however by plotting the force versus the actual length of the specimen.

3.3. Feasibility of the Framework and Code. To demonstrate the ability of the chemoelectromechanical model to represent a realistic muscle, a model of a tibialis anterior (TA) muscle is generated. The geometrical representation of the TA is based on the Visible Human data set [57], and the fiber direction

is based on diffusion tensor MRI data. The geometric model has previously been used in Röhrle et al. [18]. Within the present contribution, 10 MUs and stimulation frequencies between 6 and 30 Hz are assumed for the TA model. Detailed information on the methodology of assigning MU fiber distributions is given in [18]. The motor endplates are assumed to be located at the center of the fibers, where a depolarizing current is injected at the times of stimulation. The numerical experiment is carried out under isometric conditions. Figure 8 shows the geometry of the TA muscle and the fiber distribution (a). The fibers show the local membrane potential distribution (blue indicates the resting potential, red indicates the depolarized state). Further, the normalized muscle fiber membrane voltage (V_m , blue), normalized free calcium concentration in the myoplasm ($[Ca^{+2}]$, green), and the normalized active stress (γ , red) are plotted versus time for MUs 2, 4, 8, and 10 (see Figure 8(b)).

4. Discussion

From a modeling point of view, this work appeals to a very complex biophysical half-sarcomere model describing the entire ECC. The model contains a large number of parameters. Many of these parameters are difficult to determine, and only few are available for any muscle and any species. The most trustworthy parameter sets are probably given by Shorten et al. [11], who validated their model to experimental data for different electrical stimulation patterns on force production in soleus and extensor digitorum longus (EDL) muscles of mice for slow-twitch and fast-twitch fibers, respectively. Using in the proposed multiscale framework the described detailed biophysical model provides the basis for testing different physiological hypotheses and investigating different skeletal muscle phenomena, such as fatigue, signaling pathways, residual force enhancement/depression, myopathies, or influence of drugs in future studies.

Although the ECC model of Shorten et al. [11] describes many aspects of the entire pathway from electrical stimulation to force production, it does not consider the titin filament that has recently gained attention in the literature [58, 59]. Nevertheless, a model representing the effect of the titin filament, for example, the one by Rode et al. [60], could be included in the model of Shorten et al. [11] if conditions are of interest, where the titin filament is expected to have a significant influence.

Further, the modeling assumption that a fiber can be represented as a 1D geometrical object assumes that all parallel aligned sarcomeres within the cross section of a fiber behave identically not allowing for sarcomere inhomogeneities within the cross section of the fiber. Moreover, the embedding of the anatomically based 1D fiber meshes within the 3D mesh for the continuum mechanics and the homogenization process required due to the different meshes provide a few restrictions on the micromechanical skeletal muscle model. While assuming the electrical isolation of individual fibers is physiologically valid, the proposed framework does not distinguish individual fibers or fascicles in the mechanical model. While there exist first works on investigating the mechanical interaction of adjacent muscle fibers and fascicles

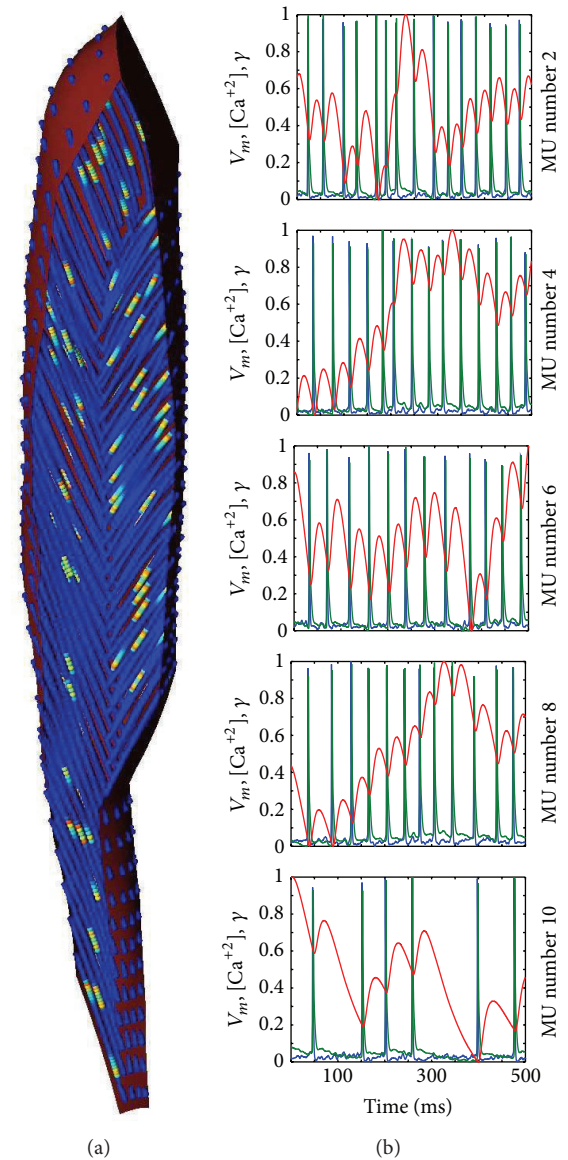


FIGURE 8: Tibialis anterior muscle. Shown is the geometry of the muscle and the fiber distribution, where the fibers indicate the local membrane potential in color (a). The normalized muscle fiber membrane voltage V_m (blue), normalized free calcium concentration in the myoplasm $[Ca^{+2}]$ (green), and normalized active stress γ (red) are plotted versus time for motor units 2, 4, 6, 8, and 10 (b).

through the extracellular connective tissue, for example, by Sharafi and Blemker [61, 62], the mechanical behavior of the fibers and the connective tissue within this framework is based on a macroscopic continuum-mechanical approach. Including micromechanical considerations within this framework, however, would lead to a computationally extremely demanding muscle model. This is particularly due to the fact that the mechanical considerations of Sharafi and Blemker [61, 62], which have only been carried out on a small block of tissue, are carried out for purely passive muscle tissue and would need to be further extended to active contractile behavior. Furthermore, material parameters of

the extracellular connective tissue and stripped muscle fibers are not readily available [61], and hence a further source of uncertainty would be introduced into the model.

Within this framework, the active stresses determined in the half-sarcomere model are homogenized and included in the continuum-mechanical constitutive equation. The homogenization is required for computational efficiency. A skeletal muscle model that would use the same number of elements for the bioelectrical and the mechanical problem no longer require any homogenization; however, this approach results in a computational model that is no longer feasible for any practical application. It should be noted that the homogenization process has little effect on the convergence behavior of the mechanical problem. This has been demonstrated in Röhrle et al. [15] by maintaining a fixed number of embedded fiber models while successively refining the number of 3D mechanical elements until homogenization is no longer required. The investigation showed very good convergence properties [15] if compared to the mechanical-only problem.

Improving the constitutive equation for describing the macroscopic behavior of skeletal muscle mechanics does not only apply to its active contribution. In general, future research needs to further focus on experimental studies and continuum-mechanical material descriptions to develop valid constitutive equations for skeletal muscle mechanics in general. Within this framework the isotropic Mooney-Rivlin material model has been extended by a contribution acting in the along-fiber stretch regime for describing the transversely isotropic material behavior of passive muscle tissue. The anisotropic contribution to the passive behavior is negligibly small in the small strain regime, and hence the Mooney-Rivlin parameters can be used to characterize the passive material behavior around the reference configuration. Based on a comparison with the infinitesimal strain theory, the consistency condition for the Mooney-Rivlin parameters yields a value of $\mu = 2(c_{10} + c_{01}) \approx 7$ kPa for the shear modulus [28], which is close to experimentally determined values [63]. However, there is some experimental evidence that under compression passive muscle tissue exhibits a stiffer behavior in the cross-fiber direction than in the fiber direction [64]. Although this material behavior can be included in a continuum-mechanical formulation [64], the material behavior of the present contribution is isotropic in the compressive range and exhibits a transversely isotropic material behavior in the along-fiber stretch region, as in most other works in this field of research; see, for example, [6, 15]. More accurate or micromechanically based subject- or muscle-specific material parameters would be desirable but are currently not available.

Despite using two different discretizations, that is, one grid for the mechanical model and a different grid for the electrophysiological model, the computational cost of the model is still very considerable. Hence, a staggered solution is proposed to further reduce the computational effort. Staggered solution schemes are often favorable when within one model different subsystems describe processes with very different characteristic time step sizes. The microscopic half-sarcomere model shows rapid changes and steep gradients, while the changes in the continuum-mechanical system occur

at a much larger time scale. The application of the staggered solution scheme implies the following assumptions. The changes in the variables in the bioelectrical field equations, (14a) and (14b), are small within one time step of the continuum-mechanical model; that is, these changes do not have a strong effect on the continuum-mechanical system. On the other hand, the changes introduced through one solution step of the mechanical system, (2), are small; that is, not updating the mechanical fields at every time step at which the bioelectrical field equations are solved introduces a rather small error (cf. Figure 5). Based on the results depicted in Figure 5, the time step for the considered problem could be chosen even larger; however, the authors have retained from this possibility as they have an extended framework in mind that also provides feedback from the mechanical to the recruitment model. In that case, it is presumed that a smaller mechanical time step might be more suitable. This, however, has to be shown in future research. Equivalent assumptions have to be made for the operator split within the bioelectrical field problem, where the diffusion equation is separated from the reaction term.

In contrast to staggered schemes, monolithic solution schemes do not rely on these assumptions. A monolithic scheme has been investigated for the bioelectrical field equations [65]; however, only a simple, phenomenological model for the reaction term has been evaluated. Further, Göktepe and Kuhl [66] propose a fully implicit approach for cardiac electromechanics. As the proposed chemoelectromechanical model uses a much more detailed, biophysical half-sarcomere model for the reaction term, the staggered schemes have been employed to reduce the overall cost while maintaining accuracy and stability for long stimulation periods. Further, the fact that the bioelectrical model is solved on a deforming domain (as a result of the continuum-mechanical model) results in monolithic solution schemes that are not so straightforward to implement.

5. Conclusions

An extensible, flexible, multiscale, and multiphysics modeling framework for nonisometric skeletal muscle mechanics has been presented. The skeletal muscle model spans the entire excitation-contraction pathway using an electrophysiological membrane model, a biophysical half-sarcomere model (including the hyperbolic force-velocity relationship) for active force generation, action potential propagation along individual muscle fibers, and a continuum-mechanical description of the macroscopic muscle tissue allowing for complex interactions with surrounding tissues. The framework is based on state-of-the-art parallelization techniques providing the basis to investigate many different aspects of skeletal muscle physiology and mechanics in the future. In particular, the extensible and flexible open-source software library OpenCMISS will provide the basis for future extensions such as including the effects of titin, neurocontrol, feedback mechanisms, and many more aspects. The key to all of that is its implementation within a single framework using novel data structures, for example, FieldML and CellML, not requiring any external data exchange, staggered solution

schemes addressing computational efficiency in the presence of different and separable time scales, and parallelization strategies.

Conflict of Interests

The authors do not have any conflict of interests with the content of the paper.

Acknowledgments

The authors would like to thank the German Research Foundation (DFG) for financial support of the project within the funding programme Open Access Publishing and the Cluster of Excellence in Simulation Technology (EXC 310/1) at the University of Stuttgart. Moreover, this work was supported by the European Research Council under the European Union's Seventh Framework Programme (FP/2007-2013)/ERC Grant Agreement no. 306757 (LEAD).

References

- [1] G. J. van Ingen Schenau, M. F. Bobbert, G. J. Ettema, J. B. de Graaf, and P. A. Huijing, "A simulation of rat edl force output based on intrinsic muscle properties," *Journal of Biomechanics*, vol. 21, no. 10, pp. 815–824, 1988.
- [2] M. G. Pandy, "Computer modeling and simulation of human movement," *Annual Review of Biomedical Engineering*, vol. 3, pp. 245–273, 2001.
- [3] M. Günther, S. Schmitt, and V. Wank, "High-frequency oscillations as a consequence of neglected serial damping in Hill-type muscle models," *Biological Cybernetics*, vol. 97, no. 1, pp. 63–79, 2007.
- [4] M. Günther and S. Schmitt, "A macroscopic ansatz to deduce the Hill relation," *Journal of Theoretical Biology*, vol. 263, no. 4, pp. 407–418, 2010.
- [5] P. Meier and R. Blickhan, "FEM-simulation of skeletal muscle: the influence of inertia during activation and deactivation," in *Skeletal Muscle Mechanics: From Mechanisms to Function*, W. Herzog, Ed., chapter 12, pp. 207–233, John Wiley & Sons, 2000.
- [6] S. S. Blemker, P. M. Pinsky, and S. L. Delp, "A 3D model of muscle reveals the causes of nonuniform strains in the biceps brachii," *Journal of Biomechanics*, vol. 38, no. 4, pp. 657–665, 2005.
- [7] O. Röhrle and A. J. Pullan, "Three-dimensional finite element modelling of muscle forces during mastication," *Journal of Biomechanics*, vol. 40, no. 15, pp. 3363–3372, 2007.
- [8] F. E. Zajac, "Muscle and tendon: properties, models, scaling, and application to biomechanics and motor control," *Critical Reviews in Biomedical Engineering*, vol. 17, no. 4, pp. 359–411, 1989.
- [9] S. S. Blemker and S. L. Delp, "Three-dimensional representation of complex muscle architectures and geometries," *Annals of Biomedical Engineering*, vol. 33, no. 5, pp. 661–673, 2005.
- [10] L. R. Smith, G. Meyer, and R. L. Lieber, "Systems analysis of biological networks in skeletal muscle function," *Wiley Interdisciplinary Reviews*, vol. 5, no. 1, pp. 55–71, 2013.
- [11] P. R. Shorten, P. O'Callaghan, J. B. Davidson, and T. K. Soboleva, "A mathematical model of fatigue in skeletal muscle force contraction," *Journal of Muscle Research and Cell Motility*, vol. 28, no. 6, pp. 293–313, 2007.
- [12] B. Hernández-Gascón, J. Grasa, B. Calvo, and J. Rodríguez, "A 3D electro-mechanical continuum model for simulating skeletal muscle contraction," *Journal of Theoretical Biology*, pp. 108–118, 2013.
- [13] J. W. Fernandez, M. L. Buist, D. P. Nickerson, and P. J. Hunter, "Modelling the passive and nerve activated response of the rectus femoris muscle to a flexion loading: a finite element framework," *Medical Engineering and Physics*, vol. 27, no. 10, pp. 862–870, 2005.
- [14] M. Böl, R. Weikert, and C. Weichert, "A coupled electromechanical model for the excitation-dependent contraction of skeletal muscle," *Journal of the Mechanical Behavior of Biomedical Materials*, vol. 4, no. 7, pp. 1299–1310, 2011.
- [15] O. Röhrle, J. B. Davidson, and A. J. Pullan, "Bridging scales: a three-dimensional electromechanical finite element model of skeletal muscle," *SIAM Journal on Scientific Computing*, vol. 30, no. 6, pp. 2882–2904, 2008.
- [16] O. Röhrle, "Simulating the electro-mechanical behavior of skeletal muscles," *IEEE Computing in Science and Engineering*, vol. 12, no. 6, pp. 48–58, 2010.
- [17] O. Röhrle, M. Sprenger, E. Ramasamy, and T. Heidlauf, "Multiscale skeletal muscle modeling: from cellular level to a multi-segment skeletal muscle model of the upper limb," in *Computer Models in Biomechanics*, G. A. Holzapfel and E. Kuhl, Eds., pp. 103–116, Springer, Amsterdam, The Netherlands, 2013.
- [18] O. Röhrle, J. B. Davidson, and A. J. Pullan, "A physiologically based, multi-scale model of skeletal muscle structure and function," *Frontiers in Physiology*, vol. 3, 2012.
- [19] C. Bradley, A. Bowery, R. Britten et al., "OpenCMISS: a multi-physics & multi-scale computational infrastructure for the VPH/Physiome project," *Progress in Biophysics and Molecular Biology*, vol. 107, no. 1, pp. 32–47, 2011.
- [20] G. R. Christie, P. M. F. Nielsen, S. Blackett, C. P. Bradley, and P. J. Hunter, "Fieldml: concepts and implementation," *Philosophical Transactions of the Royal Society A*, vol. 367, no. 1895, pp. 1869–1884, 2009.
- [21] A. Garny, D. P. Nickerson, J. Cooper et al., "CellML and associated tools and techniques," *Philosophical Transactions of the Royal Society A*, vol. 366, no. 1878, pp. 3017–3043, 2008.
- [22] C. M. Lloyd, M. D. B. Halstead, and P. F. Nielsen, "CellML: its future, present and past," *Progress in Biophysics and Molecular Biology*, vol. 85, no. 2-3, pp. 433–450, 2004.
- [23] A. J. Fuglevand, D. A. Winter, and A. E. Patla, "Models of recruitment and rate coding organization in motor-unit pools," *Journal of Neurophysiology*, vol. 70, no. 6, pp. 2470–2488, 1993.
- [24] F. Negro and D. Farina, "Decorrelation of cortical inputs and motoneuron output," *Journal of Neurophysiology*, vol. 106, no. 5, pp. 2688–2697, 2011.
- [25] J. Bonet and R. D. Wood, *Nonlinear Continuum Mechanics for Finite Element Analysis*, Cambridge University Press, 2nd edition, 2008.
- [26] A. J. M. Spencer, "Theory of invariants," in *Continuum Physics*, A. Eringen, Ed., vol. 1, pp. 239–353, Academic Press, New York, NY, USA, 1971.
- [27] A. J. M. Spencer, *Deformations of Fibre-Reinforced Materials*, Oxford University Press, 1972.
- [28] G. A. Holzapfel, *Nonlinear Solid Mechanics*, John Wiley & Sons, West Sussex, England, 2000.
- [29] Y. Zheng, A. F. T. Mak, and B. Lue, "Objective assessment of limb tissue elasticity: development of a manual indentation procedure," *Journal of Rehabilitation Research and Development*, vol. 36, no. 2, pp. 71–85, 1999.

- [30] B. Markert, W. Ehlers, and N. Karajan, "A general polyconvex strainenergy function for fiber-reinforced materials," *Proceedings in Applied Mathematics and Mechanics*, vol. 5, no. 1, pp. 245–246, 2005.
- [31] D. Hawkins and M. Bey, "A comprehensive approach for studying muscle-tendon mechanics," *Journal of Biomechanical Engineering*, vol. 116, no. 1, pp. 51–55, 1994.
- [32] A. E. Ehret, M. Böl, and M. Itskov, "A continuum constitutive model for the active behaviour of skeletal muscle," *Journal of the Mechanics and Physics of Solids*, vol. 59, no. 3, pp. 625–636, 2011.
- [33] B. R. MacIntosh, P. F. Gardiner, and A. J. McComas, *Skeletal Muscle: Form and Function*, Human Kinetics, 2nd edition, 2006.
- [34] A. V. Hill, "The heat of shortening and the dynamic constants of muscle," *Proceedings of the Royal Society B*, vol. 126, no. 843, pp. 136–195, 1938.
- [35] R. H. Adrian and L. D. Peachey, "Reconstruction of the action potential of frog sartorius muscle," *The Journal of Physiology*, vol. 235, no. 1, pp. 103–131, 1973.
- [36] W. Wallinga, S. L. Meijer, M. J. Alberink, M. Vlieg, E. D. Wienk, and D. L. Ypey, "Modelling action potentials and membrane currents of mammalian skeletal muscle fibres in coherence with potassium concentration changes in the T-tubular system," *European Biophysics Journal*, vol. 28, no. 4, pp. 317–329, 1999.
- [37] E. Ríos, M. Karhanek, J. Ma, and A. González, "An allosteric model of the molecular interactions of excitation-contraction coupling in skeletal muscle," *The Journal of General Physiology*, vol. 102, no. 3, pp. 449–481, 1993.
- [38] S. M. Baylor and S. Hollingworth, "Model of sarcomeric Ca^{2+} movements, including ATP Ca^{2+} binding and diffusion, during activation of frog skeletal muscle," *The Journal of General Physiology*, vol. 112, no. 3, pp. 297–316, 1998.
- [39] M. V. Razumova, A. E. Bukatina, and K. B. Campbell, "Stiffness-distortion sarcomere model for muscle simulation," *Journal of Applied Physiology*, vol. 87, no. 5, pp. 1861–1876, 1999.
- [40] M. V. Razumova, A. E. Bukatina, and K. B. Campbell, "Different myofilament nearest-neighbor interactions have distinctive effects on contractile behavior," *Biophysical Journal*, vol. 78, no. 6, pp. 3120–3137, 2000.
- [41] K. B. Campbell, M. V. Razumova, R. D. Kirkpatrick, and B. K. Slinker, "Myofilament kinetics in isometric twitch dynamics," *Annals of Biomedical Engineering*, vol. 29, no. 5, pp. 384–405, 2001.
- [42] K. B. Campbell, M. V. Razumova, R. D. Kirkpatrick, and B. K. Slinker, "Nonlinear myofilament regulatory processes affect frequency-dependent muscle fiber stiffness," *Biophysical Journal*, vol. 81, no. 4, pp. 2278–2296, 2001.
- [43] A. F. Huxley and R. Niedergerke, "Structural changes in muscle during contraction: interference microscopy of living muscle fibres," *Nature*, vol. 173, no. 4412, pp. 971–973, 1954.
- [44] C. Y. Scovil and J. L. Ronsky, "Sensitivity of a Hill-based muscle model to perturbations in model parameters," *Journal of Biomechanics*, vol. 39, no. 11, pp. 2055–2063, 2006.
- [45] O. Till, T. Siebert, C. Rode, and R. Blickhan, "Characterization of isovelocity extension of activated muscle: a Hill-type model for eccentric contractions and a method for parameter determination," *Journal of Theoretical Biology*, vol. 255, no. 2, pp. 176–187, 2008.
- [46] A. V. Hill, *First and Last Experiments in Muscle Mechanics*, University Press Cambridge, 1970.
- [47] B. R. Epstein and K. R. Foster, "Anisotropy in the dielectric properties of skeletal muscle," *Medical and Biological Engineering and Computing*, vol. 21, no. 1, pp. 51–55, 1983.
- [48] F. L. H. Gielen, W. Wallinga-de Jonge, and K. L. Boon, "Electrical conductivity of skeletal muscle tissue: experimental results from different muscles in vivo," *Medical and Biological Engineering and Computing*, vol. 22, no. 6, pp. 569–577, 1984.
- [49] A. J. Pullan, M. L. Buist, and L. K. Cheng, *Mathematically Modelling the Electrical Activity of the Heart: From Cell to Body Surface and Back Again*, World Scientific, 2005.
- [50] J. Sundnes, B. F. Nielsen, K. A. Mardal, X. Cai, G. T. Lines, and A. Tveito, "On the computational complexity of the bidomain and the monodomain models of electrophysiology," *Annals of Biomedical Engineering*, vol. 34, no. 7, pp. 1088–1097, 2006.
- [51] B. F. Nielsen, T. S. Ruud, G. T. Lines, and A. Tveito, "Optimal monodomain approximations of the bidomain equations," *Applied Mathematics and Computation*, vol. 184, no. 2, pp. 276–290, 2007.
- [52] J. B. Davidson, *Biophysical modelling of skeletal muscle [Ph.D. thesis]*, University of Auckland, Auckland, New Zealand, 2009.
- [53] J. Sundnes, G. T. Lines, and A. Tveito, "An operator splitting method for solving the bidomain equations coupled to a volume conductor model for the torso," *Mathematical Biosciences*, vol. 194, no. 2, pp. 233–248, 2005.
- [54] O. C. Zienkiewicz, R. L. Taylor, and J. Z. Zhu, *The Finite Element Method: Its Basis and Fundamentals*, vol. 1, Butterworth-Heinemann, 2005.
- [55] C. Linder, M. Tkachuk, and C. Miehe, "A micromechanically motivated diffusion-based transient network model and its incorporation into finite rubber viscoelasticity," *Journal of the Mechanics and Physics of Solids*, vol. 59, no. 10, pp. 2134–2156, 2011.
- [56] M. Tkachuk and C. Linder, "The maximal advance path constraint for the homogenization of materials with random network microstructure," *Philosophical Magazine*, vol. 92, no. 22, pp. 2779–2808, 2012.
- [57] V. M. Spitzer and D. G. Whitlock, "The visible human dataset: the anatomical platform for human simulation," *The Anatomical Record*, vol. 253, no. 2, pp. 49–57, 1998.
- [58] W. Herzog and T. R. Leonard, "Force enhancement following stretching of skeletal muscle: a new mechanism," *Journal of Experimental Biology*, vol. 205, no. 9, pp. 1275–1283, 2002.
- [59] D. Labeit, K. Watanabe, C. Witt et al., "Calcium-dependent molecular spring elements in the giant protein titin," *Proceedings of the National Academy of Sciences of the United States of America*, vol. 100, no. 23, pp. 13716–13721, 2003.
- [60] C. Rode, T. Siebert, and R. Blickhan, "Titin-induced force enhancement and force depression: a 'sticky-spring' mechanism in muscle contractions?" *Journal of Theoretical Biology*, vol. 259, no. 2, pp. 350–360, 2009.
- [61] B. Sharafi and S. S. Blemker, "A micromechanical model of skeletal muscle to explore the effects of fiber and fascicle geometry," *Journal of Biomechanics*, vol. 43, no. 16, pp. 3207–3213, 2010.
- [62] B. Sharafi and S. S. Blemker, "A mathematical model of force transmission from intrafascicularly terminating muscle fibers," *Journal of Biomechanics*, vol. 44, no. 11, pp. 2031–2039, 2011.
- [63] K. Hoyt, T. Kneezel, B. Castaneda, and K. J. Parker, "Quantitative sonoelastography for the in vivo assessment of skeletal muscle viscoelasticity," *Physics in Medicine and Biology*, vol. 53, no. 15, pp. 4063–4080, 2008.
- [64] M. van Loocke, C. G. Lyons, and C. K. Simms, "A validated model of passive muscle in compression," *Journal of Biomechanics*, vol. 39, no. 16, pp. 2999–3009, 2006.

- [65] M. Munteanu and L. F. Pavarino, “Decoupled schwarz algorithms for implicit discretizations of nonlinear monodomain and bidomain systems,” *Mathematical Models and Methods in Applied Sciences*, vol. 19, no. 7, pp. 1065–1097, 2009.
- [66] S. Göktepe and E. Kuhl, “Electromechanics of the heart: a unified approach to the strongly coupled excitation-contraction problem,” *Computational Mechanics*, vol. 45, no. 2-3, pp. 227–243, 2010.

Research Article

Contribution to the Determination of In Vivo Mechanical Characteristics of Human Skin by Indentation Test

Marie-Angèle Abellan, Hassan Zahouani, and Jean-Michel Bergheau

Université de Lyon, ENISE LTDS UMR 5513 CNRS, 58 rue Jean Parot, 42023 Saint-Étienne, France

Correspondence should be addressed to Marie-Angèle Abellan; marie-angele.abellan@enise.fr

Received 18 July 2013; Revised 9 September 2013; Accepted 9 September 2013

Academic Editor: Eddie Ng

Copyright © 2013 Marie-Angèle Abellan et al. This is an open access article distributed under the Creative Commons Attribution License, which permits unrestricted use, distribution, and reproduction in any medium, provided the original work is properly cited.

This paper proposes a triphasic model of intact skin in vivo based on a general phenomenological thermohydronechanical and physicochemical (THMPC) approach of heterogeneous media. The skin is seen here as a deforming stratified medium composed of four layers and made out of different fluid-saturated materials which contain also an ionic component. All the layers are treated as linear, isotropic materials described by their own behaviour law. The numerical simulations of in vivo indentation test performed on human skin are given. The numerical results correlate reasonably well with the typical observations of indented human skin. The discussion shows the versatility of this approach to obtain a better understanding on the mechanical behaviour of human skin layers separately.

1. Introduction

Human skin is the largest organ of the human body. The skin protects the body against external influences by preventing fluid loss when exposed to sun, the penetration of undesirable substances in case of pollution, and the development of diseases due to the direct application of external chemical or mechanical loads linked to clinical problems, surgery, or aesthetic treatments. The answers of this barrier to these chemical, biological, mechanical, and thermal loads depend on the person, the site on the body, the age, the health, its nutritional status, its properties, its state (intact or damaged), and its evolutions [1]. Numerous studies have shown that human skin has a stratified structure consisting from the skin outer surface inward of three main layers: the epidermis (composed of the stratum corneum and the viable epidermis), the dermis, and the hypodermis [2–6]. Dryness, microcracks, and loss of elasticity are thought to be influenced by fluid flow and the associated changes in ion concentration as a direct result of mechanical stress states. However, these phenomena are complex to understand and to model due to the strong couplings that exist between them and due to the complex behaviour of the different layers of skin soft tissues.

Studies of the mechanical behaviour of human skin have observed that the skin is a stratified nonhomogeneous,

anisotropic, nonlinear viscoelastic material which is subjected to a prestress in vivo [7–9]. In addition its properties vary with age, throughout the body and per person. Difficulties arise when trying to obtain quantitative descriptions of mechanical properties of the skin. Numerous mechanical experiments have been performed on the skin: tensile testing, suction methods, torsion tests, and indentation experiments [10–16]. For in vivo performed mechanical experiments, the measured behaviour is generally ascribed to the dermis due to the relative height of the viable epidermis and of the stratum corneum. However, the various skin layers are tied together, and it is hard to isolate the contribution of each of them. In vitro experiments give the opportunity to separate the skin layers. But in vitro experimental procedures change the mechanical properties of the individual skin layers. Moreover, it is hard to compare results obtained with different measurement conditions. This illustrates the need for an experimental system to measure the mechanical behaviour of the different skin layers in a noninvasive and objective manner and also independently of the experimental setup. The LTDS-indentation device is able to give a better understanding of the mechanical behaviour of the skin by characterizing the mechanical behaviour of several distinct skin layers in vivo without disturbing its natural stress state before the experiment [15].

To achieve this, several experimental setups are developed to load the skin mechanically, theoretical models are derived to describe the experiments, and numerical models are implemented to characterize the mechanical behaviour of the skin layers [17–25].

Within the framework of a general phenomenological thermohydrummechanical and physicochemical (THMPC) approach of heterogeneous media [22], a triphasic skin model is proposed in [18, 26] which incorporates a solid phase with three solid materials, a fluid phase and an ionic component under ambient constant conditions. Although not negligible, electrical effects are not taken into account in this model. The driving forces for transport are the gradients of the chemical potentials of the fluid and of the ions coupled with the gradients of the displacements of the different solids. In this model, skin is considered as a stratified material with three layers modelling the three outer layers of skin: the stratum corneum, the viable epidermis, and the dermis. All layers of the skin model are supposed to be made of fluid-saturated materials. Furthermore, each layer is seen as a different solid material within the solid phase, and it is described by its own behaviour law. In [18, 26], the solid materials are seen as isotropic linear elastic materials, each of them with its own elastic coefficients. In [27] the solid materials are modelled as nonlinear isotropic Mooney-Rivlin materials with one material constant, leading to the determination of three material constants in total. In [19] the solid materials are described as nonlinear isotropic Mooney-Rivlin materials with two material constants being able to face large deformations. Each solid material has its own strain energy density function of Mooney-Rivlin leading to the need to identify six material constants in total and which allow analysing the decoupled behaviour of each skin layer. These analyses have shown the capability of this model to describe the transient water flow and ion transport through damaged or undamaged skin after application of a saline solution and to gain insight on the mechanical behaviour of human skin layers separately.

The ionic component models the chemical load applied at the skin outer surface.

This paper proposes to extend this theoretical-experimental-numerical setup of human skin to the numerical simulation of in vivo indentation test. Skin is seen here as a triphasic medium with four solid materials in the solid phase, a fluid phase, and an ionic component. Furthermore, skin is considered as a stratified material with four layers modeling the four layers of skin: the stratum corneum, the viable epidermis, the dermis, and the hypodermis. All the layers are supposed to be made of fluid-saturated materials and are treated as isotropic linear materials described by their own behaviour law. The governing partial differential equations that arise from the equilibrium, the kinematic, and the constitutive equations are solved under varying physically admissible initial and boundary conditions for the ion concentrations, the fluid, and the solids proposed for describing in vivo indentation test available in the laboratory. A finite difference analysis is carried out which provides a quantitative understanding of water and ion movements through undamaged skin. The numerical simulation allows quantifying the in vivo mechanical properties of the different skin layers of soft tissue separately.

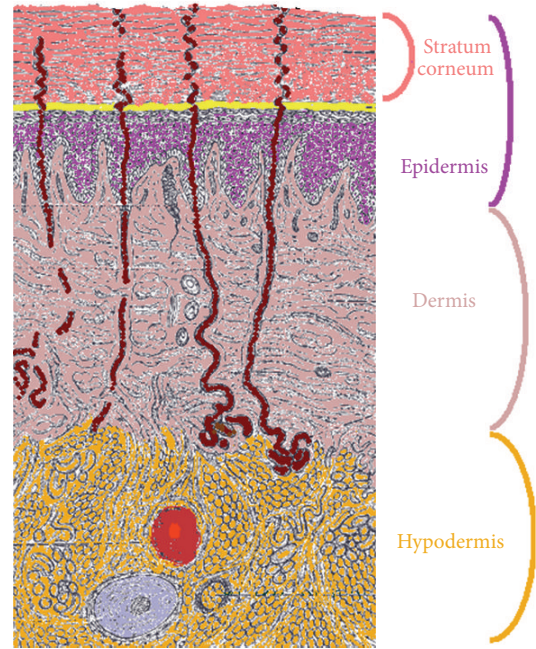


FIGURE 1: Schematic view of the cross-section of human skin showing the distinct layers.

We will first present the context of this paper linked to the histology of human skin in vivo. Then, to provide a proper setting, we will recapitulate the governing equations for a deforming porous medium including ions. The noninvasive experimental device is presented. Then, example calculations for a specimen of in vivo undamaged skin are given, and the obtained numerical results are discussed. Finally, some concluding remarks are made.

2. Histology of Skin

From the skin surface inwards, skin is composed of stratum corneum, viable epidermis, dermis, and hypodermis (Figure 1). A detailed look to these different layers shows up the following points which are of particular interest in our study.

2.1. Hypodermis. The hypodermis is an adipose tissue composed of loose fatty connective tissue found between the dermis and the muscles. It acts as an insulating layer and a protective cushion. Its thickness varies, some mm, with anatomical site, age, sex, race, and health of the individual.

2.2. Dermis. The dermis can be from 1 to 4 mm thick. It is largely composed of a very dense fibre network of collagen, elastin and minute quantities of reticulin, and a supporting matrix of amorphous ground substance, all bathed in physiological fluid. Physiological fluid provides the cells with nutrients and consists of a water solvent containing mineral and organic solutes as well as waste products from the cells. The dermis contains also microstructures like blood vessels, lymph vessels, nerve endings, sweat glands, sebaceous glands,

and hair follicles. The amorphous ground substance combines with the water of the physiological fluid to form a gel which does not leak out the dermis even under high pressure.

2.3. Viable Epidermis. The viable epidermis is a thin (10–100 μm) stratified squamous epithelial of soft keratinized living cells with nuclei, migrating to the outer skin surface: the keratinocytes. The viable epidermis is a nonvascular structure. Cells are surrounded, nourished, and bathed by a physiological fluid originating in the dermis and transported across the epidermal-dermal junction.

2.4. Stratum Corneum. The stratum corneum is a 10–25 μm thick dense coating of hard keratinized dead hexagonal flat cells: the corneocytes, held together by lipid bridges and corneosomes in what is commonly referred to as a brick-and-mortar structure. The corneocytes are the keratinocytes that were migrating to the skin outer surface and that have lost their nuclei. Although the corneocytes are nonviable cells, the stratum corneum is considered to be fully functional, particularly in terms of barrier properties, and retains metabolic functions. Because of its structure and composition, the cells of the stratum corneum have less capacity to bind water than the living cells of the viable epidermis or of the dermis.

The stratum corneum and the viable epidermis are continuously renewed by desquamation within 6 to 30 days. Cells are shed from the outside and replaced by new ones.

2.5. Consequence on the Skin Model. Skin's histology has shown that skin soft tissues are heterogeneous materials consisting of several components. If we combine this statement with the commonly admitted hypothesis that skin is a non-linear anisotropic hyperelastic and viscoelastic material, the choice is made here to derive the theoretical model for human skin soft tissues seen as a stratified triphasic material with four layers, four solids in the solid phase, one fluid in the fluid phase, and an ionic component. Figure 2 displays the studied specimen of skin where it is considered that

- (i) the four layers are as follows: layer 1 simulates the stratum corneum, layer 2 for the viable epidermis, layer 3 for the dermis, and layer 4 for the hypodermis,
- (ii) the four solids for the solid phase are as follows: solid 1 (s_1) simulates the corneocytes and the lipid mortar present in the stratum corneum, solid 2 (s_2) simulates the evolving cells of the viable epidermis, solid 3 (s_3) simulates the different cells of the dermis including the lymph and blood vessels, and solid 4 (s_4) simulates the fatty connective tissue of the hypodermis,
- (iii) the fluid (f) in the fluid phase simulates the 10% bound water in the lipid mortar of the stratum corneum plus the physiological fluid in the viable epidermis plus the physiological fluid in the dermis plus the physiological fluid in the hypodermis,
- (iv) the ionic component (i) simulates some cream deposited at the outer surface of the skin either for aesthetic or medical purposes and of which it is relevant to follow the penetration.

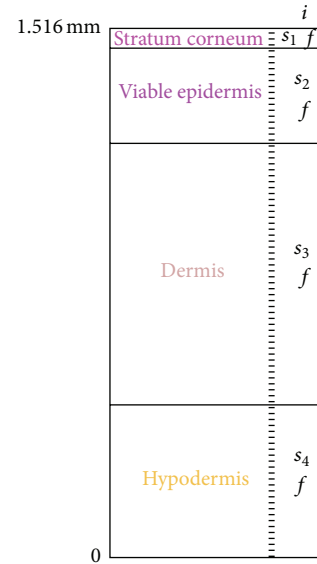


FIGURE 2: Schematic view of the cross-section of the skin specimen showing the distinct layers and components.

The study presented in the following paragraphs is based on this skin specimen.

3. Theoretical Model

Under the phenomenological hypothesis [28], the general THMPC approach of heterogeneous media [22] describes the overall material behaviour of the heterogeneous medium as a combination of the behaviour of each individual component. It is based on the principle of interaction of the components with the following assumptions:

- (i) in each infinitesimal volume of a heterogeneous medium a finite number of components are present;
- (ii) each component contributes to the total material behaviour in the same proportion as its volumetric participation given by its volumic ratio;
- (iii) all the components are extended to the total studied unit volume of heterogeneous medium.

This approach is applied here to model the human skin specimen introduced in Section 2.5 (Figure 2).

As it was said, skin is seen here as a triphasic material with four solids for the solid phase ($\pi = s_1, s_2, s_3, s_4$), one for each layer, a fluid ($\pi = f$), and an ionic component ($\pi = i$), subjected to the restriction of small displacement gradients, no mass transfer, and no chemical reactions between the constituents; the electrical effects are not taken into account, and the components will be considered as intrinsically incompressible. The studied processes occur isothermally. In addition, the initial configuration of the skin solid skeleton is chosen here as a reference domain for deriving the field equations. Hereafter, all physical quantities are assumed to be functions of the Euler variables (\mathbf{x}, t) where t is the time and \mathbf{x} is the spatial vector defining the position of the material particle in the current

configuration at time t . Hence, the implicit arguments of all vectors or tensors or scalars are the Euler variables (\mathbf{x}, t) . With these assumptions, the source of mass of constituent π coming from the other constituents present in the medium is equal to zero, and the balance of mass for each constituent π (for $\pi = s_1, s_2, s_3, s_4, f, i$) reads

$$\frac{\partial}{\partial t} \rho_\pi + \nabla \cdot [\rho_\pi \mathbf{v}_\pi] = 0 \quad (1)$$

with $\mathbf{v}_\pi(\mathbf{x}, t)$ being the absolute velocity of constituent π in $\text{m}\cdot\text{s}^{-1}$ and $\rho_\pi(\mathbf{x}, t)$ being the relative mass density of constituent π in $\text{kg}\cdot\text{m}^{-3}$ defined for $\pi = s_1, s_2, s_3, s_4, f, i$ by

$$\rho_\pi = n_\pi \rho'_\pi, \quad (2)$$

where $\rho'_\pi(\mathbf{x}, t)$ is the absolute mass density of constituent π in $\text{kg}\cdot\text{m}^{-3}$ and $n_\pi(\mathbf{x}, t)$ is the volumic ratio of constituent π . As in the remainder of this paper, the subscripts s_1, s_2, s_3, s_4, f , and i denote the solids, the fluid, and the ions, respectively. The different constituents are supposed to be intrinsically incompressible. Therefore, their absolute mass density are kept constant in this paper. Further, the sum of volumic ratio over the constituents present in the medium should equal one:

$$n_{s_1} + n_{s_2} + n_{s_3} + n_{s_4} + n_f + n_i = 1. \quad (3)$$

Neglecting inertia forces, convective terms, and the gravity acceleration, the balance of linear momentum for each constituent π (for $\pi = s_1, s_2, s_3, s_4, f, i$) reduces to

$$\nabla \cdot \sigma_\pi + \mathbf{p}'_\pi = 0 \quad (4)$$

with $\sigma_\pi(\mathbf{x}, t)$ being the Cauchy stress tensor of constituent π in Pa and $\mathbf{p}'_\pi(\mathbf{x}, t)$ being the source of momentum for constituent π coming from the other constituents in $\text{kg}\cdot\text{m}^{-2}\cdot\text{s}^{-2}$, which takes into account the possible local drag interactions between the solids, the fluid, and the ions and which satisfies the momentum production constraint:

$$\mathbf{p}'_{s_1} + \mathbf{p}'_{s_2} + \mathbf{p}'_{s_3} + \mathbf{p}'_{s_4} + \mathbf{p}'_f + \mathbf{p}'_i = 0. \quad (5)$$

Under the assumption of chemically inert fluid and ions and with solid matrix materials, the material state relation expressing the chemical potential of the fluid $\mu_f(\mathbf{x}, t)$ encompasses the interactions between solids, fluid, and ions. For the fluid, it reads

$$\mu_f = p - \Pi + \psi, \quad (6)$$

where $p(\mathbf{x}, t)$ is the fluid pressure in Pa, $\psi(\mathbf{x}, t)$ is the matrix potential accounting for fluid-solid interactions (capillary and adsorptive effects) in Pa, and $\Pi(\mathbf{x}, t)$ is the osmotic pressure accounting for fluid-ion interactions in Pa. The chemical potential of the fluid is in $\text{J}\cdot\text{m}^{-3}$. These quantities need to be experimentally determined in order to write a close mathematical problem, but they are difficult to obtain. Reference [23] considered relations between chemical potential and porosity from different references and proposes the following experimental fit:

$$p + \psi = \left(e^{9.7E-5} - e^{(9.7E-5)/n_f} \right) (9.84E + 10), \quad (7)$$

$$\Pi = 2RTc_i \quad (8)$$

with R being the universal gas constant in $\text{J} \cdot \text{K}^{-1} \cdot \text{mol}^{-1}$, T being the absolute temperature in K, and $c_i(\mathbf{x}, t)$ being the concentration of the ions per unit fluid volume in $\text{mol}\cdot\text{m}^{-3}$.

For the ionic component, the chemical potential $\mu_i(\mathbf{x}, t)$ is defined as

$$\mu_i = \mu_{i_0} + RT \ln(c_i) \quad (9)$$

with μ_{i_0} being the chemical potential of the ions in a reference state in $\text{J}\cdot\text{m}^{-3}$. Neglecting couplings between velocity and heat flux, fluid flow through a saturated porous medium with an ionic component is expressed by a generalized Darcy's law hereunder defined in terms of the gradient of the chemical potential $\mu_f(\mathbf{x}, t)$ of the fluid, the gradient of the chemical potential $\mu_i(\mathbf{x}, t)$ of the ions, and a second-order permeability tensor $K(\mathbf{x}, t)$:

$$n_f (\mathbf{v}_f - \mathbf{v}_s) = -K \cdot \left[\nabla \mu_f + \frac{n_i}{n_f} \nabla \mu_i \right]. \quad (10)$$

In a matrix-vector notation, the permeability tensor appearing in (10) is a position and time dependent function defined as

$$K(\mathbf{x}, t) = \begin{bmatrix} K_{xx}(\mathbf{x}, t) & K_{xy}(\mathbf{x}, t) & K_{xz}(\mathbf{x}, t) \\ K_{yx}(\mathbf{x}, t) & K_{yy}(\mathbf{x}, t) & K_{yz}(\mathbf{x}, t) \\ K_{zx}(\mathbf{x}, t) & K_{zy}(\mathbf{x}, t) & K_{zz}(\mathbf{x}, t) \end{bmatrix}, \quad (11)$$

where each component $K_{ij}(\mathbf{x}, t)$ for $i, j \in \{x, y, z\}$ is a function of position and time and it has the unit $\text{m}^4 \cdot \text{N}^{-1} \cdot \text{s}^{-1}$.

The diffusion of ions through the fluid phase of a porous medium is taken into account through a Fick's law-type relation by means of a second-order diffusion tensor of the ions D_i :

$$n_i (\mathbf{v}_i - \mathbf{v}_f) = -D_i \nabla \mu_i. \quad (12)$$

In a matrix-vector notation, the diffusion tensor of the ions appearing in (12) is a position and time dependent function defined as

$$D_i(\mathbf{x}, t) = \begin{bmatrix} D_{ixx}(\mathbf{x}, t) & D_{ixy}(\mathbf{x}, t) & D_{ixz}(\mathbf{x}, t) \\ D_{iyx}(\mathbf{x}, t) & D_{iyy}(\mathbf{x}, t) & D_{iyz}(\mathbf{x}, t) \\ D_{izx}(\mathbf{x}, t) & D_{izy}(\mathbf{x}, t) & D_{izz}(\mathbf{x}, t) \end{bmatrix}, \quad (13)$$

where each component $D_{ijk}(\mathbf{x}, t)$ for $j, k \in \{x, y, z\}$ is a function of position and time and it has the unit $\text{m}^2 \cdot \text{s}^{-1}$.

The stress-strain relations for the solids are elaborated under the classical assumption for heterogeneous media that the Cauchy stress tensor of the total heterogeneous medium is composed of a solid and a fluid part:

$$\sigma = \sigma_{s_1} + \sigma_{s_2} + \sigma_{s_3} + \sigma_{s_4} - pI \quad (14)$$

with σ being the Cauchy stress tensor of the total heterogeneous medium in Pa and I being the second-order identity tensor.

Under the assumption of small displacements and small strains, skin is considered as a linear isotropic elastic material and a Hooke's stress-strain relation is taken for each solid skeleton ($\pi = s_1, s_2, s_3, s_4$):

$$\sigma_\pi = D_\pi^e : \varepsilon_\pi \quad \text{for } \pi = s_1, s_2, s_3, s_4, \quad (15)$$

where $D_\pi^e(\mathbf{x}, t)$ is the elasticity tensor of the solid material π in Pa and $\varepsilon_\pi(\mathbf{x}, t)$ is the strain tensor of solid π defined by

$$\varepsilon_\pi = \nabla^s u_\pi \quad (16)$$

with $u_\pi(\mathbf{x}, t)$ being the displacement field of solid π in m. It should be noticed that the Cauchy stress tensor, the strain tensor, the elasticity tensor, and the displacement field are functions of the space and time variables. The superscript s denotes the symmetric part of the gradient operator.

For later use in Section 5, (15) can be rewritten more conveniently in a matrix-vector notation:

$$\varepsilon_\pi = E_\pi : \sigma_\pi \quad \text{for } \pi = s_1, s_2, s_3, s_4 \quad (17)$$

with

$$E_\pi = (D_\pi^e)^{-1} \quad \text{for } \pi = s_1, s_2, s_3, s_4, \quad (18)$$

where $E_\pi(\mathbf{x}, t)$ is the matrix of the elasticity compliances defined as the inverse of the matrix D_π^e of the elasticity coefficients. Each component $E_{\pi_{ij}}(\mathbf{x}, t)$ for $i, j \in \{x, y, z\}$ of the elasticity compliance matrix $E_\pi(\mathbf{x}, t)$ is space and time dependent with unit Pa^{-1} . The Cauchy stress and the strain in vector notation are given by

$$\sigma_\pi(\mathbf{x}, t) = \begin{bmatrix} \sigma_{\pi_{xx}}(\mathbf{x}, t) \\ \sigma_{\pi_{yy}}(\mathbf{x}, t) \\ \sigma_{\pi_{zz}}(\mathbf{x}, t) \\ \sigma_{\pi_{xy}}(\mathbf{x}, t) \\ \sigma_{\pi_{yz}}(\mathbf{x}, t) \\ \sigma_{\pi_{zx}}(\mathbf{x}, t) \end{bmatrix}, \quad (19)$$

$$\varepsilon_\pi(\mathbf{x}, t) = \begin{bmatrix} \varepsilon_{\pi_{xx}}(\mathbf{x}, t) \\ \varepsilon_{\pi_{yy}}(\mathbf{x}, t) \\ \varepsilon_{\pi_{zz}}(\mathbf{x}, t) \\ \varepsilon_{\pi_{xy}}(\mathbf{x}, t) \\ \varepsilon_{\pi_{yz}}(\mathbf{x}, t) \\ \varepsilon_{\pi_{zx}}(\mathbf{x}, t) \end{bmatrix}$$

with the elasticity compliance matrix

$$E_\pi(\mathbf{x}, t) = \begin{bmatrix} E_{\pi_{xx}}(\mathbf{x}, t) & E_{\pi_{xy}}(\mathbf{x}, t) & E_{\pi_{xz}}(\mathbf{x}, t) \\ E_{\pi_{yx}}(\mathbf{x}, t) & E_{\pi_{yy}}(\mathbf{x}, t) & E_{\pi_{yz}}(\mathbf{x}, t) \\ E_{\pi_{zx}}(\mathbf{x}, t) & E_{\pi_{zy}}(\mathbf{x}, t) & E_{\pi_{zz}}(\mathbf{x}, t) \end{bmatrix} = \begin{bmatrix} \frac{1}{E_\pi} & \frac{-\gamma_\pi}{E_\pi} & \frac{-\gamma_\pi}{E_\pi} & 0 & 0 & 0 \\ \frac{-\gamma_\pi}{E_\pi} & \frac{1}{E_\pi} & \frac{-\gamma_\pi}{E_\pi} & 0 & 0 & 0 \\ \frac{-\gamma_\pi}{E_\pi} & \frac{-\gamma_\pi}{E_\pi} & \frac{1}{E_\pi} & 0 & 0 & 0 \\ 0 & 0 & 0 & \frac{1+\gamma_\pi}{E_\pi} & 0 & 0 \\ 0 & 0 & 0 & 0 & \frac{1+\gamma_\pi}{E_\pi} & 0 \\ 0 & 0 & 0 & 0 & 0 & \frac{1+\gamma_\pi}{E_\pi} \end{bmatrix}, \quad (20)$$

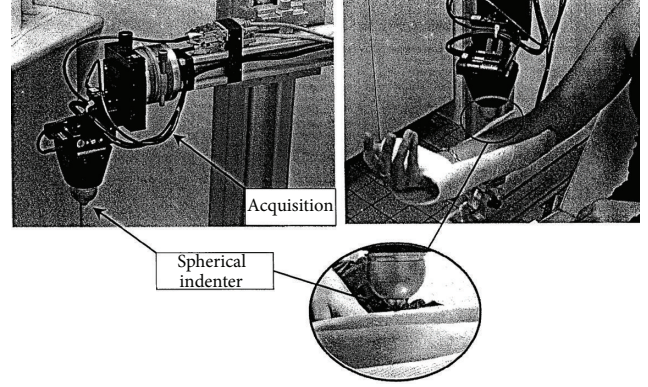


FIGURE 3: Experimental setup of the LTDS-indentation device.

where E_π is the Young modulus of the solid material π and γ_π is the Poisson's ratio of the solid material π .

The field equations, that is, the balance of mass for the fluid, the balance of mass for the ions, and the balance of momentum for the solids, are complemented by the boundary conditions which hold on complementary parts of the boundary in terms of prescribed external traction, prescribed velocity, prescribed outflow of pore fluid and prescribed pressure, prescribed outflow of ions, and prescribed chemical potential, respectively. The initial conditions which specify the displacements u_π for the solid grains $\pi = s_1, s_2, s_3, s_4$, the velocities v_π for the solid grains $\pi = s_1, s_2, s_3, s_4$, and the chemical potentials μ_π for the fluid and the ionic component $\pi = f, i$ at $t = 0$ close the initial value problem.

4. Experimental Device

The original LTDS-indentation device developed by the team of Professor Zahouani permits studying of the mechanical response of the human skin in vivo. This indentation device loads the skin mechanically by applying a controlled normal force onto the surface of the skin. The experimental setup is presented Figure 3.

The penetration depth of the rigid spherical indenter (diameter 6 mm) is recorded as a function of the normal applied force, F_{load} , during a loading-unloading experiment. The recorded curve for an indentation test performed on the volar forearm zone of a volunteer healthy adult is given in Figure 4. This location is chosen because it is easily accessible, relatively flat, and less disturbed by the natural movement of the body. It makes the indentation tests less tiring for the volunteer because of the position of the arm during the test. Therefore, it disturbs in the least possible way the skin's natural state of stress. The indentation test is realized for a constant indentation speed of $500.0 \mu\text{m/s}$ at ambient temperature and without surface treatment on skin before the test.

This loading-unloading curve is reversible with a very low hysteresis due to the dissipated energy. No plastic behaviour is observed, in the sense that there is no residual print onto the surface of the skin allowing the measurement of a plastic depth. Therefore, in this load range, it can be considered that human skin soft tissues can be modeled as elastic materials.

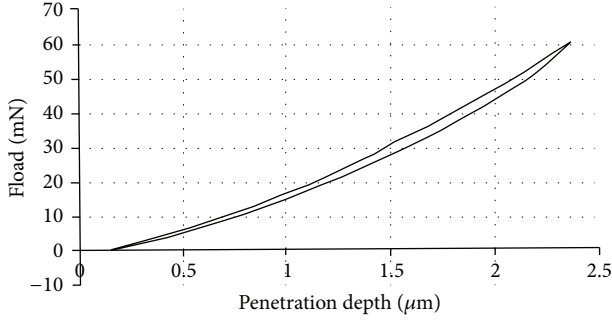


FIGURE 4: Recorded curve for a loading-unloading indentation test on the volar forearm of an adult.

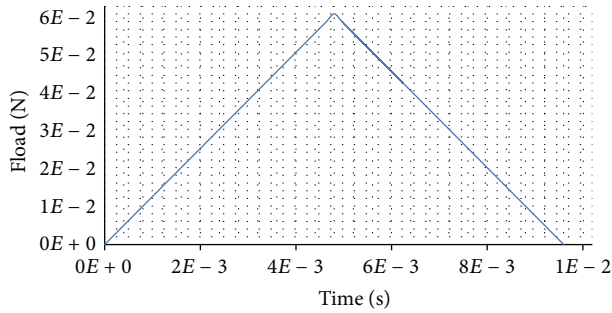


FIGURE 5: Applied mechanical load Load versus time for the loading-unloading steps of the numerical simulations.

Moreover, this recorded experimental curve (Figure 4) is reworked and gives a curve of the applied mechanical load Load versus time for the loading-unloading steps of the numerical simulations (Figure 5).

These experimental data are used in the numerical simulation, hereafter, to define physically admissible boundary and initial conditions and to help characterizing in vivo equivalent mechanical parameters of human soft tissues.

As it is not possible to measure the thickness of the skin on the inner forearm, we will assume in the following that the thickness of the skin at this part (stratum corneum + viable epidermis + dermis + hypodermis) is approximately $1516 \mu\text{m}$ ($12 \mu\text{m}$ for the stratum corneum + $102 \mu\text{m}$ for the viable epidermis + $1002 \mu\text{m}$ for the dermis + $400 \mu\text{m}$ for the hypodermis) which are mean values typical for biological soft tissues that can be found already in the literature [29]. Hence, the total response of the skin is the composite response of the individual contributions of the stratum corneum, the viable epidermis, the dermis, and the hypodermis.

5. Numerical Simulation

5.1. Finite Difference Model. A finite difference analysis has been carried out that allows for a quantitative understanding of fluid flow and ion transport through intact skin and also of the deformations of the skin layers. The spatial derivatives appearing in the field equations, that is, the balance of momentum (2) for constituents $\pi = s_1, s_2, s_3, s_4, f, i$, the balance of mass (1) for the fluid $\pi = f$, and the balance of mass

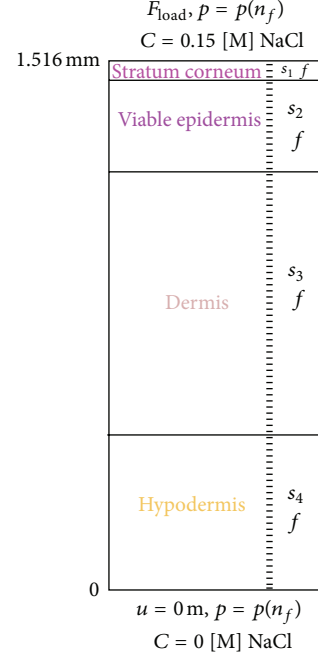


FIGURE 6: Finite difference mesh and boundary conditions.

(1) for the ions $\pi = i$, are approximated with a second-order accurate finite difference scheme. Explicit forward finite differences are used to approximate the temporal derivatives, which are first-order accurate. As implied in the field equations, the velocities of the solids, the fluid, and the ions are taken as fundamental unknowns and the displacements are obtained by integration when needed.

The constitutive relations for the solids, the fluid, and the ions are incremental relations giving directly the increment of their associated variable. All calculations are carried out for a specimen of intact skin with a depth of $1516 \mu\text{m}$ at an ambient temperature of 21°C . The thickness is assumed to be uniform within each layer. The tissue composite consists of 380 elements (Figure 6).

For the simulation, the model needs to be complemented by a set of material parameters. This set is also taken as mean values for human skin available in the literature except as regards of the mechanical parameters for which a mechanical parameters estimation procedure is carried out in Section 5.3.

5.2. Governing Equations. For this 1-Dim numerical simulation of undamaged skin, some equations and relations of Section 3 can be rewritten more simply. They are summarized below with variables that are functions of the vertical Eulerian component z of the reference frame.

- (i) *Balance of mass for $\pi = s_1, s_2, s_3, s_4, f, i$.* Equation (1) reduces to

$$\frac{\partial}{\partial t} \rho_\pi + \frac{\partial}{\partial z} [\rho_\pi v_{\pi z}] = 0 \quad (21)$$

with $v_{\pi z}(z, t)$ being the vertical component of the absolute velocity of constituent π .

- (ii) *Balance of momentum for $\pi = s_1, s_2, s_3, s_4, f, i$.* Equation (2) can be rewritten as follows:

$$\frac{\partial}{\partial z} \sigma_{\pi_{zz}} + p'_{\pi z} = 0 \quad (22)$$

with $\sigma_{\pi_{zz}}(z, t)$ being the component of the Cauchy stress tensor of constituent π in the z direction and $p'_{\pi z}(z, t)$ being the vertical component of the source of momentum for constituent π .

- (iii) *Generalized Darcy's law for the fluid $\pi = f$.* Assuming isotropic material, relation (10) leads to

$$n_f (v_{f_z} - v_{s_z}) = -K_{zz} \left[\frac{\partial \mu_f}{\partial z} + \frac{n_i}{n_f} \frac{\partial \mu_i}{\partial z} \right] \quad (23)$$

with K_{zz} being the permeability coefficient.

- (iv) *Fick's law for the ions $\pi = i$.* For isotropic material, relation (12) reduces to

$$n_i (v_{i_z} - v_{f_z}) = -D_{izz} \frac{\partial \mu_i}{\partial z}, \quad (24)$$

where D_{izz} is the diffusion coefficient for the ions.

- (v) *Stress-strain relations for the solids $\pi = s_1, s_2, s_3, s_4$.* Taking into account relations (19) and (20) into relations (17) and (16) leads to

$$\begin{aligned} \sigma_{s_1zz} &= E_{s_1} \varepsilon_{s_1zz} = E_{s_1} \frac{\partial u_{s_1z}}{\partial z}, \\ \sigma_{s_2zz} &= E_{s_2} \varepsilon_{s_2zz} = E_{s_2} \frac{\partial u_{s_2z}}{\partial z}, \\ \sigma_{s_3zz} &= E_{s_3} \varepsilon_{s_3zz} = E_{s_3} \frac{\partial u_{s_3z}}{\partial z}, \\ \sigma_{s_4zz} &= E_{s_4} \varepsilon_{s_4zz} = E_{s_4} \frac{\partial u_{s_4z}}{\partial z}, \end{aligned} \quad (25)$$

where $\sigma_{\pi_{zz}}(z, t)$ is the component of the Cauchy stress tensor of solid π on the z direction, $\varepsilon_{\pi_{zz}}(z, t)$ is the component of the strain tensor of solid π on the z direction, $u_{\pi z}(z, t)$ is the vertical component of the displacement of solid π , and $E_{s_1}, E_{s_2}, E_{s_3}$, and E_{s_4} are the Young moduli of, respectively, the stratum corneum, the viable epidermis, the dermis, and the hypodermis. The other relations of the theoretical model are used directly without being reworked.

5.3. Mechanical Parameter Estimation. An iterative procedure is used to adjust the mechanical parameters of the material model $E_{s_1}, E_{s_2}, E_{s_3}$, and E_{s_4} for, respectively, the stratum corneum, the viable epidermis, the dermis, and the hypodermis. Material parameters are set in the input file of the finite difference model. The applied load (Figure 5) is also used as an input in the finite difference model; then, the simulation runs and the numerical results are examined. The computed skin surface displacements during the loading-unloading steps are extracted and compared with the experimentally obtained axial displacement of the skin surface

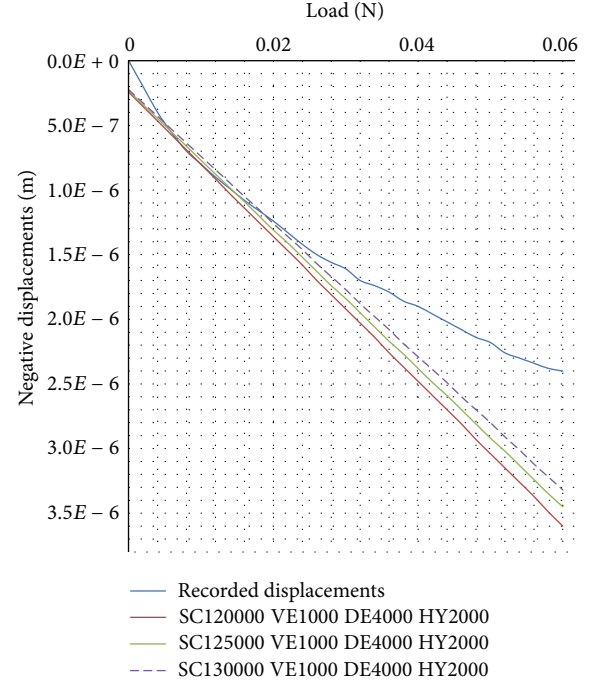


FIGURE 7: Comparison between numerical displacements curves and the experimental displacement curve for various combinations of material parameters.

under the indenter. Figure 7 displays the comparison between the experimental displacement curve and the numerically obtained surface displacements curves for various combinations of discrete values of the material parameters of both layers. The curve “SC120000 VE1000 DE4000 HY2000” corresponds to a simulation carried out with elastic moduli of $E_{s_1} = 120E3$ Pa for the stratum corneum (SC), $E_{s_2} = 1E3$ Pa for the viable epidermis (VE), $E_{s_3} = 4E3$ Pa for the dermis (DE), and $E_{s_4} = 2E3$ Pa for the hypodermis (HY). The curve “SC125000 VE1000 DE4000 HY2000” corresponds to a simulation carried out with elastic moduli of $E_{s_1} = 125E3$ Pa for the stratum corneum (SC), $E_{s_2} = 1E3$ Pa for the viable epidermis (VE), and $E_{s_3} = 4E3$ Pa for the dermis (DE), and $E_{s_4} = 2E3$ Pa for the hypodermis (HY). The curve “SC130000 VE1000 DE4000 HY2000” corresponds to a simulation carried out with elastic moduli of $E_{s_1} = 130E3$ Pa for the stratum corneum (SC), $E_{s_2} = 1E3$ Pa for the viable epidermis (VE), $E_{s_3} = 4E3$ Pa for the dermis (DE), and $E_{s_4} = 2E3$ Pa for the hypodermis (HY).

The comparison shows a minimum difference at approximately the curve “SC130000 VE1000 DE4000 HY2000”.

5.4. Numerical Model. Therefore, the skin soft tissues are modelled as isotropic linear elastic materials with an elastic modulus of $E_{s_1} = 130E3$ Pa for the stratum corneum-simulating solid s_1 , $E_{s_2} = 1E3$ Pa for the viable epidermis-simulating solid s_2 , $E_{s_3} = 4E3$ Pa for the dermis-simulating solid s_3 , and $E_{s_4} = 2E3$ Pa for the hypodermis-simulating solid s_4 . An absolute mass density $\rho'_\pi = 1330 \text{ kg}\cdot\text{m}^{-3}$ is assumed for each solid $\pi = s_1, s_2, s_3, s_4$. For the fluid, an absolute mass density $\rho'_f = 1000 \text{ kg}\cdot\text{m}^{-3}$ is adopted. For the ions, an absolute mass

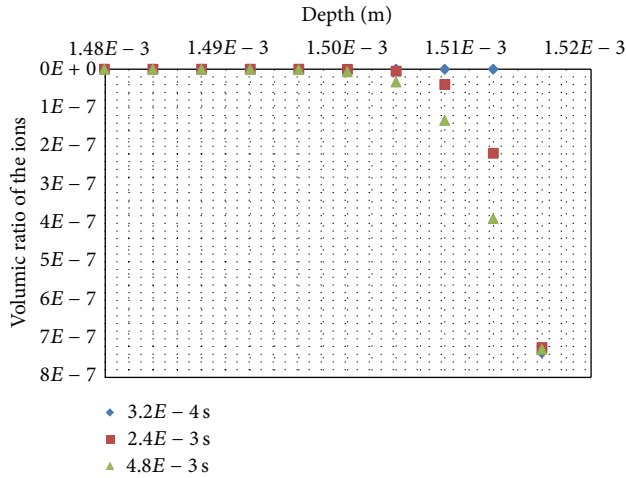


FIGURE 8: Volumic ratio of the ions.

density $\rho_i' = 1549 \text{ kg}\cdot\text{m}^{-3}$ is taken. In the calculations, the permeability $K = 1.98E-21 \text{ m}^4 \cdot \text{N}^{-1} \cdot \text{s}^{-1}$ and the diffusion coefficient $D_i = 3.3E-11 \text{ m}^2 \cdot \text{s}^{-1}$ are adopted.

Environmental conditions are assumed according to the following pattern.

- (i) Upper skin surface: a force is applied at the outer upper skin surface node equivalent to the imposed indentation load obtained from the experimental curve (Figure 5), atmospheric pressure for the fluid, the skin surface is in contact with a 0.15 [M] NaCl solution.
- (ii) Inward skin surface: the inward lower surface node is subjected to a displacement condition of 0 mm displacement, a zero flux of fluid, and a zero flux of ions.

Figure 6 gives the initial mesh and the boundary conditions taken in the simulations.

In the initial state, all layers are considered made out of fully saturated material with no ionic component. The calculus starts with an initial state based on experimental data or fit given in [23]. Moreover, with respect to the volumic ratio of the ions, it is set equal to zero for all the layers in the initial state.

6. Results and Discussion

For the above set of parameters, the computed numerical results give the evolutions of all the state variables for all the constituents with respect to space and time. They are given and discussed hereafter for some variables in terms of profiles along the specimen of intact skin in vivo.

The volumic ratios of the ions are given in Figure 8 for 3 steps of calculations, $t = 3.2E-4 \text{ s}$, $2.4E-3 \text{ s}$, and $4.8E-3 \text{ s}$ for the upper layers of skin soft tissues. They show a downward movement of the ions penetrating the stratum corneum and also the first layers of the viable epidermis.

The numerical results show that the ions penetrate till the layer with coordinate $13.92E-4 \text{ m}$ of the viable epidermis with associated decreasing magnitude of their volumic ratios: $3.69E-41$ for the layer-simulating node with coordinate

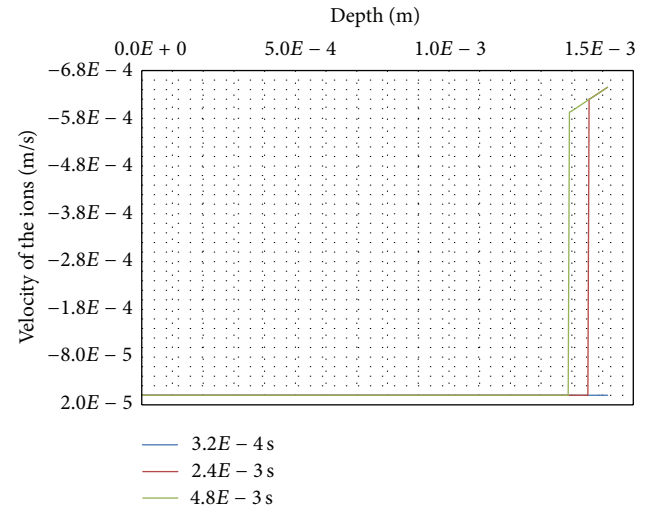


FIGURE 9: Velocity of the ions.

$13.92E-4 \text{ m}$ and $7.27E-7$ for the upper surface-simulating node with coordinate $15.16E-4 \text{ m}$.

This penetration occurs with a velocity of the ions shown in Figure 9 for the same 3 steps of calculations $t = 3.2E-4 \text{ s}$, $2.4E-3 \text{ s}$, and $4.8E-3 \text{ s}$ for the upper layers of skin soft tissues. In spite of the low diffusion coefficient of the skin soft tissues $D_i = 3.3E-11 \text{ m}^2 \cdot \text{s}^{-1}$, the order of magnitude for the velocities of the ions are quite high $-5.92E-4 \text{ m}\cdot\text{s}^{-1}$ for node with coordinate $13.92E-4 \text{ m}$ and $-6.45E-4 \text{ m}\cdot\text{s}^{-1}$ for the upper node with coordinate $15.16E-4 \text{ m}$ for time $4.8E-3 \text{ s}$. Also the velocities tend to increase with respect to time.

Figure 10 displays the linear profiles of the volumic ratio of the fluid for 5 steps of calculations $t = 3.2E-4 \text{ s}$, $2.4E-3 \text{ s}$, $4.8E-3 \text{ s}$, $7.2E-3 \text{ s}$, and $9.6E-3 \text{ s}$. The fluid volumic ratio of the skin surface (stratum-corneum-simulating nodes) changes almost immediately after application of the chemical and mechanical external loads. The volumic ratio of deeper layers of the skin (viable-epidermis-simulating nodes and the dermis-simulating nodes) reacts more slowly. The magnitude of these evolutions is low as shown in Figure 10 with the overlapping curves.

Moreover, these evolutions exhibit two different types of movement for the fluid as given by the velocities of the fluid (Figure 11). First the velocity map reveals negative velocities for all nodes of the mesh during the chemical and mechanical loading steps (from 0 s to $4.8E-3 \text{ s}$). The fluid is flowing slowly from the upper surface layers inward. Then, the velocities become positive for all nodes of the mesh during the unloading steps (from $4.8E-3 \text{ s}$ to $9.6E-3 \text{ s}$). The fluid tends to flow upward in search of a new equilibrium.

The negative displacements of the solids are presented in Figure 12 for 5 steps of calculations $t = 3.2E-4 \text{ s}$, $2.4E-3 \text{ s}$, $4.8E-3 \text{ s}$, $7.2E-3 \text{ s}$, and $9.6E-3 \text{ s}$. During the chemical and mechanical loading steps (from 0 s to $4.8E-3 \text{ s}$), the solids display a consolidation-type behaviour all along the specimen of skin soft tissues-simulating nodes.

On the contrary, during the unloading steps (from $4.8E-3 \text{ s}$ to $9.6E-3 \text{ s}$), the magnitude of the relative displacements becomes higher and the volume of the specimen

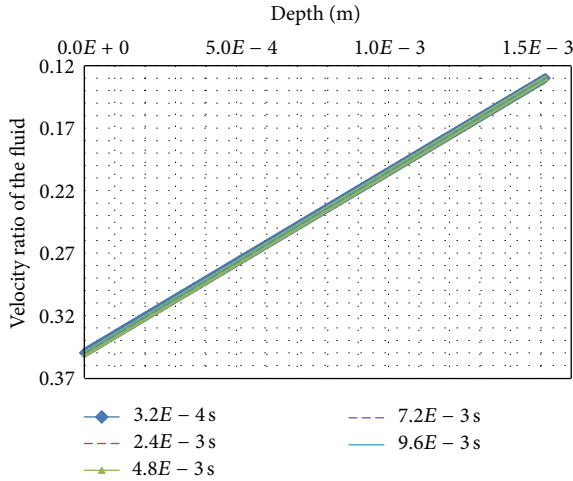


FIGURE 10: Volumic ratio of the fluid.

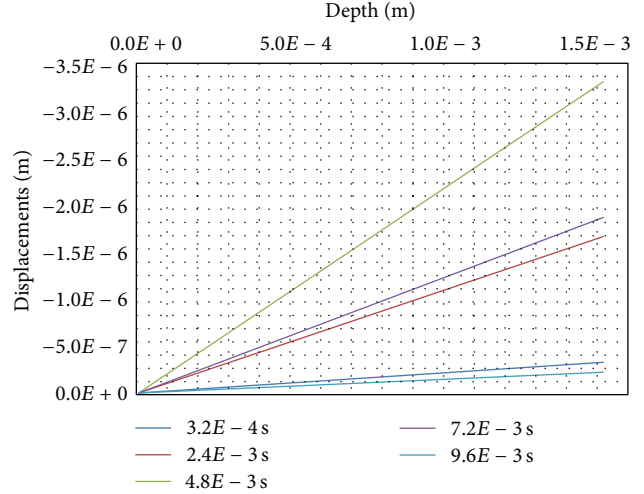


FIGURE 12: Displacements of the solids.

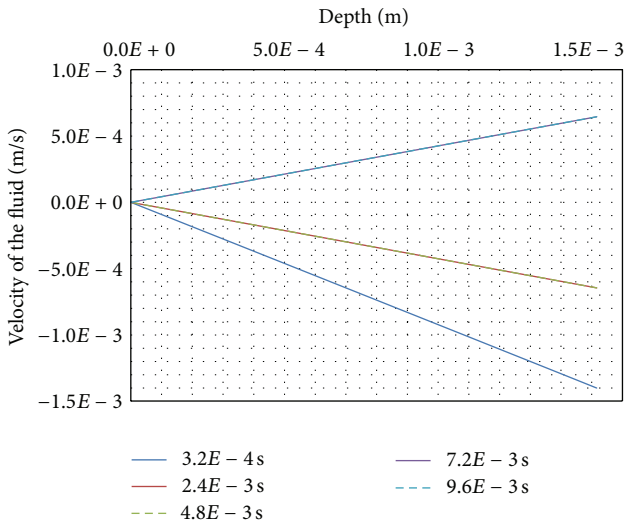


FIGURE 11: Velocity of the fluid.

increases. In spite of the choice of an isotropic linear elastic behaviour for all the skin tissues-simulating solids, it can be observed some kind of viscosity behaviour because the state at the end of the unloading steps has not yet come back to the initial one (curve $3.2E-4$ s and curve $9.6E-3$ s are not overlapping each other).

The initial state taken as an input for the specimen of human skin is based on experiments. Therefore, it includes physiological influences and couplings which are not yet taken into account in our model but which are impossible to decouple. An example is relations (7) and (8) used for the calculus of the chemical potential of the fluid. Nowadays, it is accepted that fluid pressure is generated by the heart. It pushes water out of the capillaries. On the other hand, water potential is created due to the ability of small solutes to pass through membranes. This movement induces osmosis, that is, water passing from a high concentration (of water) outside to a low concentration inside in an attempt to reach an equilibrium. There, osmotic pressure drives water back inside.

Because of the heart, the physiological fluid is constantly flowing and equilibrium is never reached. Because of the differences between fluid pressure and osmotic pressure, the flow of water pushes water outside again and influences the imbalance in solutes, favoring the net movement of physiological fluid. This influence on our model can be seen in Figure 7 at the beginning of the loading steps and at the end of the unloading steps. The studied specimen of skin is not in equilibrium at the beginning of the loading steps. It does not reach an equilibrium at the end of the unloading steps. A zero applied mechanical load F_{load} does not lead to a zero computed numerical penetration depth because the couplings between solids-fluid-ions are still imposing nonzero fluid and ions internal loads resulting in these nonzero negative displacements.

The applied chemical and mechanical external loads at the upper outer surface of the skin specimen lead to gradients of concentration of ions and to gradients of deformations for the different solids. This leads to nonzero velocities for ions initiating the penetration of the ions in the upper layers of the stratum corneum. It gives also nonzero velocities for the fluid which starts flowing downward from the upper surface of the stratum corneum to the deepest layers of the hypodermis. In search of equilibrium, new values of the fluid pressure influence the magnitude of the chemical potential of the fluid and of the chemical potential of the ions. Through the hypothesis made with relation (13) on the definition of the Cauchy stress tensor of the total medium, the evolutions of each solid is then triggered by these coupled phenomena.

Comparison with results from the literature is not easy in case of nonlinear material behaviour like in vivo skin. However, making an attempt of comparison, it can be said that the numerical results obtained with the analysis lead to qualitatively equivalent evolutions when compared with the typical observation of indented human skin in vivo [20, 21]. The dense coating of hard keratinized dead cells of the stratum corneum is rich in insoluble keratin proteins. It gives the stratum corneum its very strong tensile strength. The stratum corneum transmits almost entirely the received external mechanical load.

The viable epidermis is a stratified epithelial of soft living cells. It is very souple and answers the transmitted part of the external mechanical load by a consolidation-type behaviour. The viable epidermis takes a big part of this transmitted load.

The dermis is made up of collagen and elastin fibers embedded in a gel. The interwoven collagen fibers provide strength while the rubber-like elastin fibers account for the skin's elastic behaviour. The gel protects the soft living cells from the transmitted external mechanical load till a yield pressure is reached. The coupled behaviour of the solid matrix of the dermis and the gel leads to a consolidation-type behaviour of the dermis with a magnitude lower than the one of the viable epidermis.

The loose fatty cells of the hypodermis reacts almost like a rubber mattress with a reversible behaviour in an answer to the transmitted external mechanical load (as shown in Figure 12 with the overlapping beginning of curve $3.2E-4$ s and curve $9.6E-3$ s for the hypodermis-simulating nodes).

7. Conclusion

This paper has presented a triphasic skin model where skin is composed of four solids, a fluid, and an ionic component. Despite the large number of simplifications and assumptions, it is shown that this model is able to give information on the transient fluid flow and ion transport through skin layers when the outside surface of the skin is in contact with a saline solution. Based on this model, the numerical simulation performs reasonably well in describing indentation experiment. The estimation procedure, for the Young modulus of each layer, resulted in $E_{s_1} = 130E3$ Pa for the stratum corneum, $E_{s_2} = 1E3$ Pa for the viable epidermis, $E_{s_3} = 4E3$ Pa for the dermis, and $E_{s_4} = 2E3$ Pa for the hypodermis. To the author's knowledge, the obtained values can be said to be realistic for the stratum corneum, the dermis, and the hypodermis. A separate Young modulus for the viable epidermis has not yet been reported. However, it is thought to be physically reasonable because of the qualitatively good agreement between the obtained numerical descriptions of the overall response of the skin specimen and the experimental observations available in the literature.

In conclusion, the theoretical and numerical model presented here enable capturing deformations of the different layers of the skin composite separately. It offers perspectives for the in vivo determination of the mechanical properties of skin soft tissues.

References

- [1] G. L. Wilkes, I. A. Brown, and R. H. Wildnauer, "The biomechanical properties of skin," *Critical Reviews in Bioengineering*, vol. 1, no. 4, pp. 453–495, 1973.
- [2] G. Odland, *Structure of the Skin, Physiology, Biochemistry and Molecular Biology of the Skin*, Oxford University Press, Oxford, UK, 1991, Edited by L.A. Goldsmith.
- [3] C. Sheppard and D. Shotton, *Confocal Laser Scanning Microscopy*, Royal Microscopical Society Microscopic Handbooks, Bios Scientific Publishers, Oxford, UK, 1997.
- [4] M. Rajadhyaksha, S. González, J. M. Zavislan, R. R. Anderson, and R. H. Webb, "In vivo confocal scanning laser microscopy of human skin II: advances in instrumentation and comparison with histology," *Journal of Investigative Dermatology*, vol. 113, no. 3, pp. 293–303, 1999.
- [5] Y. Pan, E. Lankenau, J. Welzel, R. Birngruber, and R. Engelhardt, "Optical coherence—gated imaging of biological tissues," *IEEE Journal on Selected Topics in Quantum Electronics*, vol. 2, no. 4, pp. 1029–1034, 1996.
- [6] J. Ginefri, I. Darasse, and P. Crozat, "High-temperature superconducting surface coil for in vivo microimaging of the human skin," *Magnetic Resonance in Medicine*, vol. 45, pp. 376–382, 2001.
- [7] J. De Rigal and J. L. Leveque, "In vivo measurement of the stratum corneum elasticity," *Bioengineering and the Skin*, vol. 1, no. 1, pp. 13–23, 1985.
- [8] J. L. Leveque, J. De Rigal, P. G. Agache, and C. Monneur, "Influence of ageing on the in vivo extensibility of human skin at a low stress," *Archives of Dermatological Research*, vol. 269, no. 2, pp. 127–135, 1980.
- [9] A. Rochefort, *Propriétés Biomécaniques Du Stratum Corneum: Modélisation Rhéologique—Application À La Cosmétique*, Thèse de Doctorat, Université de Franche-Comté, Besançon, France, 1986.
- [10] P. G. Agache, C. Monneur, J. L. Leveque, and J. De Rigal, "Mechanical properties and Young's modulus of human skin in vivo," *Archives of Dermatological Research*, vol. 269, no. 3, pp. 221–232, 1980.
- [11] C. H. Daly, "Biomechanical properties of dermis," *Journal of Investigative Dermatology*, vol. 79, pp. 17–20, 1982.
- [12] C. Escoffier, J. De Rigal, A. Rochefort, R. Vasselet, J.-L. Leveque, and P. G. Agache, "Age-related mechanical properties of human skin: an in vivo study," *Journal of Investigative Dermatology*, vol. 93, no. 3, pp. 353–357, 1989.
- [13] J. F. M. Manschot and A. J. M. Brakkee, "The measurement and modelling of the mechanical properties of human skin in vivo—I. The measurement," *Journal of Biomechanics*, vol. 19, no. 7, pp. 511–515, 1986.
- [14] C. Pailler-Mattéi and H. Zahouani, "Analysis of adhesive behaviour of human skin in vivo by an indentation test," *Tribology International*, vol. 39, no. 1, pp. 12–21, 2006.
- [15] C. Pailler-Mattei, S. Bec, and H. Zahouani, "In vivo measurements of the elastic mechanical properties of human skin by indentation tests," *Medical Engineering and Physics*, vol. 30, no. 5, pp. 599–606, 2008.
- [16] A. Barel, W. Courage, and P. Clarys, *Suction Method For Measurement of Skin Mechanical Properties : the Cutometer*, Handbook of Non-Invasive Methods and the skinCRC Press, Boca Raton, Fla, USA, 1995, Edited by J. Serup and G B E. Jemec.
- [17] J. M. Huyghe and J. D. Janssen, "Thermo-chemo-electromechanical formulation of saturated charged porous solids," *Transport in Porous Media*, vol. 34, no. 1–3, pp. 129–141, 1999.
- [18] M.-A. Abellan, H. Zahouani, E. Feulvarch, and J.-M. Bergheau, "Modelling water and ion transport through damaged skin," in *Proceedings of the 2nd Euro-Mediterranean Conference on Bioengineering and Biomaterials (EMCBB '12)*, Fez, Morocco, July 2012.
- [19] M.-A. Abellan, E. Feulvarch, H. Zahouani, and J.-M. Bergheau, "Numerical simulation of in vivo indentation tests: determination of the mechanical properties of human skin," in *Proceedings of the 21e Congrès Français de Mécanique (CFM '13)*, pp. 26–30, Août, Bordeaux, France, 2013.

- [20] F. M. Hendriks, D. Brokken, C. W. J. Oomens, D. L. Bader, and F. P. T. Baaijens, "The relative contributions of different skin layers to the mechanical behavior of human skin in vivo using suction experiments," *Medical Engineering and Physics*, vol. 28, no. 3, pp. 259–266, 2006.
- [21] A. Hung, K. Mithraratne, M. Sagar, and P. Hunter, "Multilayer soft tissue continuum model: towards realistic simulation of facial expressions, World Academy of Science," *Engineering and Technology*, vol. 54, pp. 134–138, 2009.
- [22] P. Jouanna and M.-A. Abellan, "A generalized approach to heterogeneous media," *Transport in Porous Media*, vol. 25, no. 3, pp. 351–374, 1996.
- [23] P. M. Van Kemenade, *Water and Ion Transport Through Intact and Damaged Skin, Dissertation*, Eindhoven University of Technology, 1998.
- [24] J. Yoon, S. Cai, Z. Suo, and R. C. Hayward, "Poroelastic swelling kinetics of thin hydrogel layers: comparison of theory and experiment," *Soft Matter*, vol. 6, no. 23, pp. 6004–6012, 2010.
- [25] Y. Hu, X. Chen, G. M. Whitesides, J. J. Vlassak, and Z. Suo, "Indentation of polydimethylsiloxane submerged in organic solvents," *Journal of Materials Research*, vol. 26, no. 6, pp. 785–795, 2011.
- [26] M.-A. Abellan, E. Feulvarch, J.-M. Bergheau, and H. Zahouani, "Coupled fluid flow and ion transport through intact skin," in *Proceedings of the 38e Congrès de la Société de Biomécanique (SB '13)*, Marseille-Luminy, France, 2013.
- [27] M.-A. Abellan, E. Feulvarch, H. Zahouani, and J.-M. Bergheau, "Contribution à la caractérisation expérimentale et simulation numérique du comportement de la peau humaine in vivo: indentation sans contact," in *Proceedings of the 11e Colloque National en Calculs des Structures (CSMA '13)*, pp. 13–17, mai, Giens, France, 2013.
- [28] C. Truesdell and R. Toupin, *The Classical Field Theories, Handbuch Der Physik III/I*, Springer, Berlin, Germany, 1960.
- [29] F. M. Hendriks, *Mechanical Behaviour of Human EpiDermal and Dermal Layers in Vivo, Dissertation*, Eindhoven University of Technology, 2005.

Research Article

Theoretical Hill-Type Muscle and Stability: Numerical Model and Application

S. Schmitt,^{1,2} M. Günther,^{1,3} T. Rupp,^{1,2} A. Bayer,¹ and D. Häufle¹

¹ Department of Sports and Exercise Science, University of Stuttgart, Allmandring 28, 70569 Stuttgart, Germany

² Stuttgart Research Centre for Simulation Technology, University of Stuttgart, Pfaffenwaldring 5a, 70569 Stuttgart, Germany

³ Institute of Sports Science, Science of Motion, University of Jena, Seidelstraße 20, 07749 Jena, Germany

Correspondence should be addressed to S. Schmitt; schmitt@inspo.uni-stuttgart.de

Received 19 July 2013; Accepted 19 September 2013

Academic Editor: Zhonghua Sun

Copyright © 2013 S. Schmitt et al. This is an open access article distributed under the Creative Commons Attribution License, which permits unrestricted use, distribution, and reproduction in any medium, provided the original work is properly cited.

The construction of artificial muscles is one of the most challenging developments in today's biomedical science. The application of artificial muscles is focused both on the construction of orthotics and prosthetics for rehabilitation and prevention purposes and on building humanoid walking machines for robotics research. Research in biomechanics tries to explain the functioning and design of real biological muscles and therefore lays the fundament for the development of functional artificial muscles. Recently, the hyperbolic Hill-type force-velocity relation was derived from simple mechanical components. In this contribution, this theoretical yet biomechanical model is transferred to a numerical model and applied for presenting a proof-of-concept of a functional artificial muscle. Additionally, this validated theoretical model is used to determine force-velocity relations of different animal species that are based on the literature data from biological experiments. Moreover, it is shown that an antagonistic muscle actuator can help in stabilising a single inverted pendulum model in favour of a control approach using a linear torque generator.

1. Introduction

Research in muscle biomechanics, a vital and broad field for over 80 years now (A.V. Hill 1922: Nobel prize in physiology and medicine for his discovery relating to the production of heat in the muscle), explains the function and design of real biological muscles and therefore lays the fundament for the development of functional artificial muscles. Nevertheless, structure and functioning of biological muscles are not (yet) fully understood.

In biology, microscopic muscle models are able to predict muscle characteristics and functioning of biological muscles quite well [1–9]. Unfortunately and as a tradeoff, they require a large number of parameters. In a bionics approach it is an enormous challenge to realise all these properties of biological muscle in one artificial muscle at once [10].

Macroscopic muscle models are commonly based on phenomenology. Macroscopic muscle models are indeed of (limited) predictive character but do not incorporate any structural knowledge. Recently, the nonlinear (hyperbolic-like) Hill-type force-velocity relation was derived from simple

mechanical components [11]. It was shown that a contractile element (CE) consisting of a mechanical energy source (active element AE), a parallel damper element (PDE), and a serial element (SE) exhibits operating points with nonlinear (hyperbola-like) force-velocity dependency. In this concept, the force-velocity relation is no longer a phenomenological outcome of a black box (i.e., the CE) but rather a physical outcome of the interaction of the three elements AE, PDE, and SE. Based on this concept, it is now possible to describe in detail which structural arrangement is necessary to get a biology-like force-velocity relation on a macroscopic level. Therefore, this concept can be interpreted as a basic engineering design for the CE of a Hill-type artificial actuator [12–15]. In this paper, the meaning of the structural arrangement of the simple mechanical components already published will be revisited. Furthermore, by taking one first example of technical embodiment, it will be shown how this concept can help to construct more biologically-motivated artificial muscles. Most importantly, it can be shown that the application of a Hill-type muscle model could improve biomechanical stability. An antagonistic pair of our muscle

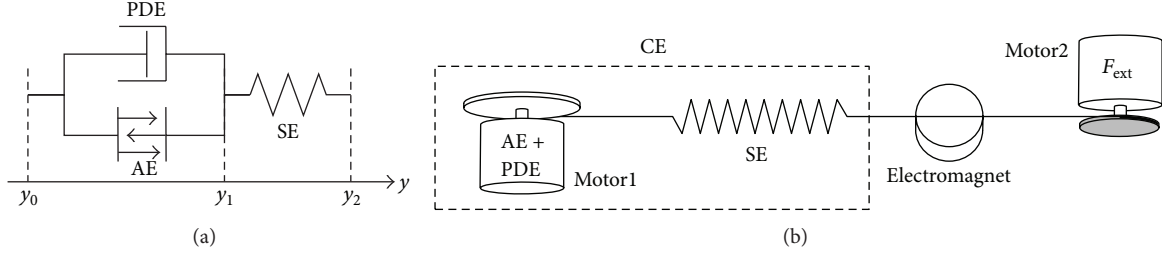


FIGURE 1: (a) Theoretical construct of the CE [11]. The CE consists of three elements: active element AE, parallel damping element PDE, and serial element SE. $y_0 = 0$ is the origin of the CE, y_1 the length of the AE/PDE, and y_2 the length of the whole CE. By choosing $\kappa_v = 0.0$ in theory, we can turn the SE off in order to represent a contractile element without any compliance. (b) Hardware design. AE and PDE were realised with an electric motor, SE with a mechanical spring. A second electric motor was used to exert a defined external force F_{ext} on the CE. The electromagnet held the muscle at constant length until release at time $t = t_{QR}$.

model theoretically shows a first demonstration of how an artificial muscle could help in the stabilisation of a technical machine. As a result, the control of an inverted pendulum can be improved by the use of a muscle-like drive in favour of a linear torque generator.

2. Material and Methods

2.1. Hill's Original Formulation of Muscle Dynamics. In his famous paper "The heat of shortening and the dynamic constants of muscle" [16], Hill firstly formulated the simple and convenient equation describing the muscle's contraction dynamics:

$$(P + a) \cdot v = b \cdot (P_0 - P), \quad (1)$$

where the symbol "P" denotes the current muscle force, "v" the respective contraction velocity of the muscle, "P₀" the muscle's maximum isometric force, and "a" and "b" Hill's so-called dynamic constants of muscle, which we call the Hill parameters.

2.2. Derivation of the Hill Parameters. In a recent paper [11] it was demonstrated that the phenomenologically found hyperbolic force-velocity relation of a concentrically contracting assembly of activated muscle fibres [16] can be derived from the simple mechanical arrangement (Figure 1(a)) of an arbitrary force generating (active) element (AE) to which a damper (PDE) is connected in parallel and a serial element (SE) in series fulfilling the force equilibrium:

$$F_{CE} = F_{SE} = F_{AE} + F_{PDE}, \quad (2)$$

where the symbol "F" denotes a force produced by the element denoted by a corresponding index and the kinematic relation for the lengths (symbols "l") of the elements AE, PDE, and SE:

$$l_{AE} = l_{PDE} = l_{CE} - l_{SE} \quad (3)$$

with l_{CE} representing the contractile element length. Note that a dot symbol "i" denotes the first time derivative of a length l , that is, an element's contraction velocity. Please refer to the appendix or [13, 15] for a more detailed description.

2.3. Technical Embodiment. The hardware implementation (Figure 1(b)) was done analogously. Both AE and PDE were realised each with an electric motor (Maxon ECmax40) [14]. The motor torque (T_{Motor}) was controlled by Maxon digital EC-motor control units (DEC 70/10). Both motors were mounted from opposite sides to the same disc with the radius $r_{disc} = 0.05$ m. The disc was used to coil up a steel rope and exert a force

$$F_{AE} + F_{PDE} = \frac{1}{r_{disc}} \cdot (T_{MotorAE} + T_{MotorPDE}) \quad (4)$$

on the rope. The force characteristics of the PDE and AE (A.1) and (A.4) were implemented in MATLAB Simulink through Real-Time Workshop and Real-Time Windows Target. Thus, the motors could exert the specified force on the steel rope as required by the theoretical construct. For the SE, a spring ($k_{SE} = 2401 \text{ Nm}^{-1}$) was tied to a steel rope. Another motor could exert a defined external force on the CE construct. As sensor signals, the motor shaft positions φ_{Motor} were recorded by optical encoders (Scancon 2RMHF 5000 pulses/revolution), representing the internal degree of freedom y_1 and the total CE length y_2 . A load cell (Transducer Techniques MLP 25 with amplifier TM0-1-24) was used to calibrate motor torques and exerted forces. All sensor data were recorded with MATLAB Simulink via a Sensoray 626 AD I/O at 1 kHz.

To investigate the force-velocity characteristics of the artificial CE, two types of experiments had to be performed. The first experiment was an isometric contraction (contraction with constant CE length: $y_2 - y_0 = \text{const.}$). For this purpose, the CE end was fixed to the electromagnet guaranteeing a constant CE length. Then the AE activation was set to $A_{AE} = 1$ (maximum activation) and the shortening of the AE (rotation of the motors) was recorded. The time from the beginning of the activation until the end of AE shortening t_{isom} and the maximum isometric force $F_{CE}(t_{isom}) = F_{CE,max}$ were evaluated.

Isotonic quick release experiments were performed to guarantee a defined $\kappa_v = 0$ (velocity ratio; please see appendix for a definition of κ_v). Each isotonic quick release contraction experiment started like an isometric contraction, only that the CE was released at $t_{QR} > t_{isom}$ ($t_{QR} = 3$ s) by releasing the electromagnet. CE contraction velocity and force were

TABLE 1: Muscle parameters ($A, B, F_{\max}, l_{\text{CE,opt}}$) determined in experiments (see reference) and muscle model parameters ($R_{\text{PDE}}, (1 - \kappa_v)D_{\text{PDE}}$), respectively, calculated (see the appendix).

Muscle	A [N]	B [m/s]	F_{\max} [N]	$l_{\text{ce,opt}}$ [m]	R_{PDE}	$(1 - \kappa_v)D_{\text{PDE}}$	Reference
Piglet gastrocnemius	3.0	0.015	30.0	0.015	0.003	2200	[17]
Cat soleus	4.8	0.042	21.0	0.033	0.011	620	[18]
Cat tenuissimus	0.05	0.057	0.18	0.032	0.600	4	[19]
Rat gastrocnemius	2.68	0.042	13.4	0.013	0.167	386	[20]
Rat tibialis anterior	4.3	0.053	4.3	0.027	0.076	162	[19]
Frog sartorius	0.18	0.012	0.67	0.031	0.287	72	[19]

evaluated shortly after t_{QR} at $t_{\text{eval}} = 3.5$ s. The values $v_{\text{CE}}(t_{\text{eval}})$ and $F_{\text{CE}}(t_{\text{eval}})$ were extracted. The experiment was performed with different external forces, ten repetitions each. The curve $F_{\text{CE}}(t_{\text{eval}})$ versus $v_{\text{CE}}(t_{\text{eval}})$ for all external forces represents the force-velocity characteristics of the artificial CE (Figure 3(a), crosses).

2.4. Representing the Variety of Biological Muscles. In a further evaluation of our theoretical approach we scaled the model parameters to represent various biological muscles of different animals (Figure 3(b)). The model parameters R_{PDE} and $(1 - \kappa_v)D_{\text{PDE}}$ were calculated (A.6) from A and B values determined in experiments for different biological muscles (Table 1).

2.5. Control of the Inverted Pendulum. A model of an inverted pendulum was used to investigate what effect muscle-like actuator characteristics could have on the control of robotic stance. For quiet stance, the task was to keep an upright posture while deflecting the ground to which the pendulum was suspended with a hinge joint. The model consisted of two rigid segments connected with a hinge joint (Figure 2). S1 had a mass of $m = 50$ kg, a moment of inertia of $J = 45.125$ kgm² (calculated around hinge joint axis), and the center of gravity was at $h_{\text{COG}} = 0.95$ m. The initial orientation of the leg/trunk segment S1 was vertical and horizontal for the foot segment S2. The pendulum could be perturbed by rotating S2 about the joint by the angle α . Three perturbations were considered: (a) a linear ramp increase of $\alpha = 1^\circ \cdot t \leq 1^\circ$ (for $0 \leq t \leq 1$, where t is the time) and $\alpha = 1^\circ$ ($t > 1$), (b) a sinusoidal oscillation $\alpha = 1^\circ \cdot \sin(2\pi t)$, and (c) a sinusoidal oscillation $\alpha = 1^\circ \cdot \sin(0.2\pi t)$.

The hinge joint could be actuated either by a direct torque generator or by an antagonistic pair of muscles (Figures 2(a), and 2(b)). The muscles were represented by two macroscopic muscle models of the same type. These muscle models incorporate the contraction dynamics, as well as a serial and a parallel elastic element representing the tendon and the passive elastic properties of soft muscle tissue. The muscle model was already described in detail in [11]. The parameters used for the muscle models are listed in Table 2. Both muscles were connected to a simple geometry as depicted in Figure 2.

Muscles and direct torque generator were controlled based on a feedback signal measuring the deviation of segment S1 from the vertical orientation. A physiological delay of $\Delta t = 0.1$ s was considered. Three different controllers were

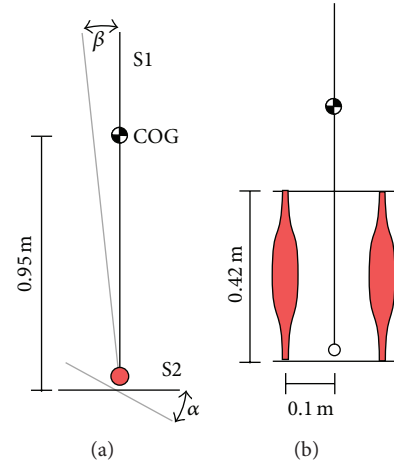


FIGURE 2: Model of the inverted pendulum. S1 represents the leg/trunk segment; S2 represents the foot. COG indicates the center of gravity location of S1. α is the angle of the foot (perturbation) and β the deviation from the upright position of S2. (a) The joint is actuated by a direct torque generator with linear characteristics. (b) The joint is actuated by two antagonistic muscles.

applied: (1) no feedback is provided, (2) a simple proportional feedback (P controller), and (3) a PID controller. MATLAB Simulink embedded ODE5 (Dormand-Prince) solver with 1 ms step size was used to solve the differential equations.

3. Results

The relation between muscle output force and its contraction velocity is the common criterion for the comparison of macroscopic muscle models. Therefore, we calculated the F - v curve (Figure 3(a)) first. The F - v curve of the presented functional artificial muscle shows a very good match with both the prediction from theory and biological experiments.

By comparing our artificial muscle prototype's force-velocity relation as shown above, we consider our approach as quite successful. The functional artificial muscle prototype exhibits contraction dynamics similar to Hill's model characteristics (Figure 3(a) [13, 15]).

In a model of the inverted pendulum, muscle-like non-linear actuator characteristics were compared against a direct torque generator (linear characteristics). The muscle-driven model did not topple, not even without feedback (first row,

TABLE 2: Parameters for the muscle model were based on a human tibialis anterior muscle (see [21] for a detailed description). The muscle model used for the study was described in detail in [17].

$l_{CE,opt}$	F_{max}	ΔW	V_{CE}	$A_{rel,0}$	$B_{rel,0}$	$l_{SEE,0}$	$\Delta U_{SEE,nll}$	$\Delta U_{SEE,l}$	$\Delta F_{SEE,0}$	D_{SE}	R_{SE}
0.1 m	10000 N	0.57	4.0	0.25	2.25 s^{-1}	0.23 m	0.1825	0.073	10000 N	0.3	0.01

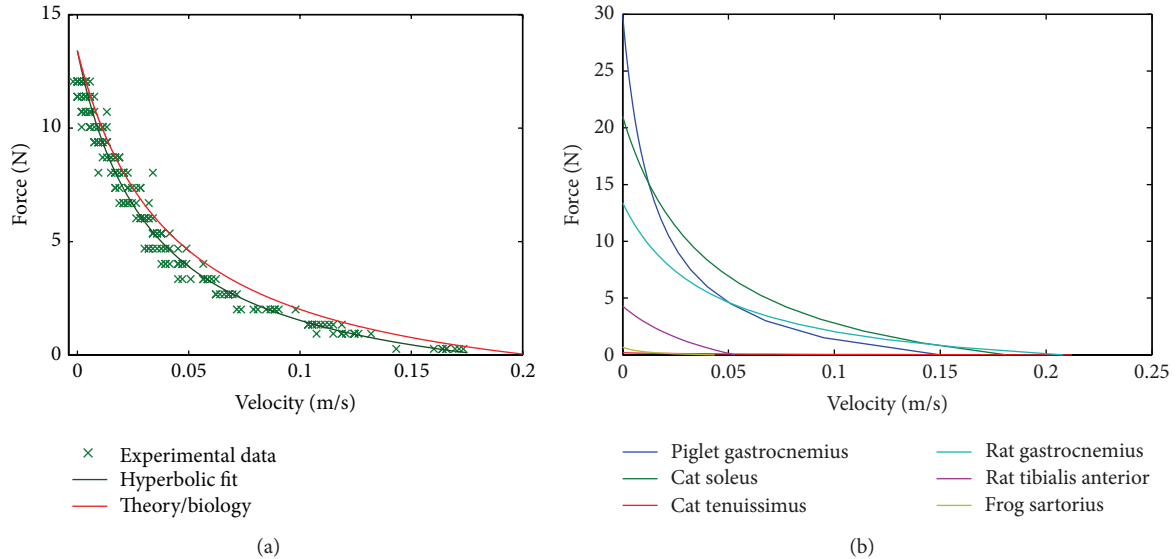


FIGURE 3: (a) Ten $F(t)$ and $v(t)$ plots for quick-release contraction experiments using 19 different external forces were recorded. Based on those $F(t)$ and $v(t)$ plots the force-velocity curve (crosses) was calculated. In direct comparison with the biological experiments (rat gastrocnemius muscle [20]) and the predictions from theory, the artificial muscle data shows a good match for both, with $\kappa_v = 0$. A hyperbola fit of the artificial muscle data results in $R^2 = .97$ [13, 15]. (b) The strength of the presented approach is shown by a comparison of $F(v)$ curves calculated for different biological muscle parameters. The respective $F-v$ curve can be plotted by just taking A and B values from experiments and calculating the parameters R_{PDE} and $(1 - \kappa_v)D_{PDE}$. The latter two parameters are necessary to build a technical muscle of that respective type.

Figure 4). Also, when using the simple P controller (middle row) the muscle-driven model performed better during all perturbations and was able to cope better with the feedback delay of $\Delta t = 0.1$ s. Using the PID controller solutions were only found, where the direct torque controller performed better (bottom row, Figure 4). Here, a solution with high gain for the integral part of the PID controller is presented. Therefore, slow perturbations could be compensated very effectively.

4. Discussion

4.1. Element Representation. A brushless dc electric drive was used for the active element (AE) which was formulated in theory [11]. The tradeoffs of these actuators are the torque-to-weight ratio and the necessity of a power supply, either over cable or by battery. Madden [22] gives an overview of the current state of the art of technical artificial muscles, their potential, and their tradeoffs. For our concept as of today, we are planning to use translational drives. Translational drives directly couple the driving forces to the movement direction and they are commercially available. However, for all electric drives one challenge remains: the storage of energy. Fortunately (or unfortunately), this is also a big issue in the automotive industry for the construction of electric vehicles.

Therefore, we think that it is likely to see great improvement in the storage technology in the near future. This would also facilitate the use of electric drives as active element in functional artificial muscles.

The passive damping element (PDE) develops forces during the contraction, which may exceed over a very short period of time, the muscle output forces several times over. The question remains whether there are comparable forces internal to the artificial muscle in other technical embodiments. Unfortunately, this is commonly not reported in the literature. In our approach, we use an electric drive to produce the damping forces that are in fact a nonpassive damper. Are there any materials or other approaches possible instead of using an electric drive as presented in this approach? A magnetorheological damping element, for example, [23]?

Fortunately, the serial element (SE) seems to be the simplest challenge for a technical representation. This element should imply nonlinear force-displacement characteristics. Even a steel rod would show the dynamic characteristics similar to that of the serial element predicted in theory. However, as a must-have, this element needs to incorporate damping characteristics, yet very small [17]. It is to see how the artificial muscle prototype behaves when including a serial element like that observed in biology and postulated in theory [11].

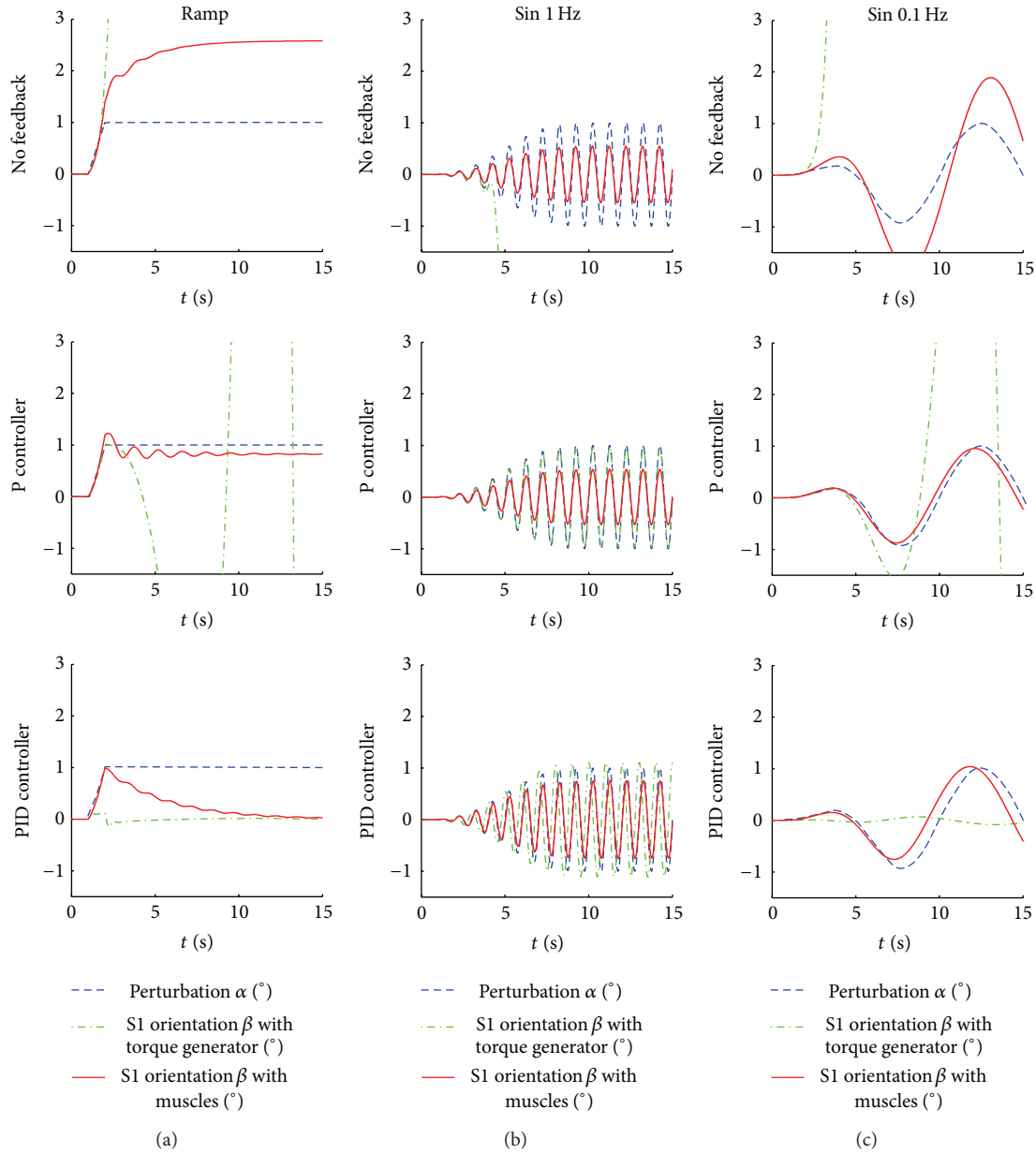


FIGURE 4: Model reactions to perturbations in foot orientation α . Control target is the upright posture ($\beta = 0^\circ$). Left column shows the reaction to a ramp perturbation, middle column to a 1 Hz, and right column to a 0.1 Hz sinusoidal perturbation. Top row is without feedback, middle row with a simple P controller (direct torque controller gain: P 500; muscle controller gain: P 1), and bottom row with a PID controller (direct torque controller gains: P 500, I 50, D 500; muscle controller gains: P 1, I 0.3, D 0.3). The feedback signal is delayed by $\Delta t = 0.1$ s.

4.2. *What is Gained Using This Approach?* Understanding biological muscle characteristics and design is of great interest in biological science. Muscle models in general help to mathematically formulate muscle characteristics. The structure of our model is in essence purely mechanical. Therefore, it can serve as a functional starting point of bionic muscle design. Phenomenological models based on biological experiments were the first to define muscle characteristics, for example, [16]. Constantly improving lab techniques allowed to observe muscle phenomena (even) in greater detail, for example, [5]. Microscopic muscle models

deduced from basic assumptions of muscle structure and/or functional relationships of single variables come into play shortly after, for example, [24]. However, the benchmark of muscle dynamics used for those microscopic models is still the phenomenological Hill relation [16]. One approach just recently succeeded in defining the macroscopic muscle characteristics without the need of any phenomenological information. In contrast, this approach was validated against the well-known experiments instead of being based on it [11]. Here, we used those findings to build a technical muscle and succeeded in the reproduction of crucial characteristics of

biological muscle. With this approach, now, the macroscopic model can be iteratively improved accompanied by the technical muscle. In that, technical models can partly replace biological experiments.

4.3. Hill-Type Models for Control. Hill-type muscle models, as an alternative to joint torque generators, have been implemented in (multibody) computer models in order to generate movement. In this regard different control theories, that is, physiologically motivated ones, for example, equilibrium point hypothesis [25, 26], virtual model control [27], and others described above, come into operation. Hence, multibody models with Hill-type muscles as actuators allow for using control theories to generate movement. This way, control approaches [28, 29] are quantitatively tested and relevant control parameters [30] are determined. Furthermore, existing and/or newly developed control theories are compared.

In this study, different control approaches, that is, no feedback, P controller, and PID controller (see Section 2), were implemented and compared in two different inverted pendulums models, that is, one with muscles and the other one with direct torque generators. From this comparison of control and actuators, it can be concluded that the implementation of muscle-like characteristics changes the model's inherent stability. Thus, it leads to a modification of successful control strategies to generate a similar movement. Furthermore, the presented arrangement of technical elements for the CE also allows for the investigation of structural changes in biological muscle used for movement control.

For further and more detailed conclusion, the presented approach will be implemented as muscle-like actuators in more complex (human) models to investigate (physiological motivated) control strategies and structural changes of muscle.

Appendix

A. Model Derivation

In order to end up with a hyperbolic relation, two further assumptions had to be made. First, the force of the PDE was assumed to be

$$F_{\text{PDE}} = d_{\text{PDE}} \cdot \dot{l}_{\text{PDE}} = d_{\text{PDE}} \cdot \dot{l}_{\text{AE}} = d_{\text{PDE}} \cdot (\dot{l}_{\text{CE}} - \dot{l}_{\text{SE}}), \quad (\text{A.1})$$

where the damping coefficient of the PDE depends linearly on the current muscle force $F_{\text{CE}} = F_{\text{SE}}$:

$$d_{\text{PDE}}(F_{\text{CE}}) = D_{\text{PDE,max}} \cdot \left((1 - R_{\text{PDE}}) \cdot \frac{F_{\text{CE}}}{F_{\text{AE,max}}} + R_{\text{PDE}} \right). \quad (\text{A.2})$$

$D_{\text{PDE,max}}$ is the maximum (at $F_{\text{CE}} = F_{\text{AE,max}}$) and R_{PDE} the normalised (to $D_{\text{PDE,max}}$) minimum (force independent) value of $d_{\text{PDE}}(F_{\text{CE}})$. Second, the gearing ratio

$$\kappa_v = \frac{\dot{l}_{\text{SE}}}{\dot{l}_{\text{CE}}} \quad (\text{A.3})$$

between internal (SE) and external (muscle) velocities was represented by an arbitrary parameter value κ_v .

The characteristics of the SE did not have to be specified. The AE is the source of mechanical energy. It may depend on length and on the macroscopic chemical state of the muscle, that is, the relative number of actively force-producing cross-bridges quantified by the normalised muscle activation $0 \leq q \leq 1$.

In order to meet the conditions of our artificial muscle experiments presented in this paper, we had to modify the just reviewed model [11] with respect to only one feature. In contrast to (6) in [11], which related the isometric force $F_{\text{CE}}(\dot{l}_{\text{CE}} = 0) = F_{\text{CE,0}}$ (see (2) for $\dot{l}_{\text{CE}} = 0$) as a linear function of contraction velocity \dot{l}_{CE} to the AE force F_{AE} , we now assume the identity

$$F_{\text{CE,0}} = F_{\text{AE}}. \quad (\text{A.4})$$

Equation (A.4) is as consistent to the set of model equations (2), (3), (A.1), (A.2), and (A.3) as is (6) in [11] to this very set.

Substituting (A.1), the explicit dependency of $d_{\text{PDE}}(F_{\text{CE}})$ on force F_{CE} and model parameters (A.2), and (A.3) into (2) makes the latter force equilibrium (2) constitute a hyperbola

$$(F_{\text{CE}} + A) \cdot \dot{l}_{\text{CE}} = -B \cdot (F_{\text{CE,0}} - F_{\text{CE}}) \quad (\text{A.5})$$

with the Hill parameters A , B and the isometric force $F_{\text{CE,0}}$ being positive and \dot{l}_{CE} consistently being negative in the shortening (concentric) case. The Hill parameters are

$$\begin{aligned} A &= \frac{R_{\text{PDE}}}{1 - R_{\text{PDE}}} \cdot F_{\text{AE,max}} \\ B &= \frac{1}{1 - R_{\text{PDE}}} \cdot \frac{1}{1 - \kappa_v} \cdot \frac{F_{\text{AE,max}}}{D_{\text{PDE,max}}} \\ &= \frac{R_{\text{PDE}}}{1 - R_{\text{PDE}}} \cdot \frac{F_{\text{AE,max}}}{F_{\text{AE}}} \cdot \dot{l}_{\text{CE,max}}, \end{aligned} \quad (\text{A.6})$$

with the corresponding maximum shortening velocity

$$\begin{aligned} \dot{l}_{\text{CE,max}} &= \frac{B}{A} \cdot F_{\text{CE,0}} = \frac{B}{A_{\text{rel}}} \\ &= \frac{1}{R_{\text{PDE}}} \cdot \frac{1}{1 - \kappa_v} \cdot \frac{F_{\text{AE}}}{D_{\text{PDE,max}}}. \end{aligned} \quad (\text{A.7})$$

The unloaded contractile element ($F_{\text{CE}} = 0$) would contract concentrically with $\dot{l}_{\text{CE}} = -\dot{l}_{\text{CE,max}}$:

$$A_{\text{rel}} = \frac{A}{F_{\text{CE,0}}} = \frac{F_{\text{AE,max}}}{F_{\text{AE}}} \cdot \frac{R_{\text{PDE}}}{1 - R_{\text{PDE}}}, \quad (\text{A.8})$$

which is defined as the Hill parameter A normalised to the current isometric force $F_{\text{CE,0}} = F_{\text{AE}}$. Note that, for given $F_{\text{CE,0}} = F_{\text{AE}}$, a concurrent parameter variation fulfilling $B/A = \text{const}$ meets the constraint $\dot{l}_{\text{CE,max}} = \text{const}$, whereas solely the curvature is changed. In our model, this is equivalent to $(1 - \kappa_v) \cdot D_{\text{PDE,max}} \cdot R_{\text{PDE}} = \text{const}$.

Acknowledgments

This work was supported by a Research Seed Capital (RisSC)—Tranche 2009 from the Ministry of Science, Research and Arts of Baden-Wuerttemberg, The University of Stuttgart (Kapitel 1403 Tit.Gr. 74), by the German Research Foundation (DFG) within the Cluster of Excellence in Simulation Technology (EXC310/1) at the University of Stuttgart, and by the German Research Foundation (DFG) within the funding programme Open Access Publishing.

References

- [1] A. F. Huxley, "Muscle structure and theories of contraction," *Progress in Biophysics and Biophysical Chemistry*, vol. 7, pp. 255–318, 1957.
- [2] A. F. Huxley, "Mechanics and models of the myosin motor," *Philosophical Transactions of the Royal Society B*, vol. 355, no. 1396, pp. 433–440, 2000.
- [3] H. E. Huxley, "Fifty years of muscle and the sliding filament hypothesis," *European Journal of Biochemistry*, vol. 271, no. 8, pp. 1403–1415, 2004.
- [4] V. Lombardi, G. Piazzesi, M. A. Ferenczi, H. Thirlwell, I. Dobbie, and M. Irving, "Elastic distortion of myosin heads and repriming of the working stroke in muscle," *Nature*, vol. 374, no. 6522, pp. 553–555, 1995.
- [5] V. Lombardi, G. Piazzesi, M. Reconditi et al., "X-ray diffraction studies of the contractile mechanism in single muscle fibres," *Philosophical Transactions of the Royal Society B*, vol. 359, no. 1452, pp. 1883–1893, 2004.
- [6] G. Piazzesi and V. Lombardi, "A cross-bridge model that is able to explain mechanical and energetic properties of shortening muscle," *Biophysical Journal*, vol. 68, no. 5, pp. 1966–1979, 1995.
- [7] M. Reconditi, M. Linari, L. Lucii et al., "The myosin motor in muscle generates a smaller and slower working stroke at higher load," *Nature*, vol. 428, no. 6982, pp. 578–581, 2004.
- [8] I. A. Telley, J. Denoth, and K. W. Ranatunga, "Inter-sarcomere dynamics in muscle fibres: a neglected subject?" *Advances in Experimental Medicine and Biology*, vol. 538, pp. 481–500, 2004.
- [9] L. Tskhovrebova and J. Trinick, "Role of titin in vertebrate striated muscle," *Philosophical Transactions of the Royal Society B*, vol. 357, no. 1418, pp. 199–206, 2002.
- [10] R. H. Baughman, "Materials science. Playing nature's game with artificial muscles," *Science*, vol. 308, no. 5718, pp. 63–65, 2005.
- [11] M. Günther and S. Schmitt, "A macroscopic ansatz to deduce the Hill relation," *Journal of Theoretical Biology*, vol. 263, no. 4, pp. 407–418, 2010.
- [12] D. F. B. Häufle, M. Günther, R. Blickhan, and S. Schmitt, "Proof of concept of an artificial muscle: theoretical model, numerical model, and hardware experiment," in *Proceedings of International Conference of Rehabilitation Robotics (ICORR '11)*, pp. 1–6, July 2011.
- [13] D. F. Häufle, M. Günther, R. Blickhan, and S. Schmitt, "Can quick release experiments reveal the muscle structure? A bionic approach," *Journal of Bionic Engineering*, vol. 9, no. 2, pp. 211–223, 2012.
- [14] D. F. Häufle, M. Günther, R. Blickhan, and S. Schmitt, "Proof of concept: model based bionic muscle with hyperbolic force-velocity relation," *Applied Bionics and Biomechanics*, pp. 1–7, 2012.
- [15] S. Schmitt, D. F. Häufle, R. Blickhan, and M. Günther, "Nature as an engineer: one simple concept of a bio-inspired functional artificial muscle," *Bioinspiration & Biomimetics*, vol. 7, Article ID 036022, 2012.
- [16] A. V. Hill, "The heat of shortening and the dynamic constants of muscle," *Proceedings of the Royal Society of London. Series B*, vol. 126, pp. 136–195, 1938.
- [17] M. Günther, S. Schmitt, and V. Wank, "High-frequency oscillations as a consequence of neglected serial damping in Hill-type muscle models," *Biological Cybernetics*, vol. 97, no. 1, pp. 63–79, 2007.
- [18] G. K. Cole, T. van den Bogert, W. Herzog, and K. Gerritsen, "Modelling of force production in skeletal muscle undergoing stretch," *Journal of Biomechanics*, vol. 29, pp. 1091–1104, 1996.
- [19] G. K. Klute, J. M. Czerniecki, and B. Hannaford, "Artificial muscles: actuators for biorobotic systems," *International Journal of Robotics Research*, vol. 21, no. 4, pp. 295–309, 2002.
- [20] J. P. van Zandwijk, M. F. Bobbert, G. C. Baan, and P. A. Huijting, "From twitch to tetanus: performance of excitation dynamics optimized for a twitch in predicting tetanic muscle forces," *Biological Cybernetics*, vol. 75, no. 5, pp. 409–417, 1996.
- [21] M. Günther and H. Ruder, "Synthesis of two-dimensional human walking: a test of the λ -model," *Biological Cybernetics*, vol. 89, no. 2, pp. 89–106, 2003.
- [22] J. D. Madden, "Mobile robots: motor challenges and materials solutions," *Science*, vol. 318, no. 5853, pp. 1094–1097, 2007.
- [23] E. Garcia, J. C. Arevalo, G. Muoz, and P. Gonzalez-De-Santos, "Combining series elastic actuation and magneto-rheological damping for the control of agile locomotion," *Robotics and Autonomous Systems*, vol. 59, no. 10, pp. 827–839, 2011.
- [24] A. F. Huxley, "A note suggesting that the cross bridge attachment during muscle contraction may take place in two stages," *Proceedings of the Royal Society of London. Series B*, vol. 183, no. 1070, pp. 83–86, 1973.
- [25] E. Bizzi, N. Hogan, F. A. Mussa-Ivaldi, and S. Giszter, "Does the nervous system use equilibriumpoint control to guide single and multiple joint movements?" *Behavioral and Brain Sciences*, vol. 15, pp. 603–613, 1992.
- [26] A. G. Feldman, "Functional tuning of the nervous system with control of movement or maintenance of a steady posture-II. Controllable parameters of the muscles," *Biophysics*, vol. 11, no. 3, pp. 565–578, 1966.
- [27] J. Pratt, C.-M. Chew, A. Torres, P. Dilworth, and G. Pratt, "Virtual model control: an intuitive approach for bipedal locomotion," *International Journal of Robotics Research*, vol. 20, no. 2, pp. 129–143, 2001.
- [28] M. F. Eilenberg, H. Geyer, and H. Herr, "Control of a powered ankle-foot prosthesis based on a neuromuscular model," *IEEE Transactions on Neural Systems and Rehabilitation Engineering*, vol. 18, no. 2, pp. 164–173, 2010.
- [29] A. S. Ghafari, A. Meghdari, and G. Vossoughi, "Feedback control of the neuromusculoskeletal system in a forward dynamics simulation of stair locomotion," *Proceedings of the Institution of Mechanical Engineers, Part H: Journal of Engineering in Medicine*, vol. 223, no. 6, pp. 663–675, 2009.
- [30] D. A. Kistemaker, A. J. Van Soest, and M. F. Bobbert, "A model of open-loop control of equilibrium position and stiffness of the human elbow joint," *Biological Cybernetics*, vol. 96, no. 3, pp. 341–350, 2007.

Research Article

Influence of Distal Resistance and Proximal Stiffness on Hemodynamics and RV Afterload in Progression and Treatments of Pulmonary Hypertension: A Computational Study with Validation Using Animal Models

Zhenbi Su,¹ Wei Tan,¹ Robin Shandas,² and Kendall S. Hunter²

¹ Department of Mechanical Engineering, University of Colorado at Boulder, Boulder, CO 80309, USA

² Department of Bioengineering, University of Colorado Denver Anschutz Medical Campus, Aurora, CO 80045, USA

Correspondence should be addressed to Kendall S. Hunter; kendall.hunter@ucdenver.edu

Received 29 May 2013; Revised 9 September 2013; Accepted 25 September 2013

Academic Editor: Eduardo Soudah

Copyright © 2013 Zhenbi Su et al. This is an open access article distributed under the Creative Commons Attribution License, which permits unrestricted use, distribution, and reproduction in any medium, provided the original work is properly cited.

We develop a simple computational model based on measurements from a hypoxic neonatal calf model of pulmonary hypertension (PH) to investigate the interplay between vascular and ventricular measures in the setting of progressive PH. Model parameters were obtained directly from *in vivo* and *ex vivo* measurements of neonatal calves. Seventeen sets of model-predicted impedance and mean pulmonary arterial pressure (mPAP) show good agreement with the animal measurements, thereby validating the model. Next, we considered a predictive model in which three parameters, PVR, elastic modulus (EM), and arterial thickness, were varied singly from one simulation to the next to study their individual roles in PH progression. Finally, we used the model to predict the individual impacts of clinical (vasodilatory) and theoretical (compliance increasing) PH treatments on improving pulmonary hemodynamics. Our model (1) displayed excellent patient-specific agreement with measured global pulmonary parameters; (2) quantified relationships between PVR and mean pressure and PVS and pulse pressure, as well as studying the right ventricular (RV) afterload, which could be measured as a hydraulic load calculated from spectral analysis of pulmonary artery pressure and flow waves; (3) qualitatively confirmed the derangement of vascular wall shear stress in progressive PH; and (4) established that decreasing proximal vascular stiffness through a theoretical treatment of reversing proximal vascular remodeling could decrease RV afterload.

1. Introduction

Pulmonary hypertension (PH) is associated with a progressive increase of pulmonary vascular resistance (PVR) and sustained elevation of mean pulmonary artery pressure (mPAP), which together contribute to the right heart dysfunction. However, recent studies showed that mPAP apparently does not correlate with either the severity of symptoms or survival. Although many recent developments employing clinical and experimental measurements have investigated symptoms [1–4] to further elucidate the roles of pulmonary arterial mechanics and hemodynamics, the individual relative importance of the components of PVR, pulmonary vascular stiffness (PVS), geometry and cardiac function are unclear in disease progression. In addition, while current

PH treatment focuses on distal vasodilation, it is unknown whether or not other treatment targets might beneficially impact right ventricular function, and as a result improve of PH treatment.

Clinical and traditional scientific studies of PH focus on changes in the distal circulation. For example, the distal pulmonary vascular bed can undergo remodeling resulting from growth of smooth-muscle cells, which narrow and restrict distal pulmonary vascular geometry. Additionally lumen obliteration, medial hypertrophy, and adventitial proliferation contribute to the distal diameter decrease and thickness increase in PH [5–7]. In severe PH, a layer of myofibroblasts and extracellular matrix also develops between the endothelium and internal elastic lamina, further thickening and narrowing distal pulmonary arterial walls [8]. The effects

of these changes, along with persistent vasodilation, are most clearly seen in decreasing right ventricular (RV) cardiac output and increasing mPAP [9–11], which together indicate increased PVR. In turn, PVR is believed to well quantify RV afterload. These pathologies are currently treated clinically with vasodilators, and further identify the traditional association between distal geometry, PVR and RV afterload, and RV failure in PH progression.

Although vascular distal remodeling and distal vessel vasculopathy are generally considered the only major contributors to PH progression [12–15], recent clinical [2, 16, 17] and basic science [1, 18, 19] research have respectively found that proximal vascular stiffness is more predictive of disease outcomes than PVR and that significant remodeling occurs in the proximal vessels of animal models of the disease. Remodeling chronically alters the stiffness of the proximal arteries through combined changes in their extracellular matrix composition and thickness [1]. Proximal stiffness has been shown to (1) regulate pressure and flow wave velocities in the pulmonary bed [20]; (2) affect afterload independent of resistance [21]; and (3) affect proximal wall shear stress (WSS) and thus potentially have impacts on cellular signaling through mechanotransduction [3]. Recent studies on the arterial compliance show that increased PVR correlates to decreased arterial compliance, which establishes a constant [22, 23] or shorten resistance-compliance time [24–26] during PH progression. The decrease in compliance, such as the proximal stiffening is also important and affects the entire vasculature, as well as increased right ventricular (RV) afterload [27, 28]. These observations indicate that the evaluation of upstream vascular stiffness could play a more prominent role in pulmonary hypertension diagnosis than is currently considered, with the current diagnostic PVR quantifying only the static component of pulmonary hemodynamics. However, the magnitude of these three effects and the overall role of PVS in progressing the disease remain unclear. Although currently there are no treatments aimed towards reducing proximal stiffness, an additional interesting question is raised whether such treatments would be beneficial to improve PH treatment.

Progression of pulmonary hypertension involves continuously changing vascular hemodynamics and remodeling of the proximal and distal arteries. It is understandably difficult to investigate an individual parameter’s effect on PH in an *in vivo* study. Here, we propose a modeling procedure to simulate PH progression by dividing it into 4 stages. At each stage we only consider system changes due to varying a single pulmonary vascular parameter, from PVR, elastic modulus (EM), and arterial thickness (h), starting with the control condition. We evaluate the role of these three key parameters in modulating input impedance and hemodynamics using a two-dimensional (2D) pulmonary vascular computational model based on *in vivo* and *ex vivo* measurements obtained from normal and chronically hypoxic neonatal calves [1, 29]. We first validate our numerical results on mPAP and the first harmonic of input impedance (Z_1) by comparing animal measurements to 17 calf specific computational models. We then perform predictive studies to assess the effects of PVR, EM, and h on the arterial pressure, WSS, impedance and

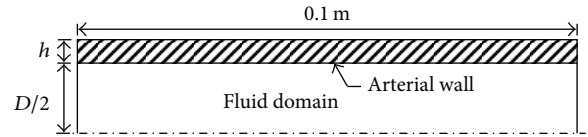


FIGURE 1: The schematic of the two dimensional symmetric pulmonary artery model (h is the thickness of the arterial wall and D is the arterial lumen diameter, the length of MPA model is 0.1 m).

RV power. Finally, the impacts of theoretical and available PH treatments are examined by reversing these parameters, thereby investigating the added effect of targeting proximal vascular remodeling for treatment in PH. We believe this simple but validated model offers important insight of PH progression and might encourage new treatment targets.

2. Methods

The ability to develop a unique and validated model for each subject and achieving reasonable solution times that allow for routine simulation are the two critical factors that motivate us to employ numerical techniques, and should enable simpler application of these techniques in both research and clinical environments. Although there have been a variety of numerical models developed by our group and others, ranging in complexity from fully three dimensional, exact geometry models to simple one dimensional bulk flow models, we believe neither fully satisfies these two critical factors. By developing a simple but still subject-specified model, an approach is proposed through which we obtain information needed to study PH progression yet perform validation with a larger number of subjects.

Our primary intent here is to examine how hemodynamics and RV power change in PH progression and during treatment. Our model consists of a single elastic tube, representing the larger upstream compliant vessels, which is modeled in two dimensional (2D) axisymmetric coordinates. Figure 1 shows the schematic of the tube model with diameter D , thickness h , and a total length of 0.1 m. Three simulation types are performed in this paper: a validation study, a PH progression study, and a PH treatment study. For the first, parameters from seventeen calves (two groups: control and hypertensive) are used to develop subject-specific models and validation occurs through comparison of multiple model results to experimental measurements. The PH progression and treatment studies then utilize mean values from the control and hypertensive groups to assess the impacts of specific parameters on afterload. Table 1 shows the parameters of the calves in control and hypertensive groups and the mean values employed, as will be explained in more detail below.

3. Numerical Model

3.1. Fluid Domain. The blood is modeled as an incompressible, laminar, Newtonian fluid with a viscosity of 3.5 mPa·s and a density of 1050 kg/m³. At model initiation, there is no flow in the domain as well as no transmural pressure.

TABLE 1: Parameters from experimental measurements to develop and validate numerical models, 8 in control and 9 in hypertensive condition. Mean \pm SD performed for each condition (arterial wall thickness, elastic modulus, PVR, and mPAP) and all cases (diameter, CO, and HR).

	No.	Thickness (mm)	Elastic modulus (kPa)	PVR (mm Hg/(L/min))	mPAP (mm Hg)	Diameter (mm)	CO (L/min)	HR (Beat/min)
Control	165	3.68	72.7	4.91	18.5	16.0	3.88	114
	166	3.44	136	4.79	29.0	19.7	6.06	147
	174	3.04	138	8.88	41.0	18.2	4.62	130
	175	2.94	105	5.17	30.0	21.8	5.80	113
	176	3.34	98.4	3.83	17.5	19.8	4.70	100
	177	3.71	64.1	5.01	18.7	19.7	3.80	94
	180	3.34	77.2	3.64	17.7	19.9	5.22	114
	181	3.52	86.0	3.08	18.0	18.9	5.85	113
Mean \pm SD		3.38 \pm 0.28	97.1 \pm 32.6	4.91 \pm 1.77	23.8 \pm 8.7			
Hyper	167	4.19	185	14.3	68.0	24	3.45	125
	168	3.50	113	19.7	39.0	18.75	5.21	118
	169	5.12	92.6	7.48	67.0	20.4	5.12	135
	170	3.60	116	13.1	51.0	20.46	4.12	122
	171	3.98	252	12.4	65.0	22.55	3.87	131
	172	3.84	267	16.8	94.0	19.94	5.36	148
	173	3.42	187	17.5	67.0	18.8	3.52	139
	178	3.90	245	19.0	81.0	20.65	5.20	117
	179	3.97	136	15.6	33.4	22.22	4.83	132
Mean \pm SD		3.95 \pm 0.51	177 \pm 66	15.1 \pm 3.8	62.8 \pm 19.2	20.1 \pm 1.9*	4.74 \pm 0.83*	120 \pm 15*

*The averaged value for all control and hypertensive cases.

At the artery model lumen the nonslip condition is applied to the fluid velocity, and normal stress is continuous across the lumen. An axisymmetric boundary is defined at the centerline of the arterial wall, thereby reducing the mesh size, and in turn, the simulation time. The inlet flow rate is transient, with pulse shape obtained from experimental *in vivo* measurements, as explained below. The outlet boundary condition of the flow domain is specified as a resistance boundary condition (32), $R = P/Q$, with P and Q being given by as the measurements mPAP and CO, respectively.

3.2. Solid Domain. The pulmonary artery wall is considered as an incompressible isotropic linear elastic model with density 1200 kg/m^3 and Poisson's ratio 0.48; the elastic moduli of the models were obtained from *ex vivo* measurements and are discussed further below. The boundary condition at each end is specified as free radial motion and zero longitudinal motion; there is no load on the exterior surface, and only internal coupled fluid pressure/shear stress is applied on the interior surface (fluid structure interface).

3.3. Solution Procedure. The CFD-ACE multiphysics package (CFD Research Corporation, CA, USA) and MATLAB (Mathworks, Natick, MA) are used to perform the numerical simulations for both fluid and solid domains, including experimental data and results processing. A rectangular mesh is generated for the axisymmetric geometry using CFD-GEOM initially containing uniform fluid and solid elements.

The mesh contains 4221 fluid nodes and 1005 solid nodes, with 201 nodes on the fluid-structure boundary. Time integration utilizes a first-order Euler approach with a time step of 2 ms. Details of the solution of the fluid and structural equations can be referred to our previous work [30–32]. Both CFD-VIEW and MATLAB are used to postprocess the resulting simulation results.

Because the resistance boundary condition coupled with wall stiffness allows for fluid storage, the simulation needs to take several cardiac cycles to become periodic. Here, we run each model for 6 continuous cardiac cycles to insure that the simulations are convergent in the transient inlet condition. A serial computer system (AMD Opteron (tm) Processor 280 2.4 GHz, 2.0 G memory) performed the simulations; typical wall time for one model is about 5 hours for a typical simulation time of 3 seconds (6 cardiac cycles).

We carried out mesh validation by comparing our baseline mesh to a $1.5 \times$ refined mesh (9331 fluid nodes, 1806 solid nodes) and verified time convergence by halving the time step (1 ms). A total 6 cardiac cycles are simulated and the fluid pressure/velocity at the end of simulations are compared with and without these temporal and spatial refinements. At nine different locations, defined in the axial direction at the inlet, midpoint, and outlet; along the radial direction at the axis of symmetry, halfway between the axis and the wall; and at the arterial wall, the fluid pressure or velocity has less than 1% change with refined mesh and less than 1% difference with refined time step, respectively.

4. Animal Data Acquisition

All studies were performed after the approval by the appropriate Institutional Animal Care and Use Committees. Seventeen newborn male dairy calves (Holstein) weighing between 35 and 50 kg were used. Data obtained from intact calves include the MPA lumen diameter, thickness, and elastic modulus (PVS); the mean MPA pressure (mPAP) and cardiac output (CO), the MPA centerline velocity time history, and pulmonary vascular input impedance (Z); several of the experimental measurements were described in previous papers [1, 2]. To make the data acquisition process clearer, these experimental methods are described briefly here.

Our *in vivo* parameters are mPAP, CO, and the MPA velocity time history [2]. A solid-state (Millar SPC-350) catheter placed in each calf MPA via the right jugular using the Seldinger technique was used to obtain pressure waveforms, while a caudal, short-axis view at the 4th intercostal space, 3–6 cm dorsal to the elbow was used to obtain pulse-wave Doppler images of instantaneous blood velocity in the MPA. Cardiac output (CO) was measured with a Swan-Ganz catheter by thermodilution in all animals. PVR was obtained from measured flow rate (CO) and pressures [11]. Finally, pulmonary distal resistance and vascular input impedance (Z) were computed from pressure and PW Doppler [11]. We note that although we have only published impedance data derived from echo and pressure measurements taken in the clinic, the post-processing for animal models is identical. *Ex vivo* measurements were taken to obtain the MPA diameter, thickness, and elastic modulus [1]. Extracted calf MPAs were processed into circumferential strips and tested on a standard material testing system (MTS Insight II, Eden Prairie, MN) to obtain *ex vivo* elastic modulus [2] over a wide range of strains. Diameter and thickness were measured using optical methods [4]. Additional work required to implement these data in the model is described below.

5. The Use of Experimental Data in the Model

5.1. Model Geometry and Elastic Properties. The model geometry and elastic properties, including the diameter, thickness, and elastic modulus, are all obtained from measurements of calf MPAs [1]. For validation, each of the seventeen models used has a subject-specific MPA diameter, thickness and elastic modulus with a single length of 0.1 m. For the simulation studies (progression and treatment), we averaged thickness and elastic modulus values from eight control and nine hypertensive animals to obtain model endpoints. Because there was no statistically significant change in the lumen diameter between control and hypertensive groups, we used one averaged diameter for all simulations. These averaged values are shown in Table 1 and indicate the true physiological changes seen during PH progression.

5.2. Inlet Flow Condition. We have previously used our inlet condition in clinical models [28]. Briefly, inlet flow velocity is assumed to be spatially constant, with magnitude determined from calf-specific or generic flow time histories and current inlet cross-sectional area. For the validation models, flow

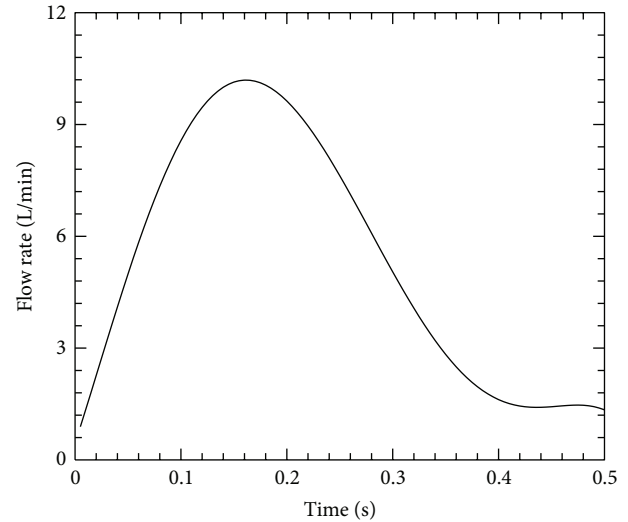


FIGURE 2: The flow rate applied in the models for control and hypertensive conditions (CO: mean 4.74 L/min, range 0.9–10.2 L/min; HR: 120 Beat/min).

time histories were obtained in a calf-specific manner by combining mean flow measurement (i.e., cardiac output) with MPA midsection blood velocity (pulse-wave Doppler). Velocity histories in five consecutive cardiac cycles were taken, averaged, and scaled to the known mean cardiac output with the area correction factor to obtain a final flow time history [11, 28, 33, 34]. After calf-specific velocity time histories were computed they were used to obtain group-averaged time-histories by first normalizing them in time with respect to their cardiac cycle length. Next, velocity at the normalized time was then averaged on a group-wise basis (8 controls, 9 hypertension). Finally the average cardiac cycle time length was implemented to redimensionalize the time.

For the predictive studies, we average heart rates of all seventeen calves and use the same heart rate for both control and hypertensive models. Because the heart rate is affected more sensitively by daily activities (such as work, walk, sleep, etc.), its effect on the PH will not be considered in this study [35]. Additionally, there was no statistically significant change in the CO between control and hypertensive groups, and we used one averaged CO and flow waveform for all simulations. The flow waveform used in the predictive models is shown in Figure 2.

5.3. Modeling of the Stiffening Process. Based on our recent vascular stiffening research in this animal model [1], there are two stiffening processes involved in PH progression: elastin remodeling and collagen engagement. The elastin remodeling yields an increase of approximately two times the linear elastic Young's modulus of the artery wall at smaller stretch ratios (defined as ratio of instantaneous lumen diameter to initial lumen diameter). Due to the engagement of vascular collagen at higher stretch, the collagen engagement is non-linear and yields a substantial increase in the incremental material modulus above the engagement stretch (the stretch

at which collagen begins to carry load). In our model, each change is simply modeled as a single increase in the linear incremental modulus as measured experimentally with *ex vivo* methods [1].

6. Post Numerical Data Processing

MATLAB codes were used (MATLAB V7.7, The Mathworks, Natick, MA) to calculate the WSS, input impedance, and ventricular powers. The WSS is $\mu(\partial u/\partial r)_{r=R}$ and derived from velocity u by fitting the near-wall velocity data with a three-point polynomial function [36]. Here, μ is the viscosity of blood, r is radial vector, and R is the local instantaneous radius of the pulmonary arterial wall. The mean WSS is time-average WSS and the pulse WSS is defined as $(WSS_{\max} - WSS_{\min})$ in one fully developed cardiac cycle. The wall pressure is obtained at the middle point between inlet and outlet boundaries, the same location of WSS. The definitions of mPAP and PP are similar to those of mean and pulse WSS. Details regarding the calculation of impedance from pressure and flow waveforms may be found in our previous works [11, 28, 33]. RV power (the rate of ventricular work) comprises potential energy and kinetic energy. The mean potential power (mean energy per unit time) and the oscillatory potential power (pulsatile energy per unit time), and the mean kinetic power and oscillatory kinetic power were calculated by using Milnor's methods [20, 35]. The mean power was calculated as $W_M = P_0 \cdot Q_0$, where P_0 and Q_0 are the zero-frequency components of the pressure and flow moduli, respectively. The oscillatory power was calculated as

$$W_O = \frac{1}{2} \sum_{n=1}^3 |Q_n|^2 |Z_n| \cos \phi_n, \quad (1)$$

here, n represents the harmonic of the fundamental frequency. Finally, total RV power was calculated as

$$W_T = W_M + W_O. \quad (2)$$

7. Statistics

With the exception of heart rate, all data from experimental measurements are presented as mean \pm SD. For validation, the first harmonic impedance Z_1 and mPAP computed in our seventeen subject-specific models were compared with the results from measurements with Student's t test. P values refer to the probability associated with the two-tailed Student's t test, and results were deemed statistically significant for P values less than 0.05. Linear regression and Bland-Altman methods [37, 38] are employed to examine the difference of impedance Z_1 and mPAP between numerical results and measurements and thereby validate the computational modeling approach. Limits of agreement (LoA), defined as the interval expected to contain 95% of the differences, were calculated and are given by the mean difference plus or minus 1.96 standard deviations. 95% confidence intervals were taken around the LoA to evaluate their precision and consistency. MATLAB codes were written (MATLAB V7.7, The Mathworks, Natick, MA) to perform the t test, linear regressions, and Bland-Altman analyses.

TABLE 2: Four stages from control to hypertensive conditions during PAH progression (each stage one parameter increased from previous stage).

Control	All parameters from control state (Table 1)
Hyper PVR	PVR: 4.91 \rightarrow 15.1 mm Hg/(L/min)
Hyper EM	EM: 97.1 \rightarrow 177 kPa
Hyper h	h : 3.38 \rightarrow 3.95 mm

8. Results

8.1. Experimental Measurements. Table 1 provides the calf experimental measurements that determined model geometry (arterial lumen diameter and arterial wall thickness), inlet flow rate (heart rate (HR) and cardiac output (CO)), material properties (*ex vivo* elastic modulus), and exit conditions (PVR). The thickness, elastic modulus, PVR, and mPAP are higher in hypertensive than those in control conditions ($P < 0.05$). There was no statistically significant change in the lumen diameter and CO as a result of hypertension. Qualitatively comparing parameters that did change between the control and hypoxic conditions, PVR (208%), elastic modulus (82%) and mPAP (164%) change substantially more than thickness (17%).

8.2. Numerical Model Validation. To validate the artery model, seventeen calf-specific simulations were performed, and the computed first harmonic modulus of input impedance (Z_1) and computed mPAP were compared to experimental measurements. Figure 3 comprises our validation comparisons. Figures 3(a) and 3(b) display linear regressions between the numerical mPAP_N results to experimental mPAP_C measurements, and between the numerical and experimental impedance Z_1 . The regressions equations are $y = 0.980x + 0.448$, $R^2 = 0.999$ ($P < 0.05$) for mPAP and $y = 1.032x - 0.275$, $R^2 = 0.941$ ($P < 0.05$) for the impedance modulus Z_1 . Figures 3(c) and 3(d) display Bland-Altman analyses for mPAP and impedance modulus Z_1 between numerical and (gold-standard) experimental results. The Bland-Altman analyses show a bias \pm LoA of 0.46 ± 1.74 mm Hg for mPAP and 0.13 ± 1.12 mm Hg/(L/min) for the impedance modulus Z_1 . Clearly the bias and LoA for mPAP are small compared to the typical pressure value, while the bias and LoA are more significant for the impedance modulus.

8.3. Study of PH Progression. The simulated effect of changes in our key parameters, namely, PVR, EM, and proximal thickness (h)—on pulmonary hemodynamics and RV power during PH progression—are studied for both progression (increases in parameters) and treatment (reduction in parameters). First we consider the progression of PH into four stages: (1) control, (2) hyper PVR (PVR: 4.91 \rightarrow 15.1 mm Hg/(L/min)), (3) hyper EM (EM: 97.1 \rightarrow 177 kPa), and finally (4) hyper h (thickness: 3.38 \rightarrow 3.95 mm), which are described in Table 2. All other parameters in control and hypertensive conditions are from the averaged experimental

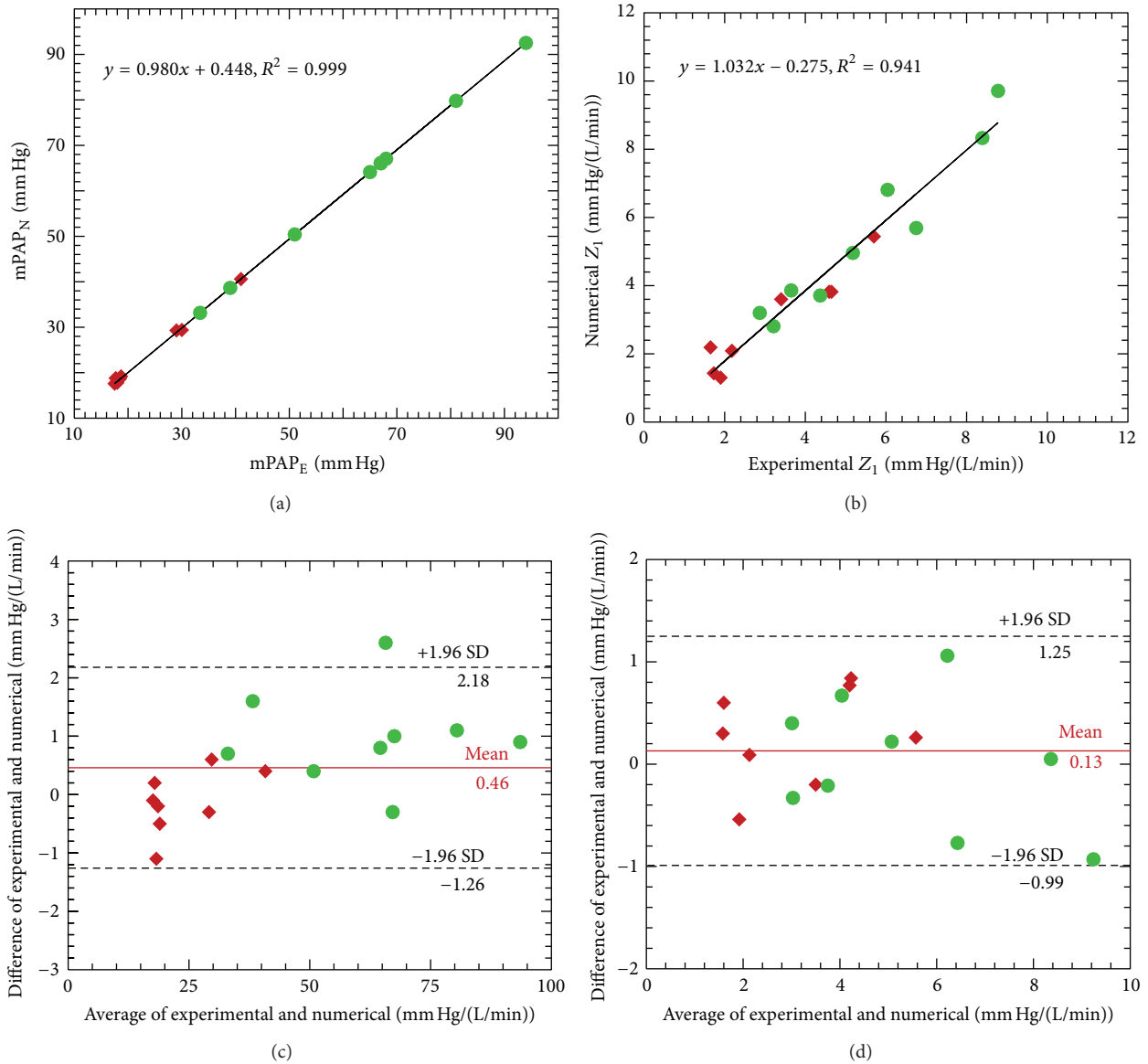


FIGURE 3: Comparison of the mean main pulmonary arterial pressure (mPAP) and input impedance modulus Z_1 between numerical (N) and experimental (E) results by linear regression (Top) and Bland-Altman (Bottom) methods (\blacklozenge : Control; \bullet : Hypertension).

measurements in Table 1. We note that due to the preserved flow rates (CO) between the control and hypoxic animal groups, pressure alone acceptably tracts pulmonary hemodynamics in this study.

Figures 4, 5, and 6 show comparison of proximal pressure, WSS and input impedance for all stages from control to hypertensive conditions during PH progression. For these and all other results, pressures and WSS are obtained at the lumen wall halfway between inlet and outlet boundaries. Increased PVR (208%) yields elevated mPAP and pulse pressure (PP); however, mPAP (209%) increases much more than PP (26.4%). Higher pressure in condition “Hyper PVR” expands the vessel to a larger cross sectional area which in turn lowers the flow velocity. As a result, WSS is reduced both in mean (to 30.9% of control) and pulse components (to

65.4% of control). The increased elastic modulus in condition “Hyper EM” stiffens the arterial wall and alters the pressure pulsatility alone, and at the same time the wall displacement is reduced and WSS is increased. The thicker arterial wall in condition “Hyper h ” has the same effect as increasing elastic modulus, in that it too increases the pulsatility of pressure and WSS. For the impedance moduli, the Z_0 is more associated with PVR and Z_1 , Z_2 are increased as EM and h increase. These impedance results agree with previous studies that found that the zero harmonic is associated with the PVR while the higher order harmonics of impedance are affected by PVS.

Figure 7 shows comparison of mean/oscillatory and RV power for all stages from control to hypertensive conditions. In the control condition, the oscillatory power contributes

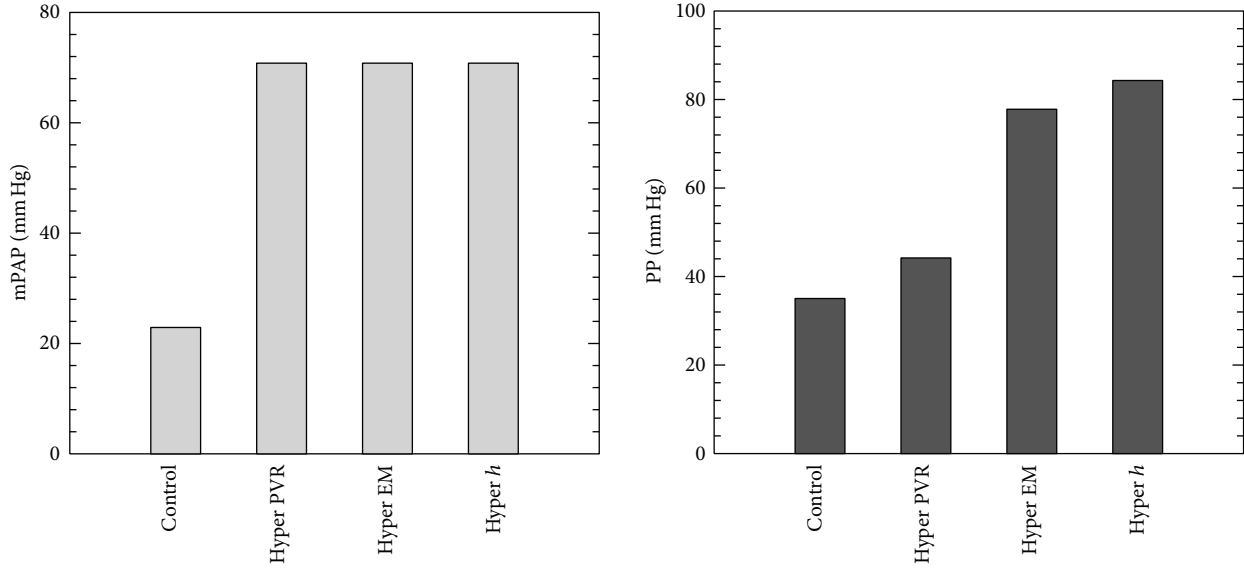


FIGURE 4: Comparison of proximal pressure for all stages from control to hypertensive conditions during PAH progression (Hyper PVR: PVR from 4.91 to 15.1 mm Hg/(L/min); Hyper EM: EM from 97.1 to 177 kPa; Hyper *h*: arterial wall thickness from 3.38 to 3.95 mm to hypertensive condition).

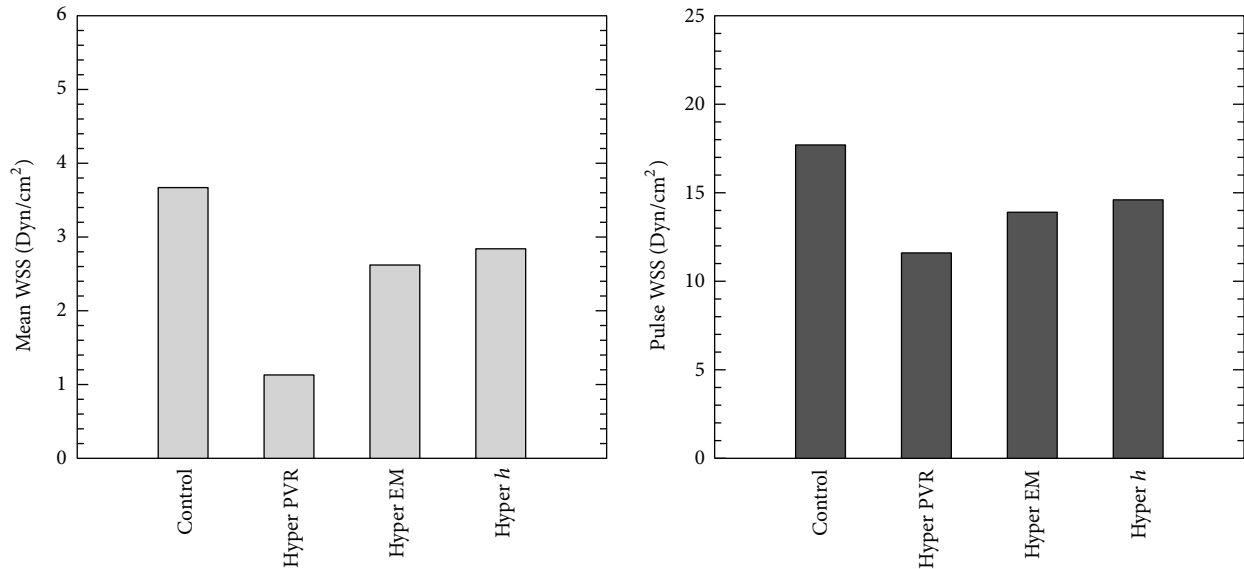


FIGURE 5: Comparison of WSS for all stages from control to hypertensive conditions during PAH progression (Hyper PVR: PVR from 4.91 to 15.1 mm Hg/(L/min); Hyper EM: EM from 97.1 to 177 kPa; Hyper *h*: arterial wall thickness from 3.38 to 3.95 mm to hypertensive condition).

38.3% of the total ventricular power, which agrees with clinical measurements for adults [35] and experimental results from other animal studies [39]. As the PVR increases at the beginning of PH progression, the mean ventricular power increases significantly while the oscillatory power decreases. This unusual relationship between oscillatory power and pulse pressure changes is likely due to the preserved cardiac function applied in the progression model. The increase in EM and *h* contribute mostly to the increase of oscillatory power, while the mean power is kept constant. As the calf progresses to the hypertensive condition, the percentage of

oscillatory power over total ventricular power decreases to 26.0%, which again is compatible with previous animal study results [39].

8.4. Effect of Treatment on Proximal Vascular Remodeling. Clinical treatment of PH focuses only on decreasing pulmonary vascular resistance, that is, relaxing distal vascular smooth muscle cells. Here, we include this effect and further examine the effects of treatment on individual parameters by applying our key parameter changes to the initially diseased model state. Thus, we start with the final model

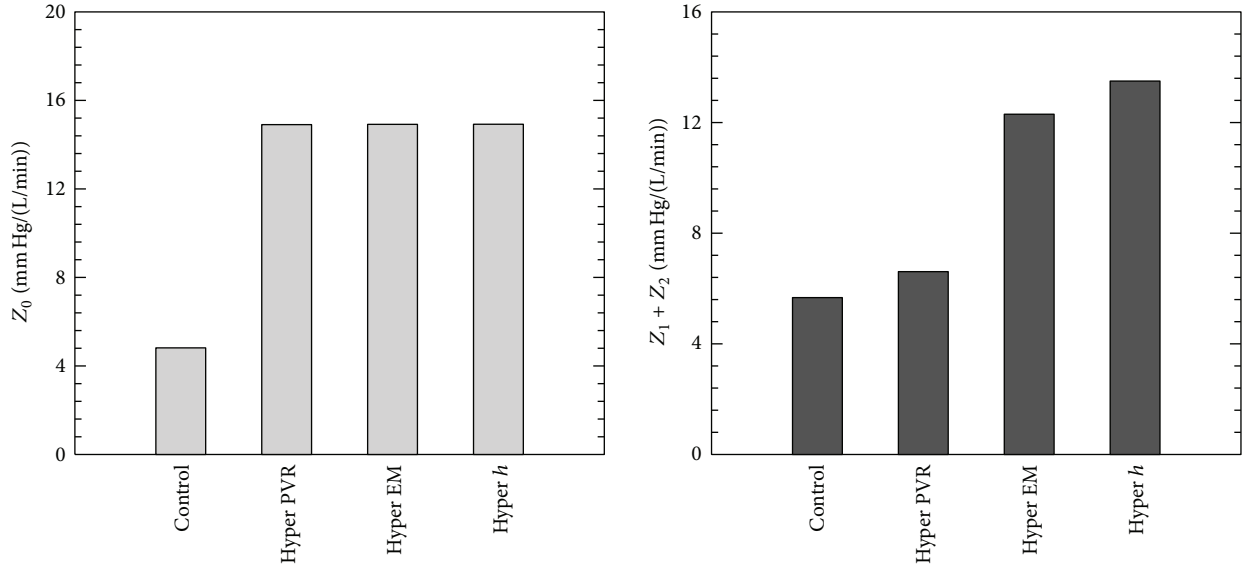


FIGURE 6: Comparison of input impedance modulus for all stages from control to hypertensive conditions during PAH progression (Hyper PVR: PVR from 4.91 to 15.1 mm Hg/(L/min); Hyper EM: EM from 97.1 to 177 kPa; Hyper h : arterial wall thickness from 3.38 to 3.95 mm to hypertensive condition).

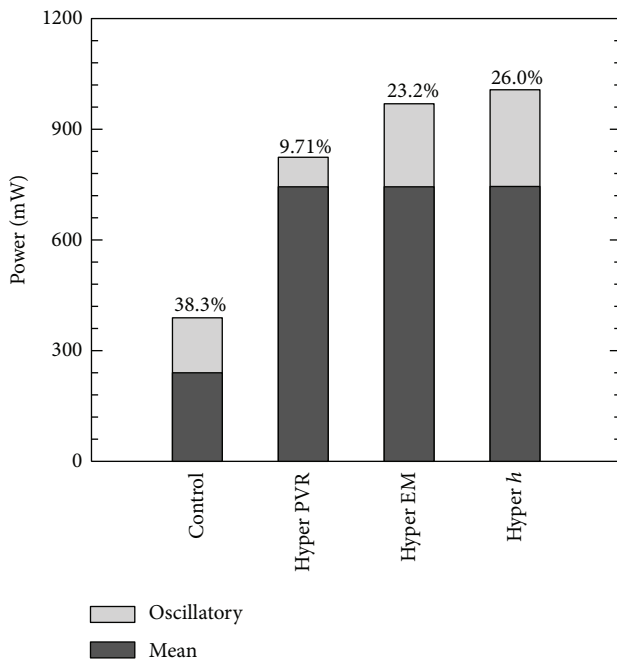


FIGURE 7: Comparison of RV powers for all stages from control to hypertensive conditions during PAH progression, percentage shown the oscillatory power over total power (Hyper PVR: PVR from 4.91 to 15.1 mm Hg/(L/min); Hyper EM: EM from 97.1 to 177 kPa; Hyper h : arterial wall thickness from 3.38 to 3.95 mm to hypertensive condition).

of our progression simulation, first apply standard clinical treatment—a vasodilator to reduce PVR—and then apply a theoretical treatment that reduces proximal remodeling, thereby lowering proximal elastic modulus and thickness;

TABLE 3: Proposed treatments on PAH with vasodilation and proximal vascular remodeling (each proposed treatment targeted to reduce one parameter from previous stage).

Hypertensive	All parameters from hypertensive state (Table 1)
Vasodilation	PVR: 15.1 \rightarrow 4.91 mm Hg/(L/min)
Lower EM	EM: 177 \rightarrow 97.1 kPa
Lower h	h : 3.95 \rightarrow 3.38 mm

this sequence is described in Table 3 and results in three treatment models.

Figures 8 and 9 show the comparison of pressure and WSS for these individually changing parameters in PH treatment. The vasodilator treatment, which reduces PVR, is also predicted to decrease both mPAP and pulse pressure dramatically. The treatments to address proximal vascular remodeling (thereby reducing the elastic modulus and thickness) do not alter mPAP but do further decrease the pulse pressure. The decreased PVR in PH treatment actually increases mean and pulsatile WSS, while treatment on proximal stiffness could reduce these changes. Figure 10 shows comparison RV power between vasodilation and theoretical proximal remodeling treatments; PVR changes significantly mean power, which contributes most to total ventricular power. Although the oscillatory component makes only a small contribution to the total, decreasing elastic modulus and arterial thickness does further reduce oscillatory power, thereby modestly reduce RV afterload. These observations suggest that decreasing or reversing proximal vascular remodeling could benefit PH treatment, in addition to the standard vasodilator approach.

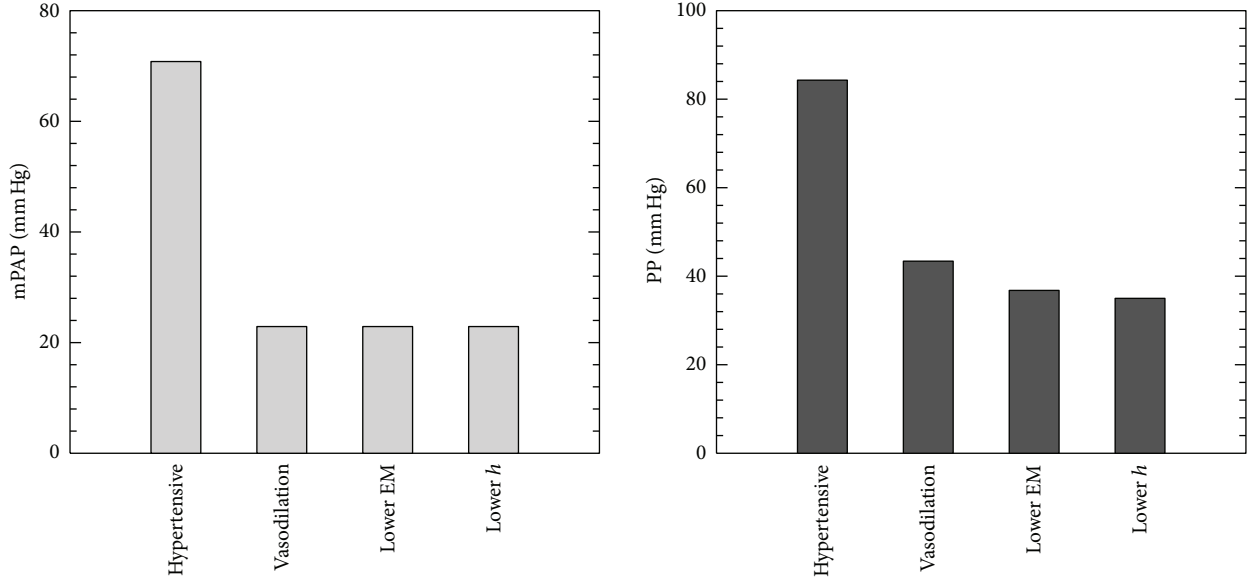


FIGURE 8: Comparison proximal pressure between vasodilation and proposed PAH treatments on proximal vascular remodeling (Vasodilation: PVR from 15.1 to 4.91 mm Hg/(L/min); Lower EM: EM from 177 to 97.1 kPa; Lower *h*: arterial wall thickness from 3.95 to 3.38 mm to control condition).

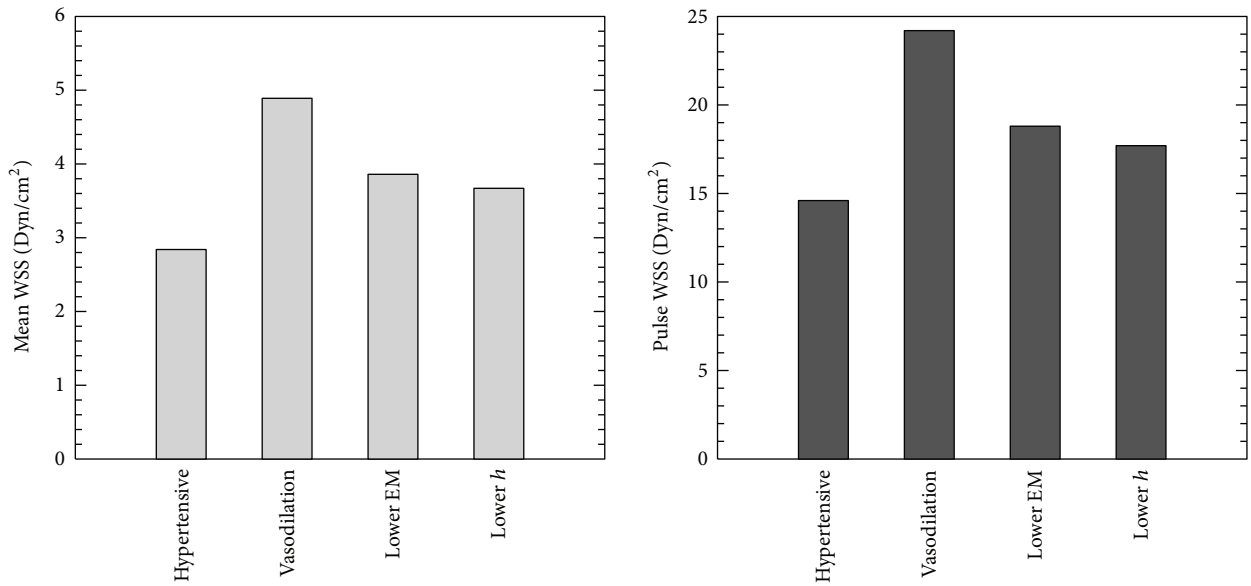


FIGURE 9: Comparison proximal WSS between vasodilation and proposed PAH treatments on proximal vascular remodeling (Vasodilation: PVR from 15.1 to 4.91 mm Hg/(L/min); Lower EM: EM from 177 to 97.1 kPa; Lower *h*: arterial wall thickness from 3.95 to 3.38 mm to control condition).

9. Discussion

Current clinical evaluation and treatment of PH focuses merely on the resistive portion of the pulmonary circuit, but many clinical studies are demonstrating that proximal stiffness strongly affects disease progression. Here, we develop and validate a simple 2D numerical model to explore the impacts of PVR and PVS in the progression and treatment of PH. The validated model results for WSS, RV power, and

impedance have implications for further basic science and clinical study, as described below.

To validate the model, we compared mPAP and input impedance modulus Z_1 between the numerical simulation and experimental measurements. Both regressions show excellent goodness of fit, which alone does not indicate correspondence; however, combined with the Bland-Altman results these comparisons support the idea that the model reasonably represents global hemodynamics through the use

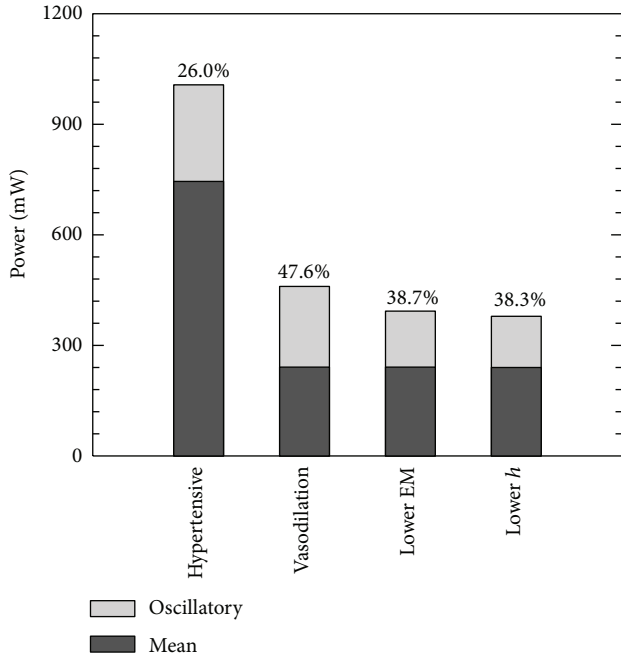


FIGURE 10: Comparison RV power between vasodilation and proposed PAH treatments on proximal vascular remodeling, percentage shown the oscillatory power over total power (Vasodilation: PVR from 15.1 to 4.91 mm Hg/(L/min); Lower EM: EM from 177 to 97.1 kPa; Lower *h*: arterial wall thickness from 3.95 to 3.38 mm to control condition).

of calf-specific model parameters. Further, general agreement exists between our model and other experimental or clinical WSS and proximal deformation results [3, 4, 40]. Finally, RV powers [35, 39] and input impedance both displayed trends which are seen in other animal models [33], as described in the results section. Such correspondence, in prediction of both global hemodynamics and general trends in local features such as WSS, gives us greater confidence in our simulated results.

Our simulation results provide evidence that the different components of afterload play unique roles in progressing PH. Increasing PVR yields severe mPAP and modest pulse pressure increases, while increasing stiffness results in only increases to pressure pulsatility. Because WSS is associated with cross sectional area, it tends to decrease during PH progression, and is associated with a more greatly distended vessel. Such changes in WSS suggest that mechanotransduction, which correlates the cellular, molecular, and tissue behaviors and pulmonary hemodynamics in blood vessels, could potentially play a role in disease progression [41]. Of note is the observation that the two components of afterload have opposite effects on WSS.

Regarding RV power, clearly, changes in PVR and elastic modulus play more important roles than changes in thickness. Previous clinical and experimental studies [35, 39] show that the oscillatory power is less of the total RV power when the PH worsens, in agreement with our progression simulations. During vasodilator treatment, we see that the

oscillatory power contributes more substantially to total RV power (47.6% versus 26% untreated); thus, for decreasing the ventricular power, the reduction of proximal vascular remodeling could be a future diagnostic target. However, even as the treatment simulation progresses to incorporate our theoretical remodeling reduction, only modest further reductions are obtained in RV power. Given the strong association between stiffness and clinical outcomes, this suggests that increased stiffness may have other deranging effects on the pulmonary circulation, such as decoupling the RV from the vessels [42].

Finally, the input impedance, which is derived from the pressure and flow profiles in pulmonary circulation, is shown as an accurate single measurement of global pulmonary hemodynamics. Several recent studies have shown that impedance can best quantify overall hemodynamics, in that it quantifies both major components, PVR and PVS. If common clinical or experimental parameters can be obtained on a noninvasive basis [33, 43, 44], our model might be used to compute impedance, and thereby provide further insight into the level and degree of PH progression through simulating patient power, general shear conditions, and exploring the degree of proximal vascular remodeling.

Overall, the effects of PVS, PVR, and proximal artery geometries on the pulmonary hemodynamics and RV power, as well as RV afterload are studied during PH progression and proposed treatment. PVS and PVR have more influences on the pulmonary hemodynamics and TV power. However, the increased PVR contributes to the increase of RV afterload, which only reflects the steady component of total RV power. The proximal stiffness is an important determinant of the oscillatory components of pulmonary hemodynamics and RV power. This agrees to the previous finding that an increase in proximal stiffness is an excellent predictor of mortality in patients with PAH and right heart failure [16, 17].

10. Limitations

With accurate experimental parameters, this simple 2D axisymmetric numerical model represents a reasonable advance in calf-specific models that are applied to larger numbers of subjects. However, as previously discussed [28], several limitations remain. 3D effects, such as nonsymmetrical spanwise flow, and complex geometry are ignored in this axisymmetric model and would influence flow pattern in the arteries and in turn affect WSS. However, our previous modeling results suggest such spanwise flows are small compared to the streamwise velocities. Although dynamic behavior of the arterial wall might be considered as linear (i.e., using an incremental modulus approach, as we have done here) during *in vivo* pulsatile flow transportation, our model could further include more realistic viscoplastic wall behavior, especially in the severe PH condition where collagen engagement plays a more important role on vascular behavior. This limitation affects the accuracy of our model, such as in the control condition, the oscillatory power contributes 38.3% of the total ventricular power, which agrees with clinical measurements for adults [35] and experimental results from

other animal studies [39] but higher than the results shown in a recent study [27]. Further, our resistance boundary condition simplifies the complex flow impedance presented by the distal vasculature to merely a resistance condition; however, the distal circulation is believed to contribute less compliance to the entire circuit, and despite using a resistance exit condition, model compliance allows for the existence of diastolic flow. Finally, our other assumptions, including constant heart rate, CO, and blood viscosity, primarily enable us to better focus our model on investigating the effect of PVR and PVS in progressing PH; such simplifications appear reasonable for these single branch models given lack of measured significant differences in the animal model. Based on all these simplifications, we have developed a numerical model that may be more easily implemented clinically with reduced construction time and runtime.

11. Conclusion

In this paper, the effects of PVR and PVS (elastic modulus and thickness) on pulmonary hemodynamics in PH progression and treatment were examined in a 2D numerical model. The model was first validated using specified data from calves in control and hypertensive conditions. In simulated disease progression, the model suggests that PVR, elastic modulus, and thickness have quantitatively different effects on pulmonary pressures, RV afterload, and power. The combined changes are shown to increase the mean and pulsatile component of hemodynamics while decreasing WSS, which supports the idea of WSS derangement in the PH condition. In simulated disease treatment, the model suggests that targeting proximal vascular remodeling, and in turn stiffness, may aid in recovery by further reducing RV afterload and power requirements. Finally, the relatively small impacts that stiffness has on RV parameters suggest that, given its newly found prominence in clinical outcomes prediction, it may affect RV function through yet undetermined pathways.

Acknowledgments

This project was supported in part by Grants from the National Institutes of Health (T32-HL072738, K24-HL081506, SCCOR-HL084923, K25-HL094749, RO1-HL114753).

References

- [1] S. R. Lammers, P. H. Kao, H. J. Qi et al., "Changes in the structure-function relationship of elastin and its impact on the proximal pulmonary arterial mechanics of hypertensive calves," *American Journal of Physiology: Heart and Circulatory Physiology*, vol. 295, no. 4, pp. H1451–H1459, 2008.
- [2] K. S. Hunter, J. A. Albietsz, P.-F. Lee et al., "In vivo measurement of proximal pulmonary artery elastic modulus in the neonatal calf model of pulmonary hypertension: development and ex vivo validation," *Journal of Applied Physiology*, vol. 108, no. 4, pp. 968–975, 2010.
- [3] A. J. Barker, C. Lanning, K. Hunter, D. Ivy, and R. Shandas, "Artery dilatation in pediatric pulmonary hypertension patients decreases hemodynamic wall shear stress," *Circulation*, vol. 118, no. 18, pp. S879–S879, 2008.
- [4] A. J. Barker, C. Lanning, and R. Shandas, "Quantification of hemodynamic wall shear stress in patients with bicuspid aortic valve using phase-contrast MRI," *Annals of Biomedical Engineering*, vol. 38, no. 3, pp. 788–800, 2010.
- [5] G. G. Pietra, F. Capron, S. Stewart et al., "Pathologic assessment of vasculopathies in pulmonary hypertension," *Journal of the American College of Cardiology*, vol. 43, no. 12, pp. 25s–32s, 2004.
- [6] J. Wang, L. Weigand, W. Lu, J. T. Sylvester, G. L. Semenza, and L. A. Shimoda, "Hypoxia inducible factor 1 mediates hypoxia-induced TRPC expression and elevated intracellular Ca^{2+} in pulmonary arterial smooth muscle cells," *Circulation Research*, vol. 98, no. 12, pp. 1528–1537, 2006.
- [7] S. Bonnet, E. D. Michelakis, C. J. Porter et al., "An Abnormal mitochondrial-hypoxia inducible factor-1 α -Kv channel pathway disrupts oxygen sensing and triggers pulmonary arterial hypertension in fawn hooded rats: similarities to human pulmonary arterial hypertension," *Circulation*, vol. 113, no. 22, pp. 2630–2641, 2006.
- [8] K. R. Stenmark, N. Davie, M. Frid, E. Gerasimovskaya, and M. Das, "Role of the adventitia in pulmonary vascular remodeling," *Physiology*, vol. 21, no. 2, pp. 134–145, 2006.
- [9] R. Naeije and S. Huez, "Right ventricular function in pulmonary hypertension: physiological concepts," *European Heart Journal*, vol. 9, pp. H5–H9, 2007.
- [10] W. W. Nichols and M. F. O'Rourke, *McDonald's Blood Flow in Arteries: Theoretical, Experimental, and Clinical Principles*, A Hodder Arnold Publication, New York, NY, USA, 4th edition, 1998.
- [11] C. E. Weinberg, J. R. Hertzberg, D. D. Ivy et al., "Extraction of pulmonary vascular compliance, pulmonary vascular resistance, and right ventricular work from single-pressure and doppler flow measurements in children with pulmonary hypertension: a new method for evaluating reactivity: in vitro and clinical studies," *Circulation*, vol. 110, no. 17, pp. 2609–2617, 2004.
- [12] K. M. Moser and N. S. Braunwald, "Successful surgical intervention in severe chronic thromboembolic pulmonary hypertension," *Chest*, vol. 64, no. 1, pp. 29–35, 1973.
- [13] P. Dartevelle, E. Fadel, S. Mussot et al., "Chronic thromboembolic pulmonary hypertension," *European Respiratory Journal*, vol. 23, no. 4, pp. 637–648, 2004.
- [14] N. Galiè and N. H. S. Kim, "Pulmonary microvascular disease in chronic thromboembolic pulmonary hypertension," *Proceedings of the American Thoracic Society*, vol. 3, no. 7, pp. 571–576, 2006.
- [15] M. M. Hoeper, E. Mayer, G. Simonneau, and L. J. Rubin, "Chronic thromboembolic pulmonary hypertension," *Circulation*, vol. 113, no. 16, pp. 2011–2020, 2006.
- [16] S. Mahapatra, R. A. Nishimura, P. Sorajja, S. Cha, and M. D. McGoon, "Relationship of pulmonary arterial capacitance and mortality in idiopathic pulmonary arterial hypertension," *Journal of the American College of Cardiology*, vol. 47, no. 4, pp. 799–803, 2006.
- [17] C. T.-J. Gan, J.-W. Lankhaar, N. Westerhof et al., "Noninvasively assessed pulmonary artery stiffness predicts mortality in pulmonary arterial hypertension," *Chest*, vol. 132, no. 6, pp. 1906–1912, 2007.
- [18] N. C. Chesler, D. N. Ku, and Z. S. Galis, "Transmural pressure induces matrix-degrading activity in porcine arteries ex vivo,"

- American Journal of Physiology: Heart and Circulatory Physiology*, vol. 277, no. 5, pp. H2002–H2009, 1999.
- [19] D. Scott-Drechsel, Z. Su, K. Hunter, M. Li, R. Shandas, and W. Tan, “A new flow co-culture system for studying mechanobiology effects of pulse flow waves,” *Cytotechnology*, vol. 64, no. 6, pp. 649–666, 2012.
- [20] W. R. Milnor, C. R. Conti, K. B. Lewis, and M. F. O’Rourke, “Pulmonary arterial pulse wave velocity and impedance in man,” *Circulation Research*, vol. 25, no. 6, pp. 637–649, 1969.
- [21] C. E. Weinberg, J. R. Hertzberg, D. D. Ivy et al., “Extraction of pulmonary vascular compliance, pulmonary vascular resistance, and right ventricular work from single-pressure and doppler flow measurements in children with pulmonary hypertension: a new method for evaluating reactivity—in vitro and clinical studies,” *Circulation*, vol. 110, no. 17, pp. 2609–2617, 2004.
- [22] N. Saouti, N. Westerhof, F. Helderma et al., “RC time constant of single lung equals that of both lungs together: a study in chronic thromboembolic pulmonary hypertension,” *American Journal of Physiology: Heart and Circulatory Physiology*, vol. 297, no. 6, pp. H2154–H2160, 2009.
- [23] J.-W. Lankhaar, N. Westerhof, T. J. C. Faes et al., “Pulmonary vascular resistance and compliance stay inversely related during treatment of pulmonary hypertension,” *European Heart Journal*, vol. 29, no. 13, pp. 1688–1695, 2008.
- [24] R. J. Tedford, P. M. Hassoun, S. C. Mathai et al., “Pulmonary capillary wedge pressure augments right ventricular pulsatile loading,” *Circulation*, vol. 125, no. 2, pp. 289–297, 2012.
- [25] A. Pagnamenta, R. Vanderpool, S. Brimiouille, and R. Naeije, “Proximal pulmonary arterial obstruction decreases the time constant of the pulmonary circulation and increases right ventricular afterload,” *Journal of Applied Physiology*, vol. 114, no. 11, pp. 1586–1592, 2013.
- [26] R. V. M. Ross, M. R. Toshner, E. Soon, R. Naeije, and J. Pepke-Zaba, “Decreased time constant of the pulmonary circulation in chronic thromboembolic pulmonary hypertension,” *American Journal of Physiology: Heart and Circulatory Physiology*, vol. 305, no. 2, pp. H259–H264, 2013.
- [27] N. Saouti, N. Westerhof, F. Helderma et al., “Right ventricular oscillatory power is a constant fraction of total power irrespective of pulmonary artery pressure,” *American Journal of Respiratory and Critical Care Medicine*, vol. 182, no. 10, pp. 1315–1320, 2010.
- [28] Z. Su, K. S. Hunter, and R. Shandas, “Impact of pulmonary vascular stiffness and vasodilator treatment in pediatric pulmonary hypertension: 21 patient-specific fluid-structure interaction studies,” *Computer Methods and Programs in Biomedicine*, vol. 108, no. 2, pp. 617–628, 2012.
- [29] K. R. Stenmark, J. Fasules, and D. M. Hyde, “Severe pulmonary hypertension and arterial adventitial changes in newborn calves at 4,300 m,” *Journal of Applied Physiology*, vol. 62, no. 2, pp. 821–830, 1987.
- [30] Y. Khunatorn, S. Mahalingam, C. G. DeGroff, and R. Shandas, “Influence of connection geometry and SVC-IVC flow rate ratio on flow structures within the total cavopulmonary connection: a numerical study,” *Journal of Biomechanical Engineering*, vol. 124, no. 4, pp. 364–377, 2002.
- [31] C. DeGroff, B. Birnbaum, R. Shandas, W. Orlando, and J. Hertzberg, “Computational simulations of the total cavo-pulmonary connection: insights in optimizing numerical solutions,” *Medical Engineering and Physics*, vol. 27, no. 2, pp. 135–146, 2005.
- [32] K. S. Hunter, C. J. Lanning, S.-Y. J. Chen et al., “Simulations of congenital septal defect closure and reactivity testing in patient-specific models of the pediatric pulmonary vasculature: a 3D numerical study with fluid-structure interaction,” *Journal of Biomechanical Engineering*, vol. 128, no. 4, pp. 564–572, 2006.
- [33] K. S. Hunter, P.-F. Lee, C. J. Lanning et al., “Pulmonary vascular input impedance is a combined measure of pulmonary vascular resistance and stiffness and predicts clinical outcomes better than pulmonary vascular resistance alone in pediatric patients with pulmonary hypertension,” *American Heart Journal*, vol. 155, no. 1, pp. 166–174, 2008.
- [34] L. Tian, K. S. Hunter, K. S. Kirby, D. D. Ivy, and R. Shandas, “Measurement uncertainty in pulmonary vascular input impedance and characteristic impedance estimated from pulsed-wave Doppler ultrasound and pressure: clinical studies on 57 pediatric patients,” *Physiological Measurement*, vol. 31, no. 6, pp. 729–748, 2010.
- [35] W. R. Milnor, D. H. Bergel, and J. D. Bargainer, “Hydraulic power associated with pulmonary blood flow and its relation to heart rate,” *Circulation Research*, vol. 19, no. 3, pp. 467–480, 1966.
- [36] H.-B. Kim, J. Hertzberg, C. Lanning, and R. Shandas, “Non-invasive measurement of steady and pulsating velocity profiles and shear rates in arteries using echo PIV: *in vitro* validation studies,” *Annals of Biomedical Engineering*, vol. 32, no. 8, pp. 1067–1076, 2004.
- [37] D. G. Altman and J. M. Bland, “Measurement in medicine—the analysis of method comparison studies,” *Statistician*, vol. 32, no. 3, pp. 307–317, 1983.
- [38] J. M. Bland and D. G. Altman, “Statistical methods for assessing agreement between two methods of clinical measurement,” *The Lancet*, vol. 1, no. 8476, pp. 307–310, 1986.
- [39] E. P. Chen, H. B. Bittner, D. M. Craig, R. D. Davis Jr., and P. Van Trigt III, “Pulmonary hemodynamics and blood flow characteristics in chronic pulmonary hypertension,” *Annals of Thoracic Surgery*, vol. 63, no. 3, pp. 806–813, 1997.
- [40] B. T. Tang, T. A. Fonte, J.A. Feinstein, C.A. Taylor, and P.S. Tsao, “Shear stress quantification and regulation of endothelial cell dysfunction in models of pulmonary arterial hypertension,” *Circulation*, vol. 114, article 81, 2006.
- [41] P. F. Davies, “Flow-mediated endothelial mechanotransduction,” *Physiological Reviews*, vol. 75, no. 3, pp. 519–560, 1995.
- [42] G. Elzinga and N. Westerhof, “Pressure and flow generated by the left ventricle against different impedances,” *Circulation Research*, vol. 32, no. 2, pp. 178–186, 1973.
- [43] R. Shandas, C. Weinberg, D. D. Ivy et al., “Development of a noninvasive ultrasound color m-mode means of estimating pulmonary vascular resistance in pediatric pulmonary hypertension: mathematical analysis, *in vitro* validation, and preliminary clinical studies,” *Circulation*, vol. 104, no. 8, pp. 908–913, 2001.
- [44] K. S. Hunter, C. J. Lanning, K. S. Kirby, D. D. Ivy, and R. Shandas, “In-vivo pulmonary vascular stiffness obtained from color M-mode tissue Doppler imaging and pressure measurements predicts clinical outcomes better than indexed pulmonary vascular resistance in pediatric patients with pulmonary arterial hypertension,” *Circulation*, vol. 118, no. 18, pp. S879–S879, 2008.

Research Article

Application of Computational Lower Extremity Model to Investigate Different Muscle Activities and Joint Force Patterns in Knee Osteoarthritis Patients during Walking

Kyung Wook Nha,¹ Ariunzaya Dorj,² Jun Feng,² Jun Ho Shin,² Jong In Kim,¹ Jae Ho Kwon,¹ Kyungsoo Kim,³ and Yoon Hyuk Kim²

¹ Department of Orthopaedic Surgery, Inje University, Ilsan Paik Hospital, Ilsan 441-706, Republic of Korea

² Department of Mechanical Engineering, Kyung Hee University, Yongin 446-701, Republic of Korea

³ Department of Applied Mathematics, Kyung Hee University, Yongin 446-701, Republic of Korea

Correspondence should be addressed to Yoon Hyuk Kim; yoonhkim@khu.ac.kr

Received 23 July 2013; Revised 13 September 2013; Accepted 16 September 2013

Academic Editor: Zhonghua Sun

Copyright © 2013 Kyung Wook Nha et al. This is an open access article distributed under the Creative Commons Attribution License, which permits unrestricted use, distribution, and reproduction in any medium, provided the original work is properly cited.

Many experimental and computational studies have reported that osteoarthritis in the knee joint affects knee biomechanics, including joint kinematics, joint contact forces, and muscle activities, due to functional restriction and disability. In this study, differences in muscle activities and joint force patterns between knee osteoarthritis (OA) patients and normal subjects during walking were investigated using the inverse dynamic analysis with a lower extremity musculoskeletal model. Extensor/flexor muscle activations and torque ratios and the joint contact forces were compared between the OA and normal groups. The OA patients had higher extensor muscle forces and lateral component of the knee joint force than normal subjects as well as force and torque ratios of extensor and flexor muscles, while the other parameters had little differences. The results explained that OA patients increased the level of antagonistic cocontraction and the adduction moment on the knee joint. The presented findings and technologies provide insight into biomechanical changes in OA patients and can also be used to evaluate the postoperative functional outcomes of the OA treatments.

1. Introduction

Osteoarthritis (OA) is regarded as a degenerative joint disease that results from loss of balance between the biological resistance of the joint and mechanical stress applied to the joint, and it is defined as conditions that lead to joint symptoms and signs associated with defects in the integrity of articular cartilage, in addition to related changes in the underlying bone at the joint margins [1, 2]. The knee is one of the most common joints afflicted by OA with aging: about 33% of people older than 65 have OA in their knee joints [2]. Many experimental and computational studies have reported that OA in the knee joint affects knee biomechanics, including joint kinematics, joint contact forces, and muscle activities, due to functional restriction and disability [3, 4].

Several experimental studies have measured periarticular knee muscle activation of OA patients during walking using

electromyography (EMG) systems [5–8] and knee joint contact forces using instrumented knee implants [9–12]. Even though direct measures would be more realistic, direct measures are invasive and require special devices, for example, instrumented implants, fine-wires, or indwelling electrodes. Although surface EMG is not invasive, it generally measures the activity of superficial muscles. In the lower extremity, surface EMG can be used to measure the activation of medial and lateral hamstrings, medial and lateral vastus, and rectus femoris, but it is difficult to estimate activation of the vastus intermedius, semimembranosus, and semitendinosus, separately [13].

The most common noninvasive method is computational analysis based on inverse dynamic analysis that uses a virtual model of the knee joint. This type of analysis allows prediction of muscle forces, mechanical stresses, and joint forces that are impossible or very difficult to measure *in vivo*. Several

studies have investigated abnormalities in individuals with OA in the knee joint from the perspectives of movement kinematics, joint loads, and joint stability [14–19]. It has been shown that OA is often accompanied by increased knee laxity and stiffness, reduced flexion angles, and increased adduction or decreased flexion moments. Knee joint constraint forces and muscle force predictions were analyzed in OA patients by inverse dynamic methods. Pain relief efficiency to knee contact force in subjects with knee OA was significantly different from that of healthy controls [20]. However, differences in muscle forces and joint contact forces between OA patients and healthy people have not been investigated in detail in the previous studies.

In this study, differences in muscle activity and joint force patterns between knee OA patients and normal subjects during walking were investigated using the motion capture data and inverse dynamic analysis with a lower extremity model. Extensor/flexor muscle activation ratio and torque ratio were calculated to compare muscle activities, and three-dimensional (3D) components (compressive, medial-lateral, and anterior-posterior) of the joint contact force were analyzed.

2. Methods

2.1. Subjects. Two groups of subjects participated in this study after providing informed consent: 11 OA patients (age, 53.8 ± 5.5 yrs; height, 160.0 ± 8.0 cm; weight, 73.1 ± 13.4 kg) who had medial knee OA diagnosed according to the criteria defined by the American College of Rheumatology (radiographic analyses or clinical tests) [1] and 10 asymptomatic participants (age, 26.7 ± 1.7 yrs; height, 164.0 ± 5.4 cm; weight, 58.5 ± 10.5 kg) with no clinical diagnosis of OA, rheumatoid arthritis, or history of knee trauma or pain. Participants were able to walk at least 40 m independently, and potential participants were excluded if they had uncontrolled systemic disease or preexisting neurological or other orthopaedic conditions affecting their ability to walk.

2.2. Experiments. A 3D motion analysis system (Hawk Digital Real Time System, Motion Analysis System, Santa Rosa, CA, USA) with 10 cameras operating at a sampling rate of 100 Hz was used to record motion capture data. In addition, four 1000 Hz force plates (MP4060, Bertec Corporation, Columbus, OH, USA) were used to measure ground reaction forces and identify gait cycle events. Thirty-seven retroreflective markers were attached to the lower extremities (bilateral anterior superior iliac spines, posterior superior iliac spines, lateral/medial femoral condyles, lateral/medial malleolus, forefeet, and heels) and the upper body (sternum, processus xiphoideus, C7 vertebra, T10 vertebra, vertex, bilateral front of head, right/left acromion, medial/lateral epicondyles, radial/ulnar styloid, and second and fifth metacarpals), based on previous positions reported in the literature [22, 23] (Figure 1). Subjects walked at a self-selected comfortable walking speed along a 6 m walkway after multiple trials to ensure that they were able to walk comfortably with consistent velocity. Data from five trials were averaged; these averaged values were used in the analysis.



FIGURE 1: Positions of 37 retroreflective markers for motion capture during gait cycles.

2.3. Dynamic Model. A dynamic model of the lower extremities was constructed to calculate kinematics and kinetics such as joint angle, angular velocity, angular acceleration, moment, joint constraint forces, and muscle forces during the gait cycle. The model consisted of 6 segments and 18 degrees-of-freedom linkages for the hip, knee, and ankle joints (Figure 2). Mass, center of gravity, and moment of inertia of each body segment were determined by scaling according to the subject's body weight and segmental lengths obtained from the markers based on [24]. Local coordinate systems for each body segment were set based on the recommendations of the International Society of Biomechanics [22, 23]. Joint centers of the hip, knee, and ankle were defined by marker positions specified in [25]. Twenty-six pairs of lower extremity muscles were then considered, and the origin and insertion sites of each muscle were extracted from the literature [21] (Figure 2).

2.4. Inverse Dynamics. Knee joint kinematic information, such as angular velocity and acceleration of the i th segment, was obtained from motion capture data by using the finite difference technique. The net joint force and moment acting on the i th body segment were then calculated starting from the distal segment with ground reaction force and moment [26, 27] by using the following equilibrium equations:

$$\begin{aligned} \vec{F}_i^e &= m_i (\vec{a}_i - \vec{g}) - \vec{F}_{i-1}^e, \\ \vec{M}_i^e &= I_i \vec{\alpha}_i + \vec{\omega}_i \times (I_i \vec{\omega}_i) - \vec{l}_i \times \vec{F}_i^e - \vec{l}_{i-1} \times \vec{F}_{i-1}^e - \vec{M}_{i-1}^e, \end{aligned} \quad (1)$$

where m_i is the i th segmental mass, \vec{a}_i is the translational acceleration vector of the i th segment's center of gravity, \vec{g} is the gravitational vector, I_i is the moment of inertia around the center of gravity of the i th segment, $\vec{\omega}_i$ and $\vec{\alpha}_i$ are the

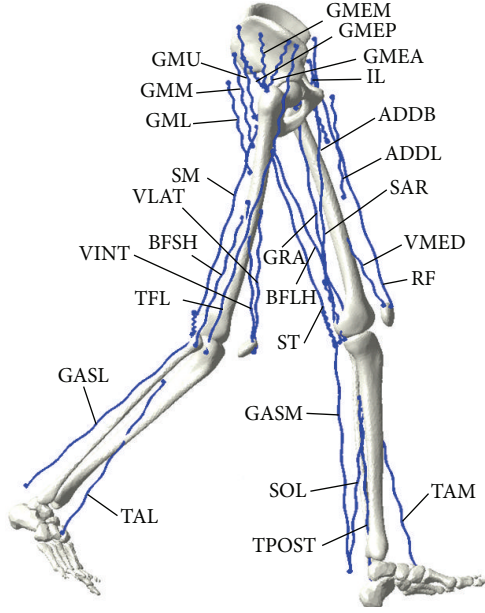


FIGURE 2: Muscles in the lower extremity model. Abbreviations are as follows [21]: vastus intermedius (VINT); vastus lateralis (VLAT); vastus medialis (VMED); rectus femoris (RF); semimembranosus (SM); semitendinosus (ST); biceps femoris long head (BFLH); biceps femoris short head (BFSH); gastrocnemius medial (GASM); gastrocnemius lateral (GASL); tensor fasciae latae (TFL); soleus (SOL); tibialis posterior (TPOST); tibialis anterior lateral (TAL); tibialis anterior medial (TAM); gluteus maximus upper (GMU); gluteus maximus middle (GMM); gluteus maximus lower (GML); gluteus medius posterior (GMEP); gluteus medius middle (GMEM); gluteus medius anterior (GMEA); adductor brevis (ADDB); adductor longus (ADDL); iliacus (IL); sartorius (SAR); and gracilis (GRA).

angular velocity and acceleration vector of the i th segment, \vec{l}_i is the distance from the segmental center of gravity of the i th segment to the distal joint center, and \vec{F}_{i-1}^e and \vec{M}_{i-1}^e are the joint force and moment acting on the distal segment, called the $(i-1)$ th segment.

The corresponding joint force and moment equilibrium equations, including muscle forces, were finally formulated for each joint during 100 intervals in one gait cycle as follows:

$$\begin{aligned} \sum_{i=1}^{26} F_i^M \vec{\tau}_i + \vec{F}^j &= \vec{F}^e, \\ \sum_{i=1}^{26} F_i^M (\vec{r}_i \times \vec{\tau}_i) &= \vec{M}^e, \end{aligned} \quad (2)$$

where F_i^M and $\vec{\tau}_i$ are the magnitude and unit direction vector of the i th muscle force, \vec{F}^j is the joint constraint force, \vec{r}_i is the location vector of the i th muscle with respect to the joint center, and \vec{F}^e and \vec{M}^e are the net joint force and moment, respectively. Muscle forces were calculated using the static optimization technique because of the redundancy of variables [12]. Maximum isometric muscle forces were assumed to be proportional to the physiological cross-sectional area (PCSA), and the maximum values dependent on the muscle

group and age were obtained from [21, 28]. The sum of stresses cubed was used as the objective function:

$$\begin{aligned} \text{Minimize} \quad & \sum_{i=1}^{26} \left(\frac{F_i^M}{A_i} \right)^3 \\ \text{subject to} \quad & 0 \leq \frac{F_i^M}{A_i} \leq \sigma_i, \quad i = 1, \dots, 26, \end{aligned} \quad (3)$$

where A_i and σ_i are the PCSA and maximum stress of the i th muscle, respectively. A customized MATLAB (The MathWorks, Natick, MA, USA) was utilized to solve the above optimization problem.

To investigate the knee extensor/flexor ratio, four muscles were selected as knee extensor muscles (VINT, VLAT, VMED, and RF) and eight muscles were chosen as flexor muscles (SM, ST, BFLH, BFSH, GASM, GASL, SAR, and GRA). The knee extensor/flexor muscle activation ratio (EFAR, A_e/A_f) and knee extensor/flexor torque ratio (EFTR, T_e/T_f) were defined as follows:

$$\begin{aligned} \frac{A_e}{A_f} &= (A_{\text{VINT}} + A_{\text{VLAT}} + A_{\text{VMED}} + A_{\text{RF}}) \\ &\quad \times (A_{\text{SM}} + A_{\text{ST}} + A_{\text{BFLH}} + A_{\text{BFSH}} \\ &\quad \quad + A_{\text{GASM}} + A_{\text{GASL}} + A_{\text{SAR}} + A_{\text{GRA}})^{-1}, \\ \frac{T_e}{T_f} &= (T_{\text{VINT}} + T_{\text{VLAT}} + T_{\text{VMED}} + T_{\text{RF}}) \\ &\quad \times (T_{\text{SM}} + T_{\text{ST}} + T_{\text{BFLH}} + T_{\text{BFSH}} \\ &\quad \quad + T_{\text{GASM}} + T_{\text{GASL}} + T_{\text{SAR}} + T_{\text{GRA}})^{-1}, \end{aligned} \quad (4)$$

where A_X and T_X represent the muscle force and the torque generated by muscle X , respectively.

2.5. Data Analysis. The estimated muscle forces and joint reaction forces were averaged for 10 subjects in the asymptomatic group. The Pearson correlation coefficients between the mean values in the asymptomatic group and those reported in a previous study [12] at 100 time steps during the gait cycle for the quadriceps (VINT, VLAT, VMED, and RF), hamstring (SM, ST, BFLH, and BFSH), and gastrocnemius (GASM and GASL) as well as the compressive joint force were analyzed to confirm the validity of the present approach. An independent sample t -test was then performed to compare the mean values of muscle forces, knee extensor/flexor ratios (EFAR and EFTR) in response to muscle activity, and peak knee joint force components (compressive, medial-lateral, and anterior-posterior) during the gait cycle between 11 OA patients (OA) and 10 normal subjects (asymptomatic), respectively. The IBM SPSS Statistics 20 (SPSS, Chicago, IL, USA) was used for the statistical analysis, and the significant difference was defined as $P < 0.05$.

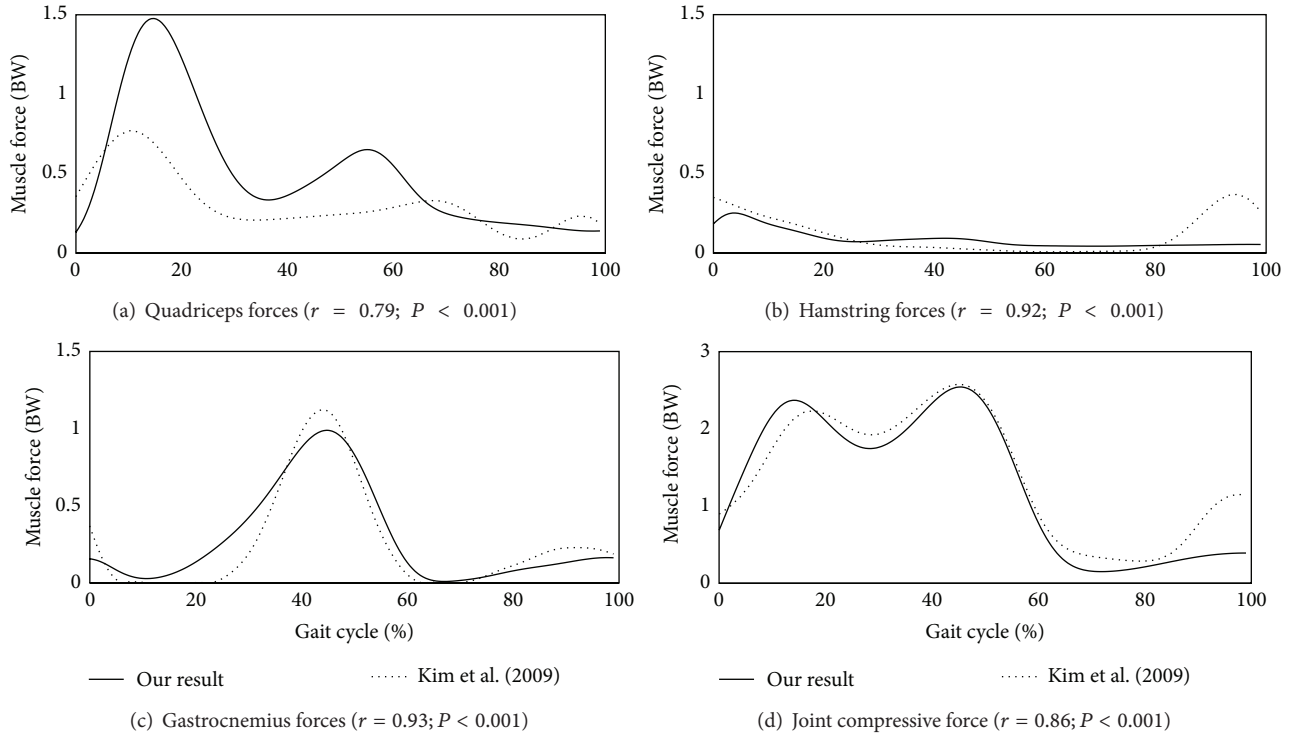


FIGURE 3: The predicted muscle forces of (a) quadriceps, (b) hamstring, (c) gastrocnemius, and (d) compressive forces and those in [12] during a gait cycle. Our results were averaged for 10 subjects in the asymptotic group, and the forces were normalized to each subject's body weight (BW). The Pearson correlation coefficients and P values were also provided.

3. Results

The averaged values in the asymptomatic group for muscle forces of the quadriceps, hamstring, and gastrocnemius as well as the compressive joint force during a gait cycle were depicted in Figure 3 with those reported in [12]. The Pearson correlation coefficients between our data and the previous data were 0.79 for quadriceps, 0.92 for hamstring, 0.93 for gastrocnemius, and 0.86 for compressive joint force with $P < 0.001$ for all cases.

The averaged muscle forces in the knee extensor muscles for both OA and asymptomatic groups are presented in Figure 4, and the P values for the t -test between the two groups were summarized in Table 1. OA patients produced significantly greater extensor muscle forces than asymptomatic subjects during the overall gait cycle in all extensor muscles. The knee flexor muscles of OA patients exerted higher BFLH muscle forces and lower BFSH muscle forces among the lateral hamstrings, while the forces exerted by the medial hamstrings (SM and ST) were similar (Figure 5 and Table 1). Muscle activation patterns of the gastrocnemius muscles (GASM and GASL) and SAR were similar, while GRA activation was higher in the OA group (Figure 5 and Table 1).

The averaged 3D components of knee joint forces for both OA and asymptomatic groups are presented in Figure 6. Compressive and medial-lateral (ML) forces calculated for OA patients were higher than those of asymptomatic subjects,

although little difference in the maximum magnitude was observed (Table 1). Anterior-posterior (AP) forces were presented similarly between the two groups (Figure 6 and Table 1).

The averaged knee extensor/flexor muscles forces and torques as well as their ratios (EFAR and EFTR) are given in Figure 7. Although there were no large differences in muscle forces or torques for flexor muscles between OA patients and normal controls, OA patients had higher values for extensor muscles (Table 1). Moreover, EFAR and EFTR were substantially higher in OA patients than control subjects for the entire duration of the gait cycle (Table 1).

4. Discussion

Muscle forces of the quadriceps (VINT, VLAT, VMED, and RF), hamstring (SM, ST, BFLH, and BFSH), and gastrocnemius (GASM and GASL) as well as the compressive joint force were consistent with those reported in [12], thereby validating our model (Figure 3). Trends in muscle and joint forces were similar, and the Pearson correlation coefficients and the P values were enough to show the strong positive correlations. In addition, the peak compressive contact force in the knee joint ranged from 2.5 to 3.1 times body weight (BW) in the asymptomatic group, consistent with the previous experimental results measured *in vivo* (1.6 to 3.5 BW) [9–12].

Previous experimental results for knee extensor and flexor muscle forces support our findings that knee extensor

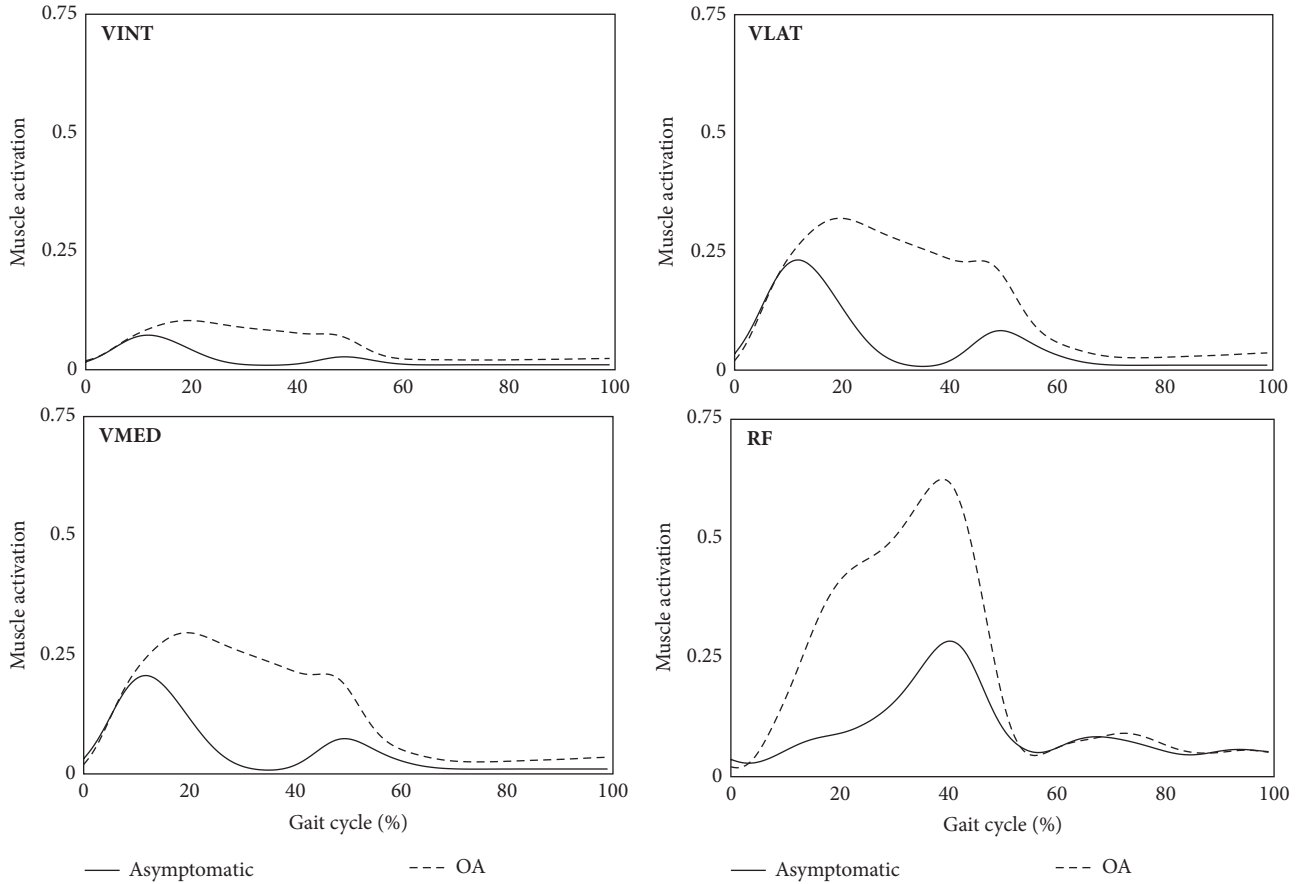


FIGURE 4: Knee extensor muscle forces for OA patients and asymptomatic subjects during a gait cycle, where the muscle forces were averaged in both groups and scaled to each muscle’s maximum isometric force (VINT, vastus intermedius; VLAT, vastus lateralis; VMED, vastus medialis; RF, rectus femoris).

muscle activity was significantly higher in individuals with knee OA than in asymptomatic controls [29]. It was also shown that the muscle activity pattern in the medial and lateral hamstrings of OA patients was different from that of control subjects [30, 31]. From a biomechanical viewpoint, an increase in the adduction angle and moment in the frontal plane may lead to the muscle activity changes we observed in OA patients [15–17].

Peak knee compressive force in the knee joint during walking was 2.55 ± 0.30 BW (mean \pm standard deviation) in the OA group, which is consistent with the previously reported results of 3.67 to 4.45 BW [32] and 1.6 to 1.8 BW [20] by considering the variety of subjects used in the different studies. The ML and AP components of knee joint force were firstly investigated in this study because OA in the knee joint is more sensitive to joint functional alterations in the frontal plane than in the sagittal plane [15–19]. In contrast to the AP component of the joint force, the ML component increased with OA. Because the direction of the ML component from medial to lateral corresponds to adduction moment in the knee, this result could explain why the adduction moment was higher in OA patients than in asymptomatic subjects [16–18].

The results indicated that EFAR and EFTR were higher in OA patients than in control subjects. Several previous studies reported 1.5–2.3 folds higher antagonistic cocontractions in OA patients than in normal subjects based on EMG measurements [3, 5, 9]. The muscle forces and torques generated by muscles in OA patients were similar to those in the asymptomatic group for flexor muscles, but much higher for extensor muscles. Given that the EFAR and EFTR indicate the level of cocontraction between the flexor and extensor muscle groups, the increase in both ratios is consistent with the experimental results. Because a biomechanical parameter has not been defined to reflect the level of co-contraction between several muscle groups the knee joint, for example, the quadriceps and hamstrings, the EFAR and EFTR may be used as indices of co-contraction. Significant differences in the EFAR and EFTR between OA patients and asymptomatic subjects indicate that these ratios can be applied to diagnose OA patients and analyze their kinematic and dynamic patterns.

There are several limitations and restrictions to this study. Anatomical information such as mass, center of gravity, moment of inertia, muscle attachment points, PCSA of the muscle, and maximum muscle forces was obtained from

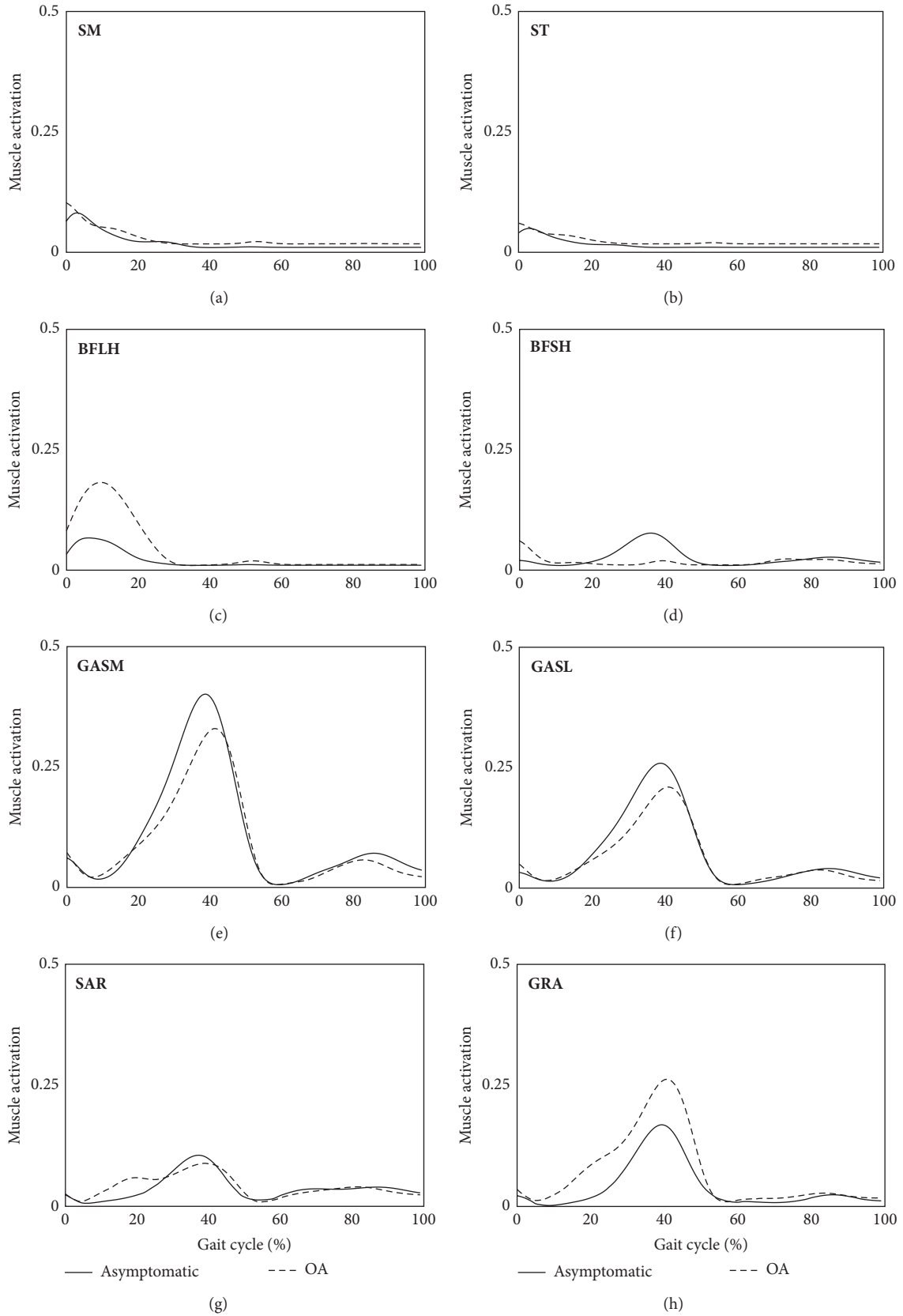


FIGURE 5: Knee flexor muscle forces for OA patients and asymptomatic subjects during a gait cycle, where the muscle forces were averaged in both groups and scaled to each muscle's maximum isometric force (SM, semimembranosus; ST, semitendinosus; BFLH, biceps femoris long head; BFSH, biceps femoris short head; GASM, gastrocnemius medialis; GASL, gastrocnemius lateralis; SAR, sartorius; GRA, gracilis).

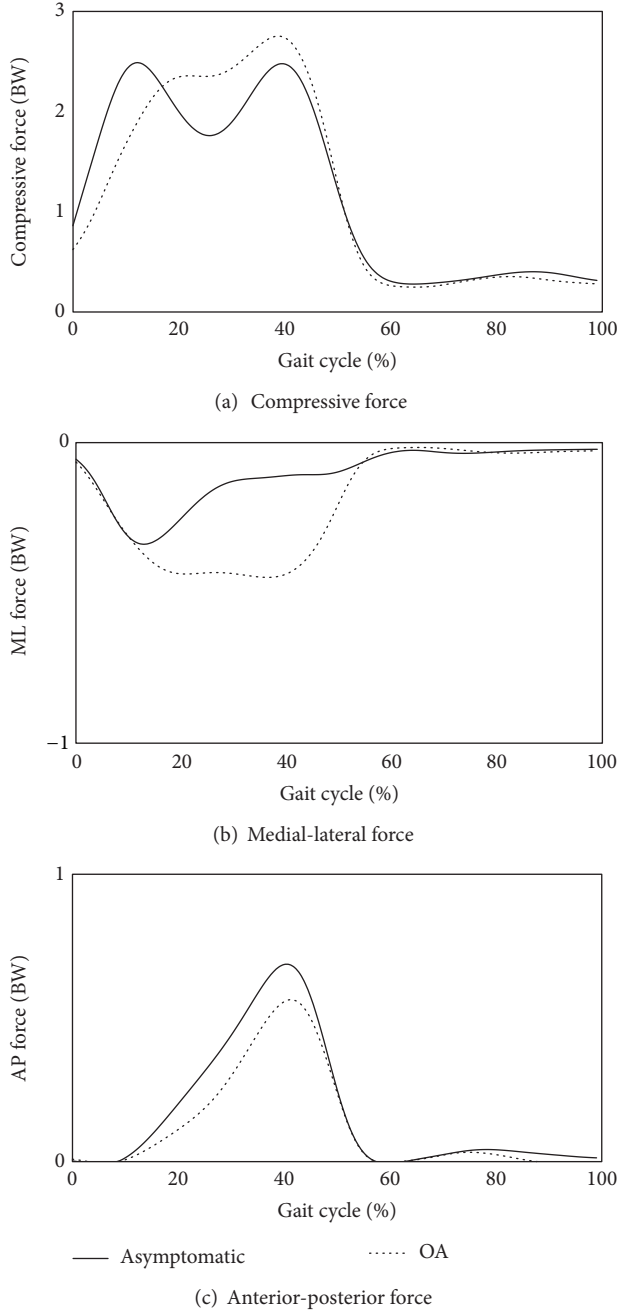


FIGURE 6: Predicted knee joint forces: (a) compressive forces (positive, tensile force; negative, compressive force), (b) medial-lateral forces (positive, medial; negative, lateral), and (c) anterior-posterior forces (positive, posterior; negative, anterior) of OA patients and asymptomatic subjects, where the joint forces were averaged in both groups and scaled to each subject’s body weight (BW).

the literature and scaled based on the weight and height of subjects, because subject-specific information is difficult to obtain. In addition, only one type of objective function was utilized in this study to compute muscle forces. Parametric studies to determine the sensitivity of the model to anatomical information as well as the optimization scheme used would enhance the reliability of the analysis.

TABLE 1: The mean \pm standard deviation and P values of independent sample t -test between OA and asymptomatic groups in mean muscle forces and peak 3D knee joint forces as well as mean knee extensor/flexor muscle forces, torques, and ratios (EFAR and EFTR), where the muscle forces and the joint forces were normalized to the maximum isometric muscle forces and the body weight (BW), respectively.

	OA ($n = 11$)	Asymptomatic ($n = 10$)	P value
Mean muscle forces			
VINT	0.051 \pm 0.020	0.020 \pm 0.005	0.001*
VLAT	0.140 \pm 0.070	0.057 \pm 0.016	0.002*
VMED	0.130 \pm 0.065	0.051 \pm 0.014	0.002*
RF	0.220 \pm 0.110	0.100 \pm 0.047	0.006*
SM	0.027 \pm 0.016	0.020 \pm 0.010	0.230
ST	0.022 \pm 0.012	0.015 \pm 0.005	0.095
BFLH	0.043 \pm 0.012	0.020 \pm 0.008	<0.001*
BFSH	0.016 \pm 0.004	0.025 \pm 0.011	0.033*
GASM	0.088 \pm 0.022	0.110 \pm 0.025	0.053
GASL	0.064 \pm 0.010	0.072 \pm 0.019	0.300
SAR	0.028 \pm 0.014	0.038 \pm 0.015	0.170
GRA	0.069 \pm 0.026	0.039 \pm 0.017	0.006*
Peak 3D knee joint forces (BW)			
Compressive force	2.72 \pm 0.21	2.47 \pm 0.21	0.047*
ML shear force	0.43 \pm 0.03	0.10 \pm 0.01	0.001*
AP shear force	0.55 \pm 0.12	0.70 \pm 0.04	0.140
Mean extensor/flexor values			
Flexor activation	0.05 \pm 0.02	0.05 \pm 0.01	0.250
Flexor torque	0.22 \pm 0.07	0.28 \pm 0.03	0.057
Extensor activation	0.13 \pm 0.05	0.05 \pm 0.01	0.026*
Extensor torque	0.25 \pm 0.08	0.19 \pm 0.04	0.043*
EFAR	3.67 \pm 1.14	2.00 \pm 0.63	0.040*
EFTR	1.82 \pm 0.40	1.27 \pm 0.34	0.048*

*Significant differences between the OA patients and the asymptomatic group ($P < 0.05$).

5. Conclusions

Inverse dynamic analysis and an optimization technique were applied to a lower extremity model with motion capture data to compare biomechanical parameters between OA patients and normal healthy subjects. OA patients had higher extensor muscle forces and lateral component of the knee joint force than normal subjects. Force and torque ratios of extensor and flexor muscles (EFAR and EFTR), which indicate the level of antagonistic cocontraction, were substantially higher in OA patients than in normal subjects. The presented findings and technologies provide insight into biomechanical changes in

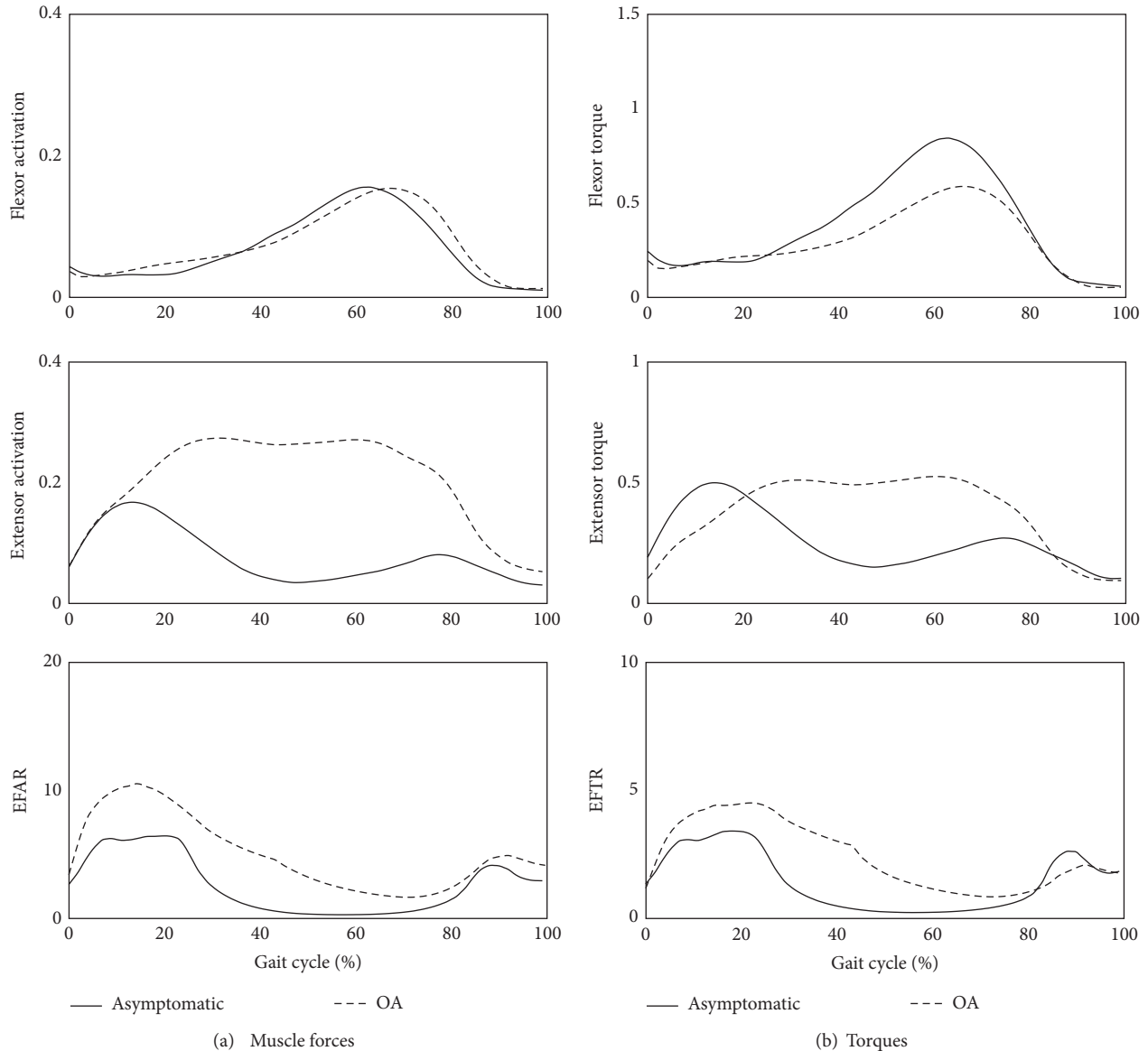


FIGURE 7: Comparison of (a) muscle forces of flexor and extensor muscle groups and EFAR and (b) torques generated by flexor and extensor muscle groups and EFTR between OA patients and asymptomatic subjects during a gait cycle, where the values were averaged in both groups.

OA patients and can also be used to evaluate the postoperative functional outcomes of the OA treatments.

Acknowledgment

This paper is supported by a 2011 Inje University research grant.

References

- [1] R. Altman, E. Asch, D. Bloch et al., "Development of criteria for the classification and reporting of osteoarthritis: classification of osteoarthritis of the knee. Diagnostic and Therapeutic Criteria Committee of the American Rheumatism Association," *Arthritis and Rheumatism*, vol. 29, no. 8, pp. 1039–1049, 1986.
- [2] D. Symmons, C. Mathers, and B. Pflieger, *Global Burden of Osteoarthritis in the Year 2000*, World Health Organization, Geneva, Switzerland, 2000.
- [3] J. D. Childs, P. J. Sparto, G. K. Fitzgerald, M. Bizzini, and J. J. Irrgang, "Alterations in lower extremity movement and muscle activation patterns in individuals with knee osteoarthritis," *Clinical Biomechanics*, vol. 19, no. 1, pp. 44–49, 2004.
- [4] M. E. van Baar, J. Dekker, J. A. M. Lemmens, R. A. B. Oostendorp, and J. W. J. Bijlsma, "Pain and disability in patients with osteoarthritis of hip or knee: the relationship with articular, kinesiological, and psychological characteristics," *Journal of Rheumatology*, vol. 25, no. 1, pp. 125–133, 1998.
- [5] C. L. Hubley-Kozey, K. J. Deluzio, S. C. Landry, J. S. McNutt, and W. D. Stanish, "Neuromuscular alterations during walking in persons with moderate knee osteoarthritis," *Journal of*

- Electromyography and Kinesiology*, vol. 16, no. 4, pp. 365–378, 2006.
- [6] C. Hubley-Kozey, K. Deluzio, and M. Dunbar, “Muscle co-activation patterns during walking in those with severe knee osteoarthritis,” *Clinical Biomechanics*, vol. 23, no. 1, pp. 71–80, 2008.
- [7] J. L. Astephen, K. J. Deluzio, G. E. Caldwell, M. J. Dunbar, and C. L. Hubley-Kozey, “Gait and neuromuscular pattern changes are associated with differences in knee osteoarthritis severity levels,” *Journal of Biomechanics*, vol. 41, no. 4, pp. 868–876, 2008.
- [8] J. A. Zeni, K. Rudolph, and J. S. Higginson, “Alterations in quadriceps and hamstrings coordination in persons with medial compartment knee osteoarthritis,” *Journal of Electromyography and Kinesiology*, vol. 20, no. 1, pp. 148–154, 2010.
- [9] D. Zhao, S. A. Banks, D. D. D’Lima, C. W. Colwell Jr., and B. J. Fregly, “In vivo medial and lateral tibial loads during dynamic and high flexion activities,” *Journal of Orthopaedic Research*, vol. 25, no. 5, pp. 593–602, 2007.
- [10] D. D. D’Lima, S. Patil, N. Steklov, S. Chien, and C. W. Colwell Jr., “In vivo knee moments and shear after total knee arthroplasty,” *Journal of Biomechanics*, vol. 40, no. 1, pp. S11–S17, 2007.
- [11] A. Mündermann, C. O. Dyrby, D. D. D’Lima, C. W. Colwell Jr., and T. P. Andriacchi, “In vivo knee loading characteristics during activities of daily living as measured by an instrumented total knee replacement,” *Journal of Orthopaedic Research*, vol. 26, no. 9, pp. 1167–1172, 2008.
- [12] H. J. Kim, J. W. Fernandez, M. Akbarshahi, J. P. Walter, B. J. Fregly, and M. G. Pandy, “Evaluation of predicted knee-joint muscle forces during gait using an instrumented knee implant,” *Journal of Orthopaedic Research*, vol. 27, no. 10, pp. 1326–1331, 2009.
- [13] C. J. de Luca, “The use of surface electromyography in biomechanics,” *Journal of Applied Biomechanics*, vol. 13, no. 2, pp. 135–163, 1997.
- [14] M. J. Robon, K. L. Perell, M. Fang, and E. Guerro, “The relationship between ankle plantar flexor muscle moments and knee compressive forces in subjects with and without pain,” *Clinical Biomechanics*, vol. 15, no. 7, pp. 522–527, 2000.
- [15] A. J. Baliunas, D. E. Hurwitz, A. B. Ryals et al., “Increased knee joint loads during walking are present in subjects with knee osteoarthritis,” *Osteoarthritis and Cartilage*, vol. 10, no. 7, pp. 573–579, 2002.
- [16] S. C. Landry, K. A. McKean, C. L. Hubley-Kozey, W. D. Stanish, and K. J. Deluzio, “Knee biomechanics of moderate OA patients measured during gait at a self-selected and fast walking speed,” *Journal of Biomechanics*, vol. 40, no. 8, pp. 1754–1761, 2007.
- [17] K. J. Deluzio and J. L. Astephen, “Biomechanical features of gait waveform data associated with knee osteoarthritis. An application of principal component analysis,” *Gait and Posture*, vol. 25, no. 1, pp. 86–93, 2007.
- [18] M. A. Hunt, T. B. Birmingham, J. R. Giffin, and T. R. Jenkyn, “Associations among knee adduction moment, frontal plane ground reaction force, and lever arm during walking in patients with knee osteoarthritis,” *Journal of Biomechanics*, vol. 39, no. 12, pp. 2213–2220, 2006.
- [19] K. R. Kaufman, C. Hughes, B. F. Morrey, M. Morrey, and K.-N. An, “Gait characteristics of patients with knee osteoarthritis,” *Journal of Biomechanics*, vol. 34, no. 7, pp. 907–915, 2001.
- [20] M. Henriksen, E. B. Simonsen, T. Alkjær et al., “Increased joint loads during walking—a consequence of pain relief in knee osteoarthritis,” *Knee*, vol. 13, no. 6, pp. 445–450, 2006.
- [21] S. L. Delp, F. C. Anderson, A. S. Arnold et al., “OpenSim: open-source software to create and analyze dynamic simulations of movement,” *IEEE Transactions on Biomedical Engineering*, vol. 54, no. 11, pp. 1940–1950, 2007.
- [22] G. Wu, S. Siegler, P. Allard et al., “ISB recommendation on definitions of joint coordinate system of various joints for the reporting of human joint motion—part I: ankle, hip, and spine,” *Journal of Biomechanics*, vol. 35, no. 4, pp. 543–548, 2002.
- [23] G. Wu, F. C. T. van der Helm, H. E. J. Veeger et al., “ISB recommendation on definitions of joint coordinate systems of various joints for the reporting of human joint motion—part II: shoulder, elbow, wrist and hand,” *Journal of Biomechanics*, vol. 38, no. 5, pp. 981–992, 2005.
- [24] P. de Leva, “Adjustments to zatsiorsky-seluyanov’s segment inertia parameters,” *Journal of Biomechanics*, vol. 29, no. 9, pp. 1223–1230, 1996.
- [25] A. L. Bell, R. A. Brand, and D. R. Pedersen, “Prediction of hip joint centre location from external landmarks,” *Human Movement Science*, vol. 8, no. 1, pp. 3–16, 1989.
- [26] D. A. Winter, *Biomechanics and Motor Control of Human Movement*, John Wiley & Sons, New York, NY, USA, 4th edition, 2009.
- [27] L. Ren, R. K. Jones, and D. Howard, “Whole body inverse dynamics over a complete gait cycle based only on measured kinematics,” *Journal of Biomechanics*, vol. 41, no. 12, pp. 2750–2759, 2008.
- [28] B. Danneskiold-Samsøe, E. M. Bartels, P. M. Bülow et al., “Isokinetic and isometric muscle strength in a healthy population with special reference to age and gender,” *Acta Physiologica*, vol. 197, supplement 673, pp. 1–68, 2009.
- [29] D. J. Rutherford, C. L. Hubley-Kozey, W. D. Stanish, and M. J. Dunbar, “Neuromuscular alterations exist with knee osteoarthritis presence and severity despite walking velocity similarities,” *Clinical Biomechanics*, vol. 26, no. 4, pp. 377–383, 2011.
- [30] C. L. Hubley-Kozey, N. A. Hill, D. J. Rutherford, M. J. Dunbar, and W. D. Stanish, “Co-activation differences in lower limb muscles between asymptomatic controls and those with varying degrees of knee osteoarthritis during walking,” *Clinical Biomechanics*, vol. 24, no. 5, pp. 407–414, 2009.
- [31] S. K. Lynn and P. A. Costigan, “Effect of foot rotation on knee kinetics and hamstring activation in older adults with and without signs of knee osteoarthritis,” *Clinical Biomechanics*, vol. 23, no. 6, pp. 779–786, 2008.
- [32] C. Richards and J. S. Higginson, “Knee contact force in subjects with symmetrical OA grades: differences between OA severities,” *Journal of Biomechanics*, vol. 43, no. 13, pp. 2595–2600, 2010.

Research Article

Numerical Stability of Partitioned Approach in Fluid-Structure Interaction for a Deformable Thin-Walled Vessel

**Kelvin K. L. Wong, Pongpat Thavornpattanapong,
Sherman C. P. Cheung, and Jiyuan Tu**

School of Aerospace, Mechanical & Manufacturing Engineering, RMIT University, P.O. Box 71, Bundoora, VIC 3083, Australia

Correspondence should be addressed to Jiyuan Tu; jiyuan.tu@rmit.edu.au

Received 15 May 2013; Accepted 2 September 2013

Academic Editor: Eduardo Soudah

Copyright © 2013 Kelvin K. L. Wong et al. This is an open access article distributed under the Creative Commons Attribution License, which permits unrestricted use, distribution, and reproduction in any medium, provided the original work is properly cited.

Added-mass instability is known to be an important issue in the partitioned approach for fluid-structure interaction (FSI) solvers. Despite the implementation of the implicit approach, convergence of solution can be difficult to achieve. Relaxation may be applied to improve this implicitness of the partitioned algorithm, but this commonly leads to a significant increase in computational time. This is because the critical relaxation factor that allows stability of the coupling tends to be impractically small. In this study, a mathematical analysis for optimizing numerical performance based on different time integration schemes that pertain to both the fluid and solid accelerations is presented. The aim is to determine the most efficient configuration for the FSI architecture. Both theoretical and numerical results suggest that the choice of time integration schemes has a significant influence on the stability of FSI coupling. This concludes that, in addition to material and its geometric properties, the choice of time integration schemes is important in determining the stability of the numerical computation. A proper selection of the associated parameters can improve performance considerably by influencing the condition of coupling stability.

1. Introduction

Fluid-structure interaction (FSI) is used widely in biomechanical computer simulations. The modelling of pulsatile blood flow in elastic vessels requires a framework that can handle the blood-vessel interaction, and the implementation of FSI can solve the time dependent biofluid flow through its elastic structure. Useful information such as the severity of vessel damage by abnormal flow, degree of plaque growth or risk of its rupture in diseased arteries, and the aggravation of atherosclerosis can be generated for medical evaluation. In general, FSI is an architecture processing the interaction of a solid structure with a dynamic fluid that can be implemented by the monolithic and partitioned approaches. A configured FSI solver can use the former approach to solve a system of governing equations for the fluid and solid domains [1]. Although FSI gives strong coupling between the two domains, the limitations are as follows:

(i) demanding computational power for solving a large system of equations;

(ii) need for further development of preconditioning;

(iii) lack of specialized capabilities that pertain to “legacy software” such as ABAQUS and ANSYS.

The partitioned approach is attractive due to its advantage of having software modularity that allows selection of an appropriate solver among the well-established solvers for each of the domains. Nevertheless, its efficiency is inferior to its monolithic counterpart due to the existence of an “added-mass instability,” which commonly occurs in problems involving large deformation and light weight structure. This causes divergence and failure before the final solution can be achieved. In order to handle this issue, small values for coupling relaxation factors of interface loads must be used in order to maintain stability. However, that will lead to a significant increase in computational time. As such, much work has been performed to search for techniques that can deal with this instability. For example, adaptive relaxation techniques that are based on using information of earlier iterations for approximating an appropriate relaxation value

and providing stability have been employed to increase the speed of calculation [2]. It is well understood that FSI solution experiences this numerical instability when the following conditions [3] are observed:

- (i) stability of FSI solution tends to be critically severe when density ratio of fluid to solid is excessively high;
- (ii) increase in fluid viscosity leads to a decrease in stability of the FSI solver, and a corresponding increase in structural stiffness improves this stability;
- (iii) temporal discretisation schemes used for FSI calculation can influence the instability condition;
- (iv) decrease in time step size used for FSI calculation can give an earlier occurrence of its instability.

The observed behaviors of instability can be explained mathematically when conditions for stability of both explicit and implicit FSI solution of a flexible cylindrical vessel are demonstrated [4]. However, the impact of time integration schemes of the fluid and solid accelerations that is used in the FSI calculation is still not fully understood and therefore justifies the need for a thorough investigation in this paper. The aim of this work is to analyze performance of FSI using a partitioned approach based on different time integration schemes that pertain to the structural mechanics. We conduct the analysis on a simplified problem of pressure wave propagation along a flexible cylindrical vessel. Influence of the parameters relating to the FSI performance can be summarized as follows:

- (i) time integration schemes for solid and fluid accelerations;
- (ii) time step size;
- (iii) ratio of fluid to solid densities.

We explore the influence of time integration schemes on a partitioned approach for fluid-structure interaction problems by organising our work in a logical manner. In Section 2, we present a mathematical description of a simplified pressure wave propagation along a flexible cylindrical vessel, fundamental FSI conditions, and the discretization schemes used for deriving the results. Section 3 provides a mathematical analysis of the stability of implicit FSI based on the different time integration schemes that are discussed. In Section 4, numerical validations and results of the same problem (that are used in Section 3) are demonstrated in order to confirm the validity of our theoretical proofs. Finally, Section 5 summarizes the influence of the time integration schemes and the associated parameters on the stability of the FSI.

2. Mathematical Background of Fluid-Structure Interaction

2.1. Governing Equations. A simplified flexible cylindrical tube of radius r , length L , thickness h_s , density ρ_s , Young's modulus E , and Poisson's coefficient ν is chosen for our mathematical analysis. It allows our mathematical and numerical examination to be performed and provides sufficient information for conducting a realistic simulation. We define a

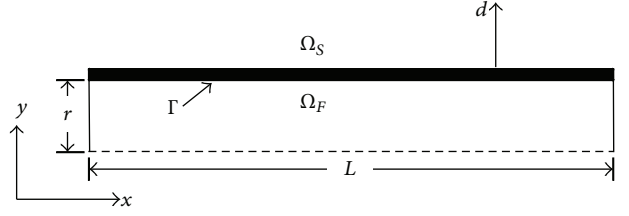


FIGURE 1: Schematic representation of the computational domain for a flexible vessel transporting fluid.

fluid domain Ω_F and a structural domain Ω_S that interact at the common boundary Γ . Deformation of cylindrical tube is allowed only in the radial and longitudinal directions. Inlet and outlet of the fluid domain are subjected to pressure boundary conditions. The schematic representation of our computational domain for a fluid through the tube is shown in Figure 1. Note that the dashed lines represent the axis of symmetry of the tube.

2.1.1. Solid Governing Equation. We refer to the governing equation of deformation for a flexible cylindrical tube in [4] as follows:

$$\rho_s h_s \frac{\partial^2 d_\Gamma}{\partial t^2} + a_0 d_\Gamma - b \frac{\partial^2 d_\Gamma}{\partial x^2} = P_\Gamma, \quad (1)$$

where $a_0 = Eh_s/r^2(1 - \nu^2)$, $b = K_T Bh_s$. Note that K_T denotes the Timoshenko shear correction factor, P_Γ is structural load on the interface Γ due to the external forcing term from the fluid, d_Γ is displacement at the interface, x is position in space, and t is position in time.

2.1.2. Fluid Governing Equations. Considering a general variable property per unit mass that is denoted as ϕ , the generic form of fluid governing equations in an Arbitrary Lagrangian-Eulerian (ALE) frame of reference is stated as

$$\underbrace{\frac{\partial \rho \phi}{\partial t}}_{\text{Temporal term}} + \underbrace{\nabla \cdot (\rho [\mathbf{v} - \mathbf{v}_c] \phi)}_{\text{Convection term}} - \underbrace{\nabla \cdot (\rho \Upsilon_\phi \nabla \phi)}_{\text{Diffusion term}} = \underbrace{S_\phi(\phi)}_{\text{Source term}}. \quad (2)$$

In the finite volume method, it is required that the governing equation is satisfied over the control volume \mathbf{V}_P around a point P . Therefore, it can be rewritten in the integral form as

$$\int_t^{t+\Delta t} \left\{ \underbrace{\frac{\partial}{\partial t} \int_{\mathbf{V}_P} \rho \phi d\mathbf{V}_P}_{\text{Temporal term}} + \underbrace{\int_{\mathbf{V}_P} \nabla \cdot \rho ([\mathbf{v} - \mathbf{v}_c] \phi) d\mathbf{V}_P}_{\text{Convection term}} - \underbrace{\int_{\mathbf{V}_P} \nabla \cdot (\rho \Upsilon_\phi \nabla \phi) d\mathbf{V}_P}_{\text{Diffusion term}} \right\} dt = \int_t^{t+\Delta t} \left\{ \underbrace{\int_{\mathbf{V}_P} S_\phi(\phi) d\mathbf{V}_P}_{\text{Source term}} \right\} dt. \quad (3)$$

2.1.3. *The Effective FSI Governing Equation.* In order to analyze stability of FSI calculation, an effective FSI governing equation can be expressed as

$$\rho_s h_s \frac{\partial^2 d_\Gamma}{\partial t^2} + a_0 d_\Gamma - b \frac{\partial^2 d_\Gamma}{\partial x^2} = P_\Gamma. \quad (4)$$

The structural load that is influenced by the fluid load $P_{\text{ext},\Gamma}$ is given by

$$P_\Gamma = P_{\text{ext},\Gamma} - \rho_f M_a \frac{\partial^2 d_\Gamma}{\partial t^2}, \quad (5)$$

where M_a denotes the added-mass operator matrix.

By coupling the two domains, we can achieve the interaction of the fluid and structure based on

$$\rho_s h_s \frac{\partial^2 d_\Gamma}{\partial t^2} + \rho_f M_a \frac{\partial^2 d_\Gamma}{\partial t^2} + a_0 d_\Gamma - b \frac{\partial^2 d_\Gamma}{\partial x^2} = P_{\text{ext},\Gamma}. \quad (6)$$

Since we are interested in studying the added-mass instability where the mass term dominates the stiffness term, some nonlinearity is neglected. This results in

$$\rho_s h_s \frac{\partial^2 d_\Gamma^s}{\partial t^2} + \rho_f M_a \frac{\partial^2 d_\Gamma^f}{\partial t^2} + a_0 d_\Gamma^s = P_{\text{ext},\Gamma}. \quad (7)$$

2.2. *Fundamental FSI Coupling Conditions.* The partitioned approach can enable the physical integration of the fluid and solid domains that is demanded by the simulation of flow through an elastic vessel. The fluid-structure interface is enforced by iteration between the structural and fluid physics modules until convergence is reached. The arbitrary mesh motion at discrete time steps can be computed by the timeintegration of the set of partial-differential equations in Section 2.1 for both the solid and fluid structures that govern the mesh motion.

The conditions required when solving FSI pertain to the kinematic and dynamic nature as suggested by numerous works (see [5] and reference therein). The kinematic condition ensures the compatibility of displacement across FSI interface and can be written as

$$d_\Gamma^f = d_\Gamma^s, \quad (8)$$

where d is displacement, d_Γ^s and d_Γ^f are the displacements of the solid and fluid interface, respectively.

Assuming that if no-slip condition is used on the fluid side of the FSI interface, this condition leads to a relationship between fluid velocity \mathbf{v}_Γ and rate of change of displacement, which can be written as

$$\hat{n} \cdot \mathbf{u}_\Gamma = \hat{n} \cdot \dot{d}_\Gamma^s. \quad (9)$$

The dynamic condition ensures the compatibility of traction across FSI interface and gives rise to

$$\hat{n} \cdot \boldsymbol{\tau}_\Gamma^s = \hat{n} \cdot \boldsymbol{\tau}_\Gamma^f, \quad (10)$$

where $\boldsymbol{\tau}_\Gamma$ represents stress on the interface.

These two conditions are normally utilized in FSI codes that adopt the partitioned approach. By implementation of the kinematic condition, fluid nodes on the FSI interface are updated according to their corresponding solid nodes. By doing the same for the dynamic condition, the equilibrium of stress on FSI interface is ensured and the fluid pressure is integrated into a fluid force, which is used in applying to the solid nodes along the interface.

2.3. Time Integration Schemes

2.3.1. *Discretization of Structural Acceleration.* The nonlinear version of the generalized- α time integration scheme that was introduced by [6] can be used for discretization of solid governing equation [7] and is given by

$$\begin{aligned} \dot{d}^{n+1} &= \dot{d}^n + [(1 - \delta) \ddot{d}^n + \delta \ddot{d}^{n+1}] \Delta t, \\ d^{n+1} &= d^n + \dot{d}^n \Delta t + \left[\left(\frac{1}{2} - \alpha \right) \ddot{d}^n + \alpha \ddot{d}^{n+1} \right] \Delta t^2, \end{aligned} \quad (11)$$

where Δt denotes the discrete time step interval.

After some mathematical manipulations, (11) can be recasted into the following equations as:

$$\begin{aligned} \dot{d}^{n+1} &= \dot{d}^n + \Delta t (1 - \delta) \ddot{d}^n + \Delta t \delta \ddot{d}^{n+1}, \\ \ddot{d}^{n+1} &= \frac{1}{\alpha \Delta t^2} (d^{n+1} + d^n) - \frac{1}{\alpha \Delta t} \dot{d}^n - \left(\frac{1}{2\alpha} - 1 \right) \ddot{d}^n. \end{aligned} \quad (12)$$

The value of structural displacement, velocity, and acceleration is interpolated between time level as

$$\begin{aligned} \ddot{d}^{n+1,\alpha} &= (1 - \alpha_m) \ddot{d}^{n+1} + \alpha_m \ddot{d}^n, \\ \dot{d}^{n+1,\alpha} &= (1 - \alpha_f) \dot{d}^{n+1} + \alpha_f \dot{d}^n, \\ d^{n+1,\alpha} &= (1 - \alpha_f) d^{n+1} + \alpha_f d^n. \end{aligned} \quad (13)$$

In order to maintain unconditional stability and second order accuracy of time integration, the following criteria must be satisfied [6]:

$$\begin{aligned} \delta &\geq \frac{1}{2}, & \alpha &\geq \frac{1}{2} \delta, & \delta &= \frac{1}{2} - \alpha_m + \alpha_f, \\ \alpha_m &\leq \alpha_f \leq \frac{1}{2}. \end{aligned} \quad (14)$$

For numerical damping, [8] suggests that these parameters can be written in terms of amplitude decay factor γ as

$$\begin{aligned} \alpha &= \frac{1}{4} (1 + \gamma)^2, & \delta &= \frac{1}{2} + \gamma, \\ \alpha_f &= 0, & \alpha_m &= -\gamma. \end{aligned} \quad (15)$$

When minimum numerical damping is applied, the values of α , δ , α_m , and α_f are set to be 1/4, 1/2, 0, and 0, respectively. These values represent time integration that has

zero numerical damping, which can be achieved by setting $\gamma = 0$. The equations for \ddot{d}^{n+1} and \dot{d}^{n+1} can be stated as

$$\begin{aligned} \dot{d}^{n+1} &= \dot{d}^n + \frac{1}{2}\Delta t \ddot{d}^n + \frac{1}{2}\Delta t \ddot{d}^{n+1}, \\ \ddot{d}^{n+1} &= \frac{4}{\Delta t^2} \left[d^{n+1} + d^n - \Delta t \dot{d}^n - \frac{\Delta t^2}{4} \ddot{d}^n \right]. \end{aligned} \quad (16)$$

After mathematical manipulation, the structural acceleration can be written in terms of deformation at different time levels as

$$\begin{aligned} \ddot{d}^{n+1,\alpha} &\approx \frac{1}{\Delta t^2} (4d^{n+1} - 16d^n + 32d^{n-1} - 20d^{n-2}) \\ &\quad - \frac{12}{\Delta t} \dot{d}^{n-2} - \ddot{d}^{n-2}. \end{aligned} \quad (17)$$

This time integration scheme cannot be put in terms of displacement only, and it has the fully recursive characteristics, which means that the calculation of time step $n + 1$ utilizes information of all previous time steps down to the initial step.

When maximum numerical damping is applied, the values of α , δ , α_m , and α_f are set to be 1, 3/2, -1, and 0, respectively. This can be achieved alternatively by setting $\gamma = 1$. Therefore, equations for \ddot{d}^{n+1} and \dot{d}^{n+1} can be written as

$$\begin{aligned} \dot{d}^{n+1} &= \dot{d}^n + \frac{1}{2}\Delta t \ddot{d}^n + \frac{3}{2}\Delta t \ddot{d}^{n+1}, \\ \ddot{d}^{n+1} &= \frac{1}{\Delta t^2} \left[d^{n+1} + d^n - \Delta t \dot{d}^n - \frac{\Delta t^2}{2} \ddot{d}^n \right]. \end{aligned} \quad (18)$$

Subsequently, this leads to

$$\ddot{d}^{n+1,\alpha} = \frac{1}{\Delta t^2} (2d^{n+1} - 5d^n + 4d^{n-1} - d^{n-2}). \quad (19)$$

2.3.2. Discretization of Fluid Acceleration. Two backward Euler schemes are used for the discretization of fluid acceleration. The first order backward Euler scheme can be written as

$$\frac{u^{n+1} - u^n}{\Delta t} = \dot{u}^{n+1}, \quad (20)$$

while the second order backward Euler scheme is

$$\frac{u^{n+1} - u^n}{\Delta t} = \frac{1}{3} \frac{u^n - u^{n-1}}{\Delta t} + \frac{2}{3} \dot{u}^{n+1}. \quad (21)$$

In this paper, only the zeroth order structural predictor is used in order to estimate the fluid deformation corresponding to structural displacement of previous time step d^n . This structural predictor can be written as

$$d_{\Gamma,P}^{n+1} = d_{\Gamma}^n. \quad (22)$$

3. Mathematical Analysis

A stability analysis of FSI calculation based on implicit coupling is presented. By adopting this implicit coupling, several iterations are needed for each time step, and relaxation is applied to maintain the stability of calculation.

3.1. Numerical Procedure of Implicit Coupling. An interface code processes the data transfer between the fluid and solid domains and mesh association across their respective processors. The following steps are used for achieving implicit coupling. Initial guess d_0^{n+1} is given and coupling iteration $m = \{0, 1, 2, 3, \dots\}$.

(1) Estimate interface deformation according to previous time or coupling step by using (22), and update the interior fluid mesh.

(2) Execute fluid solver, $F(d)$, such that

$$\tilde{P}_{m+1}^{n+1} = F(\tilde{d}_{m+1}^{n+1}). \quad (23)$$

(3) Execute solid solver, $S(P)$, such that

$$\tilde{d}_{m+1}^{n+1} = S(\tilde{P}_{m+1}^{n+1}). \quad (24)$$

(4) Apply relaxation such that

$$d_{m+1}^{n+1} = (1 - \omega) \tilde{d}_{m+1}^{n+1} + \omega d_m^{n+1}. \quad (25)$$

Note that the critical relaxation factor is denoted by ω .

(5) Check convergence. The solution is converged if the following conditions are applied:

$$\begin{aligned} r^{n+1,s} &< \varepsilon_0, & r^{n+1,s} &= d_{m+1}^{n+1} - d_m^{n+1}, \\ r^{n+1,f} &< \varepsilon_0, & r^{n+1,f} &= P_{m+1}^{n+1} - P_m^{n+1}. \end{aligned} \quad (26)$$

3.2. Stability Condition When Minimum Numerical Damping Is Applied. In this section, we discuss the analysis of explicit FSI coupling when minimum numerical damping is implemented. The discretized forms of the structural acceleration and fluid acceleration are given by

$$\begin{aligned} \ddot{d}_{\Gamma}^{n+1,s} &\approx \frac{1}{\Delta t^2} (4d_{\Gamma}^{n+1} - 16d_{\Gamma}^n + 32d_{\Gamma}^{n-1} - 20d_{\Gamma}^{n-2}) \\ &\quad - \frac{12}{\Delta t} \dot{d}_{\Gamma}^{n-2} - \ddot{d}_{\Gamma}^{n-2}, \end{aligned} \quad (27)$$

$$\ddot{d}_{\Gamma}^{n+1,f} = \frac{1}{\Delta t^2} (\tilde{d}_{\Gamma}^{n+1} - 2d_{\Gamma}^n + d_{\Gamma}^{n-1}).$$

Contrary to explicit coupling, the latest information used for calculation of FSI interface acceleration of fluid domain comes from the same time level as the one that is used for the structural acceleration. This is due to the application of relaxation factor. Then, discretization of (7) is achieved by substituting (27) to give

$$\begin{aligned} &\frac{\rho_s h_s}{\Delta t^2} \left(4\tilde{d}_{\Gamma}^{n+1} - 16d_{\Gamma}^n + 32d_{\Gamma}^{n-1} - 20d_{\Gamma}^{n-2} \right. \\ &\quad \left. - \frac{12}{\Delta t^3} \dot{d}_{\Gamma}^{n-2} - \frac{1}{\Delta t^2} \ddot{d}_{\Gamma}^{n-2} \right) \\ &\quad + \frac{\rho_f M_a}{\Delta t^2} (\tilde{d}_{\Gamma}^{n+1} - 2d_{\Gamma}^n + d_{\Gamma}^{n-1}) \\ &\quad + a_0 d_{\Gamma}^{n+1} = P_{\text{ext},\Gamma}^{n+1}. \end{aligned} \quad (28)$$

For simplification, the analysis can be done by considering only one eigenvector, \mathbf{v}_i , of solution on the interface. This is because the added-mass operator M_A is a real positive matrix. Therefore, $d_\Gamma = \Sigma d_i \mathbf{v}_i$. Notice that the added-mass operator M_A can be represented by the i th eigenvalues of M_A , μ_i . This results in

$$\begin{aligned} & \frac{\rho_s h_s}{\Delta t^2} \left(4\tilde{d}_i^{n+1} - 16d_i^n + 32d_i^{n-1} - 20d_i^{n-2} \right. \\ & \quad \left. - \frac{12}{\Delta t^3} \dot{d}_i^{n-2} - \frac{1}{\Delta t^2} \ddot{d}_i^{n-2} \right) \dots \\ & + \frac{\rho_f \mu_i}{\Delta t^2} (\tilde{d}_i^{n+1} - 2d_i^n + d_i^{n-1}) \\ & + a_0 d_i^{n+1} = \frac{\Delta t^2}{\rho_s h_s} P_{\text{ext},i}^{n+1}. \end{aligned} \quad (29)$$

By substituting (25) into (29), we obtain

$$\begin{aligned} & \frac{\rho_s h_s}{\Delta t^2} \left(\frac{4d_i^{n+1}}{\omega} - 16d_i^n + 32d_i^{n-1} - 20d_i^{n-2} \right. \\ & \quad \left. - \frac{12}{\Delta t^3} \dot{d}_i^{n-2} - \frac{1}{\Delta t^2} \ddot{d}_i^{n-2} \right) + a_0 \frac{d_{m+1,i}^{n+1}}{\omega} \dots \\ & = \left(\frac{1-\omega}{\omega} \right) \left(\frac{2\rho_s h_s}{\Delta t^2} + a_0 \right) d_{m,i}^{n+1} \\ & - \frac{\rho_f \mu_i}{\Delta t^2} (d_{m,i}^{n+1} - 2d_i^n + d_i^{n-1}) \\ & + \frac{\Delta t^2}{\rho_s h_s} P_{\text{ext},i}^{n+1}. \end{aligned} \quad (30)$$

By means of Von Neumann stability analysis [9],

$$\begin{aligned} & \frac{1}{\omega} \left(\frac{4\rho_s h_s}{\Delta t^2} + a_0 \right) d_{m+1,i}^{n+1} \\ & = \left[\left(\frac{1-\omega}{\omega} \right) \left(\frac{4\rho_s h_s}{\Delta t^2} + a_0 \right) - \frac{\rho_f \mu_i}{\Delta t^2} \right] d_{m,i}^{n+1} \dots \\ & \quad + g(d_i^n, d_i^{n-1}, d_i^{n-2}, \dot{d}_i^{n-2}, \ddot{d}_i^{n-2}, P_{\text{ext},i}^{n+1}), \\ & \frac{d_{m+1,i}^{n+1}}{d_{m,i}^{n+1}} \approx \frac{\left[((1-\omega)/\omega) (4\rho_s h_s/\Delta t^2 + a_0) - \rho_f \mu_i/\Delta t^2 \right]}{(1/\omega) (4\rho_s h_s/\Delta t^2 + a_0)} \\ & = 1 - \frac{\omega (4\rho_s h_s + a_0 \Delta t^2 + \rho_f \mu_i)}{4\rho_s h_s + a_0 \Delta t^2}. \end{aligned} \quad (31)$$

Growth factor, G

The absolute value of the growth factor has to be less than unity for the solution to be stable. That is,

$$|G| = \left| 1 - \frac{\omega (4\rho_s h_s + a_0 \Delta t^2 + \rho_f \mu_{\max})}{4\rho_s h_s + a_0 \Delta t^2} \right| < 1, \quad (32)$$

$$0 < \omega < \frac{8\rho_s h_s + 2a_0 \Delta t^2}{4\rho_s h_s + a_0 \Delta t^2 + \rho_f \mu_{\max}}. \quad (33)$$

From (33), we see that not only does the material and geometrical properties (such as fluid and solid densities, Young's modulus of the structure, and the maximum eigenvalue of added mass matrix) influence the allowable relaxation factor, but they also affect the time step size of the calculation. It can be further deduced that if the time step size is significantly small and approaches zero, (33) becomes

$$0 < \omega < \frac{8}{4 + \rho_f \mu_{\max} / \rho_s h_s}. \quad (34)$$

This means that if the time step size is sufficiently small, the Young modulus is no longer a factor that determines the criteria for stability of an implicit algorithm. Therefore, the critical value of relaxation factor converges and does not vary with a further decrease in time step size. Moreover, it can also be concluded that if $\rho_f \mu_{\max} = \rho_s h_s$, the relaxation factor has to be strictly less than 8/5 to allow convergence of solution.

3.2.1. Stability Condition When Maximum Numerical Damping Is Applied. The discretized forms of structural acceleration and fluid acceleration are

$$\begin{aligned} \ddot{d}_\Gamma^{n+1,s} &= \frac{1}{\Delta t^2} (2\tilde{d}_\Gamma^{n+1} - 5d_\Gamma^n + 4d_\Gamma^{n-1} - d_\Gamma^{n-2}), \\ \ddot{d}_\Gamma^{n+1,f} &= \frac{1}{\Delta t^2} (\tilde{d}_\Gamma^{n+1} - 2d_\Gamma^n + d_\Gamma^{n-1}). \end{aligned} \quad (35)$$

Unlike explicit coupling, the latest information used for calculation of FSI interface acceleration of fluid domain comes from the same time level as that used for structural acceleration. This is due to the application of the relaxation factor. The discretized form of (7) is achieved by substituting (35) and (45) to give

$$\begin{aligned} & \frac{\rho_s h_s}{\Delta t^2} (2\tilde{d}_\Gamma^{n+1} - 5d_\Gamma^n + 4d_\Gamma^{n-1} - d_\Gamma^{n-2}) \\ & + \frac{\rho_f M_a}{\Delta t^2} (\tilde{d}_\Gamma^{n+1} - 2d_\Gamma^n + d_\Gamma^{n-1}) + a_0 d_\Gamma^{n+1} \\ & = P_{\text{ext},\Gamma}^{n+1}, \end{aligned} \quad (36)$$

$$\begin{aligned} & \frac{\rho_s h_s}{\Delta t^2} (2\tilde{d}_i^{n+1} - 5d_i^n + 4d_i^{n-1} - d_i^{n-2}) \\ & + \frac{\rho_f \mu_i}{\Delta t^2} (\tilde{d}_i^{n+1} - 2d_i^n + d_i^{n-1}) + a_0 d_i^{n+1} \\ & = \frac{\Delta t^2}{\rho_s h_s} P_{\text{ext},i}^{n+1}. \end{aligned} \quad (37)$$

By substituting (25), (37) can be written as

$$\begin{aligned} & \frac{\rho_s h_s}{\Delta t^2} \left(\frac{2d_{m+1,i}^{n+1}}{\omega} - 5d_i^n + 4d_i^{n-1} - d_i^{n-2} \right) + a_0 \frac{d_{m+1,i}^{n+1}}{\omega} \\ & = \left(\frac{1-\omega}{\omega} \right) \left(\frac{2\rho_s h_s}{\Delta t^2} + a_0 \right) d_{m,i}^{n+1} \\ & - \frac{\rho_f \mu_i}{\Delta t^2} (d_{m,i}^{n+1} - 2d_i^n + d_i^{n-1}) + \frac{\Delta t^2}{\rho_s h_s} P_{\text{ext},i}^{n+1}, \end{aligned}$$

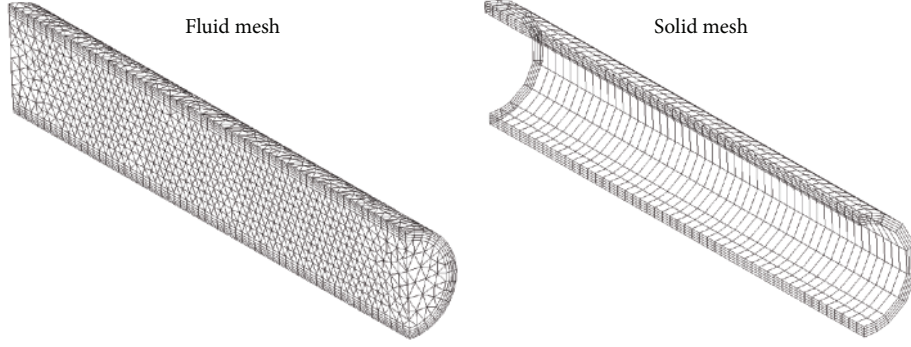


FIGURE 2: Computational meshes of the fluid and solid domains for a flexible vessel.

$$\begin{aligned}
 & \frac{1}{\omega} \left(\frac{2\rho_s h_s}{\Delta t^2} + a_0 \right) d_{m+1,i}^{n+1} \\
 &= \left[\left(\frac{1-\omega}{\omega} \right) \left(\frac{2\rho_s h_s}{\Delta t^2} + a_0 \right) - \frac{\rho_f \mu_i}{\Delta t^2} \right] d_{m,i}^{n+1} \\
 &+ g \left(d_i^n, d_i^{n-1}, d_i^{n-2}, P_{\text{ext},i}^{n+1} \right).
 \end{aligned} \tag{38}$$

By means of Von Neumann stability analysis,

$$\begin{aligned}
 \frac{d_{m+1,i}^{n+1}}{d_{m,i}^{n+1}} &\approx \frac{\left[((1-\omega)/\omega) \left(\frac{2\rho_s h_s}{\Delta t^2} + a_0 \right) - \rho_f \mu_i / \Delta t^2 \right]}{(1/\omega) \left(\frac{2\rho_s h_s}{\Delta t^2} + a_0 \right)} \\
 &= 1 - \frac{\omega \left(\frac{2\rho_s h_s}{\Delta t^2} + a_0 \Delta t^2 + \rho_f \mu_i \right)}{\frac{2\rho_s h_s}{\Delta t^2} + a_0 \Delta t^2}.
 \end{aligned} \tag{39}$$

Growth factor, G

Absolute value of the growth factor G has to be less than unity if the solution is to be stable. That is,

$$|G| = \left| 1 - \frac{\omega \left(\frac{2\rho_s h_s}{\Delta t^2} + a_0 \Delta t^2 + \rho_f \mu_{\text{max}} \right)}{\frac{2\rho_s h_s}{\Delta t^2} + a_0 \Delta t^2} \right| < 1, \tag{40}$$

$$0 < \omega < \frac{4\rho_s h_s + 2a_0 \Delta t^2}{2\rho_s h_s + a_0 \Delta t^2 + \rho_f \mu_{\text{max}}}. \tag{41}$$

From (41), the material and geometrical properties such as the densities of both the fluid and solid, Young's modulus, and eigenvalue of added-mass matrix have influence on both the allowable relaxation factor and also the time step size of the calculation. This is similar to the case when the minimum numerical damping is applied. As the time step size approaches zero, (41) becomes

$$0 < \omega < \frac{4}{2 + \rho_f \mu_{\text{max}} / \rho_s h_s}. \tag{42}$$

Here, it is proven that if time step size is very small, the Young modulus is no longer a factor determining the criteria for stability of implicit algorithm. This also means that the critical value of relaxation factor converges and does not vary with a further decrease in time step size. Moreover, it can also be concluded that if $\rho_f \mu_{\text{max}} = \rho_s h_s$, the relaxation factor has to be strictly less than $4/3$ to allow convergence of solution.

4. Numerical Results

4.1. Validation of Computational Model. Pressure pulse velocity has been widely used as an indicator of blood vessel health. In the past, only physical experiment and analytical solutions were available for obtaining the pulse velocity. Although these analytical solutions can only be used for simple geometries of blood vessel, they can serve as solid verification for numerical simulation, which are becoming popular nowadays. Therefore, a simulation of fluid-structure interaction for calculating pressure pulse velocity in a compliant vessel is conducted to verify our proposed technique in order to compare with analytical solutions such as the Moens-Korteweg equation. The results presented in this section are obtained by using the same method as that used in the next section where numerical results are presented to confirm our theoretical results.

The geometrical model of a three-dimensional tube is shown in Figure 1. The cylindrical domain has a radius of $R_s = 0.0005$ m and a total length of $L = 0.06$ m. The working fluid is modelled as incompressible fluid with fluid viscosity and density of $\mu = 0.01$ Pa·s and $\rho_f = 1,000$ kg·m³, respectively. On the other hand, the compliant vessel is modelled as isotropic material with Poisson's ratio of $\nu = 0.3$ and density of $\rho_s = 1,000$ kg·m³, respectively. Young's modulus of the solid structure is varied between $E = 50$ and 200 kPa.

Figure 2 shows the computational mesh of both solid and fluid domains that consist of 1,800 and 24,674 elements, respectively. In the fluid mesh, the laminar boundary layer has 5 layers of thin hexagonal elements, while 4 layers are used for the thickness of solid domain. The mesh in the fluid domain is Geometric Conservation Law (GCL) compliant and the architecture generates arbitrary mesh motion at discrete time steps. Now, our main aim is to validate the theoretical results.

Then, analytical sets of equations developed for pressure wave velocity are discussed next. The Moens-Korteweg equation [10, 11] is

$$c = \sqrt{\frac{E h_s}{2R_s \rho_s}}, \tag{43}$$

where c represents the pressure wave velocity.

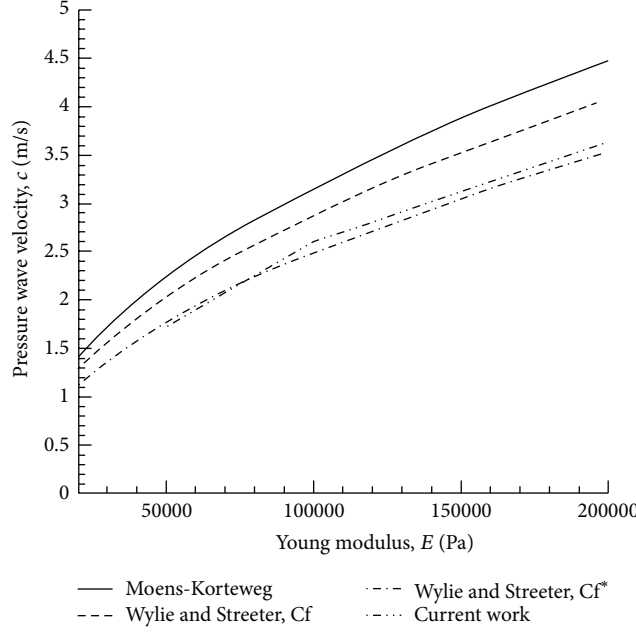


FIGURE 3: Relationship between pressure wave velocity and Young modulus of a flexible vessel.

The Wylie and Streeter equation [12] is

$$c = \varphi c_f^*, \quad (44)$$

where φ is the stress factor and c_f^* is the corrected pressure wave velocity as given by

$$\varphi = \sqrt{1 - \nu^2 \left[1 - \frac{E}{K} \left(\frac{h_s}{2r} \right) \left(1 - \frac{K\rho_f}{E\rho_s} \right) \right]^{-1}}, \quad (45)$$

$$c_f^* = \sqrt{\frac{E}{\rho_f} \left(\frac{(2R_s + 2h_s)^2}{h_s(2r + h_s)} - 2(1 - \nu) \right)^{-1}}.$$

Note that K is the bulk modulus of elasticity of the tube walls. These two equations will be utilised for the validation of numerical method used in this work. The relationship between pressure wave velocity and Young's modulus of flexible vessel illustrates adequate accuracy of the method (Figure 3).

The pressure pulse velocity is calculated by measuring the location of maximum deformation at two different times based on the sixth and eleventh millisecond. Distance between the two locations is divided by a time difference of five milliseconds in order to obtain the velocity of the pressure pulse. This location is used for the measurement as it represents the centre of the pressure wave. Figure 4 shows the contour plot of pressure wave propagation along the flexible cylindrical vessel at different Young's moduli and simulation time levels.

Next, we present a set of numerical results with different structural time integration scheme by varying the amplitude

decay factor γ . These results can be used to confirm our theoretical experiments. By our default configuration, which is used to as a reference to compare with other cases, we set vessel radius $R_s = 0.005$ m, vessel length $L = 0.06$ m, vessel thickness $h_s = 0.001$ m, solid density $\rho_s = 30,000$ kg·m³, Young's modulus $E = 750,000$ Pa, Poisson's ratio $\nu = 0.5$, fluid density $\rho_f = 1,000$ kg·m³, and fluid dynamic viscosity $\mu_f = 0.01$ Pa·s. At the initial condition, the fluid is assumed to be at rest and a pressure pulse with peak of 2,000 Pa is imposed at the inlet. The total duration of our observation T_{\max} for instability is 0.02 s. For majority of the test cases, the instability occurs at the beginning of calculation before reaching T_{\max} . In our program, the fluid acceleration is discretized by the second order accurate backward Euler scheme.

4.2. Influence of Simulation Parameters on γ versus ω Curve.

We observe a dependence of the critical relaxation factor ω on the amplitude decay factor γ . In particular, the required relaxation factors for maintaining stability become greater as the amplitude decay factor approaches zero and the structural time integration scheme becomes the average acceleration method. The numerical tests agree well with our theoretical results, and they confirm that the critical relaxation factor increases with the decrease in the structural amplitude decay factor. Moreover, it is observed that the required values of relaxation factor when using amplitude decay factor of zero can be approximately 30 percent higher than that when using amplitude decay factor of one as shown in Figure 5. By varying parameters and configurations of the FSI architecture such as (a) fluid time integration scheme, (b) time step size, and (c) fluid-solid density ratio, we can obtain information

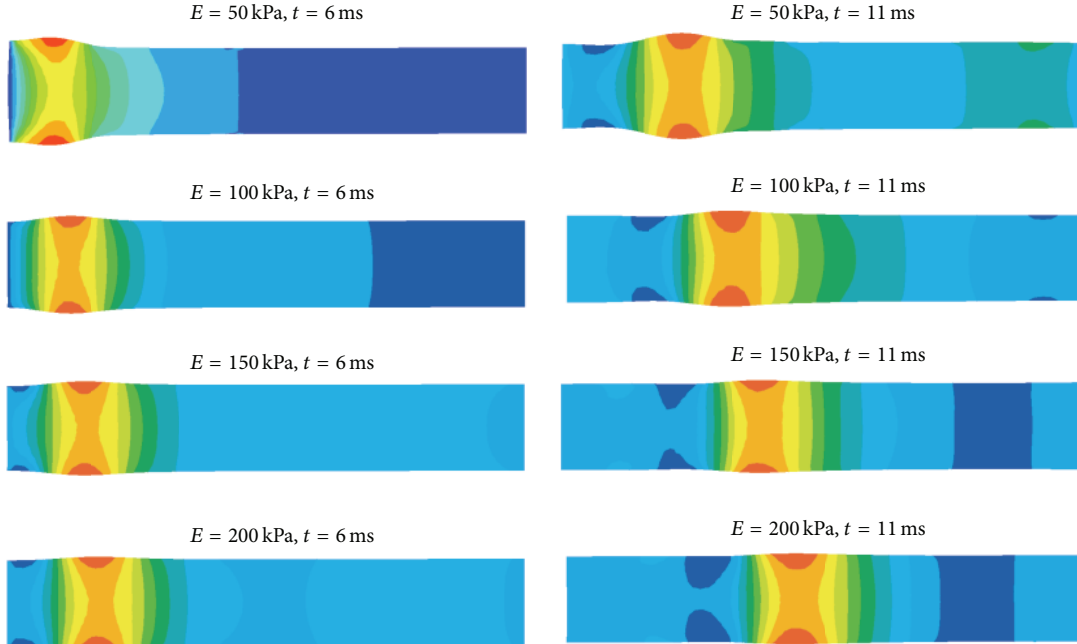


FIGURE 4: Pressure wave propagation along a flexible cylindrical vessel at various Young moduli and time levels.

on their effect on the graph of critical relaxation factor versus amplitude decay factor. For all the graphs, it can be demonstrated that the value of critical relaxation factor is inversely proportional to the value of amplitude decay factor.

First, we prove numerically the influence of the fluid time integration scheme on the FSI stability condition. By changing the discretization scheme used for fluid acceleration from the second to the first order accurate backward Euler scheme, the values of critical relaxation factor based on each value of γ increase considerably (Figure 5(a)). With $\gamma = 1$, the solution will be stable if the relaxation factor is set at lower than a conservative value of 0.7, while this threshold increases up to 0.95 when γ is set to zero.

Then, the influence of time step size on the stability of FSI calculation is tested. Here, we consider the same domain of calculation and physical parameter as before, and only time step size used for calculation is reduced from 0.001 to 0.0001 s. It is found that time step size also has considerable impact on the performance of FSI simulation. From Figure 5(b), it is shown that the values of critical relaxation factor corresponding with various values of amplitude decay factor decrease considerably when time step size is reduced. Moreover, when the time step size is further reduced to 0.00001 s, the change in critical relaxation factor remains almost unchanged. This observation agrees well with our theoretical results that when the time step size approaches zero, the value of critical relaxation factor converges as presented in Figure 5(b).

The influence of the fluid and solid structure densities on the performance of FSI calculation is considered next. The relationship between fluid-solid density ratio and the critical relaxation factor is based on different values of amplitude

decay factor. Figure 5(c) illustrates the impact that the density ratio has on variation of critical relaxation factor, which is observed to be high only when the density ratio is relatively small. Its gradient tends to vanish as we increase the density ratio value. For fluid-solid density ratio of 0.033, the variation of the critical relaxation factor in the range of $\gamma = 0$ to 1 is considerably high, while it is negligible at a density ratio of 1.

5. Conclusion

We summarize that the stability condition of FSI solution can be influenced significantly by the material densities and the relaxation factor to be implemented. Its computational cost can be greatly reduced by implementation of an appropriate structural time integration scheme. In particular, the critical relaxation factor is higher when using the structural time integration scheme that does not contain numerical damping. Furthermore, the choice of time integration schemes for discretizing fluid acceleration has a strong impact on the stability condition. Our results suggest that more accurate schemes such as the second order accurate backward Euler can lead to a more stringent condition for the stability of FSI. Another important parameter is the time step size. Then, smaller time step size results in a more restrictive condition, and as the time step size approaches zero, the value of the critical relaxation factor converges to a specific value. Another factor worth mentioning is the density ratio of fluid to solid structure. It is found that this value has a considerable impact on FSI performance, and the stability condition is invariant to the choice of structural time integration schemes in the case of high fluid-solid density ratios. However, for

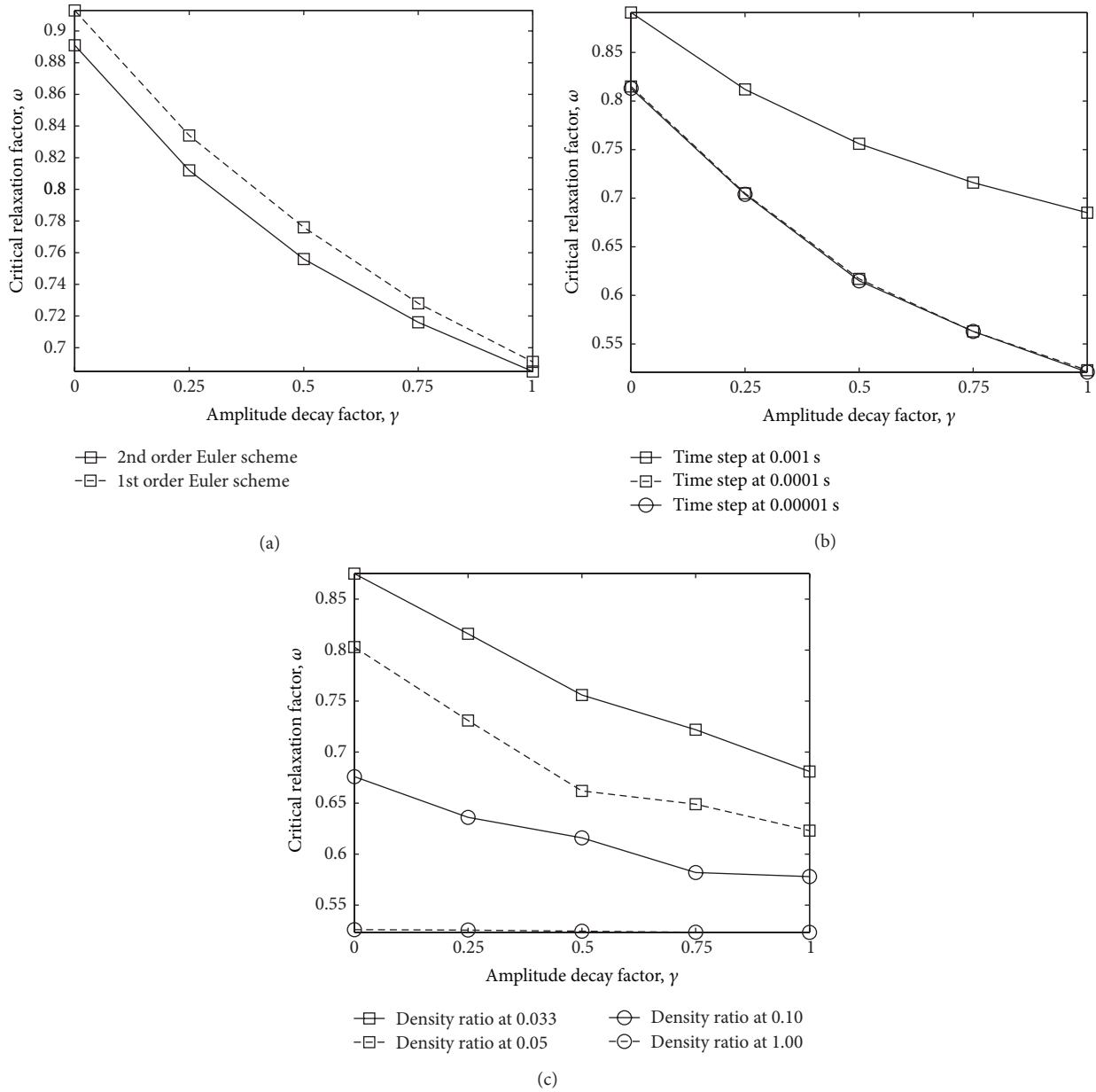


FIGURE 5: Influence of amplitude decay factor on the critical relaxation factor based on (a) fluid time integration scheme; (b) time step size; and (c) fluid-solid density ratio.

the low density ratios, this value will mainly depend on the schemes used.

References

- [1] J. Hron and S. Turek, "A monolithic FEM/multigrid solver for ALE formulation of fluid structure interaction with application in biomechanics," in *Fluid-Structure Interaction: Modelling, Simulation, Optimisation*, vol. 53, pp. 146–170, Springer, Berlin, Germany, 2006.
- [2] U. Küttler and W. A. Wall, "Fixed-point fluid-structure interaction solvers with dynamic relaxation," *Computational Mechanics*, vol. 43, no. 1, pp. 61–72, 2008.
- [3] C. Förster, W. A. Wall, and E. Ramm, "Artificial added mass instabilities in sequential staggered coupling of nonlinear structures and incompressible viscous flows," *Computer Methods in Applied Mechanics and Engineering*, vol. 196, no. 7, pp. 1278–1293, 2007.
- [4] P. Causin, J. F. Gerbeau, and F. Nobile, "Added-mass effect in the design of partitioned algorithms for fluid-structure problems," *Computer Methods in Applied Mechanics and Engineering*, vol. 194, no. 42–44, pp. 4506–4527, 2005.
- [5] W. Q. Wang and Y. Yan, "Strongly coupling of partitioned fluid-solid interaction solvers using reduced-order models," *Applied Mathematical Modelling*, vol. 34, no. 12, pp. 3817–3830, 2010.
- [6] J. Chung and G. M. Hulbert, "A time integration algorithm for structural dynamics with improved numerical dissipation: the

- generalized- α method,” *Journal of Applied Mechanics*, vol. 60, no. 2, pp. 371–375, 1993.
- [7] K. Bathe, *The Finite Element Method*, Prentice-Hall, Englewood Cliffs, NJ, USA, 1996.
- [8] W. Wood, M. Bossak, and O. Zienkiewicz, “An alpha modification of newmark method,” *International Journal of Numerical Method in Engineering*, vol. 15, p. 1562, 1981.
- [9] G. Strang, *Computational Science and Engineering*, Wellesley-Cambridge Press, Wellesley, Mass, USA, 2007.
- [10] D. Korteweg, “Über die Fortpflanzungsgeschwindigkeit des Schalles in elastischen Röhren,” *Annalen der Physik*, vol. 5, no. 12, pp. 525–542, 1878.
- [11] A. Moens, *Die Pulskurve*, Brill, Leiden, The Netherlands, 1878.
- [12] E. Wylie and V. Streeter, *Fluid Transients*, FEB Press, Ann Arbor, Mich, USA, 1983.

Research Article

The Robotic Lumbar Spine: Dynamics and Feedback Linearization Control

Ernur Karadogan¹ and Robert L. Williams II²

¹ Mechanical Engineering Department, University of Texas-Pan American, Edinburg, TX 78539, USA

² Mechanical Engineering Department, Ohio University, Athens, OH 45701, USA

Correspondence should be addressed to Robert L. Williams II; williar4@ohio.edu

Received 19 June 2013; Accepted 2 August 2013

Academic Editor: Zhonghua Sun

Copyright © 2013 E. Karadogan and R. L. Williams II. This is an open access article distributed under the Creative Commons Attribution License, which permits unrestricted use, distribution, and reproduction in any medium, provided the original work is properly cited.

The robotic lumbar spine (RLS) is a 15 degree-of-freedom, fully cable-actuated robotic lumbar spine which can mimic *in vivo* human lumbar spine movements to provide better hands-on training for medical students. The design incorporates five active lumbar vertebrae and the sacrum, with dimensions of an average adult human spine. It is actuated by 20 cables connected to electric motors. Every vertebra is connected to the neighboring vertebrae by spherical joints. Medical schools can benefit from a tool, system, or method that will help instructors train students and assess their tactile proficiency throughout their education. The robotic lumbar spine has the potential to satisfy these needs in palpatory diagnosis. Medical students will be given the opportunity to examine their own patient that can be programmed with many dysfunctions related to the lumbar spine before they start their professional lives as doctors. The robotic lumbar spine can be used to teach and test medical students in their capacity to be able to recognize normal and abnormal movement patterns of the human lumbar spine under flexion-extension, lateral bending, and axial torsion. This paper presents the dynamics and nonlinear control of the RLS. A new approach to solve for positive and nonzero cable tensions that are also continuous in time is introduced.

1. Introduction

Teaching art of palpation to medical students is a challenging task. In institutions that teach palpatory diagnosis, it is taught by using voluntary human patients who are mostly palpated by the instructor for demonstrative purposes. Meanwhile, the students usually watch the process and get to palpate only their lab partners as “patients” who are, considering the general population of medical students, relatively young and healthy (many with limited dysfunctions). It is, however, very difficult to be able to find and demonstrate a different patient for every single dysfunction that the students are taught during the lectures or in the laboratories. Therefore, it is still hard to teach and learn palpatory diagnosis for different variations of dysfunctions. The lack of a means for evaluating the transfer of practical information from the instructor to the students is another drawback that the medical schools are facing today. There exists no assessment device for instructors to objectively evaluate progress and success of the students in real-life situations.

The need for a “gold standard” to objectively assess the palpation accuracy is apparent. The design of such a device has the potential of becoming a standardized means for training medical students since the repeatability of many dysfunctions would be possible. Repeatability is a main concern in real-life medical education situations, because the properties of human soft tissue (stiffness, tenderness, etc.) can alter when it is touched by the examiner. The tissue properties are not the same even between the beginning and end of an examination. A legitimate method of evaluating the students would be comparing the first diagnosis of the instructor with the diagnosis of the student. However, when the student takes over the patient, he/she tries to diagnose movement patterns and/or the tissue properties that have already been changed due to the stimulation of the instructor.

The role of simulation in medical education is rapidly increasing. The simulations to train nurses, veterinarians, and doctors (osteopathic and allopathic) have been and are still being developed due to their effectiveness and cost-reducing advantages. These simulations can be computer based or in

the form of mannequins that can simulate some functions of the real human body such as breathing and blood pressure. Computer-based haptic simulations require the utilization of a haptic interface to interact with the virtual objects inside a computer screen. That is clearly not the case when humans really interact with real objects. For instance, the VHB [1], the only simulation that is being used to improve palpatory skills of medical students, simulates somatic dysfunctions by increased stiffness of an area on the virtual back and the users “touch” the back with PHANToM haptic devices which only stimulate the proprioceptive receptors and introduces an extra layer of disturbance between the fingers and the computer-generated objects to be sensed. Therefore, a simulation system which allows the user to interact with a real object would be a better and more effective approach.

The robotic spine concept has been studied over the past years [2–4]. These studies built humanoid robots with a flexible spine which would enhance the human-like movements of the robots and increase the range of movement of the robot’s torso. These humanoid robots dealt with the movement of the whole spine, rather than the relative position and stiffness of a vertebra with respect to the adjacent ones. They sufficiently accomplished flexible spine movements with less than the total number of vertebrae in a human spine. However, no research has yet been completed on the subject of developing a robotic spine with anatomically accurate vertebrae geometry and movements for tactile medical education and/or proficiency assessment. In this paper, the dynamic model of a robotic lumbar spine is derived and used in designing a nonlinear controller. A new method to solve for positive and nonzero cable tensions that are also continuous in time is introduced. Simulations to test the controller for the RLS are presented. In the RLS, individual vertebra is controlled by four cables that are attached to four motors. In this case, a cable-actuated robot is practical due to the space limitations between vertebrae. The robot will be controlled by a joystick or autonomously by preprogramming. The user will interact by touching the posterior aspect of the lumbar spine that is covered with a skin-like material. The user will try to find the type and region of the dysfunction by comparing the movement patterns at different configurations of the robotic lumbar spine. In this current form, the RLS will be capable of training users in terms of healthy and dysfunctional movements of the lumbar spine. Addition of the capability to adjust (rotational) stiffness of the vertebrae associated with normal and abnormal rotational limits is also underway. This will enable users to train on anatomically normal (abnormal) movement patterns as well as feel normal (abnormal) joint stiffness associated with a healthy (dysfunctional) lumbar spine.

2. Construction of the Lumbar Spine Geometry

The geometry of the lumbar spine was constructed using dimensions of an average human spine based on published experimental data [5]. All parameters used for the reconstruction of the geometry except for the facet plane and facet plane angle (ϕ) have been previously used in the literature and measured to define the morphology of the vertebrae.

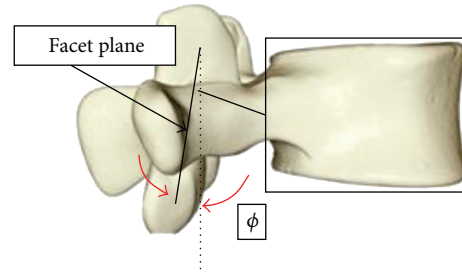


FIGURE 1: Facet plane and angle.

We, assuming sagittal symmetry, define a facet plane as the plane that connects the centers of the four facets (left/right, superior/inferior) of a vertebra. This plane (manufactured as a plate) will allow the attachment of posterior elements with various dimensions on the same vertebral body making the system modular. The facet plane angle is defined to be the angle between the facet plane and the posterior wall of the vertebral body. In modeling, a cylindrical shape is assumed for the vertebral bodies. Figure 1 shows the facet plane angle and the approximation of the vertebral bodies as cylinders. The constructed lumbar spine geometry is shown Figure 2. A detailed explanation on the construction of the lumbar spine geometry can be found in [6].

3. 3D Static Model of the Human Lumbar Spine

In order to design a device that mimics an average adult’s lumbar spine, it is necessary to have anatomically correct movement patterns of each lumbar vertebra. In this study, these movement patterns were acquired by using a three-dimensional static model of the human spine. The mathematical model includes five lumbar vertebrae and the sacrum, elastic elements that connect inferior facets of one vertebra to the superior facets of the lower one and torsion springs that represent the collective torque resisting effects of the intervertebral disc and ligaments. It has been shown with several studies [5, 7–9] that the significant motion of the vertebrae during the movement of the spine is the rotational motion. Therefore, a spherical joint is chosen to connect each vertebra to the lower one. The location of this joint is critical in order to provide anatomically correct motion for each vertebra during the movement of the entire lumbar spine. In this model, the spherical joints are located at the inferoposterior corners of the vertebral bodies since the experimental data used for validation is based on the findings from [5]. The complete details including derivation and validation of this model can be found in [10].

4. RLS Kinematics

The robotic spine, shown in Figure 3, was designed based on the study by [5] since it details how lumbar spine moves in prespecified loading conditions. In that study, the uppermost vertebrae of freshly frozen cadaveric human lumbar spines with no abnormalities were exposed to external pure

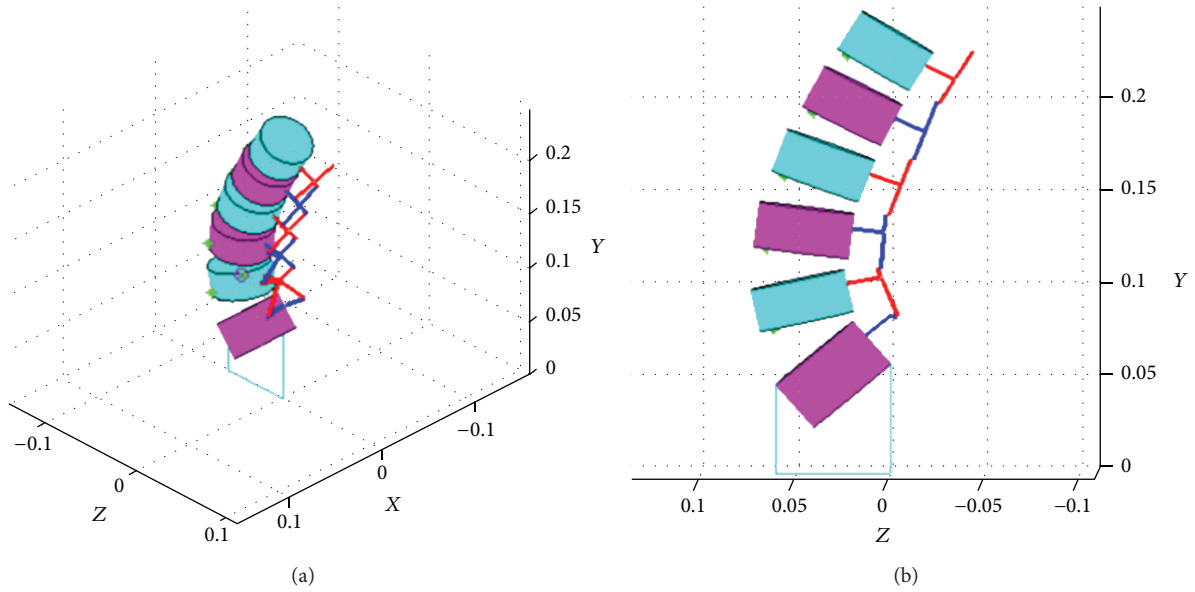


FIGURE 2: Three-dimensional geometry of the lumbar spine [6].

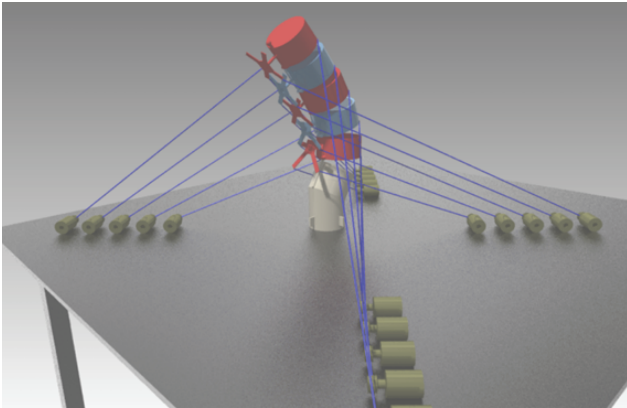


FIGURE 3: The robotic lumbar spine (RLS).

moments in order to induce motion, and both rotational and translational movements of each vertebra were recorded.

The RLS is actuated by 20 cables connected to electric motors. Every vertebra is connected to the neighboring vertebrae by spherical joints. The use of spherical joints is intentional since the rotational motion of the vertebrae is more prominent as compared to their translational motion. The location of the spherical joint for each vertebra is at the inferoposterior corner in the mid-sagittal plane of the vertebral body. These locations correspond to the origin of the coordinate frames with respect to which the angles of rotation were recorded in [5]. As discussed previously, the facet plane in Figure 1 was designed to be used as the base on which posterior elements with various dimensions can be attached.

The cable connection points on the ground are at the corners of five trapezoids. The innermost trapezoid that includes the connection points for the fifth lumbar vertebra

(L5) has posterior base length of 0.4 m, anterior base length of 0.2 m, and height of 0.15 m. The remaining four trapezoids are constructed with increasing the height of the adjacent (inner) one by 0.05 m anteriorly and 0.05 m posteriorly. This placement of the cable connections on the ground prevented cable interference during the simulations for six motion types: flexion/extension, right/left bending, and right/left axial torque [6].

5. RLS Dynamics and Control

5.1. Dynamic Model. In this section, we will develop the dynamic equations for the robotic lumbar spine. The dynamic equations can be stated in the following general format:

$$\mathbf{M}(q)\ddot{q} + \mathbf{V}(q, \dot{q}) + \mathbf{G}(q) = \boldsymbol{\tau}, \quad (1)$$

where q is the vector of generalized coordinates (joint variables), \dot{q} is the vector of generalized velocities, \mathbf{M} is the inertia matrix as a function of q , \mathbf{V} is the Coriolis/centrifugal term as a function of q and \dot{q} , \mathbf{G} is the gravity term as a function of q and $\boldsymbol{\tau}$ is the vector of generalized forces that are found by using the forces applied by the cables. Note that, for systems the links of which are actuated at the joints, $\boldsymbol{\tau}$ is independent of q when they are defined to be the joint variables (angle of rotation for revolute and distance for prismatic joints). However, as shown later in the text, $\boldsymbol{\tau}$ for the robotic lumbar spine are functions of the generalized coordinates as well. The friction is neglected during the dynamic modeling stage.

We will use the energy-based Lagrange equation to derive the equations of motion for the robotic spine. The Lagrange formulation does not require the knowledge of the constraint forces when all of the constraints in a system are *holonomic* [11]. In Newton-Euler formulation, however, the constraint forces between adjacent links must be included as variables. The robotic lumbar spine is composed of only rigid bodies

that are connected to each other via spherical joints. That is, all constraints in the system are *holonomic* constraints. The Lagrange equation can be stated as

$$\frac{d}{dt} \left(\frac{dL}{d\dot{q}} \right) - \frac{dL}{dq} = \tau, \quad (2)$$

where L is the Lagrangian and defined as the difference between the kinetic and potential energy

$$L(q, \dot{q}) = K(q, \dot{q}) - U(q). \quad (3)$$

Since the potential energy is not a function of the generalized velocities, the Lagrange equation for the i th generalized coordinate can be written as

$$\frac{d}{dt} \left(\frac{\partial K}{\partial \dot{q}_i} \right) - \frac{\partial K}{\partial q_i} + \frac{\partial U}{\partial q_i} = \tau_i. \quad (4)$$

By using the chain rule, the above equation can also be written as

$$\sum_{j=1}^n \left(\frac{d(\partial K / \partial \dot{q}_i)}{dq_j} \dot{q}_j + \frac{d(\partial K / \partial \dot{q}_i)}{d\dot{q}_j} \ddot{q}_j \right) - \frac{\partial K}{\partial q_i} + \frac{\partial U}{\partial q_i} = \tau_i, \quad (5)$$

where n is the total number of generalized coordinates.

Adapting to the general format of the dynamic equations (1), $\mathbf{M}(q)$, $\mathbf{V}(q, \dot{q})$ and $\mathbf{G}(q)$ can be deduced from (5) as:

$$\mathbf{M}(q) = \begin{bmatrix} m(q)_{11} & \cdots & m(q)_{1j} \\ \vdots & \ddots & \vdots \\ m(q)_{i1} & \cdots & m(q)_{ij} \end{bmatrix},$$

$$\mathbf{V}(q, \dot{q}) = \begin{bmatrix} v(q, \dot{q})_1 \\ \vdots \\ v(q, \dot{q})_i \end{bmatrix}, \quad (6)$$

$$\mathbf{G}(q) = \begin{bmatrix} g(q)_1 \\ \vdots \\ g(q)_i \end{bmatrix},$$

where

$$m(q)_{ij} = \frac{d(\partial K / \partial \dot{q}_i)}{d\dot{q}_j},$$

$$v(q, \dot{q})_i = \sum_{j=1}^n \left(\frac{d(\partial K / \partial \dot{q}_i)}{dq_j} \dot{q}_j \right) - \frac{\partial K}{\partial q_i}, \quad (7)$$

$$g_j(q) = \frac{\partial U}{\partial q_j} = \frac{\partial (-m_i \mathbf{g}^T {}^B T {}^i \mathbf{P}_{CGi})}{\partial q_j}$$

$$= \sum_{i=1}^{N_v} -m_i \mathbf{g}^T \frac{\partial ({}^B T)}{\partial q_j} {}^i \mathbf{P}_{CGi},$$

where m_i is the mass, ${}^B \mathbf{P}_{CGi}$ is the augmented vector involving center of gravity coordinates of the i th vertebra, $\mathbf{g} = [g_x \ g_y \ g_z \ 0]^T = [0 \ -9.806 \ 0 \ 0]^T$ is the augmented (a zero is added as the last element) gravitational acceleration since y -axis is directed upward and $[{}^B T] =$

$[{}^B T][{}^1 T] \cdots [{}^{i-1} T]$ is the 4×4 homogenous transformation matrix that represents i th vertebra coordinate system with respect to the base frame $\{B\}$. The transformation matrix of a frame with respect to the neighboring one is expressed as:

$$[{}^{i+1} T]_{4 \times 4} = \begin{bmatrix} [{}^i R]_{3 \times 3} & \{ {}^i \mathbf{P}_{(i+1)ORG} \}_{3 \times 1} \\ 0 & 1 \end{bmatrix}. \quad (8)$$

Total kinetic energy of the RLS is:

$$K = \sum_{i=1}^{N_v} {}^i K_i, \quad (9)$$

where N_v is the total number of vertebrae and ${}^i K_i$ is the kinetic energy of the i th vertebra expressed in the local vertebral frame and defined as

$${}^i K_i = \frac{1}{2} m {}^i \mathbf{V}_{G_i} \cdot {}^i \mathbf{V}_{G_i} + \frac{1}{2} {}^i \boldsymbol{\omega}_i \cdot {}^i \mathbf{H}_{G_i}, \quad (10)$$

where ${}^i \mathbf{V}_{G_i}$ is the linear velocity of the center of gravity, ${}^i \boldsymbol{\omega}_i$ is the angular velocity, ${}^i \mathbf{H}_{G_i} = {}^i \mathbf{I}_{G_i} {}^i \boldsymbol{\omega}_i$ is the angular momentum of the i th vertebra with respect to its local frame, and ${}^i \mathbf{I}_{G_i}$ is the inertia tensor.

The right hand side of (2) is composed of the generalized cable forces and the partial derivative of the potential energy with respect to joint variables (q) which is actually the gravity term, $\mathbf{G}(q)$, in the Lagrange equation. Note that $\boldsymbol{\tau}$ is the vector of generalized cable forces. The resulting generalized forces must be calculated for proper use of the Lagrange equation. The k th generalized force for the robotic lumbar spine can be written as

$$\begin{aligned} \tau_k &= \sum_{i=1}^{N_v} \sum_{j=1}^{N_c} \mathbf{t}_{ij}^T \frac{\partial ({}^B T {}^i \mathbf{P}_{ij})}{\partial q_k} \\ &= \sum_{i=1}^{N_v} \sum_{j=1}^{N_c} \mathbf{t}_{ij}^T \frac{\partial ({}^B T)}{\partial q_k} {}^i \mathbf{P}_{ij} \\ &= \sum_{i=1}^{N_v} \sum_{j=1}^{N_c} \mathbf{t}_{ij} \hat{\mathbf{L}}_{ij}^T \frac{\partial ({}^B T)}{\partial q_k} {}^i \mathbf{P}_{ij} \\ &= \mathbf{A}(q)_{15 \times 20} \{ \mathbf{t} \}_{20 \times 1}, \end{aligned} \quad (11)$$

where ${}^i \mathbf{P}_{ij}$ is the augmented position vector from the origin of the local coordinate frame of the i th vertebra to the connection point of the j th cable in $\{i\}$, $\hat{\mathbf{L}}_{ij}$ is the unit vector in the corresponding cable direction, and $[{}^B T]$ is the previously defined 4×4 homogenous transformation matrix.

5.2. Cable Tension Optimization. One of the challenges of designing a cable-actuated robot is the fact that the cables must be in tension (positive) at all times during the operation of a task. The robots with rigid links that are actuated with motors are not subject to this limitation. The RLS, being a fully cable-actuated robot, needs to be supplied with positive

cable tensions. We start with the previously derived dynamics equations (independent variables are not shown for clarity):

$$\mathbf{M}_{(m \times m)} \ddot{\mathbf{q}}_{(m \times 1)} + \mathbf{V}_{(m \times 1)} + \mathbf{G}_{(m \times 1)} = \mathbf{A}_{(m \times n)} \mathbf{t}_{(n \times 1)}, \quad (12)$$

where m is the number of degrees of freedom (=15) and n is the number of cables (=20). In order to solve for positive cable tensions we introduce an intermediate variable $\boldsymbol{\tau}_v$, which is the virtual input [12] to the system and defined as

$$\boldsymbol{\tau}_{v(n \times 1)} = \mathbf{M} \ddot{\mathbf{q}} + \mathbf{V} + \mathbf{G}. \quad (13)$$

Therefore, the dynamics equation can be written as:

$$\boldsymbol{\tau}_v = \mathbf{A} \mathbf{t}. \quad (14)$$

Equation (14) can be solved by:

$$\mathbf{t} = \mathbf{A}^+ \boldsymbol{\tau}_v + (\mathbf{I}_m - \mathbf{A}^+ \mathbf{A}) \mathbf{z}, \quad (15)$$

where $\mathbf{A}^+ = \mathbf{A}^T (\mathbf{A} \mathbf{A}^T)^{-1}$ is the Moore-Penrose pseudo-inverse of \mathbf{A} , \mathbf{I}_m is the $(m \times m)$ identity matrix, the first term on the right hand side is the particular solution and the second term is the homogenous solution which maps \mathbf{z} ($m \times 1$ vector) to the null space of \mathbf{A} . The homogenous solution can take any value making the solution nonunique. This property can be utilized to search for a solution that will generate positive cable tensions that are needed to control the RLS. On the other hand, when the homogenous solution is zero, the tensions are calculated in the least-squares sense which does not guarantee a solution that will satisfy the positive cable tensions criterion. It is also imperative to obtain positive and nonzero cable tensions in order to be able to keep the robot under control during a task. Equation (15) can also be written as [13]:

$$\mathbf{t} = \mathbf{A}^+ \boldsymbol{\tau}_v + N(\mathbf{A}) \boldsymbol{\sigma}, \quad (16)$$

where $N(\mathbf{A})$ is the $(n \times n - m)$ kernel matrix of \mathbf{A} and $\boldsymbol{\sigma}_{(n-m \times 1)} = \{\sigma_1, \sigma_2, \dots, \sigma_{n-m}\}^T$ is an arbitrary vector.

An optimization procedure can be employed with a proper objective function to solve (16) with positive and nonzero cable tensions. One of the optimization procedures is by using linear programming, which is formulated as [14]

$$\begin{aligned} \min_{\boldsymbol{\sigma}} \quad & \mathbf{f}^T \boldsymbol{\sigma}, \\ \text{such that} \quad & \mathbf{t} = \mathbf{A}^+ \boldsymbol{\tau}_v + N(\mathbf{A}) \boldsymbol{\sigma}, \\ & -N(\mathbf{A}) \boldsymbol{\sigma} \leq \mathbf{A}^+ \boldsymbol{\tau}_v - \mathbf{b}, \\ & \boldsymbol{\sigma}_l \leq \boldsymbol{\sigma} \leq \boldsymbol{\sigma}_u, \end{aligned} \quad (17)$$

where \mathbf{f} is the $(n - m \times 1)$ linear objective function vector, \mathbf{b} is the $(n \times 1)$ vector that holds minimum allowed positive tensions (lower boundary for \mathbf{t}), and $\boldsymbol{\sigma}_l$ and $\boldsymbol{\sigma}_u$ are, respectively the lower and upper boundaries for the arbitrary $\boldsymbol{\sigma}$ vector in (16). This optimization procedure, when converges to a minimum solution, produces point-wise feasible positive cable tensions that are equal or higher than the limits specified in \mathbf{b} . However, these feasible cable tensions are not

guaranteed to be continuous in time during the task. This discontinuity is not desirable since it may cause instability during real-time control of the robot. Therefore, we introduce a new optimization scheme that will result in cable tensions that are both point-wise feasible and continuous in time. The proposed optimization scheme makes use of the previous solution to be able to choose the current solution to be as close to it as possible. This scheme which minimizes the norm of the difference between the previous and current solution can be formulated as follows:

$$\begin{aligned} \min_{\boldsymbol{\sigma}_i} \quad & \|\mathbf{t}_i - \mathbf{t}_{i-1}\|, \\ \text{such that} \quad & \mathbf{t}_i = \mathbf{A}_i^+ \boldsymbol{\tau}_{vi} + N(\mathbf{A}_i) \boldsymbol{\sigma}_i, \\ & \mathbf{t}_{i-1} = \mathbf{A}_{i-1}^+ \boldsymbol{\tau}_{vi-1} + N(\mathbf{A}_{i-1}) \boldsymbol{\sigma}_{i-1}, \\ & \mathbf{t}_0 = \mathbf{b} \\ & -N(\mathbf{A}_i) \boldsymbol{\sigma} \leq \mathbf{A}_i^+ \boldsymbol{\tau}_{vi} - \mathbf{b}, \\ & \boldsymbol{\sigma}_l \leq \boldsymbol{\sigma}_i \leq \boldsymbol{\sigma}_u. \end{aligned} \quad (18)$$

In order to minimize this constrained nonlinear multivariable objective function, a numerical method can be applied. In this study, the built-in MATLAB (The MathWorks, Inc.) function *fmincon()* is used for that purpose. The effect of using the previous solution on the acquisition of positive cable tensions with the above formulation is discussed after the control problem is addressed.

5.3. Trajectory Control with Feedback Linearization. In this section, we solve the control problem for the RLS by using feedback linearization technique. Feedback linearization control, also known as computed-torque control, aims to cancel the nonlinearities of a system and reduce it to a linear system to be controlled by a linear servo law. Decomposing the controller design into model-based and servo-based portions helps solve the control problem in a more systematic way. Model-based portion contains a model of the nonlinearity and includes system parameters. Servo-based portion includes only the control law and is independent of the model-based portion and, therefore, system parameters [15]. The dynamics equation for the RLS is

$$\mathbf{M}(q) \ddot{\mathbf{q}} + \mathbf{V}(q, \dot{q}) + \mathbf{G}(q) = \boldsymbol{\tau}_v, \quad (19)$$

where $\boldsymbol{\tau}_v = \mathbf{A} \mathbf{t}$ is the virtual input to the system which was previously introduced as an intermediate variable. This virtual input is utilized to be able to find positive and nonzero cable tensions. The model-based portion of the controller is defined as

$$\boldsymbol{\tau}_v = \boldsymbol{\alpha} \boldsymbol{\tau}'_v + \boldsymbol{\beta}, \quad (20)$$

where

$$\boldsymbol{\alpha} = \mathbf{M}(q), \quad (21)$$

$$\boldsymbol{\beta} = \mathbf{V}(q, \dot{q}) + \mathbf{G}(q).$$

The servo-based portion that includes a proportional-derivative control law is

$$\boldsymbol{\tau}'_v = \ddot{\mathbf{q}}_d + \mathbf{K}_p \mathbf{e} + \mathbf{K}_d \dot{\mathbf{e}}, \quad (22)$$

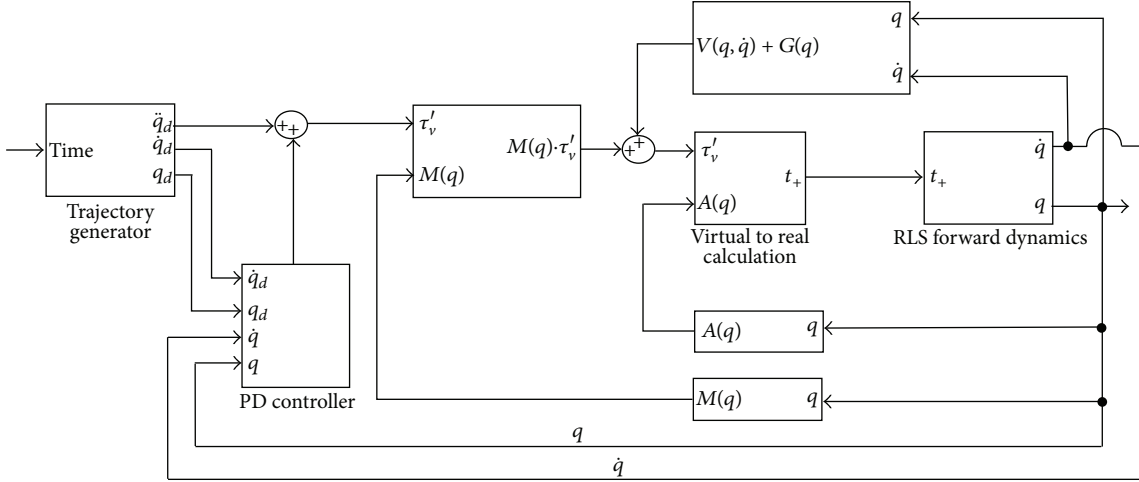


FIGURE 4: RLS controller schematic.

where $\ddot{\mathbf{q}}_d$ is the desired accelerations, \mathbf{K}_p and \mathbf{K}_d are, respectively, proportional and derivative control gain matrices. The control gains are both 15×15 and diagonal matrices which implies that the PD control law is implemented independently for each degree of freedom (i.e., angle of rotation). $\mathbf{e} = \mathbf{q}_d - \mathbf{q}$ is the servo error between desired and actual trajectories. The error dynamics of the proposed control law can be found by first plugging (22) into (20) and the resulting equation into the dynamics equation:

$$\ddot{\mathbf{q}} = \ddot{\mathbf{q}}_d + \mathbf{K}_p \mathbf{e} + \mathbf{K}_d \dot{\mathbf{e}}. \quad (23)$$

Noting that $\ddot{\mathbf{e}} = \ddot{\mathbf{q}}_d - \ddot{\mathbf{q}}$ above equation written in error space becomes

$$\ddot{\mathbf{e}} + \mathbf{K}_d \dot{\mathbf{e}} + \mathbf{K}_p \mathbf{e} = 0. \quad (24)$$

The equation above is a second-order differential equation and the coefficients now can be chosen to shape the dynamic response of the system. It should also be noted that the left-hand side of the equation must be a Hurwitz polynomial to provide a stable closed-loop response.

Controller architecture for the RLS is shown in Figure 4. It is composed of a trajectory generator, PD controller, virtual to real calculation, and the forward dynamics blocks. Trajectory generator provides the desired angles (\mathbf{q}_d) at every time step based on a quintic polynomial in order to control first and second derivatives ($\dot{\mathbf{q}}_d$, $\ddot{\mathbf{q}}_d$) of the desired angles at the beginning and end of a path segment or trajectory. These derivatives are generally set to be zero to be able to obtain smooth movement of the robot. PD controller, as discussed previously, is needed to control the robot to follow the trajectory with a diminishing error between actual and desired angles of rotation. Controller gains can be chosen to obtain desired dynamic response, and they affect the error dynamics, that is, how fast the robot can recover from an error at any given time during the task. Virtual to real calculation is necessary in order to acquire positive nonzero cable tensions (\mathbf{t}_+).

TABLE 1: Desired angles of rotation for right bending [5].

Motion segment	α ($^\circ$) [†]	β ($^\circ$) [†]	γ ($^\circ$) [†]
L5-S1	0.50	1.00	2.60
L4-L5	1.00	1.00	3.00
L3-L4	0.75	0.75	3.10
L2-L3	0.75	0.50	3.50
L1-L2	0.25	0.00	2.75

[†] α , β and γ are the angles of rotations about x -, y -, and z -axes, respectively.

The inner workings of this block were detailed previously in the section that describes the cable tension optimization.

5.4. Simulation Results. The simulations were run for six different motion types (flexion/extension, right/left lateral bendings and right/left torsions). Due to space considerations, however, the results for only (right) lateral bending motion are presented. The results for remaining motion types can be found in [10]. Lateral bending is one of the most involved motion types in terms of the existence of coupled movements. Coupled movement of vertebrae occurs when the motion to the lumbar spine is induced in one specific plane (in frontal plane for lateral bending) which causes vertebrae to move in more than one plane. The desired angles of rotations (Table 1) for the RLS are acquired from experimental data [5] which were obtained after applying 2.5 Nm pure moment about z -axis of the freshly frozen lumbosacral spine specimens. The masses of the vertebrae from L5 to L1 are 0.0125, 0.0132, 0.0123, 0.0113 and 0.0100 kg, respectively. The trajectory generator starts at 0.1 sec, and simulation is run for a total of 1.5 sec. The control gains used are 5 and 6 for \mathbf{K}_p and \mathbf{K}_d , respectively.

Figure 5 shows the commanded (desired) and actual paths followed by the RLS. The corresponding tracking errors are shown in Figure 6.

In order to test the effectiveness of the new method for solving positive continuous cable tensions, the cable

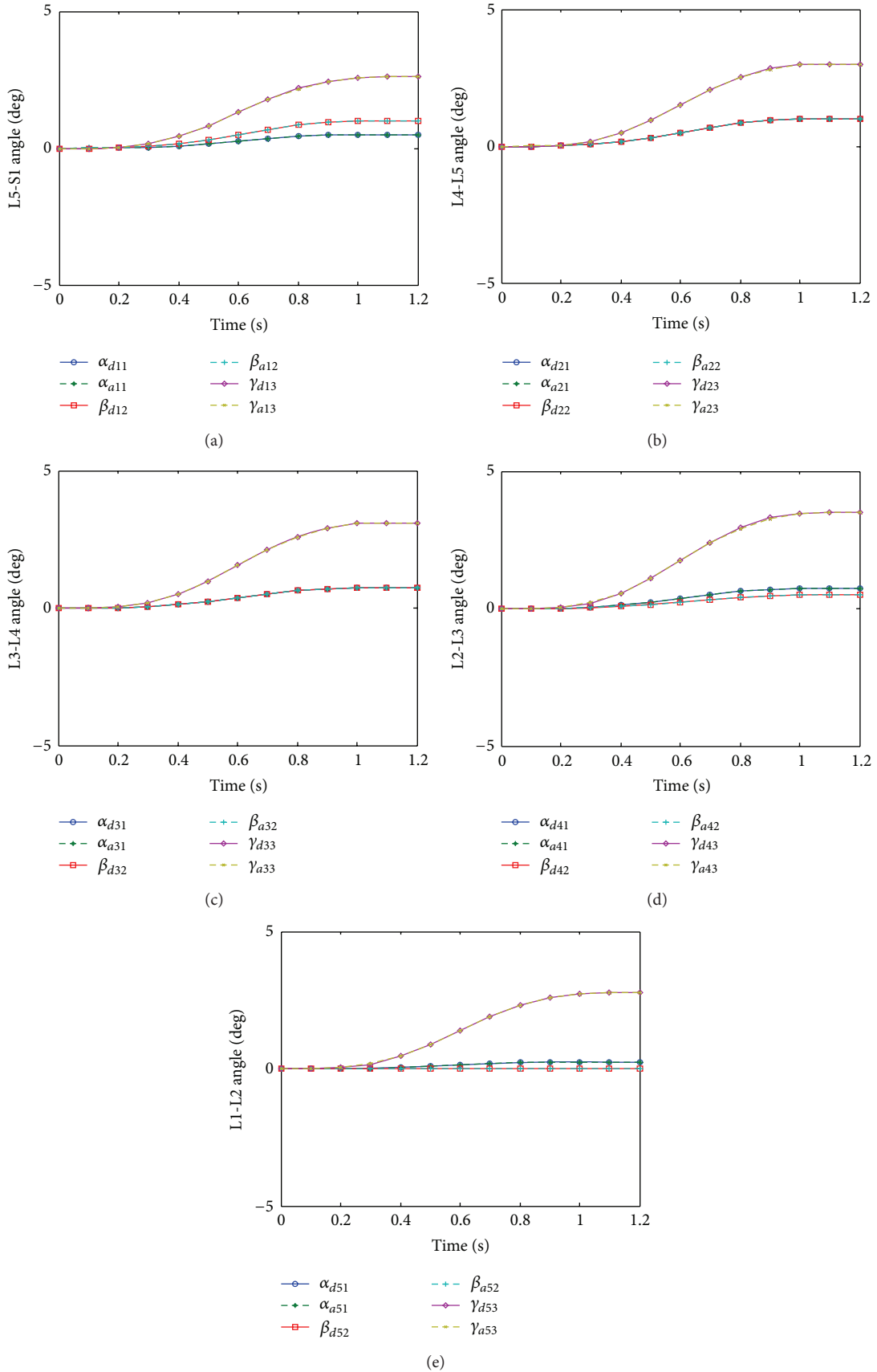


FIGURE 5: Desired and actual angles of rotations (right bending, $\alpha_d, \beta_d, \gamma_d$: desired, $\alpha_a, \beta_a, \gamma_a$: actual angles of rotation about x -, y - and z -axes, resp.).

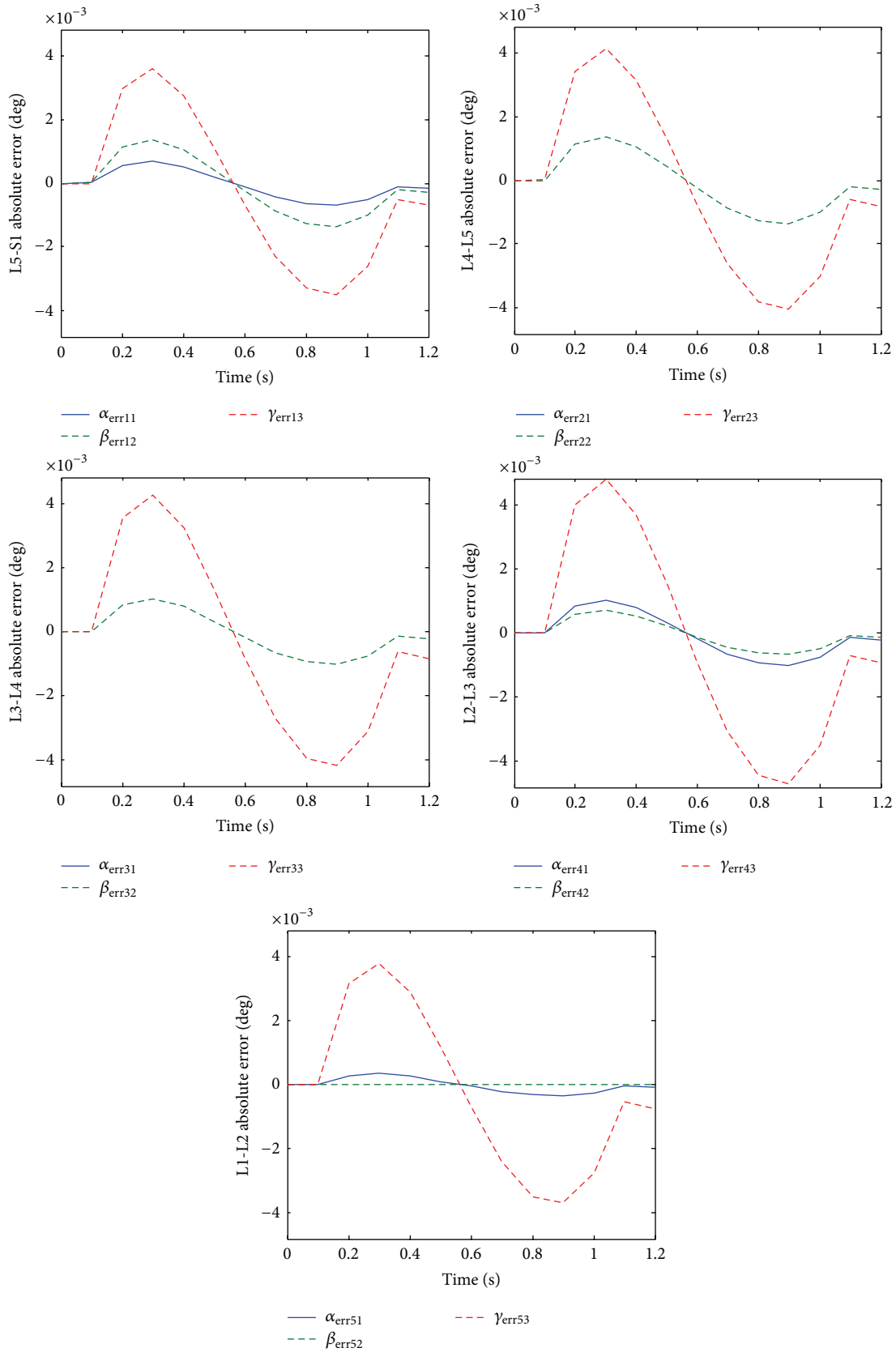


FIGURE 6: Tracking errors (right bending, $\alpha_{err} = \alpha_d - \alpha_a$, $\beta_{err} = \beta_d - \beta_a$, and $\gamma_{err} = \gamma_d - \gamma_a$).

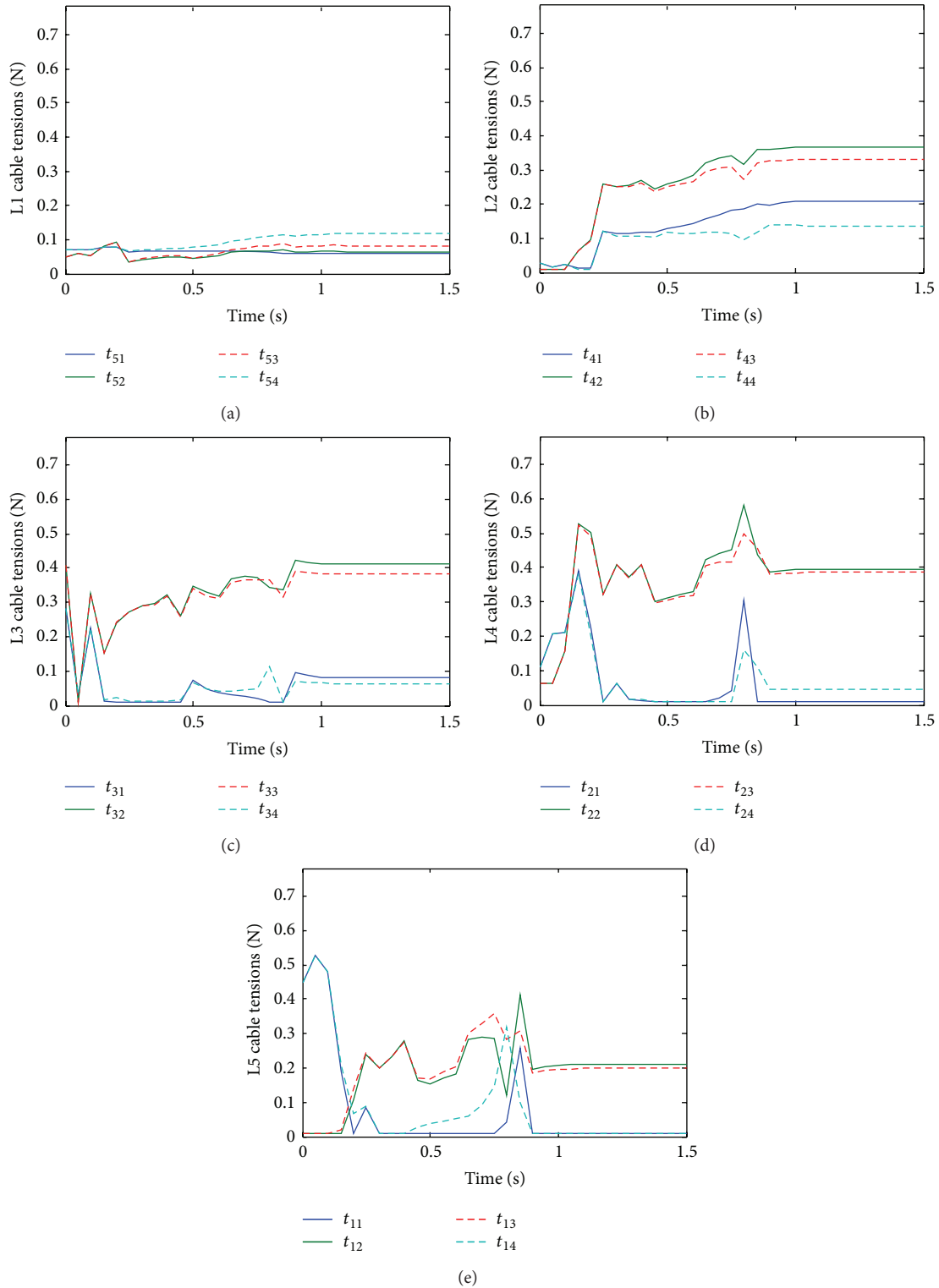


FIGURE 7: Cable tensions solved without continuity algorithm (right bending).

tensions are solved with and without implementing the proposed continuity algorithm. Figure 7 shows the cable tensions without the continuity algorithm. Even though all tensions are solved to be positive discontinuity is apparent.

Figure 8 shows the results of the simulation with the same parameters before but with the continuity algorithm. It is seen that the solved tensions are all positive and continuous in time.

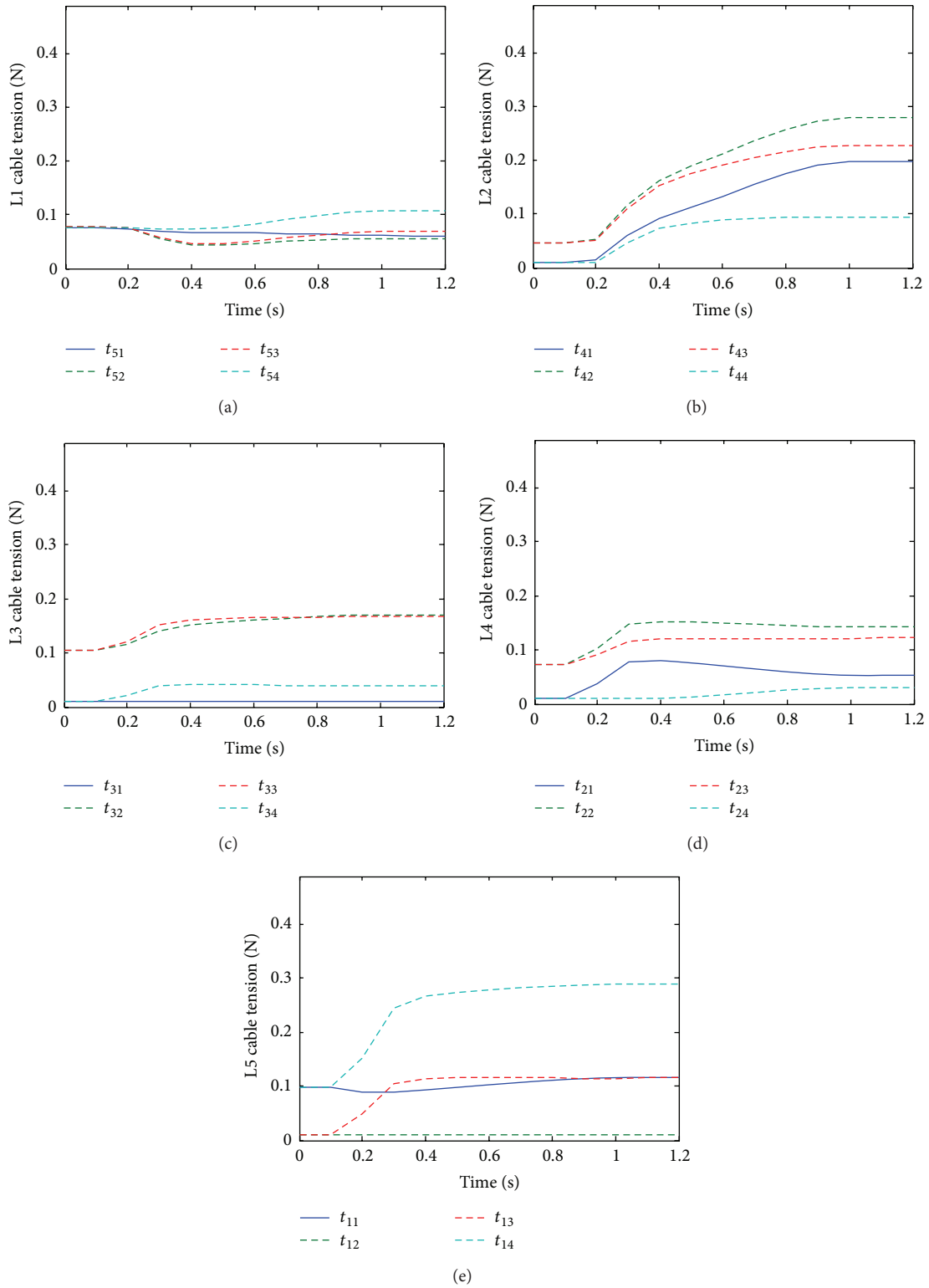


FIGURE 8: Cable tensions solved with continuity algorithm (right bending).

6. Discussion

Conceptually, the RLS was designed to support some apparent needs that the instructors and the students of institutions that teach palpatory diagnosis are currently facing. These needs can be collected under three main items:

- (1) limited variation of dysfunctions that can be practiced in a lab environment,
- (2) repeatability issues due to the inherent characteristics of tissues to change properties due to repetitive manual manipulation,
- (3) lack of an objective assessment tool to evaluate the transfer of practical knowledge from the instructor to the students.

With the RLS, there would be virtually no limit to the abnormal movement patterns to practice. These abnormal movement patterns could be programmed easily if the data are readily available, that is, if experimental data or accurate models exist. If no data are available, experience of professional experts may be utilized to generate the required data for abnormal movement patterns by trial and error until a general consensus among the experts is reached. The RLS, as any other robot, would be repeatable (to a certain degree that needs to be calculated and validated experimentally) by configuring itself correctly according to the user's input from the joystick/haptic device. As mentioned previously, there exists no assessment device for instructors to objectively evaluate progress and success of the students in real-life situations. By means of the RLS, all students can be objectively tested on identifying the normal/abnormal movement patterns of the lumbar spine. Since the RLS is also repeatable, any number of students may be tested for the same or different dysfunctions as needed.

The equations of motion were complex and highly nonlinear. This is expected due to the number of degrees of freedom considered (15 DOFs) and the actuation redundancy. Note that, for systems the links of which are actuated at the joints, τ in (1) is independent of the generalized coordinates (q) when they are defined to be the joint variables (angle of rotation for revolute and distance for prismatic joints). However, as shown in the text, τ for the robotic lumbar spine is a function of the generalized coordinates since the actuation is not performed at the spherical joints. This adds to the complexity of the equations.

The simulations for the control of the RLS showed that the tracking errors were less than 0.005 degrees for all degrees of freedom during the entire range of motion which implied that the designed controller performed as expected. The results of the simulations also showed that the new method proposed to solve for positive cable tensions was very effective in eliminating the spikes in the cable tensions. The results for all motion types, when the effect of the continuity algorithm was tested, were very similar to the results of the right lateral bending as presented here.

The RLS was designed to change configuration by a force-feedback joystick or an affordable haptic device (such as Falcon from Novint Technologies Inc.). By moving the joystick, the angles of rotations will be commanded to the RLS,

therefore representing a normal lumbar spine movement. A static model of the human lumbar spine was derived to obtain these normal movement patterns of the lumbar spine for six different types of motion. It is also planned that some abnormalities consistent with known dysfunctional movement patterns (vertebral fusion, rotational resistance of vertebra about an axis, etc.) could be mimicked based on these normal movement patterns.

7. Conclusion

The dynamic model and nonlinear control of a 15-degree-of-freedom, cable-actuated robotic lumbar spine (RLS) were presented. A new method was proposed that enables the solution of positive and continuous cable tensions for cable-actuated robots. The simulation results confirmed that the tracking errors during the simulated motion were small and the proposed continuity algorithm proved to be very effective in obtaining positive cable tensions that are also continuous in time.

References

- [1] J. N. Howell, R. R. Conatser, R. L. Williams, J. M. Burns, and D. C. Eland, "The virtual haptic back: a simulation for training in palpatory diagnosis," *BMC Medical Education*, vol. 8, article 14, 2008.
- [2] I. Mizuuchi, M. Inaba, and H. Inoue, "A flexible spine humanoid robot—development and control of the posture of the spine," in *Proceedings of the IEEE/RSJ International Conference on Intelligent Robots and Systems*, pp. 2099–2104, November 2001.
- [3] I. Mizuuchi, R. Tajima, T. Yoshikai et al., "The design and control of the flexible spine of a fully tendon-driven humanoid 'Kenta'," in *Proceedings of the IEEE/RSJ International Conference on Intelligent Robots and Systems*, pp. 2527–2532, October 2002.
- [4] L. Roos, F. Guenter, A. Guignard, and A. G. Billard, "Design of a biomimetic spine for the humanoid robot Robota," in *Proceedings of the 1st IEEE/RAS-EMBS International Conference on Biomedical Robotics and Biomechatronics, 2006 (BioRob '06)*, pp. 329–334, February 2006.
- [5] M. M. Panjabi, T. R. Oxland, I. Yamamoto, and J. J. Crisco, "Mechanical behavior of the human lumbar and lumbosacral spine as shown by three-dimensional load-displacement curves," *Journal of Bone and Joint Surgery A*, vol. 76, no. 3, pp. 413–424, 1994.
- [6] E. Karadogan and R. L. Williams II, "A cable-actuated robotic lumbar spine for palpatory training of medical students," in *Proceedings of the ASME International Design Technical Conferences, 34th Mechanisms and Robotics Conference*, pp. 309–318, Quebec, Canada, August 2010.
- [7] J. A. Sullivan, A. H. Soni, and A. G. Patwardhan, "Kinematic analysis of intervertebral motion of the human lumbar spine," Final Report, OREF, 1979.
- [8] A. H. Soni, J. A. Sullivan Jr., A. G. Patwardhan, M. R. Gudavalli, and J. Chitwood, "Kinematic analysis and simulation of vertebral motion under static load. Part I: kinematic," *Journal of Biomechanical Engineering*, vol. 102, no. 2, pp. 105–111, 1982.
- [9] M. Sharma, N. A. Langrana, and J. Rodriguez, "Modeling of facet articulation as a nonlinear moving contact problem: sensitivity study on lumbar facet response," *Journal of Biomechanical Engineering*, vol. 120, no. 1, pp. 118–125, 1998.

- [10] E. Karadogan, *A cable-actuated robotic lumbar spine as the haptic interface for palpation training of medical students [Ph.D. dissertation]*, Ohio University, Athens, Ohio, USA, 2011.
- [11] M. W. Spong, S. Hutchinson, and M. Vidyasagar, *Robot Dynamics and Control*, John Wiley & Sons, 2004.
- [12] R. L. Williams II, P. Gallina, and J. Vadia, "Planar translational cable-direct-driven robots," *Journal of Robotic Systems*, vol. 20, no. 3, pp. 107–120, 2003.
- [13] Y. Shen, H. Osumi, and T. Arai, "Manipulability measures for multi-wire driven parallel mechanisms," in *Proceedings of the IEEE International Conference on Industrial Technology*, pp. 550–554, 1994.
- [14] K. Yu, L.-F. Lee, and V. N. Krovi, "Simultaneous trajectory tracking and stiffness control of cable actuated parallel manipulator," in *Proceedings of the ASME International Design Engineering Technical Conferences and Computers and Information in Engineering Conference (IDETC/CIE '09)*, pp. 55–63, September 2009.
- [15] J. Craig, *Introduction to Robotics: Mechanics and Control*, Addison-Wesley, 1989.

Research Article

Analytical Solutions for the Mathematical Model Describing the Formation of Liver Zones via Adomian's Method

Abdelhalim Ebaid

Department of Mathematics, Faculty of Science, University of Tabuk, P.O. Box 741, Tabuk 71491, Saudi Arabia

Correspondence should be addressed to Abdelhalim Ebaid; aebaid@ut.edu.sa

Received 27 May 2013; Revised 30 June 2013; Accepted 15 July 2013

Academic Editor: Eddie Ng

Copyright © 2013 Abdelhalim Ebaid. This is an open access article distributed under the Creative Commons Attribution License, which permits unrestricted use, distribution, and reproduction in any medium, provided the original work is properly cited.

The formation of liver zones is modeled by a system of two integropartial differential equations. In this research, we introduce the mathematical formulation of these integro-partial differential equations obtained by Bass et al. in 1987. For better understanding of this mathematical formulation, we present a medical introduction for the liver in order to make the formulation as clear as possible. In applied mathematics, the Adomian decomposition method is an effective procedure to obtain analytic and approximate solutions for different types of operator equations. This Adomian decomposition method is used in this work to solve the proposed model analytically. The stationary solutions (as time tends to infinity) are also obtained through it, which are in full agreement with those obtained by Bass et al. in 1987.

1. Introduction

The dark-red liver is the body's largest single gland (1 to 1.5 kg). It is a metabolic middleman because it takes up and secretes more than 500 different kinds of molecules. The liver stores and releases glucose, keeping blood glucose levels relatively constant. The location of the liver reflects its middleman's role (Figure 1). The gland lies between the diaphragm above and the stomach and intestines below (Figure 2). Glucose and many other molecules enter the liver through the hepatic portal vein, and their products go directly through the inferior vena cava to the heart and lungs and then into the systemic circulation. The liver takes its dome-like shape from the diaphragm, which covers its superior surface, called diaphragmatic surface. The sagittal fossa divides the liver into two great lobes, right and left. The right lobe is larger and displays two smaller quadrate and caudate lobes on its visceral surface, defined by gallbladder and inferior vena cava, respectively [1]. The hepatic veins drain into the inferior vena cava arising from the posterior part of diaphragmatic surface of the liver. Visceral peritoneum binds the liver to the diaphragm and to the posterior wall of the abdomen.

Although there is an extensive bare area on the diaphragmatic surface of the liver where the peritoneum does not reach, the connective tissue attaches this area directly to the

diaphragm. Most of the blood to the liver (70–80%) comes from the portal vein, and the smaller percentage is supplied by the hepatic artery (Figure 3). All the materials absorbed via the intestines reach the liver through the portal vein, except the complex lipids which are transported mainly by lymph vessels. The position of the liver in the circulatory system is optimal for gathering, transforming, and accumulating metabolites and for neutralizing and eliminating toxic substances. This elimination occurs in the form of bile, an exocrine secretion of the liver which is important in lipid digestion. The basic structural component of the liver is the liver cell or hepatocyte. In light microscope, structural units called classic liver lobules can be seen. The liver lobule is formed of a polygonal mass of tissue about 0.7×2 mm in size (Figure 4).

In certain animals (e.g., the pig), lobules are separated from each other by a layer of connective tissue. In humans, it is difficult to establish the exact limits between different lobules since they are in close contact in most of their extent (Figure 5). In some regions, the lobules are demarcated by connective tissue containing bile ducts, lymphatic vessels, nerves, and blood vessels. These regions, located at the corners of the lobules and occupied by portal triads, are called portal spaces. The human liver contains 3–6 portal triads per lobule, each with a venule (a branch of the portal vein);

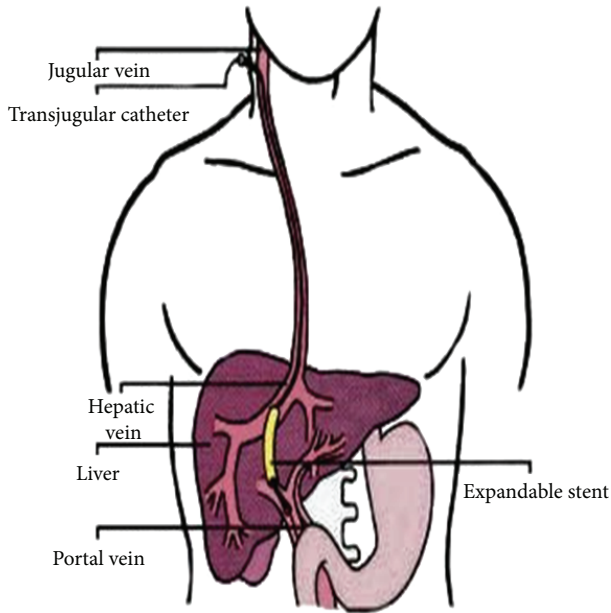


FIGURE 1

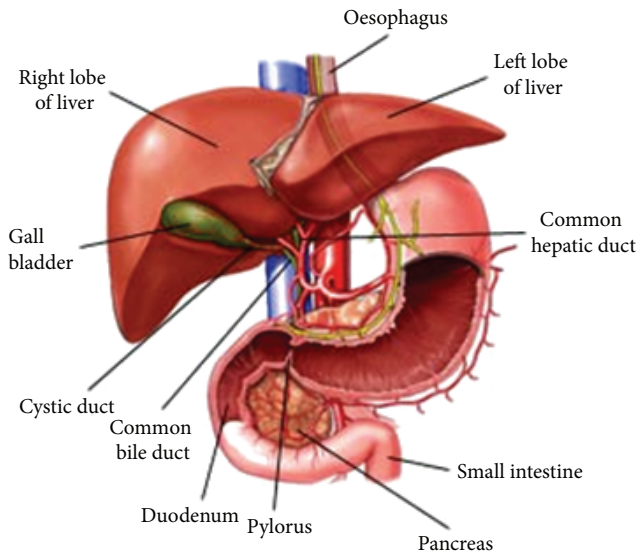


FIGURE 2

an arteriole (a branch of the hepatic artery); a duct (part of the bile duct system); and lymphatic vessels. The venule is usually the largest of these structures, containing blood from the superior and inferior mesenteric and splenic veins. An arteriole contains blood from the celiac trunk of the abdominal aorta.

The hepatocytes in the liver lobule are radially disposed and arranged like the bricks of a wall. These cellular plates are directed from the periphery of the lobule to its center and anastomose freely, forming a labyrinthine and sponge-like structure. The space between these plates contains capillaries, the liver sinusoids [2]. Portal and arterial blood mixes in the sinusoids and flows past hepatocytes, draining through

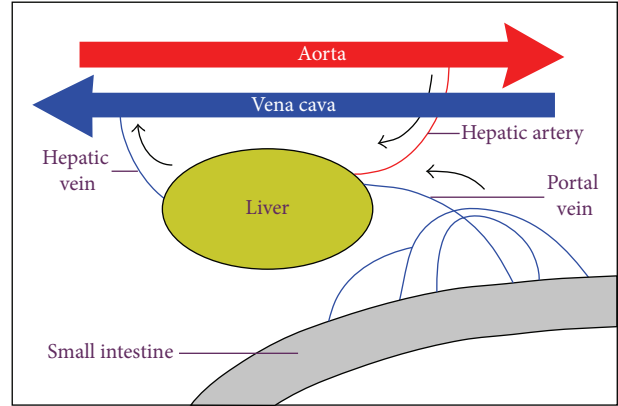


FIGURE 3

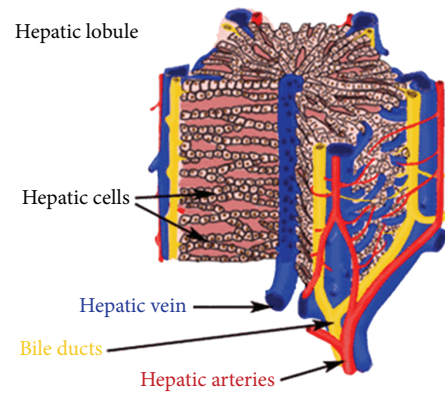


FIGURE 4

a central vein from each lobule that leads ultimately to the hepatic veins. Bile from the lobules drains into the interlobular branches of the bile duct by way of bile canaliculi. The hepatic lobules act as endocrine and exocrine glands. In endocrine secretion, hepatocytes take up and secrete molecules into the sinusoids [1].

The liver has an extraordinary capacity for regeneration. Hence, the loss of hepatic tissue by surgical removal or from the action of toxic substances is restored. The liver performs its metabolic functions with the aid of various enzymes fixed inside liver cells. These liver cells line many capillaries (hepatic sinusoids) through which the total hepatic blood flow is manifolded, whereby exchange of substances between blood flow and cells is facilitated. The interplay of the unidirectional blood flow with local metabolism generates concentration gradients of blood-borne substances (such as oxygen) between the inlet and the outlet of the liver. The unidirectionality of that blood, that is, the blood flows from the portal triads to the central vein (Figure 5), has a major influence on the mathematical structure of the model, which appears to be capable of describing the formation of zones with a jump discontinuity at a certain distance along a capillary [3].

Several metabolic functions of the liver have been found to be organized in spatial zones arranged in relation to the

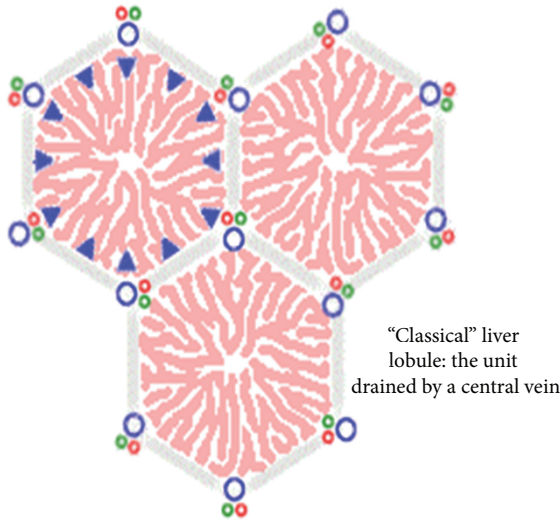


FIGURE 5

direction of hepatic blood flow, in such a way that some enzymes act almost wholly upstream others [3]. Bass et al. [3] attributed such distributions of enzymes activities to distributions of cell types. For the simplest case of two enzymes, there are two corresponding cell types, each containing only one of the enzymes; separate metabolic zones occur when all cells of one type are located upstream all cells of the other type. Furthermore, it was reported in [3] that each cell type reproduces itself by division. The mathematical model was discussed in [3], but for convenience the main steps in its derivation are repeated in the next section. The mathematical model describing the formation of liver zones is a system of nonlinear integropartial differential equations. The objective of this paper is to apply Adomian's decomposition method to the system in order to find its stationary solutions (as the time tends to infinity) and the general solutions (at any position x and any time t) for arbitrary initial conditions.

2. Mathematical Modelling and Solutions

2.1. Mathematical Formulation. About 1100 milliliters of blood flows from the portal vein into the liver sinusoids (Figure 6) each minute, and approximately an additional 350 milliliters flows into the sinusoids from the hepatic artery, the total averaging is about 1450 mL/min. This amounts to about 29% of the resting cardiac output. As the many capillaries comprising the liver are similar and act essentially in parallel, Bass et al. [3] modelled a representative capillary lined with cells of two kinds. It was suggested to put the x -axis along the blood flow, with inlet at $x = 0$ and outlet at $x = L$ [3]. The density of cells of the first kind is defined by $\rho_1(x, t)$ as a continuous representation of the number of cells of the first kind per unit length of capillary at time t at the position x . The density $\rho_2(x, t)$ of cells of the second kind is defined analogously. The total cell density $\rho_1 + \rho_2$ cannot exceed some fixed maximum density σ of cell sites, as division of the cell is limited by the familiar phenomenon of contact

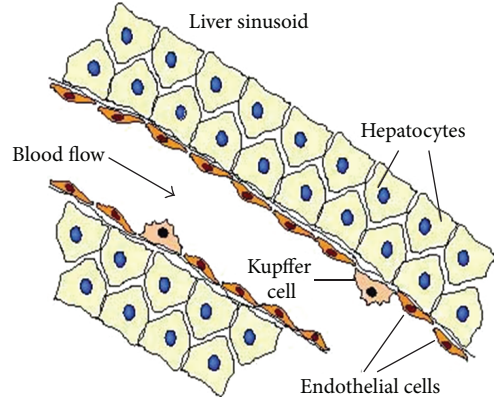


FIGURE 6

inhibition. The local rate of change $\partial\rho_1/\partial t$ of the density of cells of the first kind is assumed to consist of a growth rate term proportional to ρ_1 (self-generation) and to the density of sites available, $\sigma - \rho_1 - \rho_2$, and of a death rate term proportional to ρ_1 , with a coefficient $\beta_1(c) > 0$ dependent on the local concentration c of a controlling blood-borne substance. In what follows, for definiteness, oxygen is taken as that substance. Then

$$\frac{\partial\rho_1}{\partial t} = K_1\rho_1(\sigma - \rho_1 - \rho_2) - \beta_1(c)\rho_1, \quad (1)$$

with a constant coefficient $K_1 > 0$. A similar equation for ρ_2 is obtained from (1) by interchanging the suffices 1, 2. So

$$\frac{\partial\rho_2}{\partial t} = K_2\rho_2(\sigma - \rho_1 - \rho_2) - \beta_2(c)\rho_2. \quad (2)$$

Let f be the steady rate of blood flow through the capillary. If oxygen is transported in the x -direction predominantly by convection with the blood and used up by the two cell types at the rates $k_1\rho_1$ and $k_2\rho_2$ (with positive constants k_1, k_2), then changes in c caused by changes in ρ_1 and ρ_2 are quasisteady. Therefore, c satisfies

$$f\frac{\partial c}{\partial x} = -k_1\rho_1 - k_2\rho_2. \quad (3)$$

If (3) is integrated, then

$$c(x, t) = c_0 - \frac{1}{f} \int_0^x [k_1\rho_1(\xi, t) + k_2\rho_2(\xi, t)] d\xi, \quad (4)$$

where c_0 is the steady oxygen concentration in the blood entering the liver. It is assumed that as oxygen concentration falls, the death rate of cells increases ($d\beta_1(c)/dc \leq 0, d\beta_2(c)/dc \leq 0$), though not necessarily equally for both cell types. It is assumed that $\beta_1(c)$ has the following form (similarly for $\beta_2(c)$):

$$\beta_1(c) = \mu_1 + \nu_1(c_0 - c), \quad (5)$$

where

$$\mu_1 = \beta_1(c_0) \geq 0, \quad \nu_1 = -\left.\frac{d\beta_1}{dc}\right|_{c_0} \geq 0. \quad (6)$$

Introducing (4) and (5) into (1) and (2), we arrive at the pair of equations

$$\begin{aligned}\frac{\partial \rho_1}{\partial t} &= \rho_1 \left[K_1 (\sigma - \rho_1 - \rho_2) - \mu_1 - \frac{\nu_1}{f} \int_0^x (k_1 \rho_1 + k_2 \rho_2) d\xi \right], \\ \frac{\partial \rho_2}{\partial t} &= \rho_2 \left[K_2 (\sigma - \rho_1 - \rho_2) - \mu_2 - \frac{\nu_2}{f} \int_0^x (k_1 \rho_1 + k_2 \rho_2) d\xi \right].\end{aligned}\quad (7)$$

If $K_1 \sigma \leq \mu_1$, then $\rho_1(x, t) \rightarrow 0$ as $t \rightarrow \infty$ for all x , and similarly for ρ_2 . Therefore, it is assumed that $K_1 \sigma > \mu_1$ and $K_2 \sigma > \mu_2$. For similar reasons, it is assumed that at least one of ν_1 and ν_2 is positive (say ν_1). It is noted at once that unless the first cell type is inevitably to die out, its greatest possible specific growth rate $K_1 \sigma$ must exceed its least possible specific death rate μ_1 . Similar remarks apply for the second cell type, and accordingly it is assumed in [3] that

$$K_1 \sigma > \mu_1, \quad K_2 \sigma > \mu_2. \quad (8)$$

To obtain some preliminary heuristic ideas about the formation of zones in their model, Bass et al. [3] supposed that (7) admits solutions which at all finite times are everywhere positive and satisfy $(\rho_1 + \rho_2) < \sigma$. For such solutions, (7) can be written in the form

$$\begin{aligned}\frac{\partial}{\partial t} \ln \rho_1 &= K_1 (\sigma - \rho_1 - \rho_2) - \mu_1 - \frac{\nu_1}{f} \int_0^x (k_1 \rho_1 + k_2 \rho_2) d\xi, \\ \frac{\partial}{\partial t} \ln \rho_2 &= K_2 (\sigma - \rho_1 - \rho_2) - \mu_2 - \frac{\nu_2}{f} \int_0^x (k_1 \rho_1 + k_2 \rho_2) d\xi.\end{aligned}\quad (9)$$

Multiplying the first equation in (9) by K_2 and the second by K_1 , we have

$$\begin{aligned}\frac{\partial}{\partial t} \ln \rho_1^{K_2} &= K_1 K_2 (\sigma - \rho_1 - \rho_2) - \mu_1 K_1 \\ &\quad - \frac{\nu_1 K_1}{f} \int_0^x (k_1 \rho_1 + k_2 \rho_2) d\xi, \\ \frac{\partial}{\partial t} \ln \rho_2^{K_1} &= K_1 K_2 (\sigma - \rho_1 - \rho_2) - \mu_2 K_2 \\ &\quad - \frac{\nu_2 K_2}{f} \int_0^x (k_1 \rho_1 + k_2 \rho_2) d\xi.\end{aligned}\quad (10)$$

2.2. The Stationary Solutions. For such solutions, we can combine (10) in the form

$$\frac{\partial}{\partial t} \left[\ln \left(\frac{\rho_1^{K_2}}{\rho_2^{K_1}} \right) \right] = A - \frac{B}{f} \int_0^x (k_1 \rho_1 + k_2 \rho_2) d\xi, \quad (11)$$

where

$$A = \mu_2 K_1 - \mu_1 K_2, \quad B = \nu_1 K_2 - \nu_2 K_1. \quad (12)$$

Suppose that $\mu_2 K_1 > \mu_1 K_2$, $\nu_1 K_2 > \nu_2 K_1$, or

$$\frac{\mu_2}{K_2} > \frac{\mu_1}{K_1}, \quad \frac{\nu_2}{K_2} < \frac{\nu_1}{K_1}, \quad (13)$$

so that the constants A and B are positive. Since the integral in (11) is bounded above by $(k_1 + k_2)x\sigma$, the right-hand side of (11) is positive at all times for sufficiently small x , where

$$x < \frac{Af}{(k_1 + k_2)\sigma B}. \quad (14)$$

Volterra's argument [3] then applies: as $t \rightarrow \infty$, $\rho_1^{K_2}/\rho_2^{K_1} \rightarrow \infty$, and with ρ_1 bounded above by σ , ρ_2 must tend to zero. It is then plausible that for these values of x in (14), ρ_1 will approach a stationary form determined from the first equations of (7) with $\rho_2 = 0$, namely [3, 4],

$$K_1 (\sigma - \rho_1) - \mu_1 - \frac{\nu_1}{f} \int_0^x k_1 \rho_1 d\xi = 0. \quad (15)$$

In order to solve this equation by Adomian's decomposition method [5–13], we put the equation in the form

$$\rho_1 = \frac{c_1}{K_1} - \left(\frac{\nu_1 k_1}{f K_1} \right) \int_0^x \rho_1 d\xi, \quad (16)$$

where

$$c_i = K_i \sigma - \mu_i, \quad i = 1, 2. \quad (17)$$

According to Adomian's method, ρ_1 is assumed as

$$\rho_1 = \sum_{n=0}^{\infty} \rho_{1n}. \quad (18)$$

Substituting (18) into (16), we obtain

$$\sum_{n=0}^{\infty} \rho_{1n} = \frac{c_1}{K_1} - \left(\frac{\nu_1 k_1}{f K_1} \right) \sum_{n=0}^{\infty} \int_0^x \rho_{1n} d\xi. \quad (19)$$

Let

$$\rho_{10} = \frac{c_1}{K_1}. \quad (20)$$

Then the solution can be elegantly computed by using the recurrence relation

$$\rho_{1(n+1)} = -\frac{\nu_1 k_1}{f K_1} \int_0^x \rho_{1n} d\xi, \quad n \geq 0. \quad (21)$$

This gives

$$\begin{aligned}\rho_{11}(x) &= \left(\frac{-\nu_1 k_1}{f K_1} \right) \frac{c_1}{K_1} x, \\ \rho_{12}(x) &= \left(\frac{-\nu_1 k_1}{f K_1} \right)^2 \frac{c_1}{K_1} \frac{x^2}{2!}, \\ \rho_{13}(x) &= \left(\frac{-\nu_1 k_1}{f K_1} \right)^3 \frac{c_1}{K_1} \frac{x^3}{3!}, \\ &\vdots \\ \rho_{1n}(x) &= \left(\frac{-\nu_1 k_1}{f K_1} \right)^n \frac{c_1}{K_1} \frac{x^n}{n!}, \quad n \geq 0.\end{aligned}\quad (22)$$

According to (18), we obtain ρ_1 in the form

$$\rho_1(x) = \rho_1^*(x) = \frac{c_1}{K_1} \exp\left[-\frac{\nu_1 k_1}{f K_1} x\right]. \quad (23)$$

Set ρ_2 equal to zero and ρ_1 equal to ρ_1^* , then (11) becomes

$$\frac{\partial}{\partial t} \left[\ln\left(\frac{\rho_1^{K_2}}{\rho_2^{K_1}}\right) \right] = A - \frac{B c_1}{\nu_1} \left[1 - \exp\left(-\frac{\nu_1 k_1}{f K_1} x\right) \right]. \quad (24)$$

We note that the right-hand side of (24) decreases with increasing x and reaches zero at a value $x = x^*$ determined by

$$\exp\left(\frac{\nu_1 k_1 x^*}{f K_1}\right) = \frac{B c_1}{K_1 (\nu_1 c_2 - \nu_2 c_1)}. \quad (25)$$

Provided that

$$\nu_1 c_2 > \nu_2 c_1. \quad (26)$$

The point $x = x^*$ determined by (25) lies in the interval $(0, L)$ of interest provided that

$$\exp\left(\frac{\nu_1 k_1 L}{f K_1}\right) > \frac{B c_1}{K_1 (\nu_1 c_2 - \nu_2 c_1)}. \quad (27)$$

Under these conditions, it is then reasonable to suppose that, for $x > x^*$, the right-hand side of (11) will in fact be negative for sufficiently large values of t [3]. Volterra's argument then indicates that we can expect to find $\rho_1 \rightarrow 0$ as $t \rightarrow \infty$ for $x > x^*$. Furthermore, we may also expect that, for $x > x^*$, ρ_2 will approach a stationary form determined from the second equation of (7) by

$$K_2 (\sigma - \rho_2) - \mu_2 - \frac{\nu_2}{f} \left[\int_0^{x^*} k_1 \rho_1^* d\xi + \int_{x^*}^x k_2 \rho_2 d\xi \right] = 0. \quad (28)$$

This equation can be solved by Adomian's method; we rewrite the equation in the form

$$\rho_2 + \frac{\nu_2 k_2}{f K_2} \int_{x^*}^x \rho_2 d\xi = D, \quad (29)$$

where

$$D = \frac{\nu_1 c_2 - \nu_2 c_1}{B}. \quad (30)$$

We assume that

$$\rho_2 = \sum_{n=0}^{\infty} \rho_{2n}. \quad (31)$$

Let $\rho_{20} = D$, then the solution can be computed by using the recurrence relation

$$\rho_{2(n+1)} = -\frac{\nu_2 k_2}{f K_2} \int_{x^*}^x \rho_{2n} d\xi, \quad n \geq 0. \quad (32)$$

This gives

$$\begin{aligned} \rho_{21} &= -\frac{\nu_2 k_2}{f K_2} D (x - x^*), \\ \rho_{22} &= \left(-\frac{\nu_2 k_2}{f K_2}\right)^2 D \frac{(x - x^*)^2}{2!}, \\ &\vdots \\ \rho_{2n} &= \left(-\frac{\nu_2 k_2}{f K_2}\right)^n D \frac{(x - x^*)^n}{n!}, \quad n \geq 0. \end{aligned} \quad (33)$$

Therefore

$$\rho_2 = \rho_2^*(x) = D \exp\left[-\frac{\nu_2 k_2}{f K_2} (x - x^*)\right], \quad x > x^*. \quad (34)$$

So, as $t \rightarrow \infty$, the formation of liver zones can be described as follows:

$$\begin{aligned} \rho_1 &= \rho_1^*(x), \quad \rho_2 = 0, \quad 0 \leq x < x^*, \\ \rho_1 &= 0, \quad \rho_2 = \rho_2^*(x), \quad x^* < x \leq L. \end{aligned} \quad (35)$$

3. Analytical Solutions

In applied mathematics, Adomian's decomposition method is an effective procedure to obtain analytic and approximate solutions for different types of equations. This method is used here to obtain a general solution for the system (7). Following Bass et al. [3], we define new variables

$$t' = c_1 t, \quad x' = \frac{\nu_1 k_1}{f K_1} x, \quad v_i(t', x') = \frac{K_1}{c_1} \rho_i(t, x) \quad (36)$$

and new parameters

$$\theta = \frac{k_2}{k_1}, \quad \gamma = \frac{K_2}{K_1}, \quad \lambda = \frac{K_1 c_2}{K_2 c_1}, \quad \eta = \frac{\nu_2 K_1}{\nu_1 K_2}. \quad (37)$$

Then (7) becomes, on dropping at once the primes from the new independent variables,

$$\begin{aligned} \frac{\partial v_1}{\partial t} &= v_1 \left[1 - v_1 - v_2 - \int_0^x [v_1(t, \xi) + \theta v_2(t, \xi)] d\xi \right], \\ \frac{\partial v_2}{\partial t} &= \gamma v_2 \left[\lambda - v_1 - v_2 - \eta \int_0^x [v_1(t, \xi) + \theta v_2(t, \xi)] d\xi \right], \end{aligned} \quad (38)$$

with constant parameters

$$\theta > 0, \quad \gamma > 0, \quad \lambda > 0, \quad \eta \geq 0. \quad (39)$$

The spatial interval of interest is now $[0, \Lambda]$, where $\Lambda = (\nu_1 k_1 / f K_1) L$, and then we have [3]

$$\eta < \lambda < 1, \quad \ln\left(\frac{1 - \eta}{\lambda - \eta}\right) < \Lambda. \quad (40)$$

The stationary solutions become

$$\begin{aligned} v_1 &= e^{-x}, \quad v_2 = 0, \quad 0 \leq x < x^*, \\ v_1 &= 0, \quad v_2 = \left(\frac{\lambda - \eta}{1 - \eta} \right) e^{-\eta\theta(x-x^*)}, \quad x^* < x \leq \Lambda, \end{aligned} \quad (41)$$

where now

$$x^* = \ln \left(\frac{1 - \eta}{\lambda - \eta} \right). \quad (42)$$

For searching analytical solutions, we firstly rewrite the system we want to solve as two separate integro-partial differential equations:

$$\frac{\partial v_1}{\partial t} = v_1 \left[1 - v_1 - v_2 - \int_0^x (v_1 + \theta v_2) d\xi \right], \quad (43)$$

$$\frac{\partial v_2}{\partial t} = \gamma v_2 \left[\lambda - v_1 - v_2 - \eta \int_0^x (v_1 + \theta v_2) d\xi \right]. \quad (44)$$

According to the decomposition method, we assume that

$$v_1 = \sum_{n=0}^{\infty} v_{1n}, \quad v_2 = \sum_{n=0}^{\infty} v_{2n}. \quad (45)$$

Equation (43) can be put in the following operator form:

$$\begin{aligned} L_t v_1 &= v_1 - v_1^2 - v_1 v_2 - v_1 \int_0^x (v_1(t, \xi) + \theta v_2(t, \xi)) d\xi, \\ L_t &= \frac{\partial}{\partial t}. \end{aligned} \quad (46)$$

Applying the inverse operator $L_t^{-1}[\cdot] = \int_0^t [\cdot] dt$, on both sides of this equation, yields

$$\begin{aligned} v_1 - v_1(x, 0) &= L_t^{-1} v_1 - L_t^{-1} v_1^2 - L_t^{-1} v_1 v_2 \\ &\quad - L_t^{-1} v_1 \int_0^x (v_1 + \theta v_2) d\xi. \end{aligned} \quad (47)$$

Substituting (45) into (47), we obtain

$$\begin{aligned} v_1 &= v_1(x, 0) + L_t^{-1} \sum_{n=0}^{\infty} v_{1n} \\ &\quad - L_t^{-1} \sum_{n=0}^{\infty} \sum_{k=0}^n v_{1k} v_{1(n-k)} - L_t^{-1} \sum_{n=0}^{\infty} \sum_{k=0}^n v_{1k} v_{2(n-k)} \\ &\quad - L_t^{-1} \sum_{n=0}^{\infty} v_{1n} \int_0^x \sum_{n=0}^{\infty} (v_{1n} + \theta v_{2n}) d\xi. \end{aligned} \quad (48)$$

Now, the solution v_1 can be evaluated through the recursive scheme:

$$\begin{aligned} v_{10}(x, t) &= v_1(x, 0), \\ v_{1(n+1)}(x, t) &= L_t^{-1} v_{1n} - L_t^{-1} \left(\sum_{k=0}^n v_{1k} v_{1(n-k)} \right) \\ &\quad - L_t^{-1} \left(\sum_{k=0}^n v_{1k} v_{2(n-k)} \right) - L_t^{-1} \sum_{k=0}^n v_{1k} \\ &\quad \times \int_0^x (v_{1(n-k)} + \theta v_{2(n-k)}) d\xi, \quad n \geq 0. \end{aligned} \quad (49)$$

By similar analysis, we can get the solution v_2 by the recursive scheme:

$$\begin{aligned} v_{20}(x, t) &= v_2(x, 0), \\ v_{2(n+1)}(x, t) &= \gamma \lambda L_t^{-1} v_{2n} - \gamma L_t^{-1} \left(\sum_{k=0}^n v_{1k} v_{2(n-k)} \right) \\ &\quad - \gamma L_t^{-1} \left(\sum_{k=0}^n v_{2k} v_{2(n-k)} \right) - \gamma \lambda L_t^{-1} \sum_{k=0}^n v_{2k} \\ &\quad \times \int_0^x (v_{1(n-k)} + \theta v_{2(n-k)}) d\xi, \quad n \geq 0. \end{aligned} \quad (50)$$

For simplicity, we assume that the two types of the liver cells have the same distribution along the hepatic capillary at $t = 0$; that is,

$$\begin{aligned} v_1(x, 0) &= v_2(x, 0); \\ \text{that is, } v_{10}(x) &= v_{20}(x) = v_0(x) \text{ (say)}. \end{aligned} \quad (51)$$

By this, we can get the first few terms of Adomian's series from the recurrence relations (49) and (50) as follows:

$$\begin{aligned} v_{11}(x, t) &= v_0 [1 - 2v_0 - (1 + \theta) I_1(x)] t, \\ v_{21}(x, t) &= \gamma v_0 (\lambda - 2v_0 - \eta(1 + \theta) I_1(x)) t, \\ v_{12} &= v_0 \{ [1 - 3v_0 - (1 + \theta) I_1(x)] [1 - 2v_0 - (1 + \theta) I_1(x)] \\ &\quad - \gamma v_0 [\lambda - 2v_0 - \eta(1 + \theta) I_1(x)] - (1 + \gamma\theta\lambda) I_1(x) \\ &\quad + 2(1 + \gamma\theta) I_2(x) (1 + \gamma\eta\theta) (1 + \theta) I_3(x) \} \frac{t^2}{2!}, \\ v_{22} &= \{ [\gamma\lambda - 3\gamma v_0 - \gamma\eta(1 + \theta) I_1(x)] \\ &\quad \times [\gamma\lambda v_0 - 2\gamma v_0^2 - \gamma\eta(1 + \theta) v_0 I_1(x)] \\ &\quad - [\gamma v_0^2 - 2\gamma v_0^3 - \gamma(1 + \theta) v_0^2 I_1(x)] \\ &\quad - \gamma\eta(1 + \gamma\theta\lambda) v_0 I_1(x) + 2\gamma\eta(1 + \gamma\theta) v_0 I_2(x) \\ &\quad + \gamma\eta(1 + \theta) (1 + \gamma\eta\theta) v_0 I_3(x) \} \frac{t^2}{2!}, \end{aligned} \quad (52)$$

where

$$\begin{aligned} I_1(x) &= \int_0^x v_0 d\xi, & I_2(x) &= \int_0^x v_0^2 d\xi, \\ I_3(x) &= \int_0^x I_1(\xi) v_0 d\xi. \end{aligned} \quad (53)$$

4. Remarks

Here, we indicate that at particular values of the parameters γ , λ , and η , the solutions v_1 and v_2 are equivalent. In order to do this, we prefer to put the solutions v_1 and v_2 in the form

$$\begin{aligned} v_1(x, t) &= \alpha_0(x) + \alpha_1(x)t + \alpha_2(x)t^2 + \dots, \\ v_2(x, t) &= \beta_0(x) + \beta_1(x)t + \beta_2(x)t^2 + \dots, \end{aligned} \quad (54)$$

where

$$\begin{aligned} \alpha_0(x) &= \beta_0(x) = v_0(x), \\ \alpha_1(x) &= v_0 [1 - 2v_0 - (1 + \theta) I_1(x)], \\ \alpha_2(x) &= \frac{1}{2!} v_0 [1 - 3v_0 - (1 + \theta) I_1(x)] \\ &\quad \times [1 - 2v_0 - (1 + \theta) I_1(x)] \\ &\quad - \gamma v_0 [\lambda - 2v_0 - \eta(1 + \theta) I_1(x)] - (1 + \gamma\theta\lambda) I_1(x) \\ &\quad + 2(1 + \gamma\theta) I_2(x) + (1 + \gamma\eta\theta)(1 + \theta) I_3(x), \\ \beta_1(x) &= \gamma v_0 [\lambda - 2v_0 - (1 + \theta) I_1(x)], \\ \beta_2(x) &= \frac{1}{2!} \{ [\gamma\lambda - 3\gamma v_0 - \gamma\eta(1 + \theta) I_1(x)] \\ &\quad \times [\gamma\lambda v_0 - 2\gamma v_0^2 - \gamma\eta(1 + \theta) v_0 I_1(x)] \\ &\quad - [\gamma v_0^2 - 2\gamma v_0^3 - \gamma(1 + \theta) v_0^2 I_1(x)] \\ &\quad - \eta(1 + \gamma\theta\lambda) v_0 I_1(x) + 2\gamma\eta(1 + \gamma\theta) v_0 I_2(x) \\ &\quad + \gamma\eta(1 + \theta)(1 + \gamma\eta\theta) v_0 I_3(x) \}. \end{aligned} \quad (55)$$

Firstly, substituting $\gamma = \lambda = \eta = 1$ into the original equations (38), we obtain

$$\begin{aligned} \frac{1}{v_1} \frac{\partial v_1}{\partial t} &= 1 - v_1 - v_2 - \int_0^x (v_1 + \theta v_2) d\xi, \\ \frac{1}{v_2} \frac{\partial v_2}{\partial t} &= 1 - v_1 - v_2 - \int_0^x (v_1 + \theta v_2) d\xi. \end{aligned} \quad (56)$$

We can combine these equations in the form

$$\frac{\partial}{\partial t} [\ln v_1(x, t)] = \frac{\partial}{\partial t} [\ln v_2(x, t)]. \quad (57)$$

By integrating both sides with respect to t from 0 to t , we get

$$\ln \left[\frac{v_1(x, t)}{v_0(x)} \right] = \ln \left[\frac{v_2(x, t)}{v_0(x)} \right], \quad (58)$$

where we used the relation $v_1(x, 0) = v_2(x, 0) = v_0(x)$. Thus, $v_1(x, t) = v_2(x, t)$. Now, substituting $\gamma = \lambda = \eta = 1$ into (55), we can easily observe that

$$\alpha_0(x) = \beta_0(x), \quad \alpha_1(x) = \beta_1(x), \quad \alpha_2(x) = \beta_2(x), \quad (59)$$

which leads also to $v_1(x, t) = v_2(x, t)$.

5. Conclusion

In this paper, the Adomian decomposition method has been applied successfully to a system of nonlinear integro-partial differential equations describing the formation of liver zones. As time tends to infinity, the stationary solutions are obtained in exact forms by using Adomian's method, where full agreement with those obtained in the literature has been achieved. Also, at any time of the liver regeneration process, the analytical solutions are obtained explicitly in series form. Finally, the current solutions may shed some light on the mathematical aspects of the formation of liver zones and also on describing the distribution of the two types of the liver cells.

Acknowledgment

The author wishes to express his thanks to Professor Mostafa El-Shahed for his kind help and very valuable suggestions.

References

- [1] D. T. Lindsay, *Functional Human Anatomy*, Saunders Company, Philadelphia, Pa, USA, 1996.
- [2] L. Carlos, J. Carneiro, and R. O. Kelly, *Basic Histology*, Prentice Hall, Amazon, London, UK, 1992.
- [3] L. A. Bass, J. Bracken, K. Holmaker, and F. Jefferies, "Integro-differential equations for the self-organisation of liver zones by competitive exclusion of cell-types," *Journal of the Australian Mathematical Society*, vol. 29, pp. 156–194, 1987.
- [4] K. Holmaker, "Global asymptotic stability for a stationary solution of a system of Integro-differential equations describing the formation of liver zones," *SIAM Journal on Mathematical Analysis*, vol. 24, pp. 116–128, 1993.
- [5] G. Adomian, *Solving Frontier Problems of Physics: The Decomposition Method*, Kluwer Academic Publishers, Boston, Mass, USA, 1994.
- [6] A.-M. Wazwaz, "Adomian decomposition method for a reliable treatment of the Emden-Fowler equation," *Applied Mathematics and Computation*, vol. 161, no. 2, pp. 543–560, 2005.
- [7] A. M. Wazwaz, *Partial Differential Equations and Solitary Waves Theory*, Springer, New York, NY, USA, 2009.
- [8] M. Kumar and N. Singh, "Modified Adomian decomposition method and computer implementation for solving singular boundary value problems arising in various physical problems," *Computers and Chemical Engineering*, vol. 34, no. 11, pp. 1750–1760, 2010.
- [9] A. Ebaid, "A new analytical and numerical treatment for singular two-point boundary value problems via the Adomian decomposition method," *Journal of Computational and Applied Mathematics*, vol. 235, no. 8, pp. 1914–1924, 2011.

- [10] A.-M. Wazwaz, "A reliable study for extensions of the Bratu problem with boundary conditions," *Mathematical Methods in the Applied Sciences*, vol. 35, no. 7, pp. 845–856, 2012.
- [11] F. A. Hendi and H. O. Bakodah, "Solution of nonlinear integro-differential equation using discrete Adomian decomposition method," *Far East Journal of Mathematical Sciences*, vol. 66, no. 2, pp. 213–221, 2012.
- [12] J.-S. Duan, R. Rach, A.-M. Wazwaz, T. Chaolu, and Z. Wang, "A new modified Adomian decomposition method and its multi-stage form for solving nonlinear boundary value problems with Robin boundary conditions," *Applied Mathematical Modelling*, 2013.
- [13] A.-M. Wazwaz, R. Rach, and J.-S. Duan, "A study on the systems of the Volterra integral forms of the Lane-Emden equations by the Adomian decomposition method," *Mathematical Methods in the Applied Sciences*, 2013.

Research Article

Excitation-Contraction Coupling between Human Atrial Myocytes with Fibroblasts and Stretch Activated Channel Current: A Simulation Study

Heqing Zhan and Ling Xia

Department of Biomedical Engineering, Zhejiang University, Hangzhou 310027, China

Correspondence should be addressed to Ling Xia; xialing@zju.edu.cn

Received 2 May 2013; Revised 13 July 2013; Accepted 13 July 2013

Academic Editor: Zhonghua Sun

Copyright © 2013 H. Zhan and L. Xia. This is an open access article distributed under the Creative Commons Attribution License, which permits unrestricted use, distribution, and reproduction in any medium, provided the original work is properly cited.

Myocytes have been regarded as the main objectives in most cardiac modeling studies and attracted a lot of attention. Connective tissue cells, such as fibroblasts (Fbs), also play crucial role in cardiac function. This study proposed an integrated myocyte- I_{sac} -Fb electromechanical model to investigate the effect of Fbs and stretch activated ion channel current (I_{sac}) on cardiac electrical excitation conduction and mechanical contraction. At the cellular level, an active Fb model was coupled with a human atrial myocyte electrophysiological model (including I_{sac}) and a mechanical model. At the tissue level, electrical excitation conduction was coupled with an elastic mechanical model, in which finite difference method (FDM) was used to solve the electrical excitation equations, while finite element method (FEM) was used for the mechanics equations. The simulation results showed that Fbs and I_{sac} coupling caused diverse effects on action potential morphology during repolarization, depolarized the resting membrane potential of the human atrial myocyte, slowed down wave propagation, and decreased strains in fibrotic tissue. This preliminary simulation study indicates that Fbs and I_{sac} have important implications for modulating cardiac electromechanical behavior and should be considered in future cardiac modeling studies.

1. Introduction

Heart is considered as a composite material consisting of myocytes, Fbs, endothelial, vascular smooth muscle, neuronal cells, and fluids [1, 2]. The division and interaction of these cells and fluids keep the heart working efficiently, which is performed by a well-ordered interplay between cardiac electrophysiology, excitation propagation, and force development. The process from the electrical excitation of the myocyte to mechanical contraction is referred to as cardiac excitation-contraction coupling (ECC). Conversely, changing the cardiac mechanical environment to alter electrical activity is referred to as mechanoelectric feedback (MEF) [3]. Investigating the multiphysics and multiscale heart system involves extremely difficult experiments in order to directly observe and manipulate the process that underlies cardiac electrical and mechanical activity. To overcome these experimental challenges, some sophisticated mathematical models have been developed to gain a better insight [4–9].

To study cardiac ECC, many electromechanical (EM) models, from the molecular level of myofilaments (MFs) to the anatomy of the organs, have been developed under both normal and pathological situations [6, 10–14]. At the subcellular level, actin-myosin interaction and Ca-based activation are represented by MF models. Cellular reconstruction of electrophysiology and Ca handling are then coupled with MF models to produce EM cell models. At the organ level, electrical component is solved as a reaction-diffusion system and mechanical component is described by equations of continuum mechanics [4].

For cardiac MEF, the main focus of published studies has been placed on the function of stretch activated channels (SACs) in various noncardiac tissues [15, 16] as well as in the heart [17, 18]. The electrophysiologic effects of pulsatile stretch, stretch generated by increased preload and afterload, and acute static mechanical stretch can be explained by SAC current (I_{sac}).

The published models of ECC and MEF mainly described the properties of cardiac myocytes. However, the vasculature and connective tissue cells [19] have not been considered. Recently, it has been revealed that Fbs are numerous present in cardiac tissues with much smaller size than that of myocytes [20], and they affect the restitution properties of cardiac tissues, especially during the process of ageing and in various cardiac diseases [21–23]. Once the percentage of Fbs in the heart increases up to 10–35%, a remodeling of cardiac structure occurs, which increases muscle stiffness and reduces the coupling between adjacent muscle fiber bundles [24]. The functional roles of Fbs on cardiac electrical and mechanical activities have attracted more and more interests. Both experimental and computational studies [25–27] have confirmed that increased Fb population could lead to nonmonotonic changes in the conduction velocity and implicated that the effects of Fbs on cardiac electrophysiology and mechanics are worthy of further investigation.

Although the myocytes have been regarded as the main objectives for the cardiac electrophysiological, mechanical, and EM models [5–8], the role of Fbs has also been investigated recently using the models. By including the Fbs in the cardiac electrophysiological simulations [1, 27–29], it has been reported that myocyte-Fb coupling modulated action potential (AP) morphology and action potential duration (APD). However, to our best knowledge, due to the lack of experimental data and accurate models of Fb mechanics, the myocytes and Fbs have not yet been integrated to investigate their electromechanics interaction. The aim of this study was to propose an integrated myocyte- I_{sac} -Fb electromechanical model to investigate the effect of Fbs and stretch activated ion channel current (I_{sac}) on cardiac electrical excitation conduction and mechanical contraction. The proposed model integrated the coupling between the Fb model [30] and the myocardial electrophysiological model [31] (including I_{sac} [32]) and mechanical model [33] at the cellular level, with excitation conduction and elastic mechanics [34] at the tissue level. The developed model was validated by comparing the simulated results of excitation conduction and mechanical properties to those from previous electromechanical coupling models. Electromechanical models of central point stimulus and strain maps were illustrated to investigate the effects of Fbs and I_{sac} on cardiac excitation conduction and mechanical contraction.

2. Materials and Methods

The framework of the coupled myocyte- I_{sac} -Fb model includes two parts. The first part includes the electrophysiological and mechanical models of myocytes and Fbs at the cellular level. The cell model stems from the Courtemanche-Ramirez-Nattel (CRN) model of the human atrial AP [30] (including I_{sac} equations described by Kuijpers et al. [31]), the Rice mechanical model [32], and the Maleckar model of atrial Fbs [33]. The second part includes the models of excitation conduction and contraction of the Fb-myocyte coupling (FMC) at the tissue level. The tissue model includes cardiac excitation conduction and finite deformation, described by

the Nash model [34]. Details of the individual components and their modification from published models are described as follows.

2.1. Myocyte- I_{sac} -Fb Electrophysiological Modeling at the Cellular Level

2.1.1. Electrophysiological Model of the Human Atrial Myocyte and I_{sac} . The CRN model was employed in this study, which can accurately represent atrial AP dynamics [30]. This computationally efficient model was based on the experimental data and reproduced various AP behaviors. Equations of I_{sac} were described by Kuijpers et al. in [31]. In their model, the amount of I_{sac} was related to local stretch and can be changed during contraction.

2.1.2. Electrophysiological Model of Atrial Fbs. For the electrophysiological model of atrial Fbs, the active 1 model described by Maleckar et al. was applied in our study [33].

2.1.3. Cell-Cell Electrophysiological Coupling. The electrophysiological FMC is expressed as [33]

$$\begin{aligned} \frac{dV_{myo}}{dt} &= -\frac{(1/C_{m,myo})}{[I_{myo}(V_{myo}, t) + I_{stim} + \sum_{i=1:n} G_{gap}(V_{myo} - V_{Fb})]} \\ \frac{dV_{Fb}}{dt} &= -\frac{(1/C_{m,Fb})}{[I_{Fb}(V_{Fb}, t) - I_{gap}]}, \end{aligned} \quad (1)$$

where V_{myo} and V_{Fb} are the transmembrane potential of the human atrial myocyte and the Fb, respectively, $C_{m,myo}$ and $C_{m,Fb}$ are the membrane capacitance of the myocyte and Fb, respectively, and I_{myo} and I_{Fb} are the net membrane current of the myocyte and Fb, respectively. I_{stim} is the stimulus current applied to the myocyte membrane, and I_{gap} is the current that flows through the gap junction between the myocyte and each Fb. G_{gap} represents the gap-junctional conductance.

2.2. Myocyte- I_{sac} -Fb Mechanical Modeling at the Cellular Level: The Ca^{2+} -Force Relation. To simulate the mechanics of myocyte- I_{sac} -Fb model, the Ca^{2+} -force relation in myocyte and Fb was considered. In the present study, the computationally efficient Rice mechanical model was applied for the myocyte [32], which included phenomenological representations of both regulatory unit (RU)-RU cooperative interactions and a three-state model of crossbridge attachment and distortion [4]. In our study, this MF model was coupled to the CRN model by using the Ca concentration from the CRN model as the input to the MF model.

To the best of our knowledge, there has been no well-defined mathematical model to describe the tension in Fb. The main reasons are as follows. Firstly, there is lack of experimental data due to the small size of individual Fbs [35].

Secondly, Ca^{2+} current, as a control factor of active tension, has not been identified for membrane ionic currents in Fb [1, 33, 36, 37]. The active force of Fb was therefore ignored at the cellular level in this study.

2.3. Tissue Modeling. A two-dimensional (2D) cardiac tissue was represented by a rectangular grid of 225×225 points. Each point was regarded as a myocyte/Fbs complex. Fbs were coupled with each myocyte in two ways (longitudinal connection and lateral connection). Fbs distributed along the long axis of myocytes were referred as longitudinal connection, and along the short axis of myocytes was lateral connection. The electrical component was governed by the parabolic partial differential monodomain equation. The governing equations for the mechanical component were the stress equilibrium equations based on the large deformation theory [6]. The mechanical model proposed by Nash and Panfilov [34] was used, which included the stress equilibrium, the finite element approximations, the constitutive law, and the uniform isotonic boundary loads.

As the Fb-myocyte (F-M) ratio increases, the cardiac fibrotic remodeling leads to a progressive increase in cardiac passive stiffness [38, 39]. The common approach to modeling ischemic myocardium is to change material descriptions of passive myocardium. In this study, the material constants in passive material properties were reevaluated to show the higher elastic stiffness of fibrotic tissue. Compared with the normal tissue (the material constants with units of stress were 2 kPa and 6 kPa) [34], the material constants in fibrotic tissue were set to 4 kPa and 12 kPa, respectively. In this way, the modulus of fibrotic tissue was doubled, within the range of experiment results [40].

2.4. Numerical Methods. The system was solved numerically using custom software written in Fortran language. At the cellular level, all state variables were updated by the forward Euler method. The FDM was applied to solve the reaction-diffusion equation. Following each time integration step, all parameters of cells were updated. The active stress was then interpolated at the four-node rectangle isoparametric element Gaussian points. Stresses of these active Gaussian points were served as the inputs to the governing equations of the tissue mechanics model. The stress equilibrium equation was solved by a nonlinear least square iteration method with different material constants from different tissues.

In the 2D coupling model, a tissue size of 225×225 grid points was used to study conduction velocity (CV) of plane wave propagation for longitudinal and transverse conduction. CV was calculated as the tissue length divided by the time interval between the time of stimulation and the time of the earliest excitation at the other end of the tissue. In this set of simulations, electromechanical activities and the change of strain due to a periodic point stimulation at the centre of the tissue were investigated. Central stimulus sites were chosen to be the smallest possible square regions (5×5 computational nodes), which made it possible to produce a propagating wave. Ten periodic central stimuli with a time interval of 500 ms were applied at the centre of the 2D tissue

to ensure a stable excitation and contraction, and timing started when the 11th loop occurred. I_{sac} has been considered. For FDM, the spatial resolution in the longitudinal direction was 0.1 mm, while in the transverse direction was 0.04 mm. The temporal resolution was 0.005 ms. No-flux boundary conditions were used. For FEM, a mesh with 14×14 elements was used, which contained 16×16 grid points in plane wave and central point stimulus simulations. The temporal resolution for the mechanical model was 2 ms. Strain maps of central stimulus were also investigated.

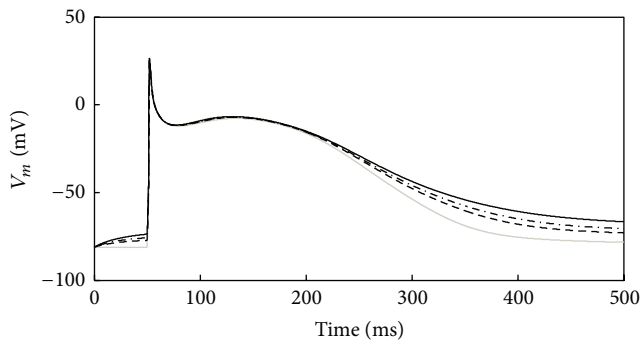
3. Results

3.1. Effects of I_{sac} and Fbs on Atrial Myocyte AP. Figure 1(a) illustrates the AP of the human atrial myocyte coupled with I_{sac} for different stretch ratios $\lambda = 1.1, 1.2,$ and 1.3 in comparison with the uncoupled control ($\lambda = 1.0$). With increasing λ of 1.0, 1.1, 1.2, and 1.3, prolonged repolarization was observed. Their corresponding AP durations at 50% repolarization (APD_{50}) were 189 ms, 196 ms, 197 ms, and 202 ms. When compared with control ($\lambda = 1.0$), an increase of 3.7%, 4.2%, and 6.9% was obtained. At 90% repolarization, more obvious increase was found. AP durations (APD_{90}) were 372 ms and 435 ms for $\lambda = 1.1, 1.2,$ with the increase of 21% and 42% in comparison with 307 ms from $\lambda = 1.0$. With $\lambda = 1.3$, the membrane potential was -64.2 mV at 500 ms, and it did not return to -69.5 mV required for APD_{90} . For the uncoupled control, the resting potential remained at -81 mV before the fast depolarization. For $\lambda = 1.1, 1.2,$ and 1.3 , it depolarized slowly within 50 ms and increased by 4.9%, 6.2%, and 8.6% at 50 ms when compared with the uncoupled control. Therefore, it can be concluded that the coupling I_{sac} prolonged repolarization and APD and depolarized the resting potential.

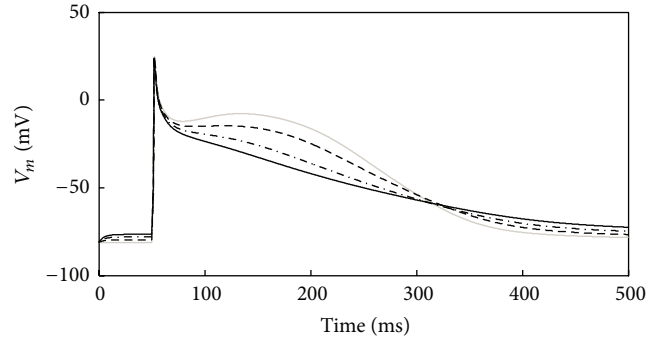
Figure 1(b) presents the repolarization for the human atrial myocyte when coupled with different numbers of Fbs (1 Fb, 2 Fbs, and 3 Fbs) in comparison with the control (no Fb). With more coupled Fbs, the membrane potential during the plateau was less depolarized, leading to a 13%, 41%, and 59% decrease (for 1, 2, and 3 Fbs) of APD_{50} when compared with control. However, for APD_{90} , they were increased by 11%, 19%, and 45%. For the resting potential within 50 ms, it increased by 2.5–6.2% as the number of coupled Fbs increased. Therefore, coupling Fbs decreased APD_{50} , prolonged APD_{90} , and depolarized the resting potential.

Similar changes were observed in myocyte AP with changed G_{gap} but with fixed number of coupled Fbs. As shown in Figure 1(c), increasing G_{gap} from 1 ns to 3 ns resulted in a 43–55% reduction of APD_{50} , an 18% increase of APD_{90} , and a 5% increase in the resting potential at 50 ms.

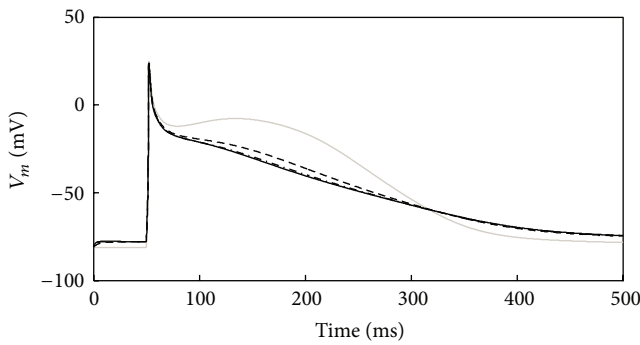
Figure 1(d) shows the APs of four different coupling schemes. An uncoupled myocyte was referred to as control. The other three schemes were myocyte coupled with I_{sac} with $\lambda = 1.1$, myocyte coupled with two Fbs with $G_{\text{gap}} = 1$ nS, and myocyte coupled with both I_{sac} and two Fbs with $\lambda = 1.1$ and $G_{\text{gap}} = 1$ ns. It can be seen that I_{sac} made the membrane potential during the plateau slightly more depolarized, while Fbs made it less depolarized. For APD_{50} , the first scheme



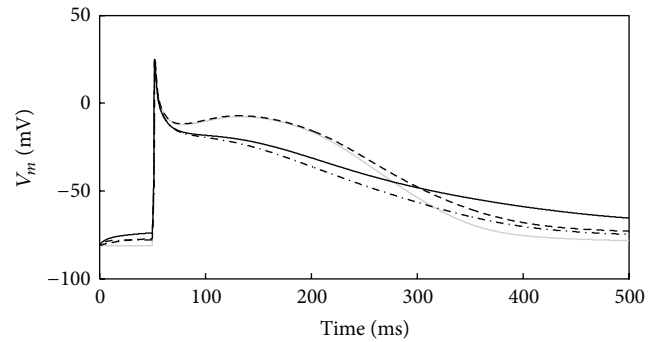
(a)



(b)



(c)



(d)

FIGURE 1: Illustration of changes in the waveform of the atrial myocyte AP. (a) 1 myocyte coupled to I_{sac} with a λ of 1.1 to 1.3. (b) 1 myocyte coupled to 1 to 3 Fbs with a G_{gap} of 1 nS. (c) 1 myocyte coupled to 2 Fbs with a G_{gap} of 1 to 3 nS. (d) 1 myocyte coupled to I_{sac} or 2 Fbs or I_{sac} and Fbs at the same time.

resulted in a 5% increase and the second scheme resulted in a 41% decrease when compared with the uncoupled control. When the myocyte was coupled with I_{sac} and Fbs together, it was reduced by 38%. For APD_{90} , coupling only with I_{sac} or Fbs produced a 21% and 19% increase. However, for the case of I_{sac} and Fbs together, the membrane potential was -62.5 mV at 500 ms, higher than the required threshold for APD_{90} . In addition, the resting potentials within 50 ms were all depolarized in the four coupling schemes. The case of coupling with both I_{sac} and Fbs had the highest increase of 9.8% when compared with the control. The increases in other two couplings were $\sim 5.5\%$.

3.2. Effects of I_{sac} and Fbs on Atrial Myocyte T_a . As shown in Figure 2, with the same coupling schemes as described in Figure 1(d) and with the cells stimulated at 1 Hz, when compared to control, the peak of T_a was slightly decreased by the coupled I_{sac} and decreased by 11% with the coupled Fbs. Coupling I_{sac} and Fbs together did not result in a further decrease in the peak in comparison with that from coupling

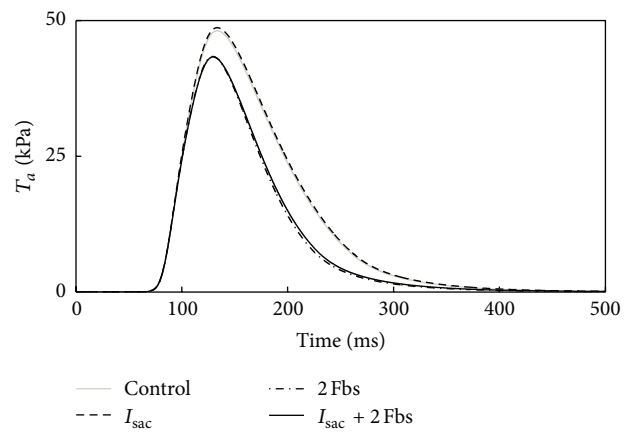


FIGURE 2: Illustration of changes in T_a of the atrial myocyte after coupling to I_{sac} , 2 Fbs, or I_{sac} and Fbs at the same time.

Fbs only. In addition, coupling Fbs (whether coupling I_{sac} or not) accelerated the reduction of T_a .

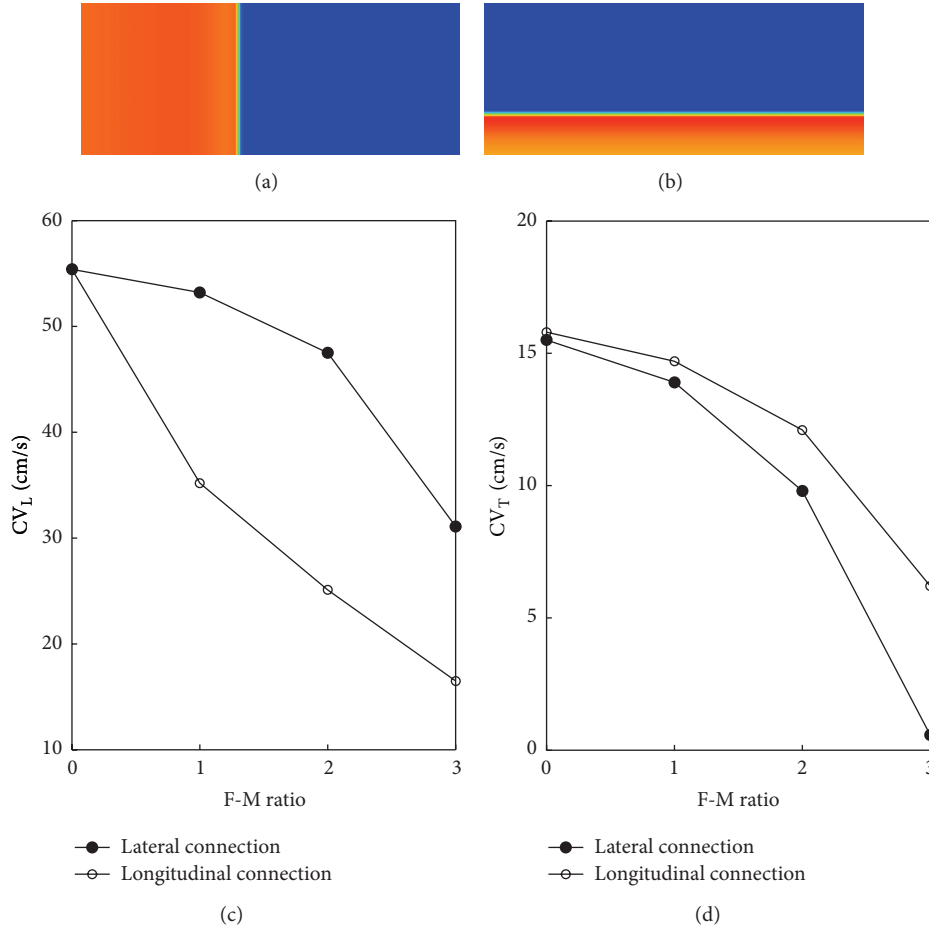


FIGURE 3: Effects of myocyte-Fbs coupling on CV: (a) longitudinal plane wave propagation, (b) transverse plane wave propagation. (c) CV_L versus F-M ratio for longitudinal and lateral connections, and (d) CV_T versus F-M ratio for longitudinal and lateral connections.

3.3. Coupling Fbs Modulate Conduction Velocity. As shown in Figure 3, with the stimulation applied at the left end (for longitudinal conduction) or the bottom (for transverse conduction) of the tissue, it was observed that CV progressively decreased as the F-M ratio increased in either case of FMC. For longitudinal connection, Fbs were coupled at both ends of the myocyte, namely, Fbs distributed along the long axis. In this situation, with the F-M ratio from 1 to 3, longitudinal CV (CV_L) decreased by 37% to 70%, and transverse CV (CV_T) decreased by 7% to 61%. For lateral connection, Fbs were coupled along the lateral sides of a myocyte, with corresponding CV_L decreased by 4% to 44%, and CV_T decreased by 10% to 96%. From Figures 3(c) and 3(d), it can be seen that longitudinal connection resulted in a larger reduction in CV_L than in CV_T , while lateral connection had a greater impact on CV_T .

3.4. 2D Simulation with Central Stimulus. Each grid in Figure 4(a) represents one atrial myocyte. Figure 4(b) gives one myocyte coupled with 2 Fbs (with an F-M ratio of 2). Figure 4(c) represents one myocyte coupled with 3 Fbs (with an F-M ratio of 3). G_{gap} in Figures 4(b) and 4(c) was 1 nS. The type of FMC was lateral connection.

In electrophysiology, it can be seen that the depolarization wave was generated in the center and spread out over time. The shape of the start of depolarization was ellipsoid. As the number of coupling Fbs increased, the conduction of excitation wave slowed down. At 40 ms, CV_L from 2 Fbs (Figure 4(b)) declined slightly when compared with 3 Fbs (Figure 4(c)). CV_T declined gradually as the F-M ratio increased, which was consistent with the results in Figure 3. Coupling with Fbs produced flat depolarization wave. As the deceleration of excitation wave, the myocytes coupled with Fbs required more time to return to the resting state. At 370 ms, tissues without Fbs and with an F-M ratio of 2 were at the resting state. However, the tissue with an F-M ratio of 3 did not reach the resting level even at 490 ms. In addition, with the contribution from I_{sac} and Fbs, the resting potential in tissues coupled with Fbs was less negative than that in the uncoupled tissue.

In mechanics, with the I_{sac} and Fbs added in the tissue, the excitation in tissues was delayed, leading to the delay of T_a in the same grid point in comparison with the uncoupled control. As a result, the deformation in coupled tissues lagged behind. At 150 ms, the contraction was obvious in Figure 4(a),

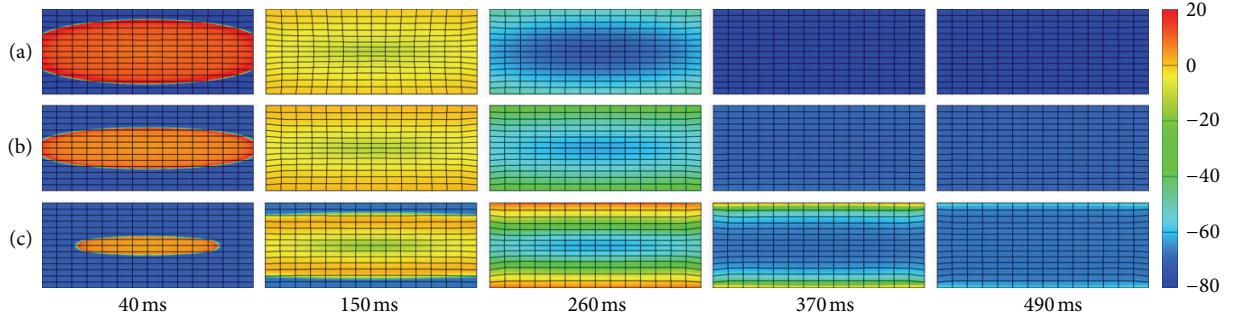


FIGURE 4: Central stimulus simulation of electromechanical coupling: (a) myocyte cells only, (b) 1 myocyte coupled to 2 Fbs with lateral connection in each grid point, and (c) 1 myocyte coupled to 3 Fbs with lateral connection in each grid point.

while imperceptible with 3 Fbs (Figure 4(c)). At 370 ms and 490 ms, meshes in Figures 4(a) and 4(b) gradually returned to relaxation along with the disappearance of propagating waves but kept contraction in Figure 4(c).

Figure 5 shows the quantitative deformations corresponding to the electromechanical activities in Figure 4. It shows that higher strains appear in the center area. In the uncoupled tissue, the maximum strain was 0.28 at 150 ms. When the F-M ratio was 2 and 3, it declined to 0.22 and 0.17, decreased by 21% and 39%. As the F-M ratio increased, it took longer to reach the maximum. As shown in Figure 5(c), due to the delay of T_a , the strain reached the peak value at 260 ms, 110 ms later than Figures 5(a) and 5(b). In addition, due to the slow conduction and less negative resting membrane in tissues with Fbs, there were still slight deformations presented in these tissues at 490 ms. Therefore, it can be concluded that coupling I_{sac} and Fbs delayed the deformation and decreased the maximum strain.

4. Discussion

The effects of coupling Fbs and I_{sac} on modulating human atrial myocyte excitability and AP morphology at the cellular level, and their effect on cardiac excitation wave conduction and contraction at the tissue level, have been investigated. The classical CRN model [30], the Rice model of the cardiac MF [32], the Maleckar model of atrial Fbs [33], and the Kuijpers model of I_{sac} [31] were employed in this study. All these models were integrated as a myocyte- I_{sac} -Fb coupling electromechanical model to investigate AP waveform and T_a of human atrial myocyte as a function of λ , G_{gap} , and the number of Fbs. For tissue models, the influence of Fbs on plane wave propagation has been studied with the electromechanical activities and strain maps provided.

4.1. Role of I_{sac} and Fbs Coupling on Human Atrial Myocyte Resting Membrane Potential, AP Waveform, and T_a . For I_{sac} , Zabel et al. explored the electrophysiological effect of sustained stretch and reported that a sustained, static load of the isolated rabbit ventricle influences repolarization and activation. The disparity of stretch effects between various locations in the ventricle resulted in an increased dispersion of repolarization [41]. Franz et al. confirmed that atrial SAC

was involved in the pathophysiology of atrial fibrillation [42, 43]. In this study, membrane potential of the myocyte coupled to I_{sac} with different λ was investigated with a prolongation of repolarization and APD and a depolarization of the resting potential for I_{sac} coupling. Our results agreed well with the observation from Shaw and Rudy that increasing K^+ concentration led to a depolarized membrane potential [44].

For Fbs, experimental research showed depolarization of neonatal rat ventricular cardiomyocyte strands when myofibroblasts interacted with myocytes [25]. Previous studies of FMC using myocyte-Fb coculture models have shown that the Fbs depolarized electrotonically coupled myocytes [1, 25, 33, 45]. MacCannell et al. showed that the resting membrane potential of the coupled myocyte was depolarized slightly (~ 2.7 mV) for up to 10 Fbs per myocyte and was insensitive to changes in G_{gap} [1]. In the study by Maleckar et al. a G_{gap} of 8 nS and two active 1Fbs resulted in a resting membrane potential elevation of 8.3 mV [33]. Our simulations also showed a depolarizing effect of coupled Fbs on resting membrane potential of the atrial myocytes. A maximum depolarization of 5.1 mV was obtained for an Fb density of 2 Fbs per myocyte with a G_{gap} of 1 nS and a maximum depolarization of 3.9 mV for a high G_{gap} (3 nS) with an F-M ratio of 2.

Coupling the human atrial myocyte with Fbs in this study also resulted in diverse effect on AP morphology during repolarization. Maleckar et al. used the FMC model with a high G_{gap} and found that Fbs functioned as strong current sources at rest and as both sources and sinks during the AP [33]. In their study, the prolongation of repolarization was early in the AP, and plateau was prolonged or shortened depending on both the Fb resting membrane potential and number of coupled Fbs [33]. MacCannell et al. compared ventricular AP when Fbs of 6 pF or 60 pF were coupled to a myocyte. The data showed that APD was shortened much more when large Fbs were coupled [1]. In our simulations, a myocyte coupled with different number of Fbs or different G_{gap} resulted in less depolarization in the membrane potential during the plateau when compared with control. Meanwhile, increasing Fbs and G_{gap} decreased APD₅₀ and prolonged APD₉₀.

Myocyte- I_{sac} -Fb coupling has been considered to investigate the resting membrane potential and AP waveform

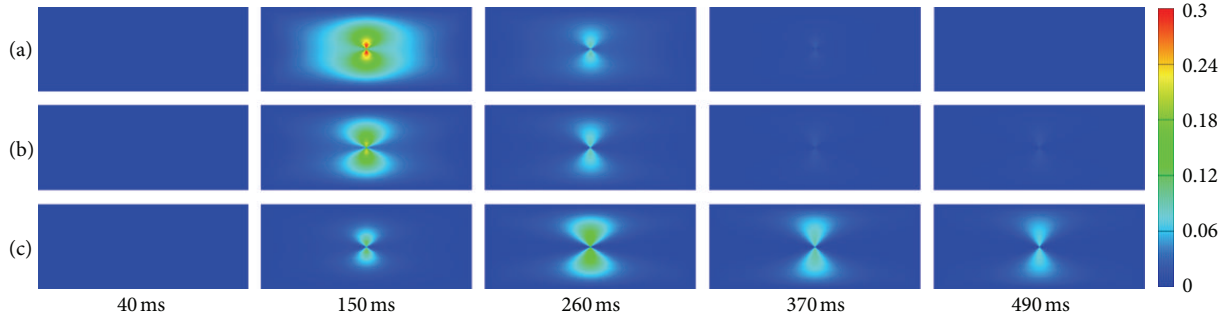


FIGURE 5: Strain maps of the central stimulus simulation: (a) myocyte cells only, (b) 1 myocyte coupled to 2 Fbs with lateral connection in each grid point, and (c) 1 myocyte coupled to 3 Fbs with lateral connection in each grid point.

of human atrial myocyte as a function of λ , G_{gap} , and the number of Fbs. Compared with only Fbs coupling or I_{sac} coupling, the myocyte- I_{sac} -Fb coupling had the highest depolarization at the resting membrane potential. However, the reduction of APD_{50} in myocyte- I_{sac} -Fb coupling was between other two couplings.

In addition to the effect on the human atrial myocyte electrophysiology, coupled Fbs and I_{sac} had important implications for the changes in T_a . In our study, T_a had the maximum value of 48.6 kPa, which was consistent with the normal range (10–75 kPa) [46]. Kerckhoffs et al. computed myofiber contraction in both nonfailing and failing hearts. Their results showed that in the failing heart model, inotropy was decreased by reducing peak fiber T_a by 27% [14]. In our study, the peak of T_a was decreased 11% with the coupled Fbs. The reason was that Fbs coupling reduced the Ca concentration and caused a reduction in T_a . Due to the strong correlation between fibrosis and heart failure [47–49], it can be expected that once the number of Fbs increased, a significant reduction would be revealed in T_a . In contrast, I_{sac} coupling did not bring much change in T_a .

4.2. Role of Fbs Coupling on CV. In an experimental study, Miragoli et al. found a biphasic effect on CV when endogenous Fbs proliferated with myocytes [25]. In a modeling study, Xie et al. showed that Fbs, whether coupled to myocytes or not, slowed conduction by creating zigzag conduction pathways [23]. In our simulation, CV_L and CV_T were investigated in both longitudinal and lateral connections. The results revealed a unidirectional decreasing in CV with Fbs coupling, which was consistent with Xie et al. [23]. However, different coupling types had different influence on CV_L and CV_T . For longitudinal connection, the conductance along the longitudinal direction dropped down, resulting in a significant decrease in CV_L . Similarly, lateral connection decreased the conductance along the transverse direction, which led to a higher reduction in CV_T .

4.3. Effects of I_{sac} and Fbs Coupling at the Tissue Level. For central stimulus simulations, the effect of Fbs on cardiac excitation conduction and contraction has been investigated in this study. Nash and Panfilov presented the same electromechanical activity due to a periodic point stimulation at

the center of the excitable medium [34]. Their modeling did not consider the biophysics of specific ionic currents and SAC channels. Meanwhile, T_a has been directly modeled using a single ODE dependent on the transmembrane potential. In our study, specific cell electrophysiological and mechanical models of myocyte and Fb were included in the electromechanical modeling. Results in Figure 4 revealed that Fbs and I_{sac} coupling slowed down the conduction of excitation wave and depolarized the resting membrane potential, which confirmed results at the cellular level (Figure 1). Furthermore, due to the higher elastic stiffness of myocardial scar tissue [38–40], deformations in tissues coupled Fbs decreased by 21–39% when compared with uncoupled control (Figure 5). Our strain maps were similar to previous modelings and clinical data [10, 50]. In [50], strains in normal regions were $-15.3 \pm 4.5\%$ and $-10.6 \pm 5.3\%$ in the infarct zone. Our calculation of strain was also in this range. On the basis of these results, we expected that once severe fibrosis occurred, strains decreased apparently due to the large stiffness in these areas, or similar to the rigid motion.

4.4. Limitations. Three limitations of this study should be mentioned. Firstly, the mechanisms of Fb mechanics should be further studied. It can be expected that once the detailed mechanical model of Fb is developed, it can be coupled to the myocyte mechanics model to simulate more precise mechanisms of myocyte- I_{sac} -Fb electromechanical coupling. Secondly, mechanosensitive currents have not been incorporated into the Fb model. However, previous studies implied that small electrical or mechanical perturbations in the cardiac Fb can alter the AP profile of the myocyte to which Fbs were coupled [51–53]. Thirdly, due to the lack of physiological data from the same species for the coupled model, only the existing experimental data relevant to each individual model was used to validate our simulation results.

5. Conclusions

In conclusion, a coupled myocyte- I_{sac} -Fb electromechanical model has been developed by integrating an active Fb model with a human atrial myocyte electrophysiological model (including I_{sac}) and a mechanical model. The effects of Fbs

and I_{sac} coupling on cardiac excitation conduction and contraction have also been investigated. The simulation results confirmed that Fbs and I_{sac} coupling resulted in diverse effects on AP morphology during repolarization, depolarized the resting membrane potential of human atrial myocyte, slowed down wave propagation and decreased strains in fibrotic tissue, and indicated that Fbs and SACs are important mechanisms in electromechanical coupling and should be considered in cardiac electromechanical modeling.

Acknowledgments

This project is supported by the 973 National Basic Research & Development Program (2007CB512100) and the National Natural Science Foundation of China (81171421, 61101046).

References

- [1] K. A. MacCannell, H. Bazzazi, L. Chilton, Y. Shibukawa, R. B. Clark, and W. R. Giles, "A mathematical model of electrotonic interactions between ventricular myocytes and fibroblasts," *Biophysical Journal*, vol. 92, no. 11, pp. 4121–4132, 2007.
- [2] F. B. Sachse, A. P. Moreno, G. Seemann, and J. A. Abildskov, "A model of electrical conduction in cardiac tissue including fibroblasts," *Annals of Biomedical Engineering*, vol. 37, no. 5, pp. 874–889, 2009.
- [3] P. Kohl and U. Ravens, "Cardiac mechano-electric feedback: past, present, and prospect," *Progress in Biophysics and Molecular Biology*, vol. 82, no. 1–3, pp. 3–9, 2003.
- [4] N. A. Trayanova and J. J. Rice, "Cardiac electromechanical models: from cell to organ," *Frontiers in Physiology*, vol. 2, p. 43, 2011.
- [5] N. A. Trayanova, "Whole-heart modeling: applications to cardiac electrophysiology and electromechanics," *Circulation Research*, vol. 108, no. 1, pp. 113–128, 2011.
- [6] N. A. Trayanova, J. Constantino, and V. Gurev, "Electromechanical models of the ventricles," *American Journal of Physiology. Heart and Circulatory Physiology*, vol. 301, no. 2, pp. H279–H286, 2011.
- [7] R. H. Clayton, O. Bernus, E. M. Cherry et al., "Models of cardiac tissue electrophysiology: progress, challenges and open questions," *Progress in Biophysics and Molecular Biology*, vol. 104, no. 1–3, pp. 22–48, 2011.
- [8] A. Carusi, K. Burrage, and B. Rodriguez, "Bridging experiments, models and simulations: an integrative approach to validation in computational cardiac electrophysiology," *American Journal of Physiology. Heart and Circulatory Physiology*, vol. 303, no. 2, pp. H144–H155, 2012.
- [9] E. M. Cherry and F. H. Fenton, "Effects of boundaries and geometry on the spatial distribution of action potential duration in cardiac tissue," *Journal of Theoretical Biology*, vol. 285, no. 1, pp. 164–176, 2011.
- [10] N. H. Kuijpers, E. Hermeling, P. H. Bovendeerd, T. Delhaas, and F. W. Prinzen, "Modeling cardiac electromechanics and mechano-electrical coupling in dyssynchronous and failing hearts: insight from adaptive computer models," *Journal of Cardiovascular Translational Research*, vol. 5, no. 2, pp. 159–169, 2012.
- [11] S. A. Niederer and N. P. Smith, "The role of the Frank-Starling law in the transduction of cellular work to whole organ pump function: a computational modeling analysis," *PLoS Computational Biology*, vol. 5, no. 4, Article ID e1000371, 2009.
- [12] S. A. Niederer and N. P. Smith, "An improved numerical method for strong coupling of excitation and contraction models in the heart," *Progress in Biophysics and Molecular Biology*, vol. 96, no. 1–3, pp. 90–111, 2008.
- [13] L. Xia, M. Huo, Q. Wei, F. Liu, and S. Crozier, "Analysis of cardiac ventricular wall motion based on a three-dimensional electromechanical biventricular model," *Physics in Medicine and Biology*, vol. 50, no. 8, pp. 1901–1917, 2005.
- [14] R. C. P. Kerckhoffs, J. H. Omens, A. D. McCulloch, and L. J. Mulligan, "Ventricular dilation and electrical dyssynchrony synergistically increase regional mechanical nonuniformity but not mechanical dyssynchrony: a computational model," *Circulation*, vol. 3, no. 4, pp. 528–536, 2010.
- [15] X.-C. Yang and F. Sachs, "Characterization of stretch-activated ion channels in *Xenopus* oocytes," *Journal of Physiology*, vol. 431, pp. 103–122, 1990.
- [16] K. Naruse and M. Sokabe, "Involvement of stretch-activated ion channels in Ca^{2+} mobilization to mechanical stretch in endothelial cells," *American Journal of Physiology. Cell Physiology*, vol. 264, no. 4, pp. C1037–C1044, 1993.
- [17] W. Craelius, V. Chen, and N. El-Sherif, "Stretch activated ion channels in ventricular myocytes," *Bioscience Reports*, vol. 8, no. 5, pp. 407–414, 1988.
- [18] J. O. Bustamante, A. Ruknudin, and F. Sachs, "Stretch-activated channels in heart cells: relevance to cardiac hypertrophy," *Journal of Cardiovascular Pharmacology*, vol. 17, supplement 2, pp. S110–S113, 1991.
- [19] I. Manabe, T. Shindo, and R. Nagai, "Gene expression in fibroblasts and fibrosis involvement in cardiac hypertrophy," *Circulation Research*, vol. 91, no. 12, pp. 1103–1113, 2002.
- [20] V. S. Petrov, G. V. Osipov, and J. Kurths, "Fibroblasts alter spiral wave stability," *Chaos*, vol. 20, no. 4, Article ID 045103, 2010.
- [21] J. M. T. De Bakker and H. M. V. Van Rijen, "Continuous and discontinuous propagation in heart muscle," *Journal of Cardiovascular Electrophysiology*, vol. 17, no. 5, pp. 567–573, 2006.
- [22] M. S. Spach, J. F. Heidlage, P. C. Dolber, and R. C. Barr, "Mechanism of origin of conduction disturbances in aging human atrial bundles: experimental and model study," *Heart Rhythm*, vol. 4, no. 2, pp. 175–185, 2007.
- [23] Y. Xie, A. Garfinkel, P. Camelliti, P. Kohl, J. N. Weiss, and Z. Qu, "Effects of fibroblast-myocyte coupling on cardiac conduction and vulnerability to reentry: a computational study," *Heart Rhythm*, vol. 6, no. 11, pp. 1641–1649, 2009.
- [24] M. A. Rossi, "Connective tissue skeleton in the normal left ventricle and in hypertensive left ventricular hypertrophy and chronic chagasic myocarditis," *Medical Science Monitor*, vol. 7, no. 4, pp. 820–832, 2001.
- [25] M. Miragoli, G. Gaudesius, and S. Rohr, "Electrotonic modulation of cardiac impulse conduction by myofibroblasts," *Circulation Research*, vol. 98, no. 6, pp. 801–810, 2006.
- [26] S. Zlochiver, V. Muñoz, K. L. Vikstrom, S. M. Taffet, O. Berenfeld, and J. Jalife, "Electrotonic myofibroblast-to-myocyte coupling increases propensity to reentrant arrhythmias in two-dimensional cardiac monolayers," *Biophysical Journal*, vol. 95, no. 9, pp. 4469–4480, 2008.
- [27] V. Jacquemet and C. S. Henriquez, "Loading effect of fibroblast-myocyte coupling on resting potential, impulse propagation, and repolarization: insights from a microstructure model,"

- American Journal of Physiology. Heart and Circulatory Physiology*, vol. 294, no. 5, pp. H2040–H2052, 2008.
- [28] Y. Xie, A. Garfinkel, J. N. Weiss, and Z. Qu, “Cardiac alternans induced by fibroblast-myocyte coupling: mechanistic insights from computational models,” *American Journal of Physiology. Heart and Circulatory Physiology*, vol. 297, no. 2, pp. H775–H784, 2009.
- [29] F. B. Sachse, A. P. Moreno, and J. A. Abildskov, “Electrophysiological modeling of fibroblasts and their interaction with myocytes,” *Annals of Biomedical Engineering*, vol. 36, no. 1, pp. 41–56, 2008.
- [30] M. Courtemanche, R. J. Ramirez, and S. Nattel, “Ionic mechanisms underlying human atrial action potential properties: insights from a mathematical model,” *American Journal of Physiology. Heart and Circulatory Physiology*, vol. 275, no. 1, part 2, pp. H301–H321, 1998.
- [31] N. H. Kuijpers, P. A. J. Hilbers, H. M. M. ten Eikelder, and M. G. J. Arts, *Cardiac electrophysiology and mechanoelectric feedback: modeling and simulation [Ph.D. thesis]*, Technische Universiteit Eindhoven, Eindhoven, The Netherlands, 2008.
- [32] J. J. Rice, F. Wang, D. M. Bers, and P. P. De Tombe, “Approximate model of cooperative activation and crossbridge cycling in cardiac muscle using ordinary differential equations,” *Biophysical Journal*, vol. 95, no. 5, pp. 2368–2390, 2008.
- [33] M. M. Maleckar, J. L. Greenstein, W. R. Giles, and N. A. Trayanova, “Electrotonic coupling between human atrial myocytes and fibroblasts alters myocyte excitability and repolarization,” *Biophysical Journal*, vol. 97, no. 8, pp. 2179–2190, 2009.
- [34] M. P. Nash and A. V. Panfilov, “Electromechanical model of excitable tissue to study reentrant cardiac arrhythmias,” *Progress in Biophysics and Molecular Biology*, vol. 85, no. 2-3, pp. 501–522, 2004.
- [35] R. A. Brown, R. Prajapati, D. A. McGruther, I. V. Yannas, and M. Eastwood, “Tensional homeostasis in dermal fibroblasts: mechanical responses to mechanical loading in three-dimensional substrates,” *Journal of Cellular Physiology*, vol. 175, no. 3, pp. 323–332, 1998.
- [36] L. Chilton, S. Ohya, D. Freed et al., “K⁺ currents regulate the resting membrane potential, proliferation, and contractile responses in ventricular fibroblasts and myofibroblasts,” *American Journal of Physiology. Heart and Circulatory Physiology*, vol. 288, no. 6, pp. H2931–H2939, 2005.
- [37] Y. Shibukawa, E. L. Chilton, K. A. MacCannell, R. B. Clark, and W. R. Giles, “K⁺ currents activated by depolarization in cardiac fibroblasts,” *Biophysical Journal*, vol. 88, no. 6, pp. 3924–3935, 2005.
- [38] A. Biernacka and N. G. Frangogiannis, “Aging and cardiac fibrosis,” *Aging and Disease*, vol. 2, no. 2, pp. 158–173, 2011.
- [39] C. H. Conrad, W. W. Brooks, J. A. Hayes, S. Sen, K. G. Robinson, and O. H. L. Bing, “Myocardial fibrosis and stiffness with hypertrophy and heart failure in the spontaneously hypertensive rat,” *Circulation*, vol. 91, no. 1, pp. 161–170, 1995.
- [40] M. F. Berry, A. J. Engler, Y. J. Woo et al., “Mesenchymal stem cell injection after myocardial infarction improves myocardial compliance,” *American Journal of Physiology. Heart and Circulatory Physiology*, vol. 290, no. 6, pp. H2196–H2203, 2006.
- [41] M. Zabel, B. S. Koller, F. Sachs, and M. R. Franz, “Stretch-induced voltage changes in the isolated beating heart: importance of the timing of stretch and implications for stretch-activated ion channels,” *Cardiovascular Research*, vol. 32, no. 1, pp. 120–130, 1996.
- [42] M. R. Franz and F. Bode, “Mechano-electrical feedback underlying arrhythmias: the atrial fibrillation case,” *Progress in Biophysics and Molecular Biology*, vol. 82, no. 1–3, pp. 163–174, 2003.
- [43] F. Bode, F. Sachs, and M. R. Franz, “Tarantula peptide inhibits atrial fibrillation,” *Nature*, vol. 409, no. 6816, pp. 35–36, 2001.
- [44] R. M. Shaw and Y. Rudy, “Electrophysiologic effects of acute myocardial ischemia: a mechanistic investigation of action potential conduction and conduction failure,” *Circulation Research*, vol. 80, no. 1, pp. 124–138, 1997.
- [45] V. Jacquemet and C. S. Henriquez, “Modelling cardiac fibroblasts: interactions with myocytes and their impact on impulse propagation,” *Europace*, vol. 9, pp. 29–37, 2007.
- [46] S. A. Niederer, P. J. Hunter, and N. P. Smith, “A quantitative analysis of cardiac myocyte relaxation: a simulation study,” *Biophysical Journal*, vol. 90, no. 5, pp. 1697–1722, 2006.
- [47] J. Pellman, R. C. Lyon, and F. Sheikh, “Extracellular matrix remodeling in atrial fibrosis: mechanisms and implications in atrial fibrillation,” *Journal of Molecular and Cellular Cardiology*, vol. 48, no. 3, pp. 461–467, 2010.
- [48] R. G. Assomull, S. K. Prasad, J. Lyne et al., “Cardiovascular magnetic resonance, fibrosis, and prognosis in dilated cardiomyopathy,” *Journal of the American College of Cardiology*, vol. 48, no. 10, pp. 1977–1985, 2006.
- [49] B. T. John, B. K. Tamarappoo, J. L. Titus, W. D. Edwards, W.-K. Shen, and S. S. Chugh, “Global remodeling of the ventricular interstitium in idiopathic myocardial fibrosis and sudden cardiac death,” *Heart Rhythm*, vol. 1, no. 2, pp. 141–149, 2004.
- [50] M. L. Antoni, S. A. Mollema, V. Delgado et al., “Prognostic importance of strain and strain rate after acute myocardial infarction,” *European Heart Journal*, vol. 31, no. 13, pp. 1640–1647, 2010.
- [51] P. Kohl, P. Camelliti, F. L. Burton, and G. L. Smith, “Electrical coupling of fibroblasts and myocytes: relevance for cardiac propagation,” *Journal of Electrocardiology*, vol. 38, no. 4, supplement, pp. 45–50, 2005.
- [52] M. B. Rook, A. C. G. Van Ginneken, B. De Jonge, A. El Aoumari, D. Gros, and H. J. Jongsma, “Differences in gap junction channels between cardiac myocytes, fibroblasts, and heterologous pairs,” *American Journal of Physiology. Cell Physiology*, vol. 263, no. 5, pp. C959–C977, 1992.
- [53] P. Kohl, A. G. Kamkin, I. S. Kiseleva, and D. Noble, “Mechanosensitive fibroblasts in the sino-atrial node region of rat heart: interaction with cardiomyocytes and possible role,” *Experimental Physiology*, vol. 79, no. 6, pp. 943–956, 1994.

Research Article

Hybrid Mesh for Nasal Airflow Studies

Mohammed Zubair,¹ Mohammed Zulkifly Abdullah,¹ and Kamarul Arifin Ahmad²

¹ School of Aerospace and Mechanical Engineering, Universiti Sains Malaysia, 14300 Nibong Tebal, Pulau Pinang, Malaysia

² Department of Aerospace Engineering, Universiti Putra Malaysia, 43400 Serdang, Selangor, Malaysia

Correspondence should be addressed to Mohammed Zubair; mdzubairmanipal@gmail.com

Received 14 May 2013; Revised 24 June 2013; Accepted 25 June 2013

Academic Editor: Eddie Ng

Copyright © 2013 Mohammed Zubair et al. This is an open access article distributed under the Creative Commons Attribution License, which permits unrestricted use, distribution, and reproduction in any medium, provided the original work is properly cited.

The accuracy of the numerical result is closely related to mesh density as well as its distribution. Mesh plays a very significant role in the outcome of numerical simulation. Many nasal airflow studies have employed unstructured mesh and more recently hybrid mesh scheme has been utilized considering the complexity of anatomical architecture. The objective of this study is to compare the results of hybrid mesh with unstructured mesh and study its effect on the flow parameters inside the nasal cavity. A three-dimensional nasal cavity model is reconstructed based on computed tomographic images of a healthy Malaysian adult nose. Navier-Stokes equation for steady airflow is solved numerically to examine inspiratory nasal flow. The pressure drop obtained using the unstructured computational grid is about 22.6 Pa for a flow rate of 20 L/min, whereas the hybrid mesh resulted in 17.8 Pa for the same flow rate. The maximum velocity obtained at the nasal valve using unstructured grid is 4.18 m/s and that with hybrid mesh is around 4.76 m/s. Hybrid mesh reported lower grid convergence index (GCI) than the unstructured mesh. Significant differences between unstructured mesh and hybrid mesh are determined highlighting the usefulness of hybrid mesh for nasal airflow studies.

1. Introduction

The anatomy of the human nasal cavity is further complicated by prevalence of anomalies and diseases. A number of researchers have used computational fluid dynamics (CFD) to study the physiology and fluid flow properties inside the nasal cavity [1–5]. A recent review on the use of CFD for drug delivery design process discussed the importance of using CFD in drug delivery in nasal cavities [6]. However, the accuracy of the CFD study depends primarily on quality and quantity of the mesh distribution. A good mesh must be able to resolve the velocity vectors and effectively capture the fluid properties at all regions inside the nasal cavity. Structured mesh, in spite of its effectiveness in resolving flow properties, is very difficult to develop inside a complicated domain like the nose. Structured mesh was employed only to model the human upper bronchial tree like the trachea and bronchii [7, 8]. Recently, Vinchurkar and Longest [9] considered the effects of various common mesh styles on grid convergence, velocity fields, and particle deposition profiles in a bifurcating respiratory model. The mesh considered included a structured multiblock hexahedral style, an

unstructured tetrahedral mesh, a flow-adaptive tetrahedral design, and a hybrid style consisting of tetrahedral and prism elements. However, the work was limited to a small bifurcating section and did not address the entire upper airway domain. It is easy to develop structured mesh in a simple bifurcating domain. But when it comes to the complicated nasal cavity, the process is very tedious and prohibitive in terms of time and cost involved. Earlier works of Hörschler et al. [10] and Zamankhan et al. [11] used a simplified nasal domain and therefore the construction of structured mesh was rendered possible. In an interesting work by Longest and Vinchurkar (2007) [12], several mesh types were compared. The hexahedral mesh was observed to have grid convergence index (GCI) values that were an order of magnitude below the unstructured tetrahedral mesh values for all resolutions considered. This cannot be expected of realistic nasal cavity obtained from actual CT scans. Hence, we find the most of the researchers use unstructured tetrahedral meshing scheme to develop the CFD model. The accuracy of such a mesh is uncertain and therefore its results cannot be utilized to quantify the understanding of flow physiology. Zubair et al. [13] highlighted the need for using hybrid mesh for nasal airflow

studies. Recently, hybrid meshes have also been introduced which combines unstructured lower-order internal elements and higher-order pyramid, prism, or hexahedral elements on the surface [12]. Typically they have the advantage of better resolution at near-wall flow field. Lee et al. [14] reportedly used a cluster of prism mesh near the surface to improve the accuracy of the model. But the work did not discuss the usefulness of such a mesh over purely unstructured mesh in the complicated biomedical domain. Some of the popular grid generation softwares Gridgen (Pointwise Inc., USA) and T-grid (Fluent Inc., USA) offer features for developing hybrid mesh.

Hybrid mesh has the ability to resolve the near wall boundary and can be used to develop mesh closer to $y^+ = 1$. Here y^+ refers to the nondimensional distance for wall-bounded flow. It is important in turbulence modeling to determine the proper size of the cells near the domain walls. Hybrid mesh is effective in resolving turbulence issues and particularly suitable for use with LES models. In the current study, numerical simulation was carried out to validate the usefulness of hybrid mesh over unstructured tetrahedral mesh. A three-dimensional (3D) nasal cavity model was reconstructed from computed tomographic images (CT) of a healthy Malaysian female. The effect of different mesh type on the fluid flow properties was evaluated.

2. Method

The study was based on an anatomical model of the normal nasal airway obtained from a CT scan of a Malaysian subject from Universiti Sains Malaysia, Medical Campus Hospital. The scan images were segmented slice by slice with an appropriate threshold value using MIMIC (Materialise, Ann Arbor, MI, USA). The 3D polyline data of the nasal cavity was processed in CATIA and meshed with unstructured tetrahedral elements using GAMBIT 2.3.16 (Fluent Inc., Lebanon). The developed 3D nasal cavity model with 10 cross-sectional plane is as shown in Figure 1. These cross-sectional planes represented different locations spanning the entire nasal cavity length and were utilized to extract information about the flow physics inside the flow domain.

The two different types of mesh are as depicted in Figure 2. Figure 2(a) represents the grid display at a location 3.5 cm from the nostril for unstructured mesh type. And Figure 2(b) shows the hybrid mesh at the same location consisting of prism elements stacked at the wall boundary. An unstructured tetrahedral mesh with 1,653,469 elements was developed from the grid independency test (refer Figure 3(a)). This was further adapted using the y^+ adaptation technique which resulted in a mesh count of 2,522,274 elements. The best possible y^+ value that could be obtained for this mesh was around 1.31. Also, a hybrid mesh with 1,691,940 elements consisting of a combination of 6 layers of prism cells near the near wall boundary and the tetrahedral elements at the remaining flow domain was obtained from grid independency study (see Figure 3(b)). An initial thickness of 3.8×10^{-5} m was maintained for the prism cell to obtain a $y^+ < 1$. The worst cell had the maximum value of skewness of about 0.86.

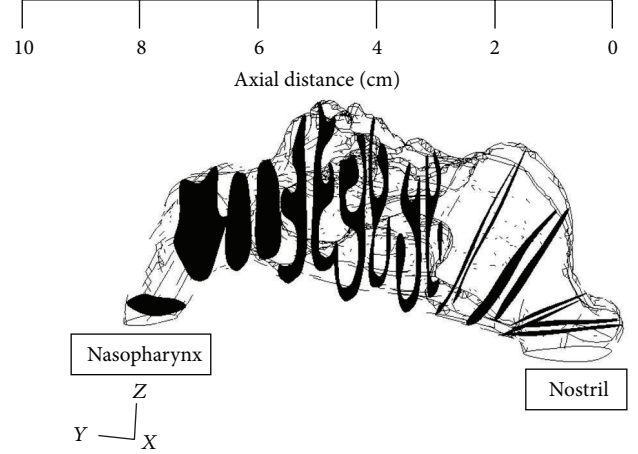


FIGURE 1: Location of the ten cross-sections along the axial length.

The nondimensional wall distance y^+ is given by

$$y^+ = \frac{u_t y}{\vartheta}, \quad (1)$$

where u_t is the skin friction velocity, y is the initial height above the wall, and ϑ is the kinematic viscosity of air.

To solve the governing mass and momentum conservation equations in each of the mesh style, the CFD package Fluent 6.3.26 (Fluent Inc., Lebanon, PA, USA) has been employed. This commercial software provides an unstructured control-volume-based solution method for both unstructured tetrahedral and hybrid mesh types. The airflow was assumed to be laminar for flow rates up to 15 L/min, and beyond 15 L/min flow was considered turbulent, as predicted by Wen et al., 2008 [1], and Segal et al., 2008 [3]. For turbulence flow, we used the SST $k-\omega$ turbulence model, a two-equation turbulence model, the suitability of which has been explored by Wen et al., 2008 [1], and Mylavaram et al. [4]. The flow boundary conditions used were as follows: (1) the nasal wall was rigid, (2) the effect of mucus was negligibly small, (3) no-slip condition at the airway wall, and (4) nasal cavity developed was without sinuses, which was commensurate with several earlier studies which neglected the effect of sinus on main flow. The mass flow inlet boundary is defined at the nostril inlet and outflow boundary condition is selected at the outlet.

2.1. Governing Equations of Flow. In the present study steady RANS equations for turbulent incompressible fluid flow with constant properties are used. The governing flow field equations are the continuity and the Reynolds averaged Navier-Stokes equations, which are given by

$$\begin{aligned} \frac{\partial u_i}{\partial x_j} &= 0, \\ \frac{\partial u_i u_j}{\partial x_j} &= -\frac{1}{p} \frac{\partial p}{\partial x_j} + \frac{\partial}{\partial x_j} (\vartheta S_{ij} - \overline{u'_i u'_j}), \end{aligned} \quad (2)$$

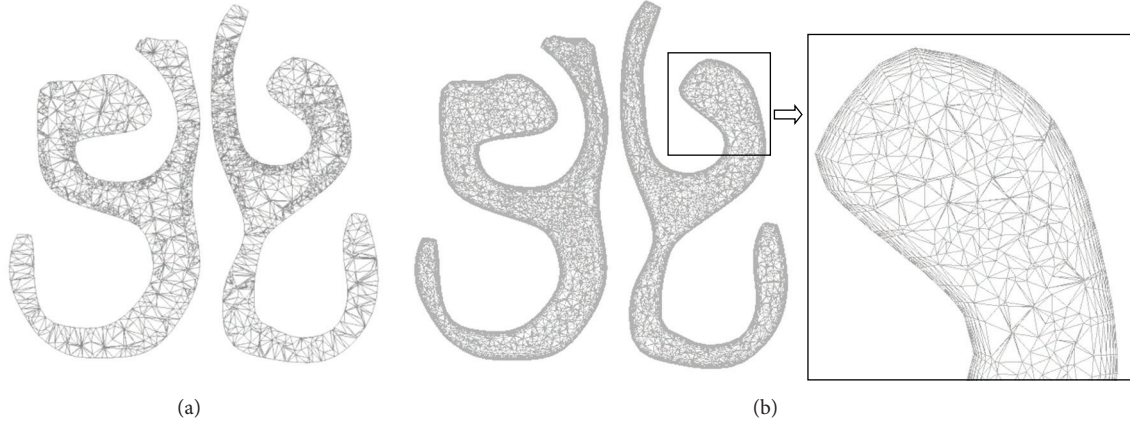


FIGURE 2: Cross-section of the nasal cavity at a distance of 4.5 cm from the nostril: (a) unstructured mesh and (b) hybrid mesh.

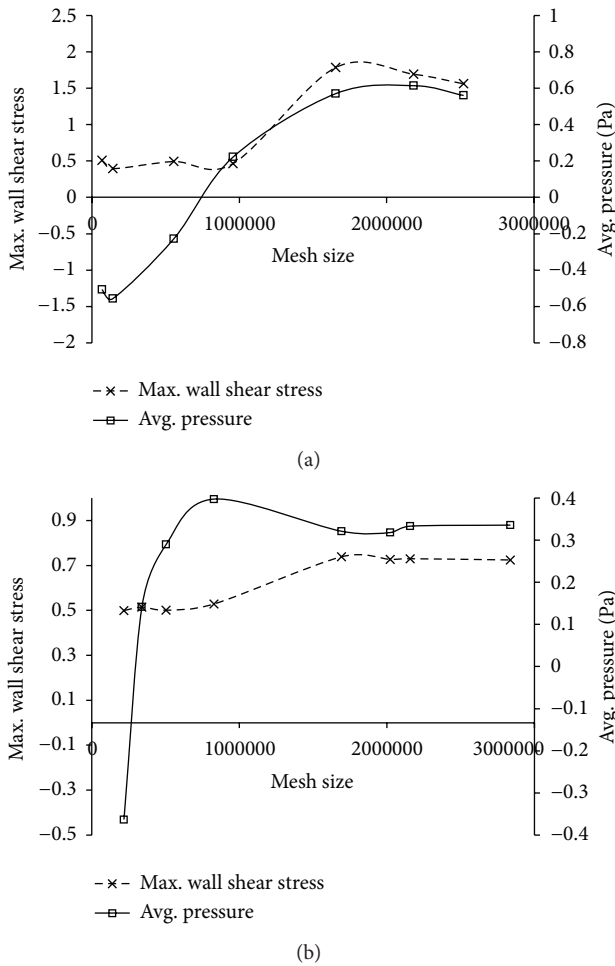


FIGURE 3: Grid independency study: (a) unstructured mesh and (b) prism mesh.

where S_{ij} is the main strain rate and calculated by

$$S_{ij} = \frac{1}{2} \left(\frac{\partial u_i}{\partial x_j} + \frac{\partial u_j}{\partial x_i} \right), \quad (3)$$

and $\overline{u_i' u_j'} = \tau_{ij}$ is the unknown turbulent or Reynolds-stress tensor and u_i represents the velocity fluctuation in i -direction. These equations are not a closed set and turbulence models are used to model the turbulent or Reynolds-stress tensor. Shear stress transport SST $k-\omega$ turbulent model closure equations are provided in the work of Menter [15].

Discretization errors arise from numerical algorithms, the mesh style and quality used to discretize the equations, and boundary conditions and is the difference between the exact solution of the governing equations and the discretized system. In this work, the Richardson's extrapolation method has been utilized to determine the mesh-related discretization errors. Celik et al. (2008) [16] and Longest and Vinchurkar (2007) [12] have presented the procedures to apply the Richardson's extrapolation (RE) method to determine the discretization error. Local and global orders of accuracy, extrapolated results, percent errors, and grid convergence indexes are calculated to ensure that a high-fidelity results has indeed been obtained. In total, 3 meshes listed in Table 1 are evaluated to determine the GCI values for each of the mesh type.

For grid sizes $h_1 < h_2 < h_3$, the local apparent order of accuracy, p , of the simulation was calculated with the following expressions, and the results are tabulated in Table 1. Here the grid refinement factor $r_{21} = h_2/h_1$ and $r_{32} = h_3/h_2$ were maintained greater than 1.3:

$$p = \frac{1}{\ln r_{21}} \left| \ln \left| \frac{\epsilon_{32}}{\epsilon_{21}} \right| + q(p) \right|, \quad (4)$$

$$q(p) = \ln \left(\frac{r_{21}^p - s}{r_{32}^p - s} \right),$$

$$s = \text{sign} \left(\frac{\epsilon_{32}}{\epsilon_{21}} \right),$$

where

$$\begin{aligned} \epsilon_{21} &= \varphi_2 - \varphi_1, \\ \epsilon_{32} &= \varphi_3 - \varphi_2. \end{aligned} \quad (5)$$

TABLE 1: Comparison of discretisation error measurement for hybrid and unstructured mesh type.

	$\varphi = \text{max. velocity (m/s)}$ at the nasal valve (hybrid mesh)	$\varphi = \text{max. velocity (m/s)}$ at the nasal valve (unstructured mesh)
$M1, M2, M3$	1691940, 504259, 218262	2022162, 450233, 136678
r_{21}	1.5	1.62
r_{32}	1.33	1.49
φ_1	4.6576	4.0123
φ_2	4.5487	4.5089
φ_3	4.1892	4.5549
P	4.03	4.7830
$\varphi_{\text{ext}}^{21}$	4.684	3.8919
e_a^{21}	2.34%	12.38%
e_{ext}^{21}	0.56%	3.09%
GCI_{fine}^{21}	0.71%	3.75%

Equations (4) are solved using an iterative procedure with an initial guess of φ_1 , where φ_n represents the result of the associated grid n .

The extrapolated values $\varphi_{\text{ext}}^{21}$ and $\varphi_{\text{ext}}^{32}$ are calculated using the following equations:

$$\varphi_{\text{ext}}^{21} = \frac{(r_{21}^p \varphi_1 - \varphi_2)}{(r_{21}^p - 1)}, \quad (6)$$

$$\varphi_{\text{ext}}^{32} = \frac{(r_{32}^p \varphi_2 - \varphi_3)}{(r_{32}^p - 1)}.$$

The relative errors, e_a^{21} and e_{ext}^{21} , are calculated by the expressions:

$$e_a^{21} = \left| \frac{\varphi_1 - \varphi_2}{\varphi_1} \right|, \quad (7)$$

$$e_{\text{ext}}^{21} = \left| \frac{\varphi_{\text{ext}}^{21} - \varphi_1}{\varphi_{\text{ext}}^{21}} \right|. \quad (8)$$

Finally, the grid convergence index for the most refined mesh is calculated using the expression:

$$GCI_{\text{fine}}^{21} = F_s \frac{e_a^{21}}{r_{21}^{\text{p,avg}} - 1}. \quad (9)$$

In (8), F_s coefficient serves as a ‘‘buffer coefficient’’ for the extrapolated error approximation GCI and its value for more refined grid cases as in the case of this study is taken as 1.25.

The investigated parameters in the sensitivity study are the maximum velocity magnitude at the nasal valve region and are performed for the case of 20 L/min. Grid convergence indices (GCI) are presented as a percent and can effectively be interpreted as the percent error of the simulation result based on grids analyzed.

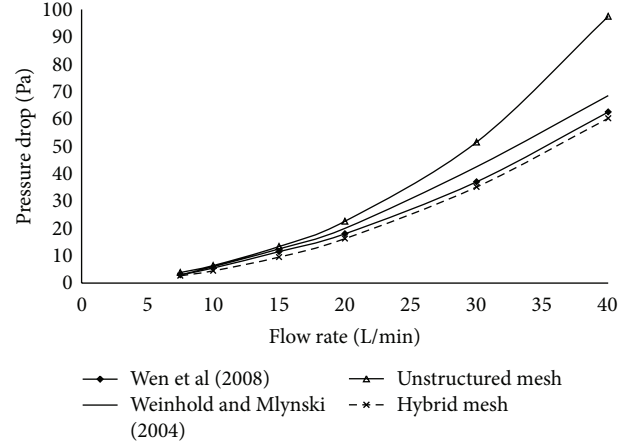


FIGURE 4: Resistance comparison for hybrid and unstructured mesh types.

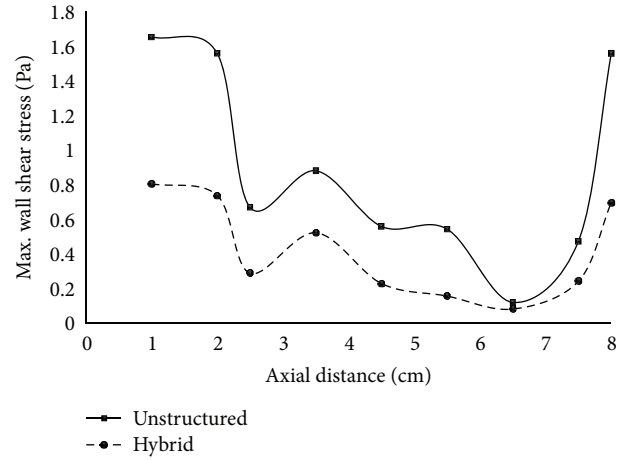


FIGURE 5: Maximum wall shear stress along the length of the nasal cavity.

3. Results and Discussion

The pressure drop obtained using the unstructured computational grid was around 22.6 Pa for a flow rate of 20 L/min, whereas a value of 17.8 Pa was determined for hybrid mesh. The pure unstructured mesh overpredicted the value when compared to that obtained by Wen et al. [1] and Weinhold and Mlynski [17] (18 Pa and 20 Pa, resp.). The resistance obtained varied from 0.026 to 0.124 Pa·sec/mL for flow rate of 7.5 L/min to 40 L/min, respectively. For a flow rate of 15 L/min, the flow resistance was 0.048 Pa·sec/mL. Garcia et al. [18] reported identical results in the range of 0.039 and 0.082 Pa·s/L for a flow rate of 15 L/min. Figure 4 presents results of hybrid mesh which were similar to that reported in literature. About 21% difference in resistance was obtained between the purely unstructured mesh and the hybrid mesh. In case of the nasal valve, located at a distance of around 2 cm from the anterior region, the maximum velocity obtained with unstructured grid was 4.18 m/s and that with hybrid mesh was 4.76 m/s. On the contrary, 4.82 m/s and

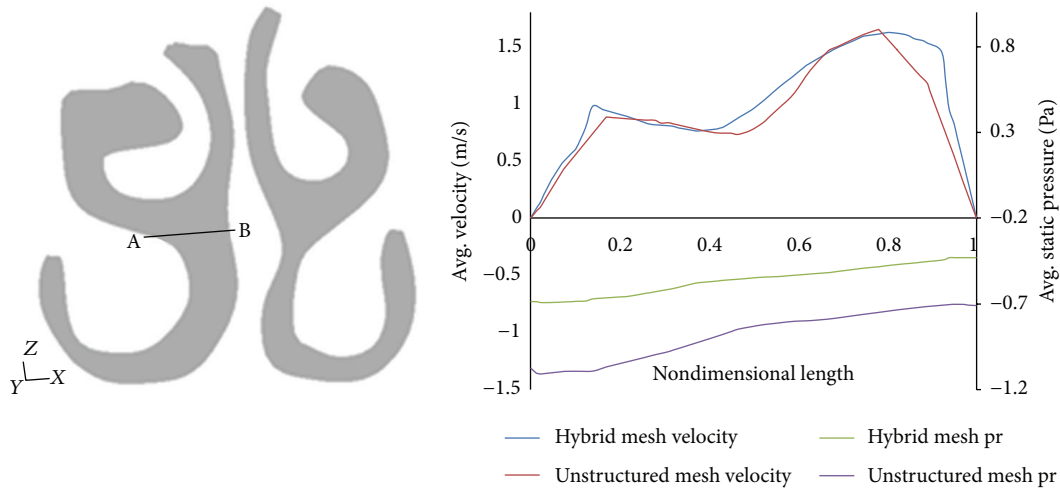


FIGURE 6: Velocity and pressure distribution along the line AB at a distance of 4.5 cm from the nostril.

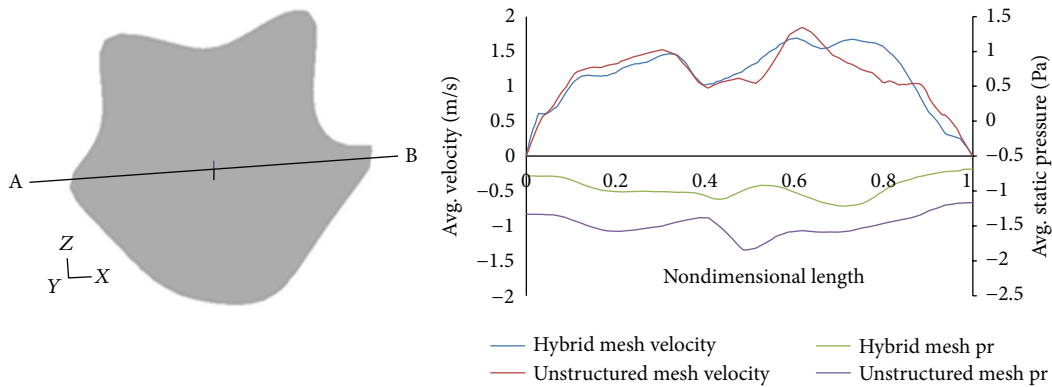


FIGURE 7: Velocity and pressure distribution along the line AB at the nasopharynx section.

3.1 m/s were reported by Xiong et al. [19] and Croce et al. [20], respectively, for the same location. Thus, considerable differences were observed in the values obtained with respect to hybrid mesh and that of pure unstructured mesh.

A wall shear stress distribution has been plotted for different cross-sections of the nasal cavity. Figure 5 clearly shows the variation in the maximum wall shear stress obtained for the two types of mesh used. The unstructured mesh is generally not very effective in resolving boundary layer phenomenon and as expected overpredicted the formation of wall shear stress. The anterior and the posterior regions registered more variations. Thus, it can be concluded that hybrid mesh which has a better mesh distribution at the boundary surface is useful in capturing the wall shear stresses.

Figures 6 and 7 show the distribution of velocity and pressure at two different locations inside the nasal cavity. These plots have been obtained along the marked line AB as shown in these figures. There is a considerable difference in the values obtained between pure unstructured tetrahedral mesh and the hybrid mesh. The unstructured mesh overpredicts the pressure values, and, moreover, the values of average static velocity in both locations were much lower for hybrid

mesh when compared to the unstructured mesh. Therefore, the results obtained using the purely unstructured mesh are not suitable for quantification of flow depicting the nasal physiological function.

Table 1 presents the comparison for discretisation error measurement. The values have been estimated at the critical location of nasal valve region. Nasal valve is the narrowest part of the nasal cavity and has significant influence on the flow parameters. Unstructured mesh and hybrid mesh behave differently and therefore have different GCI values. The relative error obtained in case of hybrid mesh was only about 2.34%, whereas that determined for unstructured mesh was as high as 12.38%. Moreover, the GCI value for hybrid mesh was ideally less than 1%, whereas for unstructured mesh it was about 3.75%. The unstructured mesh has randomly oriented tetrahedral faces, which are not in tandem with direction of flow. The prism mesh adopted at the near wall boundary provides the necessary alignment to the flow direction, thereby reducing the numerical diffusion errors in case of hybrid mesh scheme. It is probably the reason why tetrahedral mesh has higher GCI values when compared to hybrid mesh type. In context of nasal cavity, one must realize

that the nasal architecture is very complicated and is not a uniform pathway. It is a narrow tunnel lined with turbinates and mucous layer, which makes building mesh very difficult. Therefore, it is subjected to very high wall bounded flows and resolving wall layer with appropriate mesh is therefore very important. Thus the hybrid mesh is effective in reducing the diffusion errors at rugged wall boundary and prevents its dissipation into main flow. Earlier studies on bifurcating airways have reported GCI value of about 5% for unstructured mesh schemes [12]. The probable reason for reduced GCI values for unstructured mesh in this study (<5%) is due to high density of mesh cluster at the boundary wall. The y^+ of about 1.37 was reported for unstructured grid in this study. This clearly shows that mesh resolution at the corrugated nasal walls has significant importance in overcoming errors due to diffusion. However, developing dense mesh along the wall surface using the unstructured tetrahedral type mesh will add to the increased mesh count and thereby is expensive and would take considerably longer duration to solve the equations. On the other hand, hybrid mesh provides a degree of control over mesh resolution in wall boundaries, and mesh with $y^+ = 1$ is easily generated. Therefore, hybrid mesh has several advantages over a purely tetrahedral mesh type. Moreover, the SST $k-\omega$ turbulence model employed in this work may also contribute to the lower GCI values. SST $k-\omega$ turbulence models were reported to be very useful in wall-bounded flows and have successfully been adopted in many studies in the past [21, 22]. However, further studies are required to authenticate the choice of turbulence models in concluding the lower GCI values for both types of meshes used. Nevertheless, hybrid mesh owing to their ease of development and boundary layer resolution is compatible with complicated geometrical domains such as nasal cavity.

Most of the earlier researchers have employed unstructured mesh in order to evaluate the flow physics inside the complicated nasal domain. It is difficult and time consuming to develop structured meshes. In the absence of structured meshes, hybrid mesh has several advantages over purely unstructured mesh. Hybrid mesh gives better resolution of boundary layer phenomenon. It is particularly useful if one is considering precision turbulence models like the large eddy simulation (LES) models which require well-refined meshes at the wall boundaries [14]. The current study has demonstrated that pure unstructured meshes are not sufficient to resolve the flow features inside the nasal cavity and hence hybrid mesh should be considered in all future nasal flow studies.

4. Conclusion

The usefulness of hybrid mesh over unstructured mesh has been quantified. There is considerable difference in the values of properties that are obtained using unstructured tetrahedral mesh and that of hybrid mesh. Hybrid mesh is easy to develop when compared to pure structural mesh providing good control over the mesh density and is considered useful in resolving wall bounded flows. The complicated anatomy of the nasal cavity makes it difficult to develop structured meshes, and since the unstructured mesh is not accurate

enough to capture the flow physics, hybrid mesh offers the best alternative.

Conflict of Interests

The authors do not have any conflict of interests with the content of this paper.

Acknowledgments

One of the authors is a postdoctoral fellow at Universiti Sains Malaysia and acknowledges the support of the RUGS grant from University Sains Malaysia and Universiti Putra Malaysia.

References

- [1] J. Wen, K. Inthavong, J. Tu, and S. Wang, "Numerical simulations for detailed airflow dynamics in a human nasal cavity," *Respiratory Physiology and Neurobiology*, vol. 161, no. 2, pp. 125–135, 2008.
- [2] Y. S. Cheng, H. C. Yeh, R. A. Guilmette, S. Q. Simpson, K. H. Cheng, and D. L. Swift, "Nasal deposition of ultrafine particles in human volunteers and its relationship to airway geometry," *Aerosol Science and Technology*, vol. 25, no. 3, pp. 274–291, 1996.
- [3] R. A. Segal, G. M. Kepler, and J. S. Kimbell, "Effects of differences in nasal anatomy on airflow distribution: a comparison of four individuals at rest," *Annals of Biomedical Engineering*, vol. 36, no. 11, pp. 1870–1882, 2008.
- [4] G. Mylavarapu, S. Murugappan, M. Mihaescu, M. Kalra, S. Khosla, and E. Gutmark, "Validation of computational fluid dynamics methodology used for human upper airway flow simulations," *Journal of Biomechanics*, vol. 42, no. 10, pp. 1553–1559, 2009.
- [5] V. N. Riazuddin, M. Zubair, M. Z. Abdullah et al., "Numerical study of inspiratory and expiratory flow in a human nasal cavity," *Journal of Medical and Biological Engineering*, vol. 31, no. 3, pp. 201–206, 2011.
- [6] M. Kleven, M. C. Melaaen, and P. G. Djupesland, "Computational fluid dynamics (CFD) applied in the drug delivery design process to the nasal passages: a review," *Journal of Mechanics in Medicine and Biology*, vol. 12, no. 1, Article ID 1230002, 17 pages, 2012.
- [7] M. A. Nagels and J. E. Cater, "Large eddy simulation of high frequency oscillating flow in an asymmetric branching airway model," *Medical Engineering and Physics*, vol. 31, no. 9, pp. 1148–1153, 2009.
- [8] M. Mihaescu, S. Murugappan, M. Kalra, S. Khosla, and E. Gutmark, "Large Eddy simulation and Reynolds-Averaged Navier-Stokes modeling of flow in a realistic pharyngeal airway model: an investigation of obstructive sleep apnea," *Journal of Biomechanics*, vol. 41, no. 10, pp. 2279–2288, 2008.
- [9] S. Vinchurkar and P. W. Longest, "Evaluation of hexahedral, prismatic and hybrid mesh styles for simulating respiratory aerosol dynamics," *Computers and Fluids*, vol. 37, no. 3, pp. 317–331, 2008.
- [10] I. Hörschler, Ch. Brücker, W. Schröder, and M. Meinke, "Investigation of the impact of the geometry on the nose flow," *European Journal of Mechanics B*, vol. 25, no. 4, pp. 471–490, 2006.

- [11] P. Zamankhan, G. Ahmadi, Z. Wang et al., "Airflow and deposition of nano-particles in a human nasal cavity," *Aerosol Science and Technology*, vol. 40, no. 6, pp. 463–476, 2006.
- [12] P. W. Longest and S. Vinchurkar, "Effects of mesh style and grid convergence on particle deposition in bifurcating airway models with comparisons to experimental data," *Medical Engineering and Physics*, vol. 29, no. 3, pp. 350–366, 2007.
- [13] M. Zubair, M. Z. Abdullah, A. H. Suzina, I. Rushdan, I. L. Shuaib, and K. A. Ahmad, "A critical overview of CFD modeling of nasal airflow," *Journal of Medical and Biological Engineering*, vol. 32, no. 2, pp. 77–84, 2012.
- [14] J. H. Lee, Y. Na, S. K. Kim, and S. K. Chung, "Unsteady flow characteristics through a human nasal airway," *Respiratory Physiology & Neurobiology*, vol. 172, pp. 136–146, 2010.
- [15] F. R. Menter, "Two-equation eddy-viscosity turbulence models for engineering applications," *AIAA journal*, vol. 32, no. 8, pp. 1598–1605, 1994.
- [16] I. B. Celik, U. Ghia, P. J. Roache, C. J. Freitas, H. Coleman, and P. E. Raad, "Procedure for estimation and reporting of uncertainty due to discretization in CFD applications," *ASME Journal of Fluids Engineering*, vol. 130, no. 7, 4 pages, 2008.
- [17] I. Weinhold and G. Mlynski, "Numerical simulation of airflow in the human nose," *European Archives of Oto-Rhino-Laryngology*, vol. 261, no. 8, pp. 452–455, 2004.
- [18] G. J. M. Garcia, N. Bailie, D. A. Martins, and J. S. Kimbell, "Atrophic rhinitis: a CFD study of air conditioning in the nasal cavity," *Journal of Applied Physiology*, vol. 103, no. 3, pp. 1082–1092, 2007.
- [19] G. Xiong, J. Zhan, K. Zuo, J. Li, L. Rong, and G. Xu, "Numerical flow simulation in the post-endoscopic sinus surgery nasal cavity," *Medical and Biological Engineering and Computing*, vol. 46, no. 11, pp. 1161–1167, 2008.
- [20] C. Croce, R. Fodil, M. Durand et al., "In vitro experiments and numerical simulations of airflow in realistic nasal airway geometry," *Annals of Biomedical Engineering*, vol. 34, no. 6, pp. 997–1007, 2006.
- [21] T. K. Zhen, M. Zubair, and K. A. Ahmad, "Experimental and numerical investigation of the effects of passive vortex generators on Aludra UAV performance," *Chinese Journal of Aeronautics*, vol. 24, no. 5, pp. 577–583, 2011.
- [22] A. K. Long, M. Zubair, and K. A. Ahmad, "A static thrust measurement of two types of perforated solid propellant grain configurations," *Journal of Aerospace Engineering*, vol. 25, no. 4, pp. 653–659, 2011.

Research Article

Multiobjective Optimization Design of Spinal Pedicle Screws Using Neural Networks and Genetic Algorithm: Mathematical Models and Mechanical Validation

Yongyut Amaritsakul,¹ Ching-Kong Chao,¹ and Jinn Lin²

¹ Department of Mechanical Engineering, National Taiwan University of Science and Technology 43, Section 4, Keelung Road, Taipei 106, Taiwan

² Department of Orthopaedic Surgery, National Taiwan University Hospital 7, Chung-Shun South Road, Taipei 100, Taiwan

Correspondence should be addressed to Jinn Lin; jinn@ntu.edu.tw

Received 6 June 2013; Accepted 8 July 2013

Academic Editor: Zhonghua Sun

Copyright © 2013 Yongyut Amaritsakul et al. This is an open access article distributed under the Creative Commons Attribution License, which permits unrestricted use, distribution, and reproduction in any medium, provided the original work is properly cited.

Short-segment instrumentation for spine fractures is threatened by *relatively high* failure rates. Failure of the spinal pedicle screws including breakage and loosening may jeopardize the fixation integrity and lead to treatment failure. Two important design objectives, bending strength and pullout strength, may conflict with each other and warrant a multiobjective optimization study. In the present study using the three-dimensional finite element (FE) analytical results based on an L_{25} orthogonal array, bending and pullout objective functions were developed by an artificial neural network (ANN) algorithm, and the trade-off solutions known as Pareto optima were explored by a genetic algorithm (GA). The results showed that the knee solutions of the Pareto fronts with both high bending and pullout strength ranged from 92% to 94% of their maxima, respectively. In mechanical validation, the results of mathematical analyses were closely related to those of experimental tests with a correlation coefficient of -0.91 for bending and 0.93 for pullout ($P < 0.01$ for both). The optimal design had significantly higher fatigue life ($P < 0.01$) and comparable pullout strength as compared with commercial screws. Multiobjective optimization study of spinal pedicle screws using the hybrid of ANN and GA could achieve an ideal with high bending and pullout performances simultaneously.

1. Introduction

The treatment goals of spinal fractures include deformity correction, neurological decompression, and fixation of the instability [1]. Transpedicle screw fixators can achieve reduction, decompression, and fixation at the same time, and provide high fixation stability for early mobilization [2–4]. One important principle of spinal fixation is to minimize the instrumentation levels to reduce the surgical trauma, preserve the motion segments, and avoid junctional arthritis and late back pain caused by long-segment instrumentation which may increase load at the adjacent segments [5]. However, *relatively high* failure rates with this short-segment instrumentation which fixes only one level above and below

the fractured vertebra have been reported [1]. Failure of the pedicle screws including breakage and loosening may jeopardize the fixation integrity and lead to treatment failure [6–8]. Especially, broken pedicle screws trapped in the vertebral bodies are difficult to retrieve and may interfere with subsequent revision surgeries [9]. Thus, the design rationale of pedicle screws is to increase bending strength to resist breakage and pullout strength to resist loosening simultaneously [10–12]. However, these two design objectives are closely related to the screws' structures and may conflict with each other [10, 13–15]. Improving one objective may cause deterioration of the other. Therefore, optimization studies to improve both design objectives simultaneously are critical but still *rare* in the literature [16].

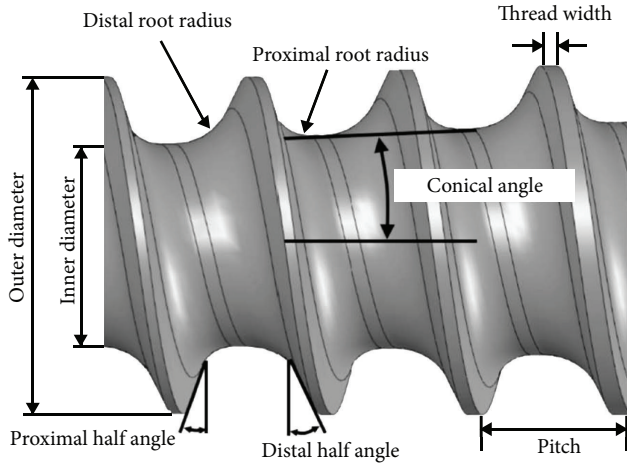


FIGURE 1: Illustration of structural variables for the spinal pedicle screw.

In the present study, computer aided engineering (CAE) with high calculation technology was applied. The pedicle screws were analyzed with finite element (FE) models, and then artificial neural network (ANN) algorithms were adopted to model the analytical process. The optimal screw design was achieved via an evolutionary multiobjective approach with a genetic algorithm (GA) [15]. Last, mechanical tests were conducted to validate the optimal design by comparison with commercially available devices.

2. Materials and Methods

2.1. Screw Structures and Orthogonal Array of Taguchi Robust Design Methods [15]. In this study the outer diameter of the pedicle screws was fixed at 7 mm. Among the eight independent structural variables of pedicle screws, six of them were analyzed including beginning position of conical angle (BP), inner diameter (ID) at the screw tip, proximal root radius (PRR), pitch (P), proximal half angle (PHA), and thread width (TW) (Figure 1). The design space of these structural variables was determined according to commonly used pedicle screws and previous studies [1, 15]: 0–36 mm for BP, 3.8–5.5 mm for ID, 0.4–1.0 mm for PRR, 2.6–4.0 mm for P, 5–20° for PHA, and 0.1–0.3 mm for TW (Table 1). The distal root radius and distal half angle were fixed at 1 mm and 25°, respectively, because of minimal effects on the mechanical performance of the screws [17, 18]. An L_{25} orthogonal array for six factors with five levels was selected for optimization study. This orthogonal array ensures a balanced comparison of levels of each structural variable and represents the entire experimental space. The structural variables were equally divided to 5 levels and put in the L_{25} orthogonal array. All the screw designs in the orthogonal array fulfilled the geometric constraints [15].

2.2. FE Models. Three-dimensional solid models of the spinal pedicle screws inserted at the center of a cylinder were first created by the CAD software SolidWorks 2005 (SolidWorks, Concord, MA, USA) and then imported into the CAE

software ANSYS 10 Workbench (ANSYS Inc., Canonsburg, PA, USA) with the use of the Parasolid format (Figure 2). The screw was 45 mm, and the cylinder was 60 mm in length. The pedicle screw was free-meshed with high order 10-node tetrahedral elements, and the cylinder was map-meshed with 20-node hexahedral elements with the element size of 1.2 mm. Surface-to-surface contact elements were used for the interface between the pedicle screw and cylinder with a frictionless condition. No axial rotation of the constructs was allowed. The elastic modulus of titanium pedicle screws was 114 GPa. The Poisson's ratio was 0.3 for both pedicle screw and cylinder. The thread valleys with stress concentration were remeshed, and the numerical convergence was confirmed by increasing mesh density.

For bending strength, a cantilever bending setup was used to simulate the worst-case scenario of total corpectomy conditions. The cylinders with an outer diameter of 20 mm were made from homogeneous polyoxymethylene with an elastic modulus of 2.6 GPa. The screw head was constrained, and a compressive force of 225 N was applied to the cylinder with a lever arm of 40 mm (Figure 2(a)). In the postprocessing, the maximum tensile stress of the pedicle screw was recorded to represent the bending strength. Lower maximum tensile stress represented longer fatigue life and higher bending strength, and vice versa. For pullout strength, to simulate the worst case scenario of osteoporosis, the cylinder with an outer diameter of 30 mm was assumed to be osteoporotic bone with an elastic modulus of 137.5 MPa. The effects of bone compaction caused by conical screws were simulated by adjusting the elastic modulus of the bone surrounding the conical core according to the density change of the surrounding bone [11]. Density change was calculated on the basis of the volume reduction caused by the compaction. The elastic modulus of bone was assumed to be a power-law function of the density with an exponent of 2. In the loading condition, an axial displacement of 0.01 mm was applied to the end surface of the pedicle screw. The boundary conditions were constraints at the outer surface of the cylinder (Figure 2(b)). In the postprocessing, total reaction force on screws, defined as the summation of the resultant axial force at the surface of the screw, was recorded. Higher total reaction force represented stronger pullout strength.

2.3. Artificial Neural Network Modeling. ANN as a regression device containing layers of computing nodes with remarkable information processing capability can detect nonlinearities by machine learning and adaptability based on the least-squares algorithm [19]. In the current study, because of the complexity of FE analyses, ANN was used to replace the FE models of bending strength and pullout strength for construction of the objective functions for multiobjective optimization studies. The supervised feed-forward error-backpropagation learning models with sigmoid activation function were developed. Six structural variables were used as inputs, and single output was either maximum tensile stress or total reaction force (Figure 3). A three-layered ANN based on the 25 screw designs in the orthogonal array with three neurons in one hidden layer was used as the learning set. Another testing set with 10 randomly selected screw designs

TABLE 1: Design variables of the pedicle screws, FE analytical results and ANN models.

No.	BP (mm)	ID (mm)	PRR (mm)	P (mm)	PHA (°)	TW (mm)	MTS-FE (MPa)	MTS-ANN (MPa)	TRF-FE (N)	TRF-ANN (N)
1	0	3.80	0.40	2.60	5.00	0.10	464.49	464.71	39.93	39.99
2	0	4.23	0.55	2.95	8.75	0.15	416.30	415.05	38.40	38.59
3	0	4.65	0.70	3.30	12.50	0.20	399.83	392.63	35.56	35.75
4	0	5.08	0.85	3.65	16.25	0.25	377.19	382.49	31.37	31.26
5	0	5.50	1.00	4.00	20.00	0.30	380.56	377.39	26.36	26.48
6	9	3.80	0.55	3.30	16.25	0.30	452.25	457.14	38.37	38.38
7	9	4.23	0.70	3.65	20.00	0.10	415.59	419.10	36.48	36.57
8	9	4.65	0.85	4.00	5.00	0.15	404.94	405.94	33.66	33.72
9	9	5.08	1.00	2.60	8.75	0.20	432.04	427.96	33.96	33.82
10	9	5.50	0.40	2.95	12.50	0.25	393.19	404.48	35.67	35.54
11	18	3.80	0.70	4.00	8.75	0.25	468.89	468.30	36.74	36.80
12	18	4.23	0.85	2.60	12.50	0.30	576.54	574.13	37.94	37.90
13	18	4.65	1.00	2.95	16.25	0.10	444.50	437.91	35.72	35.71
14	18	5.08	0.40	3.30	20.00	0.15	429.80	416.79	36.65	36.33
15	18	5.50	0.55	3.65	5.00	0.20	391.64	397.72	33.37	33.49
16	27	3.80	0.85	2.95	20.00	0.20	608.56	617.34	37.47	37.15
17	27	4.23	1.00	3.30	5.00	0.25	532.07	529.34	36.37	36.23
18	27	4.65	0.40	3.65	8.75	0.30	491.02	481.84	36.73	36.58
19	27	5.08	0.55	4.00	12.50	0.10	460.59	463.83	34.67	34.41
20	27	5.50	0.70	2.60	16.25	0.15	463.35	469.46	35.14	35.44
21	36	3.80	1.00	3.65	12.50	0.15	919.85	918.26	35.19	35.31
22	36	4.23	0.40	4.00	16.25	0.20	787.66	789.04	34.90	35.05
23	36	4.65	0.55	2.60	20.00	0.25	770.40	765.61	36.66	36.90
24	36	5.08	0.70	2.95	5.00	0.30	605.92	611.19	35.97	36.01
25	36	5.50	0.85	3.30	8.75	0.10	527.13	526.30	33.54	33.46
26	25.4	4.7	0.748	3.1	9.53	0.255	488.62	483.69	36.59	36.41
27	0.5	5.093	0.885	3.59	5.68	0.183	375.29	380.79	31.47	31.64
28	31.05	5.144	0.624	3.947	18.07	0.11	504.19	510.02	34.01	33.62
29	16.87	4.3	0.774	3.507	8.95	0.156	444.71	436.37	36.46	36.73
30	25.02	5.46	0.546	3.347	6.58	0.3	429.47	427.33	34.48	34.43
31	10.24	3.87	0.577	3.135	9.515	0.28	447.07	465.53	38.51	38.73
32	6.696	4.79	0.448	3.241	18.58	0.152	412.10	401.96	37.189	37.16
33	23.25	4.39	0.463	2.86	6.16	0.187	495.95	506.34	38.365	38.56
34	21.55	5.334	0.745	2.943	17.91	0.115	420.82	424.14	34.036	34.89
35	31.64	5.49	0.543	3.528	14.39	0.294	476.86	472.29	34.167	33.80

No. 1–25, learning set; No. 26–35, testing set. MTS represents maximum tensile stress. TRF represents total reaction force.

outside the orthogonal array was used to supervise the learning process. The input quantities were normalized to a range from -1 to 1 , and the output quantities were normalized to a range from 0 to 1 . The initial weights and the biases between -1 to 1 were randomly assigned. Both learning rate and the coefficient of momentum term were set at 0.5 . The new weight and bias were updated as the error between the predicted and the target performance was minimized. Generally, the learning and testing errors kept decreasing during computing iterations. The process was terminated when the testing errors were minimal. The ANN models were run 100 times with different initial weights, and the best model with the least test error was selected for optimization study. The ANN is coded by Microsoft Visual Basic (Redmond, WA).

2.4. Multiobjective Optimization with GAs. GA is commonly used for multiobjective optimization by using stochastic operators (Figure 4). The biobjective problem of the screw functions could be expressed by an aggregated weighted-sum fitness function (F): $F = w \cdot F_{\text{bending}} + (1 - w) \cdot F_{\text{pullout}}$, where F_{bending} was the normalized objective function of bending; F_{pullout} was the normalized objective function of pullout; w , the given weight, was systematically changed from 0 to 1 to assess the different combinations of both performances. Both objective functions were transformed into the-larger-the-better problem before aggregation, and the fitness function (F) was maximized. The algorithm was initiated with a population with 40 randomly selected chromosomes. Each chromosome was composed of six design parameters with

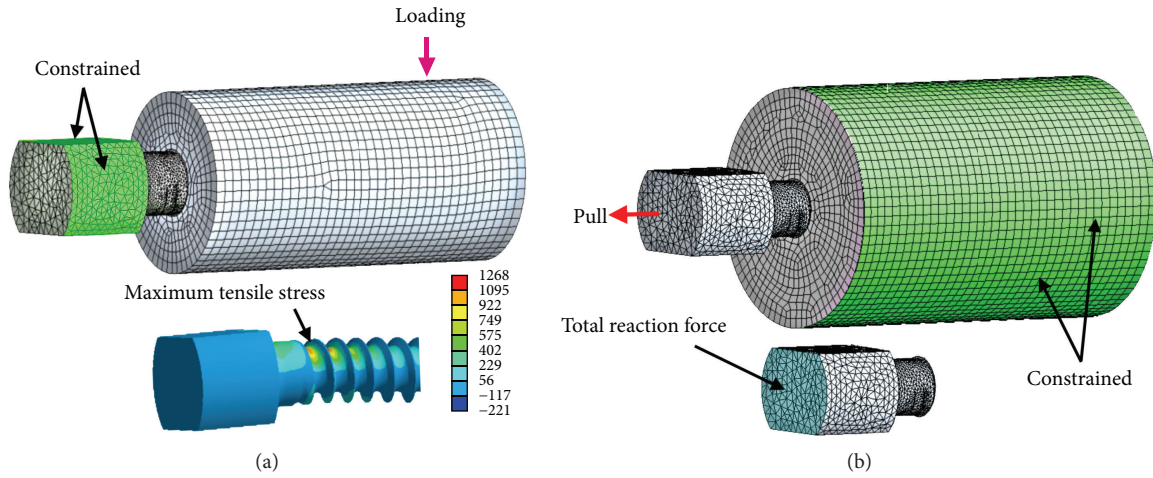


FIGURE 2: Finite element models: bending (a) and pullout (b).

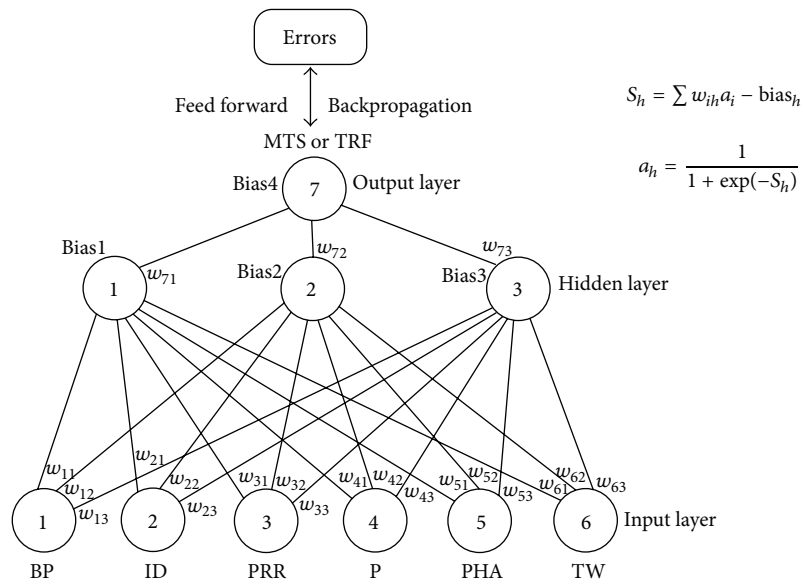


FIGURE 3: Three-layer feed-forward error-backpropagation neural network model.

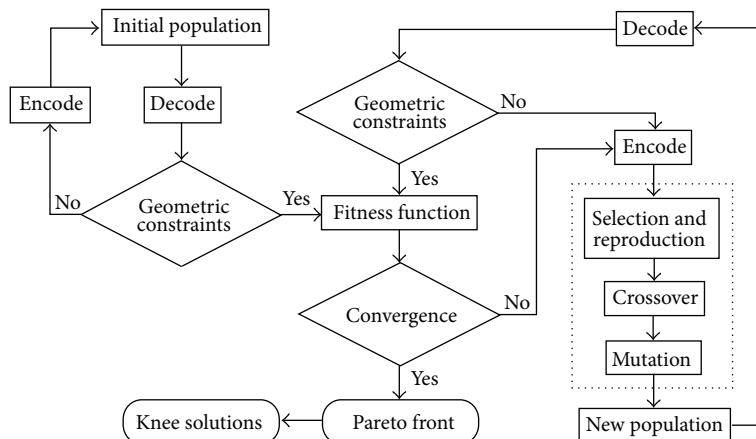


FIGURE 4: Flowchart of evolutionary optimality in GAs.



FIGURE 5: Tested pedicle screws: (a) Synthes, (b) A-Spine, (c) Moss Miami, (d) Viper, and (e) Optimal.

42 bits of zeros and ones. The optimization process included selection, reproduction, and termination. Roulette wheel selection replicates the fitter solutions found in the population. Then a second generation population was reproduced from those selected through genetic operators: *crossover* and *mutation*. The crossover rate and the mutation rate were 90% and 1%, respectively. If the new generations fulfilled the constraints, the fitness of the new populations was calculated and reselected again. The process was repeated and terminated until the highest ranking solution's fitness converged. The program of GAs was also developed by Microsoft Visual Basic. The optimization strategy produced a set of Pareto front with nondominant solutions, which meant there were no solutions better than those in both objectives. The optimal design range at the knee region of the Pareto front was subjectively defined as a less than 2% difference between the normalized objectives. The knee solutions were validated with FE analyses and compared with the commercially

available pedicle screws. Ten thousand randomly selected screw designs were used to validate the Pareto set obtained in GA.

2.5. Mechanical Validation Tests. The results in the mathematical studies were validated by mechanical tests as conducted in the literature [1]. One optimal design randomly selected from the knee region of the Pareto front was compared with the four commercially available pedicle screws with a 7 mm outer diameter in both bending and pullout tests: Synthes (Synthes, Paoli, PA, USA), A-Spine (A-Spine Asia, Taipei, Taiwan), Moss Miami, and Viper (DePuy Spine, Raynham, MA, USA) (Figure 5). The structures of the commercial screws were measured by measuring microscope (Meiji MC-50T, New York Microscope, Hicksville, NY). To make the comparison fair, the screws were manufactured with the same titanium alloy by the same process. The mechanical tests were conducted on a materials testing machine (Bionix 858,

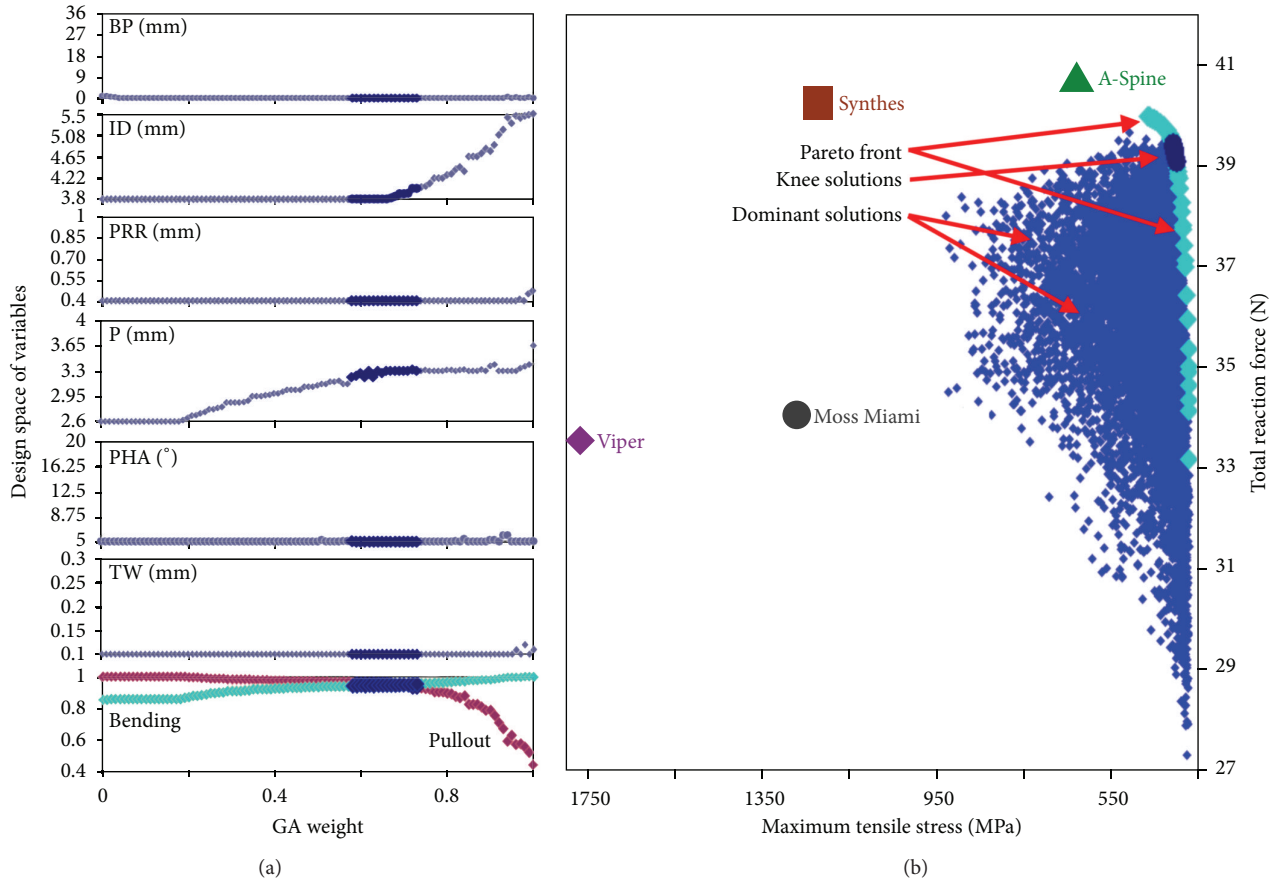


FIGURE 6: Optimization results: (a) changes of the values of structural variables related to the normalized objective functions of bending and pullout corresponding to given weights in GA. (b) Pareto plot with knee solutions.

MTS Corporation, Minneapolis, MN, USA), and the testing setup was similar to that in the FE models. In bending, polyoxymethylene cylinders (Universal Plastics, Auckland, New Zealand) representing the vertebrae could eliminate the interspecimen variability and prevent specimen failure during experiments. Sinusoidal waveform cyclic loading fatigue tests with a frequency of 10 Hz were performed with screws submerged in a saline bath at 37°C. The maximal load of the cyclic testing was 410 N with a stress ratio of 10%. The tests were terminated when the screws cracked or the number of testing cycles was more than one million [6]. The number of cycles at failure was recorded. For pullout, cellular polyurethane foam (Pacific Research Laboratories, Vashon, WA, USA) conforming to the standard of ASTM F1839-97 [20] can prevent the widely varying testing results. Two densities of the foam—0.32 and 0.16 gm/cm³ with a compressive modulus of 137.5 and 23 MPa and a porosity of 71% and 86%, respectively—were used to simulate cancellous bones with osteoporosis. For a fair comparison, the predrill hole was the same size as that of the ID of each screw at the screw tip. Thus, the conical screws could generate bone compaction during screw insertion. The screws were freely extracted in longitudinal direction with a loading rate of 5 mm/minute. The maximum load was defined as the pullout strength.

3. Results

In FE analyses, total element number ranged from 122,550 to 189,224 for bending and from 142,066 to 278,211 for pullout. The maximum tensile stress in bending tests was located at the proximal threads near the screw hub. The pedicle screws in pullout tests had negligible deformation because the bone was assumed osteoporotic (Figure 2). These two findings were compatible with the results in the mechanical tests. In ANN analyses, the computing iteration was 10000 cycles for bending and 5000 cycles for pullout. The differences between prophetic outputs obtained in ANN models and FE results were minimal. For bending, the mean absolute error was 1% (0.05~3%) for learning and 1.64% (0.03~4.13%) for testing. For pullout, the mean absolute error was 0.4% (0.03~0.88%) for learning and 0.78% (0.08~2.51%) for testing.

The solutions of GA converged after 300 generations (see Supplementary Materials available at <http://dx.doi.org/10.1155/2013/462875>). The main factors that affected the Pareto set were ID and pitch (Figure 6), which increased along with the weight (w). In the knee region, the weight ranged from 0.60 to 0.72. The corresponding range of the structural variables was 3.8 to 4.06 mm for ID and 3.21 to 3.3 mm for pitch; the fixed variables were 0 mm for BP, 0.4 mm for PRR, 5° for PHA, and 0.1 mm for TW. The bending

TABLE 2: Structures and results of FE analyses and mechanical tests of four commercially available pedicle screws and the optimal design. Values were expressed as mean (standard deviation).

Mechanical properties	Synthes type	A-Spine type	Moss Miami type	Viper type	Optimal design
BP (mm)	0	0	40	cylindrical	0
CD (mm)	2.76	4	4.61	4.4	3.8
PRR (mm)	0.22	0.1	3	3	0.4
P (mm)	2	2	2.95	2.87	3.3
PHA (°)	0	0	31.35	29.93	5
TW (mm)	0.1	0.1	0.2	0.33	0.1
Maximum tensile stress (MPa)	1220	628	1268	1766	422
Total reaction force (N)	40.25	40.77	33.53	34.04	39.1
Fatigue life (10^3 cycles)	13.77 (4.62)	46.53 (15.9)	8.52 (1.35)	—	>1000
Pullout strength, 0.32 g/cm ³ (N)	2148 (144)	2068 (117)	1598 (56)	1553 (84)	2009 (74)
Pullout strength, 0.16 g/cm ³ (N)	1015 (74)	951 (48)	705 (48)	662 (63)	825 (52)

Cyclic loading tests of Viper type screws were not completed because the screws yielded quickly during the tests.

strength and the pullout strength ranged between 92% and 94% of their maxima. The exactitude of knee solutions closely approximated the results of FE analyses. The ten thousand randomly selected screw designs were all dominant solutions in Pareto plot. The commercially available pedicle screws were far away from the knee solutions. The A-Spine and Synthes type screws had high pullout strength but relatively low bending strength. Moss Miami and Viper type screws were low in both bending strength and pullout strength.

In the mechanical tests, the logarithm of the fatigue life was closely related to the maximum tensile stress obtained in FE analyses with a correlation coefficient of -0.91 ($P < 0.01$), and the pullout strength was closely related to the total reaction force with a correlation coefficient of 0.93 ($P < 0.01$) (Table 2). The optimal designs had significantly higher fatigue lives ($>10^6$ cycles) than all the commercial screws by an analysis of variance test ($P < 0.01$, resp.), and pullout strength was higher than Moss Miami and Viper screws ($P < 0.01$ for both foam densities). Synthes and A-Spine screws had higher pullout strength than optimal designs, but the bending strength was relatively low because of a very small pitch (2 mm). This was compatible with the findings in FE analyses.

4. Discussion

In order to reduce the incidence of fixation failure in short-segment fixation for spinal fractures, different kinds of interventions have been developed, including combined anterior instrumentation [21], bone cement augmentation [22], transpedicular vertebroplasty [23], and so forth. However, these methods are threatened by complications [1]. Improvement of the pedicle screw design to achieve better bending strength and bone holding power is still the most basic step to prevent failure of fixation. Investigating only one mechanical performance of bending strength or pullout strength of the pedicle screws exclusively might lead to undetected compromise of the other one, because these two objectives would conflict with each other in the design process [1, 15]. In the present study, with adequate control of the design space,

the two mechanical performances of the screws were investigated simultaneously with ANN and GA for multiobjective optimization analysis.

FE analysis, a powerful tool for biomechanical researches on structures with complicated loading and boundary conditions [24, 25], can be reliably used for predicting the bending strength and pullout strength of orthopedic screws [17, 18]. In the present study, the FE models could be well validated by mechanical tests in both bending and pullout tests with very high correlation coefficients. However, because of the sophisticated computation process, FE analyses are not suitable for multiobjective design optimization studies. Therefore, the ANN algorithms, which have the special advantage of functional approximation with fast computation, can be used as surrogate functions of FE models for multiobjective optimization studies.

ANN, a nonlinear statistical data modeling tool, uses learning rules to develop models and parallel computing to find answers. These neurocomputing procedures mimic information processing and knowledge acquisition in human brains. ANN can construct complex relationships between input variables and output performances and process not only values but also texts, images, and voices [19, 26]. Its attractiveness comes from the remarkable information processing characteristics of the biological systems such as nonlinearity with better fit to the data, high parallelism, robustness, fault tolerance, learning, ability to handle imprecise and fuzzy information, and their capability to generalize. Our previous optimization study of tibial locking screws developed objective functions with least-squares linear regression models [15]. However, with more complex trends in the conical core design of pedicle screws in the present study, linear regression analysis with high order polynomials might fit badly at the extreme of the independent variables or in data with limiting behaviors, because polynomials do not have asymptotics [27]. ANN viewed as generalizations of “super regression” can outperform statistical regression with regard to prediction accuracy. This superiority increases as the dimensionality and/or nonlinearity of the problem increases. Classically, development of an ANN requires partitioning of the parent

database. This may decrease the statistical power. In the present study, use of all the datasets in the orthogonal array in the training and 10 testing datasets randomly selected from the entire parametric space outside the orthogonal array could avoid this disadvantage and increase the predictability.

Many real-world problems involve multiple competing objectives. The two objectives of pedicle screws, bending strength and pullout strength, are conflicting and characterized by the fact that improving one objective may jeopardize the other [15]. The present multiobjective optimization study used a weighted-sum function and GA to develop Pareto optima that were trade-off solutions for the conflicting objectives [28]. The solutions at the knee region of the Pareto front, characterized by the fact that a small improvement in either objective might cause a substantial change in the other, were considered the most suitable trade-offs (the optimal designs) by designers. The bending strength and the pullout strength of the optimal designs ranged between 92% and 94% of their maxima. This indicated that with minimal compromise of one objective, the other still could maintain a relatively high performance. However, this multiobjective optimization principle is not adequately considered in the design of commercially available pedicle screws. The Synthes and A-Spine type screws with a very small pitch (2 mm) had very high pullout strength, but such a small pitch led to a sharp root radius and high tensile stress. A small increase of maximum tensile stress might markedly decrease the fatigue life because of the logarithmic relationship. This was the reason why small pitch was not included in the design space of the present study. In contrast, both Viper and Moss Miami type screws with a cylindrical core had low bending and pullout strength. They were dominated designs, very far away from the knee region. Basically, tapering of the ID from the screw tip all the way to the screw hub may increase the bending strength and pullout strength simultaneously. Especially, elimination of the step-off at the screw hub can increase the fatigue strength substantially [1]. This explained higher fatigue life in A-Spine type and optimal design screws. Viper type screws with a smaller core at the screw hub for better adjustability of the polyaxial design might jeopardize the bending strength extremely.

The present study has potential pitfalls. First, ANN is an empirical model and its success depends on both the quality and quantity of the data. Although only 25 datasets were used for training, the ANN model still could accurately reflect the FE results, because the orthogonal array could fairly represent the entire parametric space and the FE data were relatively noise free, as compared with clinical data. Second, a different outer diameter and range of design space might affect the ranges of the optimal design. The present study considered only screws with an outer diameter of 7.0 mm, but the design space could cover the important ranges of the pedicle screw design. Third, GAs are stochastic iterative processes and do not guarantee a global optimality. However, the optimal designs in the present study with fitness levels up to 92% or 94% of their maxima were already practically acceptable. Fourth, the ANN is criticized as a “black box” method. One cannot exactly explain what interactions are modeled in the hidden layers, and there is still no specific method to define

the optimal hidden layers. However, these did not affect the method’s robustness in the present optimization study. Last, the optimal design was closely related to the relative weight between the bending strength and pullout strength (1 : 1 in the present study). The selection depended on the factors linked to the problem and a thorough knowledge of them.

In conclusion, the ANN model could reliably approximate the results of sophisticated mathematical analyses of pedicle screws. The model could be used to solve the problems of conflicting objectives of pedicle screws with evolutionary GA. The trade-off optimal solutions obtained in this optimization study could achieve an ideal with high performance in both bending and pullout tests. The present method proves beneficial to both manufacturers who design implants and surgeons who select the best product to prevent failure in the treatment of spine fractures.

Conflict of Interests

There is no conflict of interests in the present study.

Acknowledgment

The present study was financially supported by National Science Counsel, Grant no. NSC 98–2320-B-002-007-MY3.

References

- [1] C.-K. Chao, C.-C. Hsu, J.-L. Wang, and J. Lin, “Increasing bending strength and pullout strength in conical pedicle screws: biomechanical tests and finite element analyses,” *Journal of Spinal Disorders & Techniques*, vol. 21, no. 2, pp. 130–138, 2008.
- [2] P. L. Sanderson, R. D. Fraser, D. J. Hall, C. M. J. Cain, O. L. Osti, and G. R. Potter, “Short segment fixation of thoracolumbar burst fractures without fusion,” *European Spine Journal*, vol. 8, no. 6, pp. 495–500, 1999.
- [3] P. G. Katonis, G. M. Kontakis, G. A. Loupasis, A. C. Aligizakis, J. I. Christoforakis, and E. G. Velivassakis, “Treatment of unstable thoracolumbar and lumbar spine injuries using Cotrel-Dubouset instrumentation,” *Spine*, vol. 24, no. 22, pp. 2352–2357, 1999.
- [4] A. R. Vaccaro, D. H. Kim, D. S. Brodke et al., “Diagnosis and management of thoracolumbar spine fractures,” *Instructional Course Lectures*, vol. 53, pp. 359–373, 2004.
- [5] A. Mahar, C. Kim, M. Wedemeyer et al., “Short-segment fixation of lumbar burst fractures using pedicle fixation at the level of the fracture,” *Spine*, vol. 32, no. 14, pp. 1503–1507, 2007.
- [6] J. L. Stambough, F. El Khatib, A. M. Genaidy, and R. L. Huston, “Strength and fatigue resistance of thoracolumbar spine implants: an experimental study of selected clinical devices,” *Journal of Spinal Disorders*, vol. 12, no. 5, pp. 410–414, 1999.
- [7] D.-Y. Cho, W.-Y. Lee, P.-C. Sheu et al., “Treatment of thoracolumbar burst fractures with polymethyl methacrylate vertebroplasty and short-segment pedicle screw fixation,” *Neurosurgery*, vol. 53, no. 6, pp. 1354–1361, 2003.
- [8] K. E. Ponnusamy, S. Iyer, G. Gupta, and A. J. Khanna, “Instrumentation of the osteoporotic spine: biomechanical and clinical considerations,” *The Spine Journal*, vol. 11, no. 1, pp. 54–63, 2011.
- [9] J. S. Vanichkachorn, A. R. Vaccaro, M. J. Cohen, and J. M. Cotler, “Potential large vessel injury during thoracolumbar pedicle

- screw removal: a case report,” *Spine*, vol. 22, no. 1, pp. 110–113, 1997.
- [10] K. Willett, T. C. Hearn, and A. V. Cuncins, “Biomechanical testing of a new design for Schanz pedicle screws,” *Journal of Orthopaedic Trauma*, vol. 7, no. 4, pp. 375–380, 1993.
- [11] C.-C. Hsu, C.-K. Chao, J.-L. Wang, S.-M. Hou, Y.-T. Tsai, and J. Lin, “Increase of pullout strength of spinal pedicle screws with conical core: biomechanical tests and finite element analyses,” *Journal of Orthopaedic Research*, vol. 23, no. 4, pp. 788–794, 2005.
- [12] S. D. Cook, S. L. Salkeld, T. Stanley, A. Faciane, and S. D. Miller, “Biomechanical study of pedicle screw fixation in severely osteoporotic bone,” *The Spine Journal*, vol. 4, no. 4, pp. 402–408, 2004.
- [13] J. Lin, S.-J. Lin, H. Chiang, and S.-M. Hou, “Bending strength and holding power of tibial locking screws,” *Clinical Orthopaedics & Related Research*, no. 385, pp. 199–206, 2001.
- [14] K. Okuyama, K. Sato, E. Abe, H. Inaba, Y. Shimada, and H. Murai, “Stability of transpedicle screwing for the osteoporotic spine: an in vitro study of the mechanical stability,” *Spine*, vol. 18, no. 15, pp. 2240–2245, 1993.
- [15] C.-C. Hsu, C.-K. Chao, J.-L. Wang, and J. Lin, “Multiobjective optimization of tibial locking screw design using a genetic algorithm: evaluation of mechanical performance,” *Journal of Orthopaedic Research*, vol. 24, no. 5, pp. 908–916, 2006.
- [16] C.-K. Chao, J. Lin, S. T. Putra, and C.-C. Hsu, “A neurogenetic approach to a multiobjective design optimization of spinal pedicle screws,” *Journal of Biomechanical Engineering*, vol. 132, no. 9, Article ID 091006, 6 pages, 2010.
- [17] S.-M. Hou, C.-C. Hsu, J.-L. Wang, C.-K. Chao, and J. Lin, “Mechanical tests and finite element models for bone holding power of tibial locking screws,” *Clinical Biomechanics*, vol. 19, no. 7, pp. 738–745, 2004.
- [18] C.-K. Chao, C.-C. Hsu, J.-L. Wang, and J. Lin, “Increasing bending strength of tibial locking screws: mechanical tests and finite element analyses,” *Clinical Biomechanics*, vol. 22, no. 1, pp. 59–66, 2007.
- [19] N. B. Karayiannis and A. N. Venetsanopoulos, *Artificial Neural Networks: Learning Algorithms, Performance Evaluation, and Applications*, Kluwer Academic, Boston, Mass, USA, 1993.
- [20] R. F. Allen, N. C. Baldini, P. E. Donofrio, E. L. Gutman, E. Keefe, and J. G. Kramer, *Standard Specification for Rigid Polyurethane Foam for Use as a Standard Material for Testing Orthopedic Devices and Instruments (F1839-97)*, The American Society for Testing and Materials, West Conshohocken, Penn, USA, 1998.
- [21] P. M. Kallemeier, B. P. Beaubien, G. R. Buttermann, D. J. Polga, and K. B. Wood, “In vitro analysis of anterior and posterior fixation in an experimental unstable burst fracture model,” *Journal of Spinal Disorders & Techniques*, vol. 21, no. 3, pp. 216–224, 2008.
- [22] M.-C. Chang, C.-L. Liu, and T.-H. Chen, “Polymethylmethacrylate augmentation of pedicle screw for osteoporotic spinal surgery: a novel technique,” *Spine*, vol. 33, no. 10, pp. E317–E324, 2008.
- [23] A. Alanay, E. Acaroglu, M. Yazici, A. Oznur, and A. Surat, “Short-segment pedicle instrumentation of thoracolumbar burst fractures: does transpedicular intracorporeal grafting prevent early failure?” *Spine*, vol. 26, no. 2, pp. 213–217, 2001.
- [24] F. H. Dar, J. R. Meakin, and R. M. Aspden, “Statistical methods in finite element analysis,” *Journal of Biomechanics*, vol. 35, no. 9, pp. 1155–1161, 2002.
- [25] M. Viceconti, S. Olsen, L.-P. Nolte, and K. Burton, “Extracting clinically relevant data from finite element simulations,” *Clinical Biomechanics*, vol. 20, no. 5, pp. 451–454, 2005.
- [26] S. Agatonovic-Kustrin and R. Beresford, “Basic concepts of artificial neural network (ANN) modeling and its application in pharmaceutical research,” *Journal of Pharmaceutical and Biomedical Analysis*, vol. 22, no. 5, pp. 717–727, 2000.
- [27] P. Royston and D. G. Altman, “Regression using fractional polynomials of continuous covariates: parsimonious parametric modelling,” *Applied Statistics*, vol. 43, no. 3, pp. 429–467, 1994.
- [28] I. Taga, A. Funakubo, and Y. Fukui, “Design and development of an artificial implantable lung using multiobjective genetic algorithm: evaluation of gas exchange performance,” *ASAIO Journal*, vol. 51, no. 1, pp. 92–102, 2005.

Research Article

Standardization of Malaysian Adult Female Nasal Cavity

**Chih Fang Lee,¹ Mohd. Zulkifly Abdullah,²
Kamarul Arifin Ahmad,³ and Ibrahim Lutfi Shuaib⁴**

¹ School of Aerospace Engineering, Engineering Campus, Universiti Sains Malaysia, 14300 Nibong Tebal, Pulau Pinang, Malaysia

² School of Mechanical Engineering, Engineering Campus, Universiti Sains Malaysia, 14300 Nibong Tebal, Pulau Pinang, Malaysia

³ Department of Aerospace Engineering, Universiti Putra Malaysia, 43400 Serdang, Selangor, Malaysia

⁴ Advanced Medical & Dental Institute, Universiti Sains Malaysia, 13200 Kepala Batas, Pulau Pinang, Malaysia

Correspondence should be addressed to Chih Fang Lee; chihfang@hotmail.my

Received 16 May 2013; Accepted 31 May 2013

Academic Editor: Eddie Ng

Copyright © 2013 Chih Fang Lee et al. This is an open access article distributed under the Creative Commons Attribution License, which permits unrestricted use, distribution, and reproduction in any medium, provided the original work is properly cited.

This research focuses on creating a standardized nasal cavity model of adult Malaysian females. The methodology implemented in this research is a new approach compared to other methods used by previous researchers. This study involves 26 females who represent the test subjects for this preliminary study. Computational fluid dynamic (CFD) analysis was carried out to better understand the characteristics of the standardized model and to compare it to the available standardized Caucasian model. This comparison includes cross-sectional areas for both half-models as well as velocity contours along the nasal cavities. The Malaysian female standardized model is larger in cross-sectional area compared to the standardized Caucasian model thus leading to lower average velocity magnitudes. The standardized model was further evaluated with four more Malaysian female test subjects based on its cross-sectional areas and average velocity magnitudes along the nasal cavities. This evaluation shows that the generated model represents an averaged and standardized model of adult Malaysian females.

1. Introduction

The human nasal cavity consists of two symmetrically complex three-dimensional nasal passages that are separated in the middle by the nasal septum. During inspiration, air flows into the nasal cavity from the nostrils and then reaches the smallest cross-sectional area, the nasal valve, before reaching the tortuous turbinates region that forms large cross-sectional areas covered with mucous layers and cilia. These moist regions play an important role for the humidification, warming, and cleaning of the inspired air by entrapping the air-borne particles as well as moistening the air by evaporation [1]. Then, the turbinates region will guide the airflow towards the posterior region of the nasal cavity which is the nasopharynx.

Objective measurement methods are also very common in studies related to nasal geometry where it is used to determine cross-sectional area nasal airway resistance, and also visualization of the human nose. Shelton and Eiser carried out an evaluation of active anterior and posterior

rhinomanometry in normal subjects [2]. Suzina et al. used active anterior rhinomanometry (AAR) for the objective assessment of the nasal airway resistance in normal adult Malays [3]. However, these methods have their limitations in measuring the precise velocity of the airflow as well as in evaluating the local nasal resistance in every portion of the nasal cavities [4]. In addition to that, the complex nasal anatomy consists of numerous thin airway channels that prevent direct experimental measurements of the flow patterns inside the nose [5].

In recent years, with the rapid development in computer resources, there have been increasingly wide and deep applications of the CFD technique to studying the airflow characteristics in the human nasal cavity and hence its correlation with the symptoms and functions of the human nose [6–11]. Majority of these studies used a combination of different softwares (e.g., Mimics, Amira, and ICEM-CFD) to produce numerical nasal cavity models. In addition to that, there are a few review papers in this area, such as Bailie et al. [12], Leong et al. [13], and Zubair [14]. A better understanding of the nose

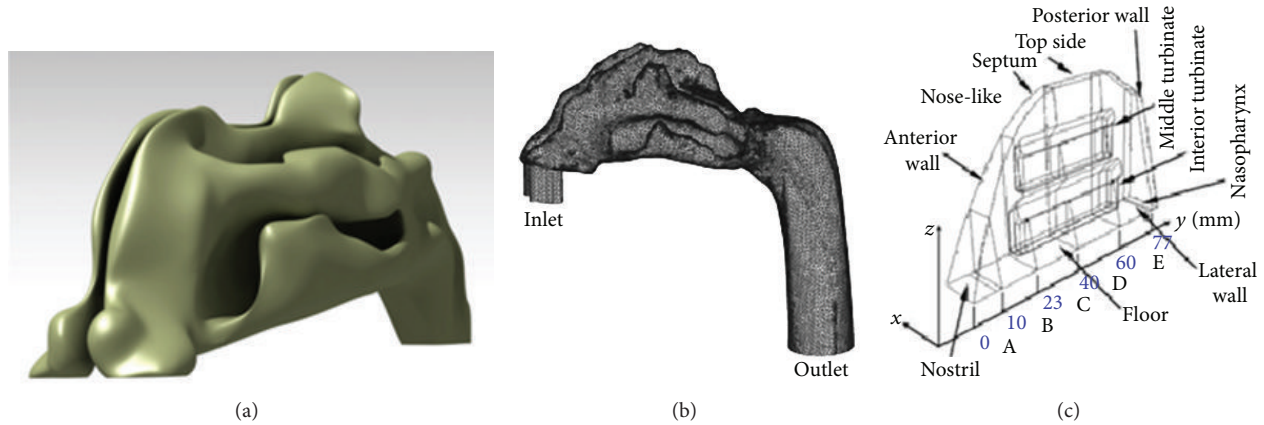


FIGURE 1: Models of the nasal cavity: (a) Anatomically identical model, (b) nasal cavity with additional inlet tube and extended nasopharynx, and (c) simplified nose-like model (figures obtained from Shi et al. [20] and Elad et al. [6]).

physiology, pathophysiology during normal breathing, and the postprocessing techniques of the flow patterns in nasal cavities can be achieved using CFD [15–17]. CFD was implemented to study the various aspects of respiratory airflow generated from the branching network tubes that make up the tracheal-bronchial tree. The model developed from the study of Lai et al. was able to provide an overall insight into the effect of fluid flow in the human upper respiratory airways [18]. Wide range of CFD applications were not only limited to upper respiratory airflow as Do et al. utilized CFD to analyse the three-dimensional haemodynamics of a typical stenotic coronary artery bypass grafting (CABG). The study demonstrated how numerical investigation can give an insight into the haemodynamic of various configurations of CABG under various physiological conditions [19].

Generally, researchers used identical models as shown in Figure 1(a) as they replicate the exact structures of the nasal passageway, with only slight modifications to the structures for simplification purposes. Geometrical models varied with the type of studies performed. Therefore, models from a healthy human who does not possess any obvious pathological symptoms and vice versa are required for a better understanding and visualization of a normal nasal airflow [4, 10, 11, 16, 21, 22]. For example, Garcia et al. conducted a research using nasal cavity of a patient with primary atrophic rhinitis [1, 23]. This allows different conditions especially patients with chronic diseases to be analyzed and information to be obtained, which is vital in providing treatment for such cases. Furthermore, Croce et al. used a realistic plastinated human model which is anatomically conserved with left and right nasal cavities for experimental purposes. This model was scanned to obtain CT images for specific three-dimensional reconstruction procedures that were implemented for numerical simulations [24]. Results from both models were compared for validation purposes to ensure the accuracy of the analysis. A study on nanoparticle or vapour deposition which was carried out by Shi et al. required not only the typical anatomical model but also some additional geometry as shown in Figure 1(b). A short inlet tube was added to the nostril to prevent simple plug flow from

entering the nostrils, and a certain length of actual airway was added to the nasopharynx to obtain proper outlet conditions [20].

Other than anatomically identical models, Elad et al. implemented a nose-like model as shown in Figure 1(c), which was a simplified model of the nose generated using average data of human nasal cavities [6]. The superior turbinate was omitted because the airflow in this region is very small. This generalized nose-like model simplified the complex structures of the three-dimensional nasal cavities and allowed removal or addition of various features to the model. These changes were very useful for the different types of comprehensive analysis to be carried out with ease [25]. For the analysis of air-conditioning capacity, the nose-like model was able to yield similar results to the anatomical model [26]. Horschler et al. investigated the impact of the geometry on the nasal airflow by using different models of human nasal cavity with and without turbinates [27]. Although all these models were able to produce reliable data, these researches only focused on certain unique individuals, and the results do not represent general population.

The interindividual difference of the unique characteristic of nasal cavity becomes a crucial issue in the comparison of results among different researches [17, 24, 28, 29]. Doorly et al. suggested that the establishment of rational methods to characterize and compare different anatomies would be very helpful in the future [8]. There is no guideline or benchmark that can be made as a reference when comparing the various results obtained. Therefore, this leads to the creation of a standardized model that will be used to represent a certain population. Liu et al. developed a method to scale, orient, and align the nasal geometries of 30 sets of CT scans of healthy subjects. The research also mentioned the importance of a standardized model for future experimental and numerical studies of inhaled aerosols [30].

The objective of this research is to create a standardized adult Malaysian female nasal cavity using a new approach that is simpler and applicable to a larger population. This standardized model was compared to existing standardized models from past researches to review the differences

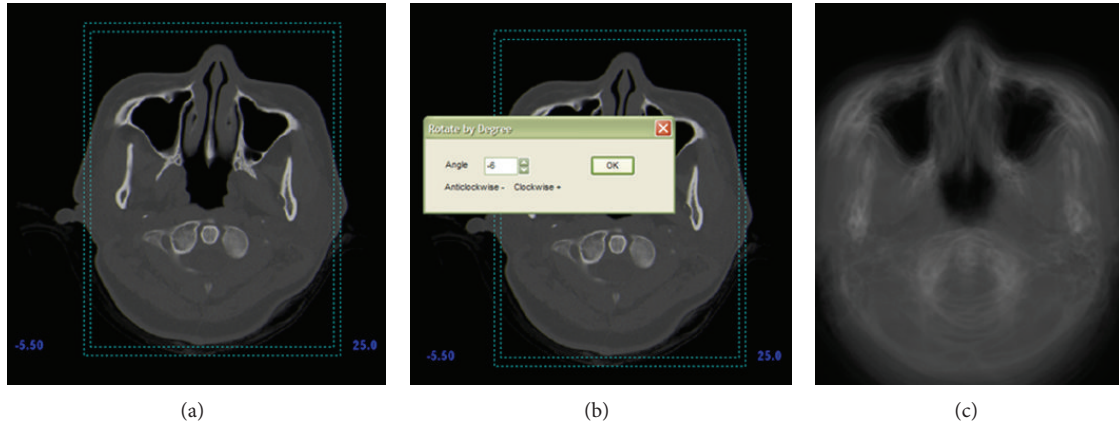


FIGURE 2: (a) Cropping image, (b) rotating image, and (c) average image obtained.

due to the different types of population based on geographical differences. Large differences especially in cross-sectional areas were observed from the Malaysian standardized model when compared to the Caucasian model. Thus, this proves that the standardized model is a good addition to the existing nasal models used in past researches.

2. Materials and Methods

This paper discusses the new methods in generating the standardized model in details. This method is a new approach as it is different compared to the method implemented by Liu et al. [30]. A complete set of average images used to generate the standardized model can be created in less than a few hours, saving time and cost as well as human labour. Developing the CT scans into three-dimensional model requires extra detail especially in determining the boundary layer of the nasal cavity and strict guidance from a rhinologist. Generation of the standardized nasal geometry involves several important steps that can be divided into three major parts. The first part is construction of geometry, followed by meshing of geometry, and finally running and analyzing the results. For this research, the standardized Malaysian female nasal cavity was created, and analysis was carried out to understand and verify the averaged model.

The first part of methodology involved generation of the standardized nasal cavity from two-dimensional CT scans of 26 sets of normal healthy Malaysian females' cavities that were obtained from the Advanced Medical Department of Universiti Sains Malaysia. The CT scans were transferred into MIMICS (Materialise, USA) to generate a three-dimensional model of the nasal cavity. Axial, coronal, and sagittal views of the nasal cavity were obtained from MIMICS, but only sets of axial images (captured from the anterior to the posterior of nasal cavity) were used in generating the averaged standardized nasal cavity. Axial images are able to show the complex geometry such as turbinates more clearly compared to other orientations. In order to generate the standardized model, an image processing program was executed to calculate the average pixel values in every axial image. The first axial images of all the 26 sets of CT scans were grouped together, and

average values were calculated to generate the first axial image for the standardized model. These methods were repeated for all the 37 images per test subject. This is a slightly tedious process, but only a few minutes are required to complete an average axial image. This study used CT images of both left and right nasal cavities to produce the averaged images. Several important precautions need to be taken such as cropping of the images. Since the size of the human head varies from individual to individual, the dimension, resolution, and position of the nasal cavity were maintained. The dimensions were measured from the septum with a crop ratio of 4 : 3 using the automatic cropping function of image cropper as shown in Figure 2(a). Another important detail that requires attention is the orientation of the nasal cavity during the CT scan as the subjects tend to position their heads in different directions. The entire image was rotated to a certain angle as shown in Figure 2(b) which ensures that the straight nasal septum can be viewed to obtain accurate average pixel values. The nasal septum plays an important role as it acts as a reference line for cropping as well as rotation of the images. Therefore, subjects with septum deviations are omitted from this research with the help of a rhinologist. Only healthy female subjects were used in this study. Figure 2(c) shows one of the final averaged images located in the middle of the nasal cavity from axial view. The different lines were created from all 26 images of different subjects.

A total of 37 new axial averaged images obtained from averaging of 26 test subjects were then imported to MIMICS to create a three-dimensional model as shown in Figure 3. Some functions like thresholding and editing the masks in MIMICS were used to facilitate the generation of the model. These functions were used to eliminate unwanted areas and to distinguish soft tissues and bone structures as well as empty spaces. The threshold in MIMICS neglected the soft tissues along nasal cavity as the nasal cavity was assumed to be decongested. The first draft of the standardized model can be seen in Figure 3 with some minor rough surfaces, but overall the structure seems to be well constructed.

The three dimensional polylines data from MIMICS were then imported to CATIA V5 (Dassault Systèmes) for smoothening the rough surfaces and to delete unwanted

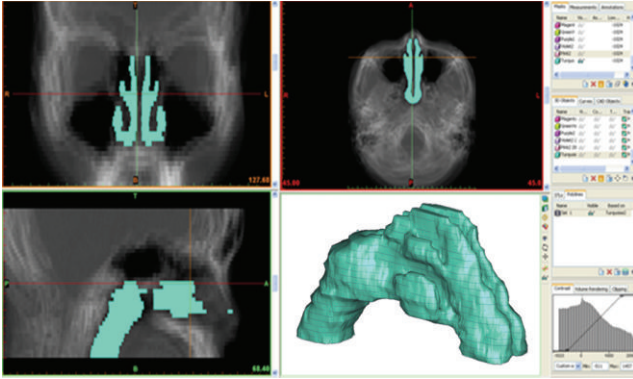


FIGURE 3: Creation of three-dimensional model in MIMICS.

vertices. Figure 4 shows how the standardized model is transformed from the raw polylines into the final standardized model that was used for analysis. All of the figures shown are actually just hollow surfaces. However, this model was converted into a fully solid volume for meshing purposes in GAMBIT 2.3.16 (Fluent Inc., Lebanon, USA).

Secondly, the methodology is focused on the meshing of the geometry. The standardized model generated from CATIA V5 was then imported to Gambit as a volume to perform volume meshing as shown in Figure 4(c). The grid independence study was carried out to determine the best mesh using unstructured tetrahedral meshing ranging from 500,000 to 3,000,000 elements. Lack of meshing elements especially at the thin turbinates region inside the nasal cavity will cause failure in capturing nasal airflow in the crucial areas. The results showed that the grid dependency study resulted in an optimized meshing of 1,109,123 elements, and the computational results are validated with the pressure drop obtained from Kim and Son [31] and Wen et al. [15, 17] as shown in Figure 5.

Finally, the last part of this methodology involved running the analysis and analyzing the results. The numerical simulation was performed using finite volume method provided by FLUENT 6.3.26 (Fluent, Lebanon, USA) for better understanding of the new standardized model. The simulation was based on the Navier-Stokes equations by representing the general equations for three-dimensional flow of incompressible and viscous fluids [28]. This study focused only on laminar airflow simulation for normal, resting breathing with a flow rate of 7.5 L min^{-1} [32, 33]. The boundary conditions defined were based on previous works [28, 34]. The nasal wall was assumed to be rigid, with no slip boundary condition, and effects of mucous were assumed to be negligible. The nostril inlet was defined by mass flow inlet, and the outlet at nasopharynx was defined by the outflow boundary condition. Any backflow at the outlet was assumed to be at 32.6°C and 100% relative humidity as imposed in FLUENT [1]. Nasal hair was also not considered as it is proven that it has no significant effect on the flow within the nasal cavity [35]. Paranasal sinuses were excluded in the creation of the standardized model as most researches (both computational and experimental as well as disease and

nondisease cases) only focus on the study of nasal airflow and do not consider paranasal sinuses in analyses [1, 4, 6–8, 11, 15, 17, 21, 22, 24, 29, 30, 33, 34, 36–40]. The sinuses were deemed to have negligible impact on the gross airflow patterns due to the small openings (ostia) with minimal cross-sectional area [11, 24].

The same methodology was repeated for the generation and analysis of two half-models and four more female nasal cavities. One of the half-models was cut from the standardized model while the other was obtained from Liu et al. (generated from 30 sets of Caucasian nasal cavities). Both models were compared in order to view the differences between the standardized model of different populations based on geographical differences as well as the methods applied in their generation. Meanwhile, the four Malaysian female subjects were carefully chosen from the 26 test subjects based on their ages and races. These four models were used for comparison with the standardized model to prove that the generated standardized model represents an average model of a Malaysian female nasal cavity. The information for all the 26 subjects is presented in Table 1. It was previously mentioned that the methodology for the current study is suitable for a large population. However, only 26 subjects were asked to participate in this study as it is only a preliminary study. Another reason which limits the number of subjects for this study is the lack of data as most patients with nasal pain or diseases are only willing to do the CT scans. Therefore, it is harder to obtain samples of healthy cases for the current study.

3. Results and Discussion

Results obtained from the standardized model generated from 26 female subjects were presented and discussed in two major parts. The first part is the comparison of two half-models; one is from the generated standardized model (labelled as Model A), and the other half-model is obtained from the research of Liu et al. [30] (labelled as Model B) for discussions of various results obtained from the CFD analysis. Comparisons were carried out by studying the cross-sectional areas, average velocity magnitudes, and contours coloured by velocities at four main cross-sections along the nasal cavities for both models. Based on the comparisons, variations among the standardized model of both geographically different nasal cavities can be obtained thus proving the requirement for a standardized model of different populations. The second part was only focused on the generated standardized model and the four nasal cavities chosen from the group of test subjects. Evaluation was carried out on all five complete models by comparing its cross-sectional areas and average velocity magnitudes at four cross-sections along the nasal cavities. The results obtained prove that the generated standardized model is able to represent the averaged adult Malaysian female nasal cavity.

3.1. Comparison of the Half-Models. The generated standardized model, Model A, is 99.312 mm in length which is relatively close to the average value presented in Table 1 while

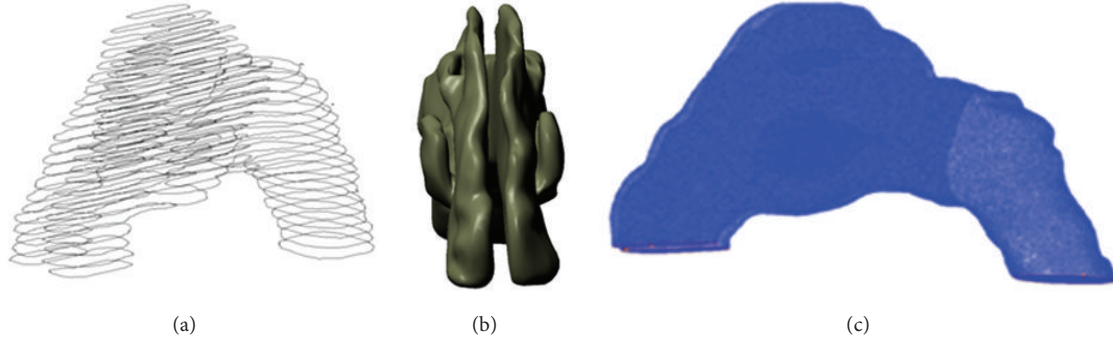


FIGURE 4: (a) Polylines from MIMICS, (b) smooth 3D nasal cavity from CATIA, and (c) meshing of geometry.

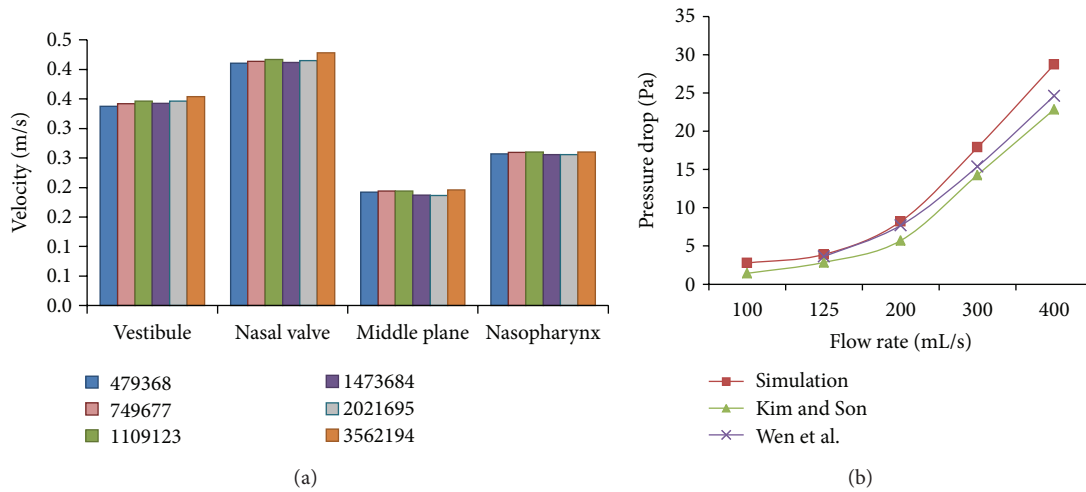


FIGURE 5: (a) Mesh dependency study at mass flow rate of 125 mL/s and (b) pressure drop versus mass flow rate.

the half-model obtained from Liu et al., Model B, is 109.73 mm in length. Both models are shown in Figure 6 with obvious differences in the structures, both horizontally and vertically. Model B shows obvious existence of superior meatus, longer middle region of all turbinates, shorter nasopharynx, and an imprecise vestibule shape. On the other hand, Model A shows only inferior and middle meatuses, longer nasopharynx region, and a more accurate representation of the nasal vestibule. Longer nasopharynx region is more relevant to ensure proper outlet condition during CFD analysis [20]. Based on the observation made on all the 26 subjects, the inconsistent visibility of the superior meatuses caused Model A to consist only of superior and middle meatuses. Cutting planes as shown in Figure 6 were implemented to obtain the required information because of the variation of lengths among the models. These cutting planes allowed comparison to be carried out at certain locations along the nasal cavities. There are a total of 8 cutting planes with the first one being A, located at the vestibule which is slightly upward from the inlet. The second cutting plane B is located at the nasal valve, which is the smallest cross-section of the nasal cavity. The third cutting plane, plane 1, C is located at the starting of the inferior meatus while the middle plane E is located at the middle of all the meatuses and

plane 4 G is located at the end of the inferior meatus. Both planes 2, D, and 3, F, are located in between of C-E and E-G, respectively. Finally, the nasopharynx H is located at the end of the nasal cavity near the outlet.

Cross-sectional areas along the nasal cavities are presented in Figure 7 for a more thorough comparison of both models. It is noticeable that Model B has a smaller cross-sectional area compared to Model A as shown in Figures 6 and 7. This is due to the more slender shape of Model B. The cross-sectional area of Model A is higher except for the outlet due to the longer nasopharynx region of the model. Model A shows the lowest cross-sectional area located at the nasal valve and the highest cross-sectional area located at the middle plane of the meatuses. The sudden decline on plane 4 was caused by the ending of the meatuses. Both models were obtained from different populations at different geographical locations thus causing the variation in the cross-sectional areas. From a visual observation, it seems that the Malaysian nose is comparatively smaller in size and length when compared to the Caucasian nose. However, the result indicated in Figure 7 clearly shows otherwise. This shows that the outer nose appearance cannot be used to estimate the cross-sectional areas of the inner nasal cavity.

TABLE 1: Table of information for 26 female subjects in current study.

Subject	Age	Race	Length, mm	Distance between slices, mm	Used for comparison
1	37	Indian	98.44	2.5	Yes
2	35	Indian	98.58	2.5	No
3	34	Chinese	104.92	2.5	No
4	38	Indian	103.48	2.5	No
5	39	Chinese	96.82	2.5	No
6	24	Chinese	107.93	2.5	No
7	43	Chinese	99.63	2.5	No
8	37	Chinese	97.61	2.5	No
9	40	Chinese	103.31	2.5	No
10	34	Indian	99.55	2.5	No
11	23	Chinese	101.80	2.5	No
12	38	Chinese	102.31	2.5	No
13	31	Chinese	98.52	2.5	No
14	20	Malay	96.05	2.5	No
15	24	Malay	94.28	2.5	Yes
16	36	Malay	94.66	2.5	No
17	40	Malay	90.86	2.5	No
18	39	Indian	99.08	2.5	No
19	32	Indian	97.92	2.5	No
20	43	Indian	100.69	2.5	Yes
21	21	Chinese	87.08	2.5	No
22	34	Malay	95.34	2.5	No
23	34	Malay	105.81	2.5	No
24	31	Chinese	94.72	2.5	Yes
25	45	Malay	87.72	2.5	No
26	40	Malay	102.06	2.5	No
Min	20	—	87.08	—	—
Max	45	—	107.93	—	—
Median	36	—	98.55	—	—
Average	34	—	98.43	—	—

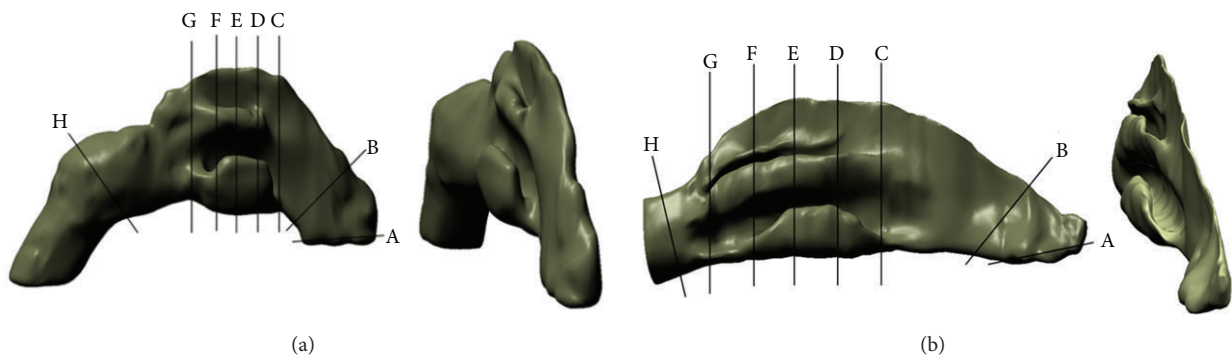


FIGURE 6: Half-models: (a) model from current study, Model A, and (b) model obtained from Liu et al. [30], Model B. Cutting planes: A = vestibule, B = nasal valve, C = plane 1, D = plane 2, E = middle plane, F = plane 3, G = plane 4, and H = nasopharynx.

The capabilities of CFD to present useful information on nasal cavities are undeniable, as it has been presented by various researches for over a decade [21, 41–43]. For this paper, CFD analysis was carried out to further investigate the differences between both standardized models. Figure 8

shows the graphs of average velocity magnitudes while the contours of velocities are illustrated in Table 2. Contours of velocities were chosen for discussion as they clearly show the physical differences of both models as well as the airflow analysis in the nasal cavities. Obvious differences

TABLE 2: Contours of velocities for both models.

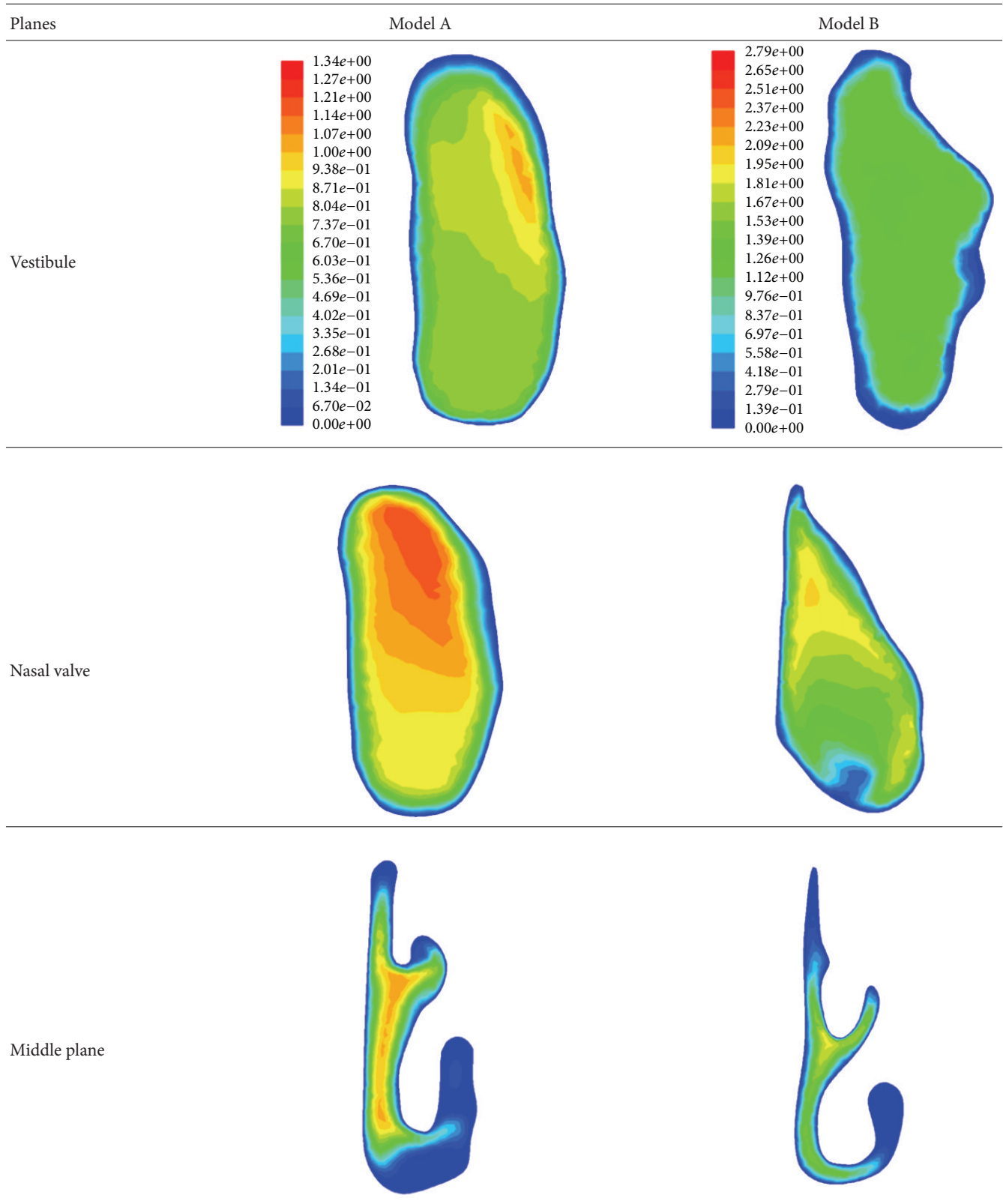


TABLE 2: Continued.

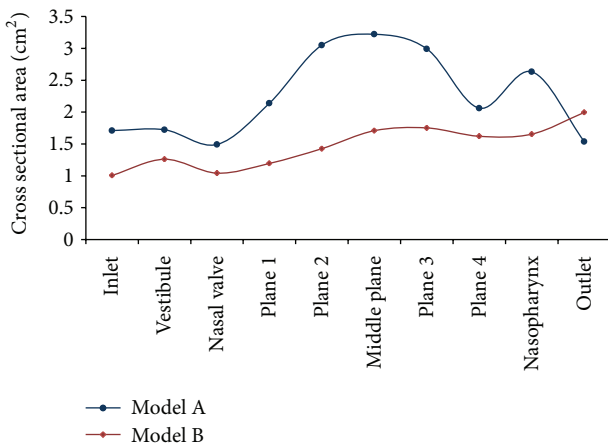
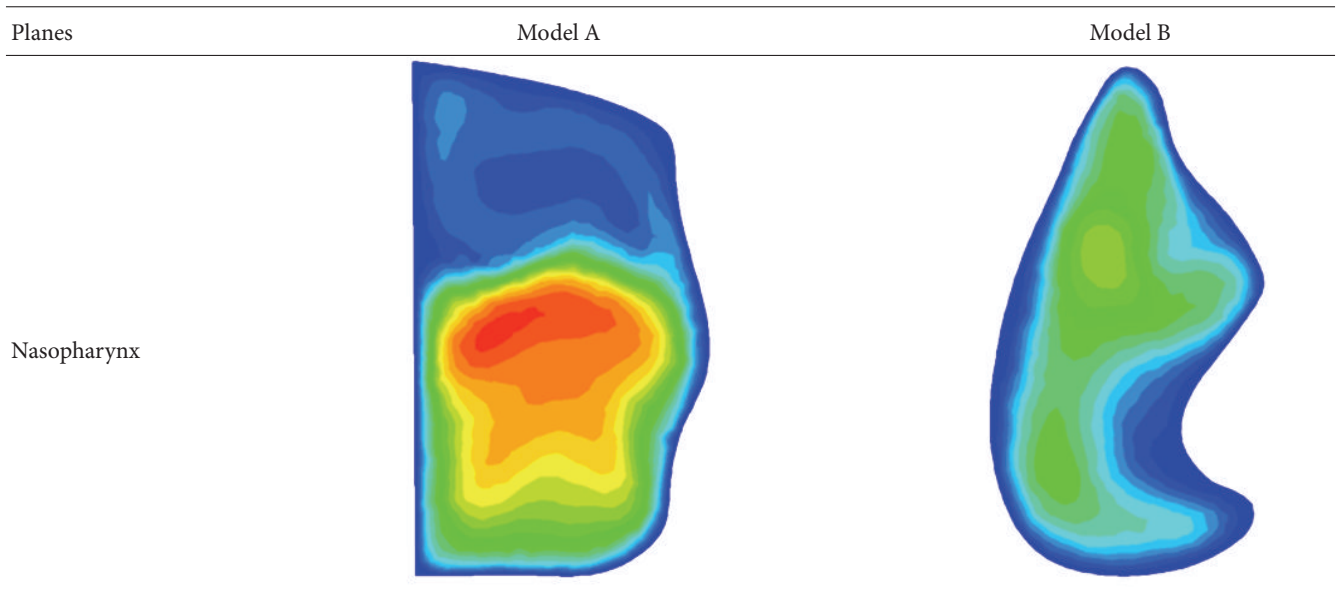


FIGURE 7: Cross-sectional areas along nasal cavities.

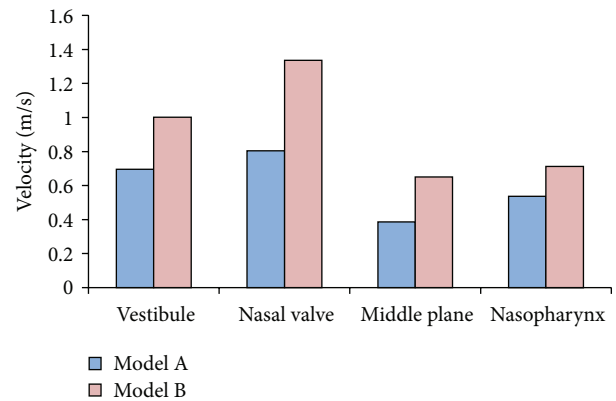


FIGURE 8: Graph of average velocity magnitudes at four cross-sections.

were observed from both models as indicated in Figure 8 and Table 2. All this information was obtained from four main cross-sections along the nasal cavity, which are the vestibule, nasal valve, middle plane, and nasopharynx. Model A shows a vestibule and nasal valve that is more oval in shape while Model B shows an inconsistent shape. Thinner middle plane was observed for Model B compared to Model A, which showed a rounder shape of meatuses. Higher average velocity magnitudes were obtained for Model B for all cross-sections due to the smaller cross-sectional areas as indicated in Figure 6. On the other hand, lower average velocity magnitudes were obtained for Model A due to the generalized averaged model having a larger airway channel compared to Model B. Model B was created based on both female and male models while Model A only focused on Malaysian females. Similar patterns can be examined from both models as the highest velocity resulted from the nasal valve, which is the airflow restrictor before entering the meatus region.

Increment in average velocity was observed from vestibule to nasal valve, which decreased at the middle plane and finally increased again at the nasopharynx as its cross-sections become smaller. Lower velocities were obtained from the middle plane regions as the meatuses function to enlarge the surface area exposed to the air. This increases the heat and moisture exchange inside the nasal cavity. The percentages of differences of velocity magnitudes between both models were relatively high, which are 30% for vestibule, 40% for nasal valve and middle plane, and 25% for nasopharynx. These big differences strongly support the importance of having a standardized model that represents different populations and to generate a standardized model based on a larger group of test subjects.

3.2. Comparisons of Model A with 4 Other Female Models. Comparisons made with Model B from the research of Liu et al. [30] are not sufficient to prove that Model A can be used

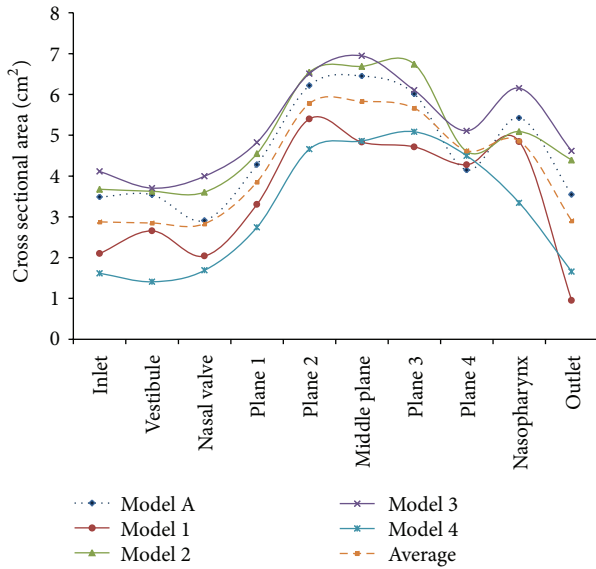


FIGURE 9: Cross-sectional area comparisons of Model A and other 4 models.

to represent an averaged adult Malaysian female nasal cavity. Thus, further investigations were carried out by analysing four female models chosen from the group of 26 subjects by taking into consideration their races and age range. Only four models were chosen for the comparison. Figure 9 shows the cross-sectional areas of all the five models and the average value calculated from the models. Model 1 and Model 4 seem to be smaller in size compared to Model A while Model 2 and Model 3 are slightly larger. The difference between Model A and the calculated average values is less than 20% for all cross-sections. Hence, this methodology was able to create a standardized model that is a very close approximation to the ideal average model. Based on the graphs, all the models possess similar patterns of cross-sectional areas. It was also noticed that an adult Malaysian female has relatively large vestibule and meatuses but a smaller nasopharynx.

Additional analysis was performed to enhance the understanding of this standardized Model A. It is noticed from Figure 10 that Model 1 and Model 4 possess higher average velocity magnitudes while Model 2 and Model 3 show lower average velocity magnitudes compared to Model A. This is due to the cross-sectional areas as indicated in Figure 9. Average velocity magnitudes obtained from Model A were very close to the average values from all the models. Similar patterns of all the models also proved that the models give consistent results of a characterized Malaysian female nasal airflow. Therefore, it was concluded that Model A represents the averaged Malaysian female nasal cavity.

4. Conclusions

A standardized model is required for studies involving human nasal cavities to avoid interindividual differences during comparison of results. The methodology mentioned in this research is applicable for a large group of subjects. Therefore,

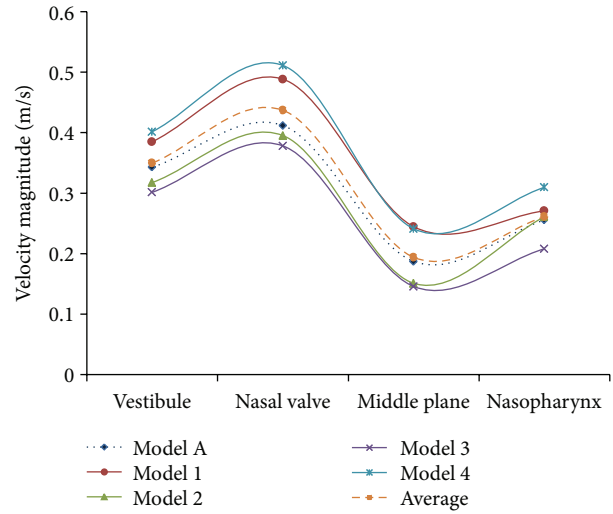


FIGURE 10: Graphs of average velocity magnitudes at four cross-sections along the nasal cavity.

this is a good novelty approach to create a standardized model to represent certain populations. In addition, it is found from this research that there are clear differences between two standardized models from different geographical locations. Future work should be carried out for a larger number of test subjects to obtain a more accurate model. As a conclusion, the model generated from this study was proven to be a good and accurate representation of the adult Malaysian female nasal cavity. This new standardized model is available via corresponding author for various fields of researches.

Conflict of Interests

The authors have no conflict of interests to report.

Acknowledgment

The authors acknowledge the support provided through the Research University (RU) Grant nos. 1001/PAERO/814074 and 1001/PAERO/8045055 by Universiti Sains Malaysia in carrying out this work.

References

- [1] G. J. M. Garcia, N. Bailie, D. A. Martins, and J. S. Kimbell, "Atrophic rhinitis: a CFD study of air conditioning in the nasal cavity," *Journal of Applied Physiology*, vol. 103, no. 3, pp. 1082–1092, 2007.
- [2] D. M. Shelton and N. M. Eiser, "Evaluation of active anterior and posterior rhinomanometry in normal subjects," *Clinical Otolaryngology and Allied Sciences*, vol. 17, no. 2, pp. 178–182, 1992.
- [3] A. H. Suzina, M. Hamzah, and A. R. Samsudin, "Active anterior rhinomanometry analysis in normal adult Malays," *Journal of Laryngology and Otology*, vol. 117, no. 8, pp. 605–608, 2003.
- [4] S. Ishikawa, T. Nakayama, M. Watanabe, and T. Matsuzawa, "Visualization of flow resistance in physiological nasal respiration: analysis of velocity and vorticities using numerical

- simulation,” *Archives of Otolaryngology—Head and Neck Surgery*, vol. 132, no. 11, pp. 1203–1209, 2006.
- [5] I. Weinhold and G. Mlynski, “Numerical simulation of airflow in the human nose,” *European Archives of Oto-Rhino-Laryngology*, vol. 261, no. 8, pp. 452–455, 2004.
 - [6] D. Elad, M. Wolf, and T. Keck, “Air-conditioning in the human nasal cavity,” *Respiratory Physiology and Neurobiology*, vol. 163, no. 1–3, pp. 121–127, 2008.
 - [7] D. J. Doorly, D. J. Taylor, A. M. Gambaruto, R. C. Schroter, and N. Tolley, “Nasal architecture: form and flow,” *Philosophical Transactions of the Royal Society A*, vol. 366, no. 1879, pp. 3225–3246, 2008.
 - [8] D. J. Doorly, D. J. Taylor, and R. C. Schroter, “Mechanics of airflow in the human nasal airways,” *Respiratory Physiology and Neurobiology*, vol. 163, no. 1–3, pp. 100–110, 2008.
 - [9] G. Xiong, J. Zhan, K. Zuo, J. Li, L. Rong, and G. Xu, “Numerical flow simulation in the post-endoscopic sinus surgery nasal cavity,” *Medical and Biological Engineering and Computing*, vol. 46, no. 11, pp. 1161–1167, 2008.
 - [10] J. H. Lee, Y. Na, S. Kim, and S. Chung, “Unsteady flow characteristics through a human nasal airway,” *Respiratory Physiology and Neurobiology*, vol. 172, no. 3, pp. 136–146, 2010.
 - [11] D. J. Taylor, D. J. Doorly, and R. C. Schroter, “Inflow boundary profile prescription for numerical simulation of nasal airflow,” *Journal of the Royal Society Interface*, vol. 7, no. 44, pp. 515–527, 2010.
 - [12] N. Bailie, B. Hanna, J. Watterson, and G. Gallagher, “An overview of numerical modelling of nasal airflow,” *Rhinology*, vol. 44, no. 1, pp. 53–57, 2006.
 - [13] S. C. Leong, X. B. Chen, H. P. Lee, and D. Y. Wang, “A review of the implications of computational fluid dynamic studies on nasal airflow and physiology,” *Rhinology*, vol. 48, no. 2, pp. 139–145, 2010.
 - [14] M. Zubair, “Review: a critical overview of limitations of CFD modeling in nasal airflow,” *Journal of Medical and Biological Engineering*, vol. 32, article 77, 2012.
 - [15] J. Wen, K. Inthavong, J. Tu, and S. Wang, “Numerical simulations for detailed airflow dynamics in a human nasal cavity,” *Respiratory Physiology and Neurobiology*, vol. 161, no. 2, pp. 125–135, 2008.
 - [16] S. Zachow, A. Steinmann, T. Hildebrandt, and W. Heppt, “Understanding nasal airflow via CFD simulation and visualization,” in *Proceeding of the Computer Aided Surgery Around the Head*, pp. 173–176, Pro Business, 2007.
 - [17] J. Wen, K. Inthavong, Z. F. Tian, J. Y. Tu, C. L. Xue, and C. G. Li, “Airflow patterns in both sides of a realistic human nasal cavity for laminar and turbulent conditions,” in *Proceedings of the 16th Australasian Fluid Mechanics Conference (AFMC ’07)*, pp. 68–74, Gold Coast, Australia, December 2007.
 - [18] T. C. Lai, Y. S. Morsi, and M. Singh, “Numerical characterization of the flow field in a four-generation airway,” *Journal of Mechanics in Medicine and Biology*, vol. 8, no. 1, pp. 55–74, 2008.
 - [19] H. Do, A. A. Owida, W. Yang, and Y. S. Morsi, “Numerical simulation of the haemodynamics in end-to-side anastomoses,” *International Journal for Numerical Methods in Fluids*, vol. 67, no. 5, pp. 638–650, 2011.
 - [20] H. Shi, C. Kleinstreuer, and Z. Zhang, “Laminar airflow and nanoparticle or vapor deposition in a human nasal cavity model,” *Journal of Biomechanical Engineering*, vol. 128, no. 5, pp. 697–706, 2006.
 - [21] K. Inthavong, Z. F. Tian, and J. Y. Tu, “CFD simulations on the heating capability in a human nasal cavity,” in *Proceedings of the 16th Australasian Fluid Mechanics Conference (AFMC ’07)*, pp. 842–847, Gold Coast, Australia, December 2007.
 - [22] K. Zhao, P. W. Scherer, S. A. Hajiloo, and P. Dalton, “Effect of anatomy on human nasal air flow and odorant transport patterns: implications for olfaction,” *Chemical Senses*, vol. 29, no. 5, pp. 365–379, 2004.
 - [23] G. J. M. Garcia, G. Mitchell, N. Bailie, D. Thornhill, J. Watterson, and J. S. Kimbell, “Visualization of nasal airflow patterns in a patient affected with atrophic rhinitis using particle image velocimetry,” *Journal of Physics: Conference Series*, vol. 85, no. 1, Article ID 012032, 2007.
 - [24] C. Croce, R. Fodil, M. Durand et al., “In vitro experiments and numerical simulations of airflow in realistic nasal airway geometry,” *Annals of Biomedical Engineering*, vol. 34, no. 6, pp. 997–1007, 2006.
 - [25] S. Naftali, R. C. Schroter, R. J. Shiner, and D. Elad, “Transport phenomena in the human nasal cavity: a computational model,” *Annals of Biomedical Engineering*, vol. 26, no. 5, pp. 831–839, 1998.
 - [26] S. Naftali, M. Rosenfeld, M. Wolf, and D. Elad, “The air-conditioning capacity of the human nose,” *Annals of Biomedical Engineering*, vol. 33, no. 4, pp. 545–553, 2005.
 - [27] I. Hörschler, C. Brücker, W. Schröder, and M. Meinke, “Investigation of the impact of the geometry on the nose flow,” *European Journal of Mechanics B*, vol. 25, no. 4, pp. 471–490, 2006.
 - [28] V. N. Riazuddin, M. Zubair, M. Z. Abdullah et al., “Numerical study of inspiratory and expiratory flow in a human nasal cavity,” *Journal of Medical and Biological Engineering*, vol. 31, no. 3, pp. 201–206, 2011.
 - [29] J. T. Kelly, A. K. Prasad, and A. S. Wexler, “Detailed flow patterns in the nasal cavity,” *Journal of Applied Physiology*, vol. 89, no. 1, pp. 323–337, 2000.
 - [30] Y. Liu, M. R. Johnson, E. A. Matida, S. Kherani, and J. Marsan, “Creation of a standardized geometry of the human nasal cavity,” *Journal of Applied Physiology*, vol. 106, no. 3, pp. 784–795, 2009.
 - [31] S. K. Kim and Y. R. Son, “An investigation on airflow in abnormal nasal cavity by PIV,” in *Proceedings of the PSFVIP-4*, June 2003.
 - [32] Y. Liu, E. A. Matida, J. Gu, and M. R. Johnson, “Numerical simulation of aerosol deposition in a 3-D human nasal cavity using RANS, RANS/EIM, and LES,” *Journal of Aerosol Science*, vol. 38, no. 7, pp. 683–700, 2007.
 - [33] S. K. Kim and S. K. Chung, “An investigation on airflow in disordered nasal cavity and its corrected models by tomographic PIV,” *Measurement Science and Technology*, vol. 15, no. 6, pp. 1090–1096, 2004.
 - [34] M. Zubair, V. N. Riazuddin, M. Z. Abdullah et al., “Airflow inside the nasal cavity: visualization using computational fluid dynamics,” *Asian Biomedicine*, vol. 4, no. 4, pp. 657–661, 2010.
 - [35] I. Hahn, P. W. Scherer, and M. M. Mozell, “Velocity profiles measured for airflow through a large-scale model of the human nasal cavity,” *Journal of Applied Physiology*, vol. 75, no. 5, pp. 2273–2287, 1993.
 - [36] R. A. Segal, G. M. Kepler, and J. S. Kimbell, “Effects of differences in nasal anatomy on airflow distribution: a comparison of four individuals at rest,” *Annals of Biomedical Engineering*, vol. 36, no. 11, pp. 1870–1882, 2008.

- [37] I. Hörschler, M. Meinke, and W. Schröder, “Numerical simulation of the flow field in a model of the nasal cavity,” *Computers and Fluids*, vol. 32, no. 1, pp. 39–45, 2003.
- [38] S. K. Kim and J. R. Haw, “An investigation on airflow in pathological nasal airway by PIV,” *Journal of Visualization*, vol. 7, no. 4, pp. 341–348, 2004.
- [39] C. Xu, S. Sin, J. M. McDonough et al., “Computational fluid dynamics modeling of the upper airway of children with obstructive sleep apnea syndrome in steady flow,” *Journal of Biomechanics*, vol. 39, no. 11, pp. 2043–2054, 2006.
- [40] F. Chometon, P. Gillieron, J. Laurent et al., “Aerodynamics of nasal airways with application to obstruction,” in *Proceedings of the 6th Triennial International Symposium on Fluid Control, Measurement and Visualization*, pp. 65–71, 2000.
- [41] K. Hemtiwakorn, N. Phoocharoen, S. Tungjitusolmun, and C. Pintavirooj, “Nasal airflow simulation in human using a computational fluid dynamics (CFD),” in *Proceedings of the 2nd Biomedical Engineering International Conference (BMEiCON '09)*, 2009.
- [42] S. Zachow, A. Steinmann, T. Hildebrandt, R. Weber, and W. Heppt, “CFD simulation of nasal airflow: towards treatment planning for functional rhinosurgery,” *International Journal of Computer Assisted Radiology and Surgery*, vol. 1, no. 7, pp. 165–167, 2006.
- [43] K. Smith, *CFD analysis of pressure and flow characteristics of the human nose [Degree of Bachelor of Science]*, Worcester Polytechnic Institute.